UNIVERSITÀ DI PARMA

UNIVERSITÀ DEGLI STUDI DI PARMA

DOTTORATO DI RICERCA IN SCIENZA E TECNOLOGIA DEI MATERIALI

XXXVI CICLO

Molecular functional materials: molecules and aggregates towards the thermodynamic limit

Coordinatore
Prof. Enrico Dalcanale

Relatore
Prof.ssa Anna Painelli

Dottorando
Davide Giavazzi

Anni accademici 2020/21 - 2022/2023

Contents

Introduction

Molecular functional materials are in the spotlight of scientific research as the most promising path towards innovative applications in sustainable and recyclable optoelectronic devices, in bioimaging, sensing, photonics, teleommunications etc.[1–11] The virtually infinite possibilities offered by organic synthesis allow for an extremely fine tuning of the molecular properties for improved performances. In this context, theoretical modeling is an essential tool to guide the synthesis, providing clear design strategies for optimized systems. Quantum chemical calculations, available to the scientific community in a large number of software packages, represent one of the most successful and widely exploited approaches to address molecular systems. However, the collective properties of a material are not simply the sum of molecular properties[12] and therefore are often beyond the scope of standard computational tools. A material has to be considered as a whole, as a macroscopic thermodynamic object, and a proper treatment of the interaction with the environment is crucial in pushing a microscopic molecular system *towards the thermodynamic limit*.

Two issues in this respect must be faced. The first and most generally recognized issue falls under the broad definition of *environmental effects*. As aforementioned, the properties of a molecular system are determined not just by the properties of the molecules themselves, as calculated, e.g., via *gas phase ab initio* calculations, but are crucially affected by intermolecular interactions. Wildly different environments define the most rich and diverse array of phenomena. The variability is substantial, ranging, for example, from liquid solution to a molecular dispersion in a solid matrix, from a completely disordered amorphous phase to ordered aggregates and crystals. Polar solvation dynamics, static and dynamical disorder, excitonic effects are just some examples of the many possible phenomena that determine the photophysics of the material and its properties like, e. g., charge transport and mobility and energy transfer.

A second, more subtle issue arises from the fact that materials are macroscopic systems, so that a reliable and complete description of their behavior and properties cannot be obtained focusing on the microscopic domain of molecular quantum mechanics, but requires entering the fascinating world of *open quantum systems*[13], as to effectively connect the microscopic quantum realm of a single (or a few) molecule and the macroscopic world. Energy dissipation is crucial to bridge the gap between quantum mechanics and thermodynamics. An explicit quantum mechanical treatment of a system large enough to ensure a realistic evolution of energy fluxes is clearly unfeasible. Open quantum system approaches offer an elegant strategy to overcame this limit. In few words, out of the macroscopic object a *system* is identified, corresponding to the portion of the object or to the subset of degrees of freedom of interest. This system interacts with the rest of the world, *the bath*, that acts as a thermal reservoir.

In this thesis, both the abovementioned issues are faced with reference to a specific family of molecular systems, the so-called charge transfer

(CT) dyes. CT dyes are a wide class of chromophores whose low energy physics is successfully modeled by *essential state models* (ESMs), where few electronic states are coupled to few effective vibrational coordinates in a non-adiabatic picture.[14–22] Specifically, environmental effects on the photophysics of CT dyes in different environments are addressed in the next chapters. The journey is divided in two main parts. In the first part the world of open quantum systems is entered to describe the relaxation of a single photoexcited chromophore in gas phase, in solution or in solid matrices. The second part is then dedicated to molecular aggregates and crystals.

In chapter 1, the well known and widely applied ESM for a polar (donor-acceptor) dye is extended to describe the relaxation dynamics following coherent photoexcitation. To this aim the Redfield approach to open quantum systems is adopted.[23, 24] Subtleties and technicalities of the coupling with the bath are carefully analyzed setting a solid basis for subsequent work. The approach is validated *via* simulations of time resolved emission spectra.

In chapter 2 the model is extended to account for polar solvation. The polar environment is treated classically as an overdamped coordinate whose dynamics is governed by the Smoluchowski equation. The model is applied to investigate the static and dynamical dielectric properties of organic amorphous matrices commonly used as dispersion media for the emitters in organic light emitting diodes (OLEDs). The simulation of time-resolved emission spectra of a solvatochromic polar dye (a microscopic polarity sensor) in solvents and solid amorphous matrices of different polarity validates the model and allows to extract for the first time significant information about the relaxation times of these materials, opening a novel perspective on solid state solvation.

Chapter 3 initiates the second part of the thesis, introducing the world of molecular aggregates and presenting the celebrated Frenkel-Holstein (FH) Hamiltonian for aggregates of molecules interacting via electrostatic forces.[25–29] Special focus is put on the interplay between nearest neighbor and next-nearest neighbor interactions in defining the vibronic bandshapes in absorption spectra. The FH Hamiltonian is then used to simulate polarized absorbance spectra of crystalline thin films of SQIB, a squaraine dye suited for photovoltaic applications.[30–37]

In chapter 4 molecular aggregates are addressed in the framework of essential state models, making a clear connection with the standard exciton model discussed in chapter 3. The Redfield relaxation model set up in chapter 1 is applied to dimers of dipolar chromophores in a unified and comprehensive picture able to describe both exciton delocalization in homodimers and resonance energy transfer in heterodimers.

In chapter 5, bigger and chiral aggregates are addressed, tackling the problem of chiral proline-derived squaraine aggregates. Squaraines represent a remarkable family of quadrupolar dyes whose aggregates show diverse and interesting properties, including the panchromatic absorption spectrum of nanoparticles and thin films. The general picture is far from clear, with the origin of these peculiar features being alternatively attributed to either disorder or to intermolecular charge transfer (ICT) interactions. A new set of experimental data comprising absorption and circular dichroism spectra of a series of chiral proline-derived squaraine

aggregates adds a further piece to the puzzle. In the attempt to elucidate the role of disorder and intermolecular charge transfer, an essential state model extended to account for ICT is used to address chiroptical properties of the aggregates at hand. While a firm conclusion is not yet reached, significant insights are obtained about the physics of these intriguing and fascinating systems.

Part I

Relaxation dynamics for a single molecule

1

Understanding how an excited molecule dissipates energy after (photo)-excitation is a central topic in molecular spectroscopy, to address both time-resolved experiments[38–43] and spectral lineshapes in steady-state experiments.[44] On a more fundamental vein, relaxation phenomena play a pivotal role when connecting the microscopic world of quantum mechanics with the macroscopic world of thermodynamics:[45] a deep understanding and control of relaxation processes will allow for the design of molecular and supramolecular systems with predefined relaxation patterns that could be used to manipulate the energy fluxes at the microscopic level.[46, 47]

To account for energy dissipation the fascinating world on open quantum systems has to be entered, where the molecular system of interest is somehow coupled to the surrounding environment. Several approaches are available to couple a molecular system to a thermal bath, the oldest and simplest ones, relying on a perturbative treatment of a Markovian bath, are due to Redfield[23] and Lindblad.[48] More advanced approaches have been proposed,[49], among which the numerically exact hierarchical equation of motion (HEOM) approach plays a prominent role. The HEOM, a computationally demanding technique, has been applied successfully in several cases[49–53] but, typically, molecular vibrations are not explicitly included into the system, but are clamped into the bath. On the other hand, the less demanding Redfield model is widely exploited up to these days,[54–60] particularly to simulate spectroscopic properties of systems where vibrational coupling is prominent.

Vibrational degrees of freedom, allowing for the exchange of small energy parcels with the surrounding, play a major role in molecular relaxation. When interested in the relaxation of electronic states, vibrations can be included in the thermal bath, leading to simple and flexible approaches.[50, 53, 61] However, following this strategy the vibrational relaxation occurring e.g. after coherent excitation cannot be accounted for and it is not possible to address vibrational spectra. Moreover, as recently demonstrated by the experimental observation of vibronic coherence transfer in the bacterial reaction center,[62] specific vibrational states are directly involved in the coherence transfer process, leading to a behavior that cannot be captured in models where molecular vibrations are clamped in the spectral density. Finally, some molecular vibrations are strongly coupled to the electronic system, making it impossible to adopt relaxation models, like e.g. the Redfield model, that only works in the weak-coupling regime.[23, 53, 63]

Here a model is presented to address relaxation dynamics as needed to calculate steady-state and time-resolved optical spectra of a large family of dyes, called charge-transfer (CT) or donor-acceptor (DA) dyes. These dyes are extensively studied for their solvatochromic behavior,[15, 64] their large NLO responses,[65–68] as fluorescent labels in microscopy

The work presented in this chapter is published in *Phys. Chem. Chem. Phys.*, *24* (9), 5555-5563, **2022**.

applications,[69, 70] and as microscopic polarity sensors.[64, 71, 72] The Redfield approach to open quantum systems is adopted to account for energy dissipation and a careful analysis of the model is presented in order to define solid and reliable guidelines to deal with this delicate topic.

This chapter is structured as follows: in section 1.1 a general introduction to quantum dynamics and open quantum systems is proposed, together with a focus on the Redfield approach. Section 1.2 presents the adopted model for the molecular system. In section 1.3 then relaxation dynamics of such a system is investigated exploring different possibilities for the coupling with the environment. The analysis continues in section 1.4, where the model is extended to account for several coupled vibrational modes, and in section 1.5 the calculation of absorption and time-resolved emission spectra is addressed. Finally, section 1.6 concludes the chapter.

1.1 Open quantum systems: a general introduction

1.1.1 Density matrix and Liouville-von Neumann equation

Wavefunctions and Schrödinger equation

In quantum mechanics the state of a system is represented by a normalized vector in the Hilbert space. To build the desired space and to represent and manipulate a state, a basis set has to be defined. A wise choice is to work with an orthonormal basis set, i. e. a set of mutually orthogonal normalized functions. Given $\{|\phi_n\rangle\}$ the chosen orthonormal basis set (Dirac notation is used), the *wavefunction* representing the state $|\psi\rangle$ and defining all its properties is expressed in the general form of a linear combination of the basis functions:

$$|\psi\rangle = \sum_n c_n |\phi_n\rangle. \tag{1.1}$$

Linear Hermitian operators are associated to the physical observables, whose expectation values are calculated as $\langle\psi|\hat{A}|\psi\rangle$ ($\hat{A}$ being a general Hermitian operator). The time evolution of a quantum mechanical state is dictated by the notorious Schrödinger equation

$$\frac{\partial|\psi(t)\rangle}{\partial t} = -\frac{i}{\hbar}H|\psi(t)\rangle \tag{1.2}$$

where $\hbar$ is the Planck constant and H is the quantum Hamiltonian, i. e. the operator associated with the energy of the considered system. If the Hamiltonian is time independent, eq. 1.2 is easily integrated:

$$|\psi(t)\rangle = |\psi(0)\rangle e^{-\frac{i}{\hbar}Ht}. \tag{1.3}$$

Accordingly, once a system is prepared in a given state $|\psi(0)\rangle$, the Hamiltonian fully defines the time evolution of the system. It is generally convenient to choose as a basis set the eigenstates of the Hamiltonian, i. e. the solutions of the eigenvalue equation[1]:

1: Eq. 1.4 is also referred to as the *time-independent* (or *stationary*) Schrödinger equation.

$$H|n\rangle = E_n|n\rangle. \tag{1.4}$$

On this basis, $|\psi(t)\rangle$ reads:

$$|\psi(t)\rangle = \sum_n |n\rangle\langle n|\psi(t)\rangle = \sum_n c_n(t)|n\rangle \tag{1.5}$$

where the time dependence is acquired by the coefficients of the wavefunction $c_n(t)$, the states $|n\rangle$ being time independent. By plugging eq. 1.5 in eq. 1.2, the following expression for $|\psi(t)\rangle$ is finally obtained:

$$|\psi(t)\rangle = \sum_n c_n(0)e^{-\frac{i}{\hbar}E_n t}|n\rangle \tag{1.6}$$

where $c_n(0)$ are the coefficients of the initial state $|\psi(0)\rangle$.

The density matrix

A wavefunction fully defines a quantum state and all its properties, however it is often more convenient (and it will hopefully be clear why by the end of this section) to use another object to represent a state. This object is the density matrix (or density operator) ρ, that for a *pure state*[2] $|\psi\rangle$ is defined as the projector:

2: By definition, a pure state is a state described by a wavefunction.

$$\rho = |\psi\rangle\langle\psi|. \tag{1.7}$$

Consider, for the sake of clarity, a pure state $|\psi\rangle$ represented on the three dimensional basis $\{|n\rangle, n = 1,2,3\}$, the wavefunction and the corresponding density matrix read:

$$|\psi\rangle = \begin{pmatrix} c_1 \\ c_2 \\ c_3 \end{pmatrix}, \qquad \rho = \begin{pmatrix} c_1c_1^* & c_1c_2^* & c_1c_3^* \\ c_2c_1^* & c_2c_2^* & c_2c_3^* \\ c_3c_1^* & c_3c_2^* & c_3c_3^* \end{pmatrix}. \tag{1.8}$$

If it is true that a wavefunction completely defines a state, it is not true that all the states can be described by a single wavefunction. In fact, most often the state of a system is not pure, being rather represented as a statistical mixture of states, with probability p_k of being in state $|\psi_k\rangle$. For this *mixed state*, the density matrix is:

$$\rho = \sum_k p_k|\psi_k\rangle\langle\psi_k|. \tag{1.9}$$

where of course $\sum_k p_k = 1$. A mixed state is therefore a state that cannot be described by a single wavefunction.

Density matrices offer an effective tool to deal with mixed states, a particularly useful feature to describe systems approaching the macroscopic (read thermodynamic) limit. For a pure state in a n-th dimensional space, a wavefunction-based and a density matrix-based description of the system require the same amount of information, i. e. the n expansion coefficients. A wavefunction-based description of a statistical mixture would require the knowlegde of the the n coefficients for each one of the k wavefuntions and relevant probabilities, while the density matrix allows to deal with whatever degree of complexity and dimension with just n^2 numbers. Part of the information is clearly lost (the explicit expression of

all the wavefunctions and the associate probabilities), but in most cases the complete information is either too much to be handled or simply not known.[3]

3: Eq 1.9 is just a definition of the density operator, in most of the practical cases one builds the operator relying on either experimental or theoretical assumptions, without knowing all coefficients and probabilities.

Given the definition in eq. 1.9, the expectation value of a generic operator $\hat{A}$ is calculated as:

$$\langle \hat{A} \rangle = \sum_k p_k \langle \psi_k | \hat{A} | \psi_k \rangle = Tr\{\rho \hat{A}\} = Tr\{\hat{A}\rho\}. \tag{1.10}$$

For both mixed and pure states, the density matrix shows some characteristic properties:

- is Hermitian;
- the diagonal elements ρ_{aa} are nonnegative. Since they represent the probabilities to find the system in the relevant basis states, they are called *populations*, while off diagonal elements ρ_{ab} are generally complex and are called *coherences*;
- $Tr\{\rho\} = 1$, with $Tr\{\cdot\}$ indicating the sum over the diagonal elements;
- $Tr\{\rho^2\} \leq 1$, where the equality holds true for pure states.

The *purity* of a system is therefore defined as $P = Tr\{\rho^2\}$, while the *coherence* is calculated as $C = P - \sum_{aa} \rho_{aa}^2$.

Liouville-von Neumann equation

4:
$$\frac{\partial |\psi(t)\rangle}{\partial t} = -\frac{i}{\hbar} H |\psi(t)\rangle$$
$$\frac{\partial \langle \psi(t)|}{\partial t} = \frac{i}{\hbar} \langle \psi(t)| H$$

Given the definition in eq. 1.9 and exploiting the Schrödinger equation[4], the temporal evolution of the density matrix can be evaluated as:

$$\begin{aligned} \frac{\partial \rho(t)}{\partial t} &= \sum_k p_k \frac{\partial |\psi_k(t)\rangle}{\partial t} \langle \psi_k(t)| + \sum_k p_k |\psi_k(t)\rangle \frac{\partial \langle \psi_k(t)|}{\partial t} \\ &= -\frac{i}{\hbar} H \sum_k |\psi_k(t)\rangle\langle\psi_k(t)| + \frac{i}{\hbar} \sum_k |\psi_k(t)\rangle\langle\psi_k(t)| H \\ &= -\frac{i}{\hbar} (H\rho(t) - \rho(t)H) \end{aligned} \tag{1.11}$$

yielding the Liouville-von Neumann equation:

$$\frac{\partial \rho(t)}{\partial t} = -\frac{i}{\hbar} [H, \rho(t)] \tag{1.12}$$

with a general solution in the case of a stationary (time independent) Hamiltonian

$$\rho(t) = e^{-\frac{i}{\hbar} Ht} \rho(0) e^{\frac{i}{\hbar} Ht}. \tag{1.13}$$

5: Sandwiching eq. 1.12 between two eigenstates of H one obtain:

$$\begin{aligned} \frac{\rho_{ab}}{\partial t} &= -\frac{i}{\hbar} (\langle a|H\rho|b\rangle - \langle a|\rho H|b\rangle) \\ &= -\frac{i}{\hbar} (E_a \langle a|\rho|b\rangle - E_b \langle a|\rho|b\rangle) \\ &= -i \frac{E_a - E_b}{\hbar} \rho_{ab} = -i\omega_{ab}\rho_{ab} \end{aligned}$$

that can be integrated to give eq. 1.14.

If the system is represented on the basis of the eigenstates of the stationary H, the time evolution of the density matrix elements is[5]:

$$\rho_{ab}(t) = \rho_{ab}(0) e^{-i\omega_{ab}t} \tag{1.14}$$

where $\omega_{ab} = (E_a - E_b)/\hbar$. Therefore for a given initial state $\rho(0)$ populations (i. e. the diagonal elements) are constant and coherences (off-diagonal elements) oscillate in time with a frequency equal to the energy difference between the respective diagonal states.
The Liouville-von Neumann equation is the analog of the Schrödinger

equation for the density matrix. This analogy becomes even more clear when it is rewritten in the form:

$$\frac{\partial \rho(t)}{\partial t} = -\frac{i}{\hbar}\mathscr{L}\rho(t) \tag{1.15}$$

where $\mathscr{L} = [H, \cdot]$ is the Liouville superoperator, a four indices tensor operating on a matrix. In the explicit expression for the ab matrix element eq. 1.15 reads:

$$\frac{\partial \rho_{ab}}{\partial t} = -\frac{i}{\hbar}\sum_{c,d}\mathscr{L}_{ab,cd}\rho_{cd} \tag{1.16}$$

with

$$\mathscr{L}_{ab,cd} = H_{ac}\delta_{bd} - H^*_{bd}\delta_{ac}. \tag{1.17}$$

1.1.2 Towards open quantum systems: the reduced density matrix

The Schrödinger or the Liouville-von Neumann equation allow to calculate the time evolution of the system of interest. Once defined a Hamiltonian H, all the rules are set, but here lies at the same time both the most elegant and powerful aspect of these equations and their biggest limitation. How many degrees of freedom do you need in order to set up a realistic simulation? A system evolving in time according to the Liouville equation is a *closed* system: it is entirely defined by its Hamiltonian H and it does not exchange neither energy nor matter with the outside. Actually, there is no outside. Reality is a bit more complex: once defined a system (a molecule for example) one will find that in the real world the chosen system is interacting with something else (e. g., solvent molecules for a molecule in solution) and regardless of how much effort is put in including a more and more detailed description of the system, there will always be something outside (the solvent interacts with the walls of the container, heat is exchanged with the surrounding air and so on...). Therefore in principle, in order to apply the equations presented in the previous section, a reliable simulation would be obtained only in the extreme case in which the whole universe is explicitly accounted for and included in the Hamiltonian. The answer to our question: too many degrees of freedom to be handled. This is clearly an exaggeration and the whole universe doesn't have to be accounted for, but yet the number of degrees of freedom that can be explicitly treated is fairly limited and even a conceptually simple process like energy dissipation due to the interaction with the solvent is non tractable with a closed model. Hence, the need to move from *closed* to *open quantum systems*. In an open quantum system only a portion of the universe is observed and explicitly described by the Hamiltonian but the interaction with the surrounding environment is somehow taken into account, even if not explicitly included. New equations of motion have to be developed for such open systems, but at first a proper tool has to be defined to describe the system. This tool is the *reduced density matrix*.

Once defined the system of interest (S), the rest of the universe can be dubbed as a generic bath (B) and the total Hamiltonian can be written in the form:

$$H = H_S(q_S) + H_B(q_B) + H_I(q_S, q_B) \tag{1.18}$$

where q_S and q_B are the degrees of freedom of the system and bath, respectively, and H_I defines the system-bath interaction. A convenient basis set to represent the whole problem is the direct product between the eigenstates of H_S and H_B (indicated with latin and greek letters, respectively).[6] Since the interest is in the system, only system observables (i. e., only depending on the system degrees of freedom) are addressed. The expectation value of the general system observable $\hat{A}(q_S)$ is:

6: $H_S(q_S)|a\rangle = E_a|a\rangle$
$H_B(q_B)|\alpha\rangle = E_\alpha|\alpha\rangle$

$$\begin{aligned}\langle\hat{A}(q_S)\rangle &= Tr\{\rho\hat{A}(q_S)\} = \sum_{a,b}\sum_{\alpha,\beta}\langle a\alpha|\rho|b\beta\rangle\langle b\beta|\hat{A}(q_S)|a\alpha\rangle \\ &= \sum_{a,b}\sum_{\alpha,\beta}\langle a\alpha|\rho|b\beta\rangle\langle b|\hat{A}(q_S)|a\rangle\langle\beta|\alpha\rangle \\ &= \sum_{a,b}\sum_{\alpha}\langle a\alpha|\rho|b\alpha\rangle\langle b|\hat{A}(q_S)|a\rangle\end{aligned} \tag{1.19}$$

where the orthonormality of the bath eigenstates, $\langle\beta|\alpha\rangle = \delta_{\alpha,\beta}$, has been used. The reduced density matrix element ab is now defined as:

$$\sigma_{ab} = \sum_{\alpha}\langle a\alpha|\rho|b\alpha\rangle = Tr_B\langle a|\rho|b\rangle \tag{1.20}$$

where Tr_B is the partial trace over the bath degrees of freedom. Eq. 1.19 therefore yields:

$$\langle\hat{A}(q_S)\rangle = \sum_{a,b}\sum_{\alpha}\langle a\alpha|\rho|b\alpha\rangle\langle b|\hat{A}(q_S)|a\rangle = \sum_{a,b}\sigma_{ab}A_{ba}(q_S) = Tr\{\sigma\hat{A}(q_S)\}. \tag{1.21}$$

Given the definition in eq 1.20, the reduced density matrix maintains the same properties as the total matrix ρ exposed in the previous section and most importantly it maintains the dimension of the system, but yet due to the trace over the bath degrees of freedom it contains information about the interaction with the bath.

It is worth to point out that the definition of the reduced density matrix does not depend on either the strength of the system-bath interaction or on its nature. As long as the total Hamiltonian can be written in the form of eq. 1.18 and the observables of interest only depend on the system degrees of freedom, the picture holds true. The definition of the boundary between the system and the bath is completely arbitrary. In the most intuitive scenario the system is a molecule or a group of molecules and the bath the surrounding environment, but one might also be interested for example in just selected degrees of freedom of a molecule, like e. g. its electronic degrees of freedom, plugging into the bath the molecular vibrations.

1.1.3 Dissipative dynamics of an open quantum system: Redfield master equation

The Liouville equation (eq. 1.15) governs the time evolution of a closed system and for the Hamiltonian in eq. 1.18 it can be written as:

$$\frac{\partial\rho(t)}{\partial t} = -\frac{i}{\hbar}\left(\mathscr{L}_S + \mathscr{L}_B + \mathscr{L}_I\right)\rho(t) \tag{1.22}$$

where the Liouville superoperator $\mathcal{L}$ has been partitioned in the three contributions of the Hamiltonian in eq. 1.18. Eq. 1.22 can be manipulated to obtain the equation of motion for the reduced density matrix of the system. To this end, a superoperator $\mathcal{P}$ is defined that projects the total density matrix ρ on the states of the system, giving a direct product of the system reduced density matrix and the thermalized equilibrium bath reduced density matrix ρ_B^{eq}:

$$\mathcal{P}\rho = \rho_B^{eq} \otimes Tr_B\{\rho\} = \rho_B^{eq} \otimes \sigma. \tag{1.23}$$

Along with the complementary superoperator $\mathcal{Q} = 1 - \mathcal{P}$, $\mathcal{P}$ is used to derive out of eq. 1.22 the time evolution of $\mathcal{P}\rho$ and hence of σ. The following exact *generalized master equation* (also known as the Nakajima-Zwanzig equation [73]) is obtained:

$$\frac{\partial\sigma(t)}{\partial t} = -\frac{i}{\hbar}\mathcal{L}_S\sigma(t) + \left(\frac{i}{\hbar}\right)^2 \int_0^t d\tau \mathcal{G}(\tau)\sigma(t-\tau) \tag{1.24}$$

where the first term of the right-hand side describes the Liouville-von Neumann time evolution for the system and all the effects due to the interaction with the bath fall in the second term, with the so-called friction kernel $\mathcal{G}(\tau)$ reading:

$$\mathcal{G}(\tau) = Tr_B\{\mathcal{L}_I e^{\tau\mathcal{Q}(\mathcal{L}_S+\mathcal{L}_B+\mathcal{L}_I)}\mathcal{Q}\mathcal{L}_I\rho_B^{eq}\}. \tag{1.25}$$

Eq. 1.24 is exact and essentially as hard to solve as the Liouville equation for the total operator ρ since the complete dynamics of the bath is still included. Therefore, approximations are introduced to make the problem treatable. In particular:

- the system-bath coupling $\mathcal{L}_I$ is neglected in eq. 1.25 (Born approximation). In this way only second order terms in the system-bath coupling H_I are kept. Clearly this approximation is valid only when the system-bath coupling is weak;
- $\sigma(t-\tau)$ is replaced by $\sigma(t)$, assuming that $\mathcal{G}(\tau)$ decays faster compared to the evolution of $\sigma(t)$ (Markov approximation);
- the upper limit of the integral in eq. 1.24 is extended to infinity, assuming a fast decay of the integrand (i. e. a short bath correlation time). This means that the bath is considered to be always at the equilibrium and the relaxation tensor become time independent (stationary relaxation tensor approximation).

The integral in eq. 1.24 depends now only on τ and can be evaluated independently of the state of the subsystem $\sigma(t)$ to give the Redfield master equation:

$$\frac{\partial\sigma(t)}{\partial t} = -\frac{i}{\hbar}\mathcal{L}_S\sigma(t) + \mathcal{R}\sigma(t) \tag{1.26}$$

where the Redfield relaxation tensor $\mathcal{R}$ contains all the information about the influence of the bath on the system. The time evolution of the matrix elements of σ, expanded on the basis of the eigenstates of the system H_S, is given by the set of coupled linear differential equations:[23, 54–56, 74, 75]

$$\frac{\partial}{\partial t}\sigma_{ab}(t) = -i\omega_{ab}\sigma_{ab}(t) + \sum_{c,d}\mathcal{R}_{ab,cd}\sigma_{cd}(t) \tag{1.27}$$

where $\omega_{ab} = \frac{E_a - E_b}{\hbar}$ and the terms of the Redfield tensor $\mathcal{R}_{ab,cd}$ can be arranged as:

$$\mathcal{R}_{ab,cd} = -\delta_{d,b} \sum_e \Gamma^+_{ae,ec} - \delta_{a,c} \sum_e \Gamma^-_{de,eb} + \Gamma^+_{db,ac} + \Gamma^-_{db,ac} \tag{1.28}$$

where the Fourier-Laplace transforms of correlation functions of the system-bath coupling operator matrix elements (also known as the *kinetic coefficients*) are introduced:

$$\Gamma^+_{db,ac} = \frac{1}{\hbar^2} \int_0^\infty d\tau e^{-i\omega_{ac}\tau} \langle H^I_{db}(\tau) H^I_{ac}(0) \rangle_b \tag{1.29}$$

$$\Gamma^-_{db,ac} = \frac{1}{\hbar^2} \int_0^\infty d\tau e^{-i\omega_{db}\tau} \langle H^I_{db}(0) H^I_{ac}(\tau) \rangle_b \tag{1.30}$$

where H^I_{ij} is the ij matrix element of the interaction Hamiltonian $\hat{H}_I$. The angle brackets $\langle \cdot \rangle_b$ indicate the average over the equilibrium bath state and

$$H^I_{ij}(\tau) = e^{\frac{i}{\hbar}\hat{H}_B \tau} \hat{H}^I_{ij} e^{-\frac{i}{\hbar}\hat{H}_B \tau}, \tag{1.31}$$

$\hat{H}_B$ being the bath Hamiltonian.

The form of the tensor $\mathcal{R}_{ab,cd}$ offers a neat interpretation of the different components of the dynamics: $\mathcal{R}_{aa,cc}$ terms describe a population transfers among the system states a and c, $\mathcal{R}_{ab,ab}$ decoherence phenomena, $\mathcal{R}_{aa,cd}$ and $\mathcal{R}_{ab,cc}$ population to coherence and coherence to population transfer, respectively, and $\mathcal{R}_{ab,cd}$ coherence to coherence transfer.

Since the dimension of the Redfield tensor grows with the fourth power of the dimension of the system, accounting for all the $\mathcal{R}_{ab,cd}$ terms becomes quickly computationally very expensive. A series of approximations can be done in this respect, only accounting for the $\mathcal{R}_{ab,cd}$ terms that are most relevant in the dynamics. In the pseudo non-secular approximation[76] only the terms with $|\omega_{ab} - \omega_{cd}| \leq \alpha$ are accounted for, α being a fixed threshold. The more stringent secular approximation only accounts for the resonant terms, i. e. terms with $|\omega_{ab} - \omega_{cd}| = 0$. If also these resonant terms are neglected the Bloch approximation is recovered, leading to a completely uncoupled evolution of populations and coherences:

$$\frac{\partial}{\partial t}\sigma_{aa}(t) = \sum_c \mathcal{R}_{aa,cc}\sigma_{cc}(t) \tag{1.32}$$

$$\frac{\partial}{\partial t}\sigma_{ab}(t) = -i\omega_{ab}\sigma_{ab}(t) + \mathcal{R}_{ab,ab}\sigma_{ab}(t). \tag{1.33}$$

Finally, it is important to underline that, even if the reduced density matrix approach allows to account for the interaction with the surroundings without the need of an explicit treatment of the environmental degrees of freedom, nevertheless the bath and system-bath interaction Hamiltonians have to be defined and manipulated making the approach phenomenological in nature. The bath Hamiltonian is an effective Hamiltonian and its definition, together with the definition of its interaction with the system, is arbitrary. In this chapter, the process of interest is the relaxation of a (photo)excited charge transfer chromophore and in the next sections, after defining the system and a general form for the bath, different possibilities for the system-bath coupling will be explored

in the spirit of defining reliable guidelines for the effective modeling of molecular relaxation, setting the basis for the investigation of more complex processes in the next chapters.

1.2 The system: a charge transfer dipolar chromophore

Almost all systems investigated in this thesis belong to the large family of charge transfer (CT) dyes. In these molecules, a π-conjugated bridge connects electron donor (D) and electron-acceptor (A) groups in polar ($D-\pi-A$)[14–18], quadrupolar ($D-\pi-A-\pi-D$ or $A-\pi-D-\pi-A$)[18–20] and octupolar ($D(-\pi-A)_3$ or $A(-\pi-D)_3$)[21, 22] geometries. The low-energy physics of these dyes is governed by the charge resonance between D and A groups. Essential state models (ESMs) are a useful tool to comprehensively describe these molecules in a unified framework. In ESMs, a minimal set of electronic states representing the main charge resonating structures of the relevant system is considered. Specifically two, three and four states are required for dipolar, quadrupolar and octuploar chromophores, respectively. To fully characterize the spectroscopic behavior of CT dyes, the model must also include molecular vibrations to account for the geometrical relaxation that accompanies charge resonance.[14, 77–79] Essential state models are semiempirical in nature and have been validated experimentally on a very large number of dyes, succesfully describing their linear and non-linear spectral properties.[15, 79, 80] Moreover, ESMs set the basis to understand solvatochromism[15, 17, 79] of such systems and more generally to rationalize environmental effects in molecular aggregates and crystals.[81–86]

1.2.1 Essential State Model for a DA dye

The system investigated in this chapter is a dipolar chromophore. In a dipolar dye an electron donor (D) and an electron acceptor (A) group are connected *via* a π-conjugated bridge. Figure 1.1 shows the chemical structures of a few selected DA dyes.The molecules resonate between the two limiting structures $D-\pi-A$ and $D^+-\pi-A^-$.[14–18] The essential state model then accounts for two electronic states $|N\rangle$ and $|Z\rangle$, corresponding to the neutral and zwitterionic structures, respectively. The two states are separated by an energy gap $2z_0$ and are mixed by a matrix element $-\tau$. The electronic Hamiltonian reads:

$$\hat{H}_{el} = \begin{pmatrix} 0 & -\tau \\ -\tau & 2z_0 \end{pmatrix} = -\tau\hat{\sigma} - 2z_0\hat{\rho} \tag{1.34}$$

where $\hat{\sigma} = |N\rangle\langle Z| + |Z\rangle\langle N|$ and $\hat{\rho} = |Z\rangle\langle Z|$ are the hopping and ionicity operators and $2z_0$ and τ are semiempirical parameters. The diagonalization of the Hamiltonian gives the two eigenstates as a combination of the basis states:

$$|G\rangle = \sqrt{1-\rho}|N\rangle + \sqrt{\rho}|Z\rangle \tag{1.35}$$

$$|E\rangle = -\sqrt{\rho}|N\rangle + \sqrt{1-\rho}|Z\rangle \tag{1.36}$$

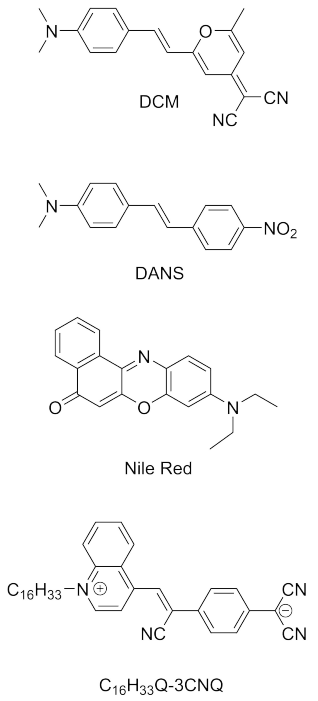

Figure 1.1: Structures of four selected DA dyes. From top to bottom: 4-(dicyanomethylene)-2-methyl-6-(4-dimethylamino-styryl)-4H-pyran (DCM), 4dimethylamino-4'-ntrostilbene (DANS), 9-(diethylamino)-5H-benzo [a]phenoxazin-5-one (Nile Red) and γ-(n-hexadecyl) quinolinium tricyanoquinodimethanide (C_16H_33Q-3CNQ).

where $\rho = \langle G|\hat{\rho}|G\rangle$ measures the degree of charge transfer in the ground state. The ρ value is related to the model parameters as:

$$\rho = \frac{1}{2}\left(1 - \frac{z_0}{\sqrt{z_0^2 + \tau^2}}\right). \tag{1.37}$$

Dyes with $\rho < 0.5$ have a mainly neutral ground state, while dyes with $\rho > 0.5$ have a mainly zwitterionic ground state.
The electric dipole moment operator, necessary to calculate optical spectra and to simulate impulsive excitations, is defined as

$$\hat{\mu} = \begin{pmatrix} 0 & 0 \\ 0 & \mu_0 \end{pmatrix} = \mu_0 \hat{\rho} \tag{1.38}$$

where all matrix elements of the dipole moment operator on the chosen basis are neglected with respect to μ_0, the large dipole moment of the zwitterionic state.[87]

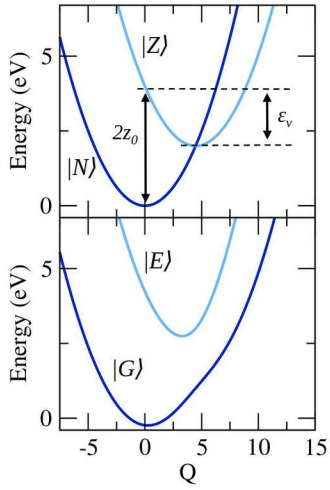

Figure 1.2: Q-dependence of the diabatic (top panel) and adiabatic (bottom panel) energies for the two electronic states.

A single effective vibrational coordinate $\hat{Q}$ is introduced to account for electron-vibration coupling.[14, 78, 79, 88] The two electronic basis states are assigned a harmonic potential energy curve with the same frequency ω_v, but displaced minima. The total Hamiltonian reads:

$$\hat{H}_S = -\tau\hat{\sigma} + \left[2z_0 - \sqrt{\hbar\omega_v \varepsilon_v}\left(\hat{a} + \hat{a}^\dagger\right)\right]\hat{\rho} + \hbar\omega_v\left(\hat{a}^\dagger\hat{a} + \frac{1}{2}\right) \tag{1.39}$$

where the creation and destruction operators are related to the (dimensionless) coordinate as $\hat{Q} = \hat{a} + \hat{a}^\dagger$, the standard vibrational coordinate being $\hat{Q}^s = \sqrt{\frac{\hbar}{2\omega}}\hat{Q}$. The vibrational relaxation energy ε_v measures the energy gained in the $|Z\rangle$ state upon relaxation, as sketched in figure 1.2.

To obtain the eigenstates of the complete system, the problem is treated in a non-adiabatic approach. The Hamiltonian in eq. 1.39 is written on the vibronic basis obtained as the direct product between the two-dimensional electronic basis ($|N\rangle$ and $|Z\rangle$) and the eigenstates of the harmonic oscillator in the last term of eq. 1.39. In order to make the problem numerically tractable the vibrational basis is truncated to the first M eigenstates of the oscillator, with M large enough as to ensure convergence of relevant properties.[89, 90]. A basis state has then the form $|X\rangle|n\rangle$, where X is either N or Z and n, the vibrational quantum number, ranges from 0 to $M-1$. The numerical diagonalization of the resulting Hamiltonian matrix gives the vibronic eigenstates ad eigenvalues of the molecular system. The model for each dye has to be parametrized against experiment (or possibly against *ab initio* results). Typically, model parameters relevant to CT dyes show a limited variability, with $\tau \sim 0.5 - 1.5$ eV, $z \sim -0.2 - 1$ eV, $\varepsilon_v \sim 0.2 - 0.6$ eV, $\hbar\omega_v \sim 0.14 - 0.2$ eV.[14–22]

1.3 Opening the system: experimenting with the coupling to the environment

In section 1.1 the phenomenological nature of relaxation models has been discussed. Here, after defining the bath Hamiltonian, different possibilities for the system-bath interaction are explored and the results are compared and discussed.

A quantum bath constituted by an infinite ensemble of quantum harmonic oscillators is introduced:

$$\hat{H}_B = \sum_i \hbar\omega_i \left(\hat{b}_i^\dagger \hat{b}_i + \frac{1}{2}\right) \tag{1.40}$$

where $\hat{b}_i^\dagger$ and $\hat{b}_i$ are the creation and annihilation operators associated with the i-th bath coordinate, i ranging from one to infinity to cover all possible frequencies. Due to its large dimension, the bath stays undisturbed at thermal equilibrium.

In the most straightforward way, a *linear* coupling is introduced between the molecular vibrational coordinate $\hat{Q}$ and the bath coordinates $\hat{B}_i = \hat{b}_i^\dagger + \hat{b}_i$[7]:

$$\hat{H}_I^{lin} = \sum_i g_i \hat{B}_i \hat{Q} = \sum_i g_i \left(\hat{b}_i^\dagger \hat{d} + \hat{b}_i \hat{d}^\dagger + \hat{b}_i^\dagger \hat{d}^\dagger + \hat{b}_i \hat{d}\right) \tag{1.41}$$

where g_i measures the strength of the coupling between the i-th bath mode and the molecular coordinate.

This interaction Hamiltonian is sometimes simplified only accounting for terms where a quantum is exchanged between the system and the bath (*bilinear* coupling):[63, 91–95]

$$\hat{H}_I^{bil} = \sum_i g_i \left(\hat{b}_i^\dagger \hat{d} + \hat{b}_i \hat{d}^\dagger\right). \tag{1.42}$$

This simplified interaction Hamiltonian however imposes an additional constraint on top of energy conservation (strictly enforced by Redfield equations): if a quantum $\hbar\omega_i$ is destroyed (created) in the bath, not only the energy of the molecular system must increase (decrease) of the same amount (energy conservation), but this must also occur with the concomitant increase (decrease) of one unit in the number of molecular vibrational quanta. This last requirement is implicitly satisfied as long as the molecular system closely resembles a harmonic oscillator, and in this limit it actually reduces to the so-called rotating wave approximation (RWA).[44] However, in strongly anharmonic and/or strongly non-adiabatic systems the two Hamiltonians in eqs. 1.41 and 1.42 are different and the bilinear coupling might kill some important relaxation channels. While not strictly appropriate,[13, 96] the bilinear coupling Hamiltonian in eq. 1.42 is sometimes generally referred to as RWA.

In either eqs. 1.41 and 1.42, the strength of the system-bath interaction is defined by the coupling constants g_i. Since the frequencies of the bath oscillators ω_i are spread all over the frequency axis, it is usual to define

7: As for $\hat{Q}$, $\hat{B}_i$ is a dimensionless coordinate, the corresponding dimensional coordinate being $\hat{B}_i^s = \sqrt{\frac{\hbar}{2\omega_i}}\hat{B}_i$.

the coupling strength in terms of a spectral density function:

$$\mathcal{J}(\omega) = \sum_i |g_i|^2 \delta(\omega - \omega_i). \tag{1.43}$$

In the model presented in section 1.2, the most strongly coupled vibrational modes are explicitly introduced in the system, therefore the bath only describes weakly coupled vibrational modes as well as the interaction with a generic environment like a non-polar solvent (polar solvation is strongly coupled to electrons in DA dyes and will be addressed in chapter 2). In these conditions, a generic smooth form of the spectral density is acceptable.[97] In the simplest case, the same coupling strength is imposed to all bath coordinates, setting the spectral density to a constant:[91, 93–95]

$$\mathcal{J}(\omega) = \frac{\hbar^2}{\pi}\gamma. \tag{1.44}$$

Other shapes for the spectral density are possible. A commonly adopted form is the so called Debye spectral density:[98]

$$\mathcal{J}(\omega) = \frac{\hbar^2}{\pi}\frac{\omega/\omega_c}{1+\omega^2/\omega_c^2}\eta \tag{1.45}$$

where η is a dimesionless parameter that measures the strength of the system-bath coupling and ω_c is the cut-off frequency. In the following, results obtained adopting a *linear* and *bilinear* coupling are compared (eqs. 1.41 and 1.42 respectively), together with the effects of a constant vs. a Debye spectral density.

Once the system-bath interaction is defined in terms of $\hat{H}_I$ and spectral density, closed expressions for the kinetic coefficients $\Gamma^+_{db,ac}$ and $\Gamma^-_{db,ac}$ (eqs. 1.29 and 1.30) and hence for the Redfield tensor (eq. 1.28) can be derived. Assuming a linear system-bath coupling (eq. 1.41) and remembering eq. 1.31, the correlation function in eq. 1.29 gives:

$$\begin{aligned}
\langle H^I_{db}(\tau)H^I_{ac}(0)\rangle_b &= \left\langle \sum_i g_i q_{db} e^{\frac{i}{\hbar}H_B\tau}\hat{B}_i e^{-\frac{i}{\hbar}H_B\tau} \sum_j g_j^* q_{ac}\hat{B}_j \right\rangle_b \\
&= q_{db}q_{ac}\sum_{ij} g_i g_j^* \left\langle e^{\frac{i}{\hbar}H_B\tau}\left(\hat{b}_i^\dagger + \hat{b}_i\right)e^{-\frac{i}{\hbar}H_B\tau}\left(\hat{b}_j^\dagger + \hat{b}_j\right)\right\rangle_b \\
&= q_{db}q_{ac}\sum_{ij} g_i g_j^* \left\langle e^{\frac{i}{\hbar}H_B\tau}\hat{b}_i^\dagger e^{-\frac{i}{\hbar}H_B\tau}\hat{b}_j^\dagger + e^{\frac{i}{\hbar}H_B\tau}\hat{b}_i^\dagger e^{-\frac{i}{\hbar}H_B\tau}\hat{b}_j \right. \\
&\left. + e^{\frac{i}{\hbar}H_B\tau}\hat{b}_i e^{-\frac{i}{\hbar}H_B\tau}\hat{b}_j^\dagger + e^{\frac{i}{\hbar}H_B\tau}\hat{b}_i e^{-\frac{i}{\hbar}H_B\tau}\hat{b}_j \right\rangle_b
\end{aligned} \tag{1.46}$$

where $q_{db(ac)}$ are the matrix elements of the operator $\hat{Q}$. Terms that create (annihilate) two vibraional excitations (i. e. terms containing $\hat{b}^\dagger\hat{b}^\dagger$ and $\hat{b}\hat{b}$) vanish when tracing over the bath states and can therefore be neglected, together with all the terms where $\hat{b}^\dagger$ and $\hat{b}$ operate on different oscillators. The double sum over i and j hence reduces to a single sum and the correlation function can be written as:

$$\langle H^I_{db}(\tau)H^I_{ac}(0)\rangle_b = q_{db}q_{ac}\sum_i |g_i|^2\langle\hat{b}_i^\dagger(\tau)\hat{b}_i\rangle_b + q_{db}q_{ac}\sum_i |g_i|^2\langle\hat{b}_i(\tau)\hat{b}_i^\dagger\rangle_b. \tag{1.47}$$

The trace over the bath equilibrium state gives:

$$\langle \hat{b}_i^\dagger(\tau)\hat{b}_i\rangle_b = e^{i\omega_i\tau}\langle \hat{n}_i\rangle_b = e^{i\omega_i\tau}n(\omega_i) \tag{1.48}$$

$$\langle \hat{b}_i(\tau)\hat{b}_i^\dagger\rangle_b = e^{-i\omega_i\tau}\left[\langle \hat{n}_i\rangle_b + 1\right] = e^{-i\omega_i\tau}\left[n(\omega_i) + 1\right] \tag{1.49}$$

where $\hat{n}_i$ is the bosonic number operator associated to the i-th bath mode, $\hat{n}_i = \hat{b}_i^\dagger\hat{b}_i$, that in the last step is substituted with the Bose-Einstein distribution function $n(\omega_i) = \left(e^{\frac{\hbar\omega_i}{kT}} - 1\right)^{-1}$, accounting for thermal equilibrium. Considering eqs. 1.48 and 1.49 and introducing the form $\mathcal{J}(\omega) = \sum_i |g_i|^2\delta(\omega - \omega_i)$ for the spectral density, eq. 1.47 become:

$$\begin{aligned}\langle H_{db}^I(\tau)H_{ac}^I(0)\rangle_b =& q_{db}q_{ac}\int_0^\infty d\omega\mathcal{J}(\omega)e^{i\omega\tau}n(\omega) \\ &+ q_{db}q_{ac}\int_0^\infty d\omega\mathcal{J}(\omega)e^{-i\omega\tau}\left[n(\omega)+1\right]\end{aligned} \tag{1.50}$$

Finally, the kinetic coefficient $\Gamma^+_{db,ac}$ is evaluated plugging eq. 1.50 in eq. 1.29:

$$\begin{aligned}\Gamma^+_{db,ac} =& \frac{q_{db}q_{ac}}{\hbar^2}\int_0^\infty d\tau e^{-i\omega_{ac}\tau}\int_0^\infty d\omega\mathcal{J}(\omega)e^{i\omega\tau}n(\omega) \\ &+ \frac{q_{db}q_{ac}}{\hbar^2}\int_0^\infty d\tau e^{-i\omega_{ac}\tau}\int_0^\infty d\omega\mathcal{J}(\omega)e^{-i\omega\tau}\left[n(\omega)+1\right]\end{aligned} \tag{1.51}$$

$$\begin{aligned}\Gamma^+_{db,ac} =& \frac{q_{db}q_{ac}}{\hbar^2}\int_0^\infty d\omega\mathcal{J}(\omega)n(\omega)\int_0^\infty d\tau e^{-i(\omega_{ac}-\omega)\tau} \\ &+ \frac{q_{db}q_{ac}}{\hbar^2}\int_0^\infty d\omega\mathcal{J}(\omega)\left[n(\omega)+1\right]\int_0^\infty d\tau e^{-i(\omega-\omega_{ca})\tau}\end{aligned} \tag{1.52}$$

$$\begin{aligned}\Gamma^+_{db,ac} =& \frac{q_{db}q_{ac}}{\hbar^2}\int_0^\infty d\omega\mathcal{J}(\omega)n(\omega)\left[\pi\delta(\omega_{ac}-\omega) - \frac{i}{\omega_{ac}-\omega}\right] \\ &+ \frac{q_{db}q_{ac}}{\hbar^2}\int_0^\infty d\omega\mathcal{J}(\omega)\left[n(\omega)+1\right]\left[\pi\delta(\omega-\omega_{ca}) - \frac{i}{\omega-\omega_{ca}}\right]\end{aligned} \tag{1.53}$$

where $\delta(\omega_{ac} - \omega)$ and $\delta(\omega - \omega_{ca})$ ensures the conservation of energy, imposing the resonance between the bath and system frequencies. The imaginary part of eq. 1.53 is neglected yielding:[63]

$$\Gamma^+_{db,ac} = \frac{q_{db}q_{ac}}{\hbar^2}\pi\mathcal{J}(\omega_{ac})n(\omega_{ac}) + \frac{q_{db}q_{ac}}{\hbar^2}\pi\mathcal{J}(\omega_{ca})\left[n(\omega_{ca})+1\right] \tag{1.54}$$

Since the integrals span positive frequencies, eq. 4.26 (and all analogous expressions in the following) has to be read as:

$$\Gamma^+_{db,ac} = \frac{q_{db}q_{ac}}{\hbar^2}\pi\mathcal{J}(\omega_{ac})n(\omega_{ac}) \quad \text{for} \quad \varepsilon_a > \varepsilon_c \tag{1.55}$$

$$\Gamma^+_{db,ac} = \frac{q_{db}q_{ac}}{\hbar^2}\pi\mathcal{J}(\omega_{ca})\left[n(\omega_{ca})+1\right] \quad \text{for} \quad \varepsilon_a < \varepsilon_c \tag{1.56}$$

and for $\varepsilon_a = \varepsilon_c$, $\Gamma^+_{db,ac}$ vanishes as the spectral density is imposed to vanish at $\omega = 0$ ($\mathcal{J}(0) = 0$).

The same derivation applied to $\Gamma^-_{db,ac}$ (eq. 1.30) leads to:

$$\Gamma^-_{db,ac} = \frac{q_{db}q_{ac}}{\hbar^2}\pi\mathcal{J}(\omega_{bd})n(\omega_{bd}) + \frac{q_{db}q_{ac}}{\hbar^2}\pi\mathcal{J}(\omega_{db})\left[n(\omega_{db})+1\right]. \tag{1.57}$$

Along similar lines, the *bilinear* interaction Hamiltonian (eq. 1.42) leads to:

$$\Gamma^{+}_{db,ac} = \frac{d_{db}d^{\dagger}_{ac}}{\hbar^2}\pi\mathcal{J}(\omega_{ac})n(\omega_{ac}) + \frac{d^{\dagger}_{db}d_{ac}}{\hbar^2}\pi\mathcal{J}(\omega_{ca})\left[n(\omega_{ca})+1\right] \quad (1.58)$$

$$\Gamma^{-}_{db,ac} = \frac{d_{db}d^{\dagger}_{ac}}{\hbar^2}\pi\mathcal{J}(\omega_{bd})n(\omega_{bd}) + \frac{d^{\dagger}_{db}d_{ac}}{\hbar^2}\pi\mathcal{J}(\omega_{db})\left[n(\omega_{db})+1\right]. \quad (1.59)$$

1.3.1 Linear vs. bilinear coupling

Once the kinetic coefficients entering the relaxation tensor $\mathcal{R}$ are obtained, the Redfield equation (eq. 1.27) can be solved. The eigenstates of the molecular Hamiltonian $\hat{H}_S$ (eq. 1.39) are adopted as the basis set for the dynamics and the Short Iterative Arnoldi (SIA) algorithm[24, 99] with 1 fs time integration step is used to propagate in time the equations of motion. Temperature is set to 298 K. The initial state is prepared as to simulate a coherent (i. e. impulsive) vertical excitation from the ground state. Since the frequency of the molecular vibration is larger than the thermal energy, only the lowest molecular eigenstate $|\phi_1\rangle$ is appreciably populated before excitation and the coherent state is prepared as:[78]

$$|\Psi^*(t=0)\rangle \propto \sum_{k=2}^{N} |\phi_k\rangle\langle\phi_k|\hat{\mu}|\phi_1\rangle \quad (1.60)$$

where $|k\rangle$ runs over the non-adiabatic molecular eigenstates. The corresponding density matrix is $\sigma(0) = |\Psi^*\rangle\langle\Psi^*|$. In the following, unless differently specified, results for 4-(dicyanomethylene)-2-methyl-6-(4-dimethylamino-styryl)-4H-pyran (DCM, structure in figure 1.1) are shown. The relevant model was already parametrized (parameters in table 1.1) and validated against experiment.[15, 79]

	z_0	$-\tau$	ε	$\hbar\omega$
DCM	1.14	0.88	0.456	0.172

Table 1.1: Molecular model parameters for DCM (all quantities in eV).

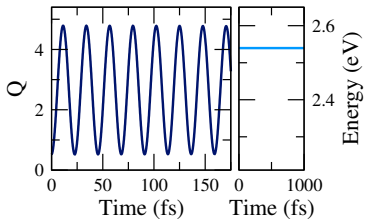

Figure 1.3: Dynamics of the closed system: time evolution of $\langle\hat{Q}\rangle$ (left panel) and the energy of the system (right panel).

As long as the molecule is treated as a closed system (i. e. when the Liouville-von Neumann equation is solved for the system Hamiltonian $\hat{H}_S$ without any interaction with the surrounding environment) the time evolution of the coherent excited state is trivial: energy is conserved and the expectation value of $\hat{Q}$ coherently oscillates in time with constant amplitude[78], as shown in fig. 1.3.

The interaction with the bath allows for the molecule to dissipate energy and thus to relax towards the ground state. Fig. 1.4 summarizes the relaxation dynamics calculated adopting the linear system-bath coupling (eq. 1.41) and a constant spectral density (eq. 1.44) with γ=5 ps^{-1}. Even if the system-bath coupling is described in terms of the single parameter γ, the resulting dynamics clearly shows two different regimes. At first, the system relaxes from the initial coherent excited state to the lowest vibrational level of the electronic excited manifold (hereinafter, the Kasha state) with a characteristic time of $\sim$ 100 fs (first energy drop in panel **a**). The motion on $\hat{Q}$ is initially coherent (panel **b**) but as the population is transferred from higher vibronically excited states to the Kasha state (eigenstate 16 here, panel **c**) coherence drops to zero (panel **d**) and the oscillations on $\hat{Q}$ are completely lost. Subsequently, a much slower and incoherent dynamics enters into play, bringing the system to the ground state with a characteristic time of 1.9 ns. During this incoherent relaxation the purity of the system drops down to $\sim$ 0.5 and is then completely

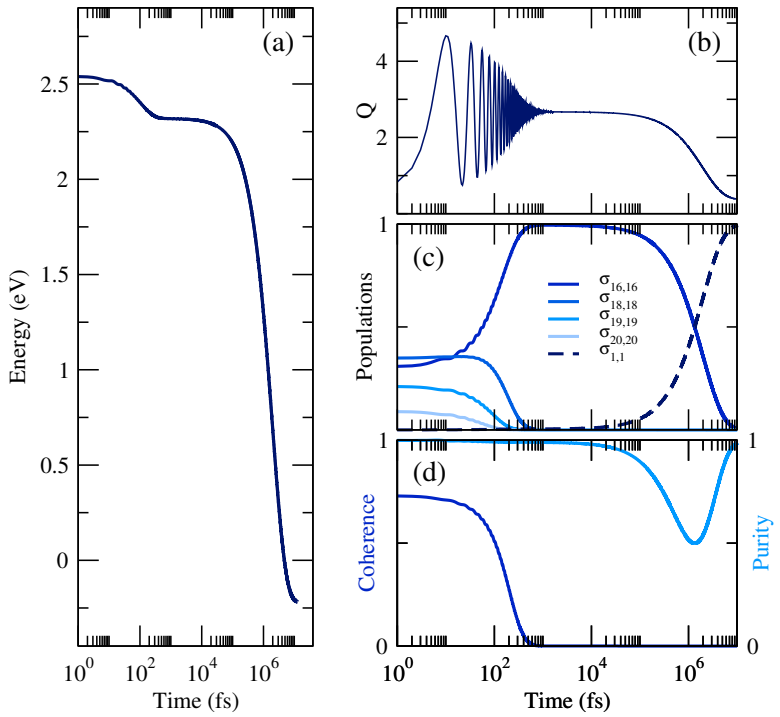

Figure 1.4: Relaxation dynamics of coherently excited DCM with linear system bath coupling and constant spectral density ($\gamma = 5\ \mathrm{ps}^{-1}$). Time evolution of the energy of the system (**a**), $\langle\hat{Q}\rangle$ (**b**), populations of the most relevant eigenstates (**c**) and coherence and purity (**d**).

regained when all the population is finally transferred back to the ground state (panels **c** and **d**). In addition to the calculated molecular trajectory, figure 1.5 shows the adiabatic potential energy curves for the excited and the ground state obtained by the adiabatic diagonalization of the 2x2 Hamiltonian in eq. 1.39 for different Q values. Although the dynamics is calculated in a non-adiabatic picture, the results are perfectly consistent with the adiabatic potential energy curves: in the first fast relaxation the system coherently explores the excited state curve and reaches its minimum (also accounting for the zero point energy), then it slowly starts its incoherent run towards the ground state minimum.

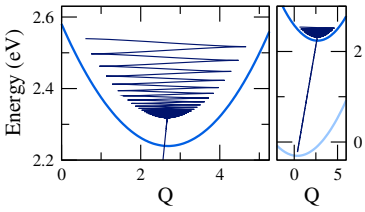

Figure 1.5: Relaxation dynamics of coherently excited DCM with linear system bath coupling and constant spectral density ($\gamma = 5\ \mathrm{ps}^{-1}$). Evolution of the system energy as a function of $\langle\hat{Q}\rangle$. Adiabatic potential energy curves for the excited (blue line) and ground (light blue line) states are shown as a reference.

The results are fully in line with the Kasha rule of optical spectroscopy that states that, in most cases, the vibrational relaxation is much faster than typical fluorescence lifetimes (1-10 ns), so that fluorescence always occurs from the vibrationally cold excited state (precisely, the Kasha state). The specific value adopted for γ was selected as to reproduce typical vibrational relaxation rates in excited molecular states (~ 100 fs[100]) and the subsequent relaxation towards the ground state turns out naturally in the relevant regime (few nanoseconds). It is impressive that the very simple model adopted here is able to account for the two very different timescales, even if a constant spectral density is considered.

Figure 1.6 compares the energy decays obtained with linear (same as in fig. 1.4, panel **a**) and bilinear (eq. 1.42) system-bath coupling (the same constant spectral density as in fig 1.4 is used). An exponential fit of the first vibrational relaxation gives identical relaxation times (100 and 105 fs) for the two models: indeed this relaxation involves states that resemble, to a good approximation, the eigenstates of a harmonic oscillator. In this case, as discussed above, the relaxation channels that are suppressed by the bilinear coupling are not effective and the two models give basically the same results. On the other hand, the subsequent relaxation towards

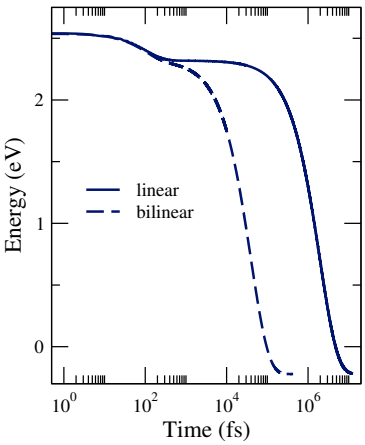

Figure 1.6: Energy decays obtained with linear (continuous line, same as in fig. 1.4 panel **a**) and bilinear (dashed line) system-bath coupling. Constant spectral density is used.

the ground state involves states that belong to two different electronic manifolds and are non-adiabatically coupled. In these conditions, the terms killed by the bilinear coupling do operate and the relaxation time of 0.04 ns obtained with the bilinear approximation is two orders of magnitude smaller than the relaxation time of 1.9 ns obtained with the full linear coupling. Quite interestingly, the presence of additional relaxation channels in the complete model leads to a slower relaxation rate, suggesting that the channels neglected by the bilinear coupling are more effective in the back transfer of energy from the bath to the system than the other way around.

1.3.2 The spectral density

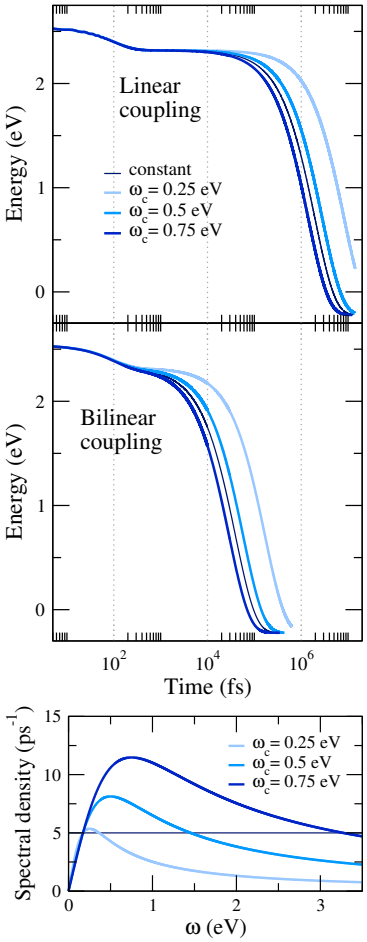

Figure 1.7: Bottom panel: constant and Debye spectral densities (in unit of $\hbar^2/\pi$) with different cut-off frequencies (reported in legend). Top panel: time-evolution of the system energy calculated with the four spectral densities imposing linear and bilinear system-bath coupling.

The assumption of a constant spectral density demonstrates very clearly that the two relaxation regimes found for the vibrational and electronic relaxation are intrinsic to the model and do not rely on the specific shape of the spectral density. However, a well-behaved spectral density should vanish both at low and high frequencies. The Debye spectral density in eq. 1.45 is a simple and common choice complying with the two requirements. To make meaningful comparisons, we consider three different values of the cut-off frequency, $\hbar\omega_c$= 0.25, 0.5 and 0.75 eV and adjust the η parameter as to have the same value for the spectral density at the frequency of the molecular vibration. The four different spectral densities (including the constant one) are shown in the bottom panel of figure 1.7. Energy decays obtained with the four different spectral densities and adopting the linear and bilinear system-bath coupling are reported in the top panels. Having selected the spectral densities in such a way that the coupling strength is the same at the molecular vibrational frequency ($\sim$ 0.172 eV), it is not surprising that the first vibrational relaxation is basically unaffected by the specific choice of the spectral density. On the other hand, the rate of the subsequent electronic relaxation increases with the strength of the system-bath coupling at the frequencies of the electronic excitation ($\sim$ 2.5 eV). The same result on different timescales holds true for both linear and bilinear coupling.

The observation of two distinctively different timescales for the vibrational and electronic relaxations is a robust result that survives the bilinear approximation as well as the different choices of spectral densities. However, unless a specific form of the spectral density can be extracted from independent calculations, the absolute relaxation times evaluated with the Redfield model are arbitrary and their magnitude depend quite unavoidably on the details of the adopted model. Nevertheless, the relative ratio among rates of different processes treated in the same framework is a significant outcome of the approach.

1.4 Increasing the complexity of the molecular model: multimode dynamics

Accounting for a single coupled vibrational mode is a clear simplification of a general model where, for asymmetric molecules like DCM, $3N-6$ modes are in principle coupled to the electronic system (where N is the number of atoms). Indeed, the number of modes having a sizable coupling to the electronic degrees of freedom is in general much smaller, corresponding to a few units, as it turns out from the analysis of Raman spectra and of vibrational solvatochromism.[101–103] In any case, the coupled coordinate described so far does not correspond to a specific molecular vibration, but defines a sort of reaction coordinate along which the dye readjusts its geometry following excitation. The vibrational relaxation energy associated with this effective coordinate is the overall molecular relaxation energy, while the vibrational frequency (typically in the 1200-1500 cm^{-1} range) can be fixed to best reproduce the vibronic structure of electronic spectra. The approach works well in different contexts, but a more detailed picture is needed to address vibrational spectra.[103]

When two or more vibrational modes are explicitly introduced in the molecular Hamiltonian, the way to define the system-bath coupling and the effects that the chosen model has on the dynamics are neither unique nor trivial. The two different relaxation regimes with their characteristic features and timescales are a significant result and a fundamental benchmark in this context.

The multimode molecular Hamiltonian is an extension of the molecular Hamiltonian in Eq. 1.39:

$$\begin{aligned}\hat{H}_{S,m} = -\tau\hat{\sigma} + \left[2z_0 - \sum_{\alpha=1}^{m}\sqrt{\hbar\omega_\alpha\varepsilon_\alpha}\left(\hat{d}_\alpha^\dagger + \hat{d}_\alpha\right)\right]\hat{\rho} \\ + \sum_{\alpha=1}^{m}\hbar\omega_\alpha\left(\hat{d}_\alpha^\dagger\hat{d}_\alpha + \frac{1}{2}\right)\end{aligned} \tag{1.61}$$

where m is the number of coupled modes (up to 3 in the following) and $\hat{d}_\alpha^\dagger$ ($\hat{d}_\alpha$) is the creation (annihilation) operator for the α-th vibrational mode with frequency ω_α and relaxation energy ε_α. The total relaxation energy (ε_v in eq 1.39) is distributed over the coupled modes ($\sum_\alpha \varepsilon_\alpha = \varepsilon_v$) and the vibrational frequencies are chosen so that $\sum_\alpha \hbar\omega_\alpha = m\hbar\omega_v$. The Hamiltonian is written and diagonalized on the vibronic space product of the two electronic states times the eigenstates of the m harmonic oscillators, truncating the vibrational states at a total maximum of M vibrational quanta.

When more than a single coordinate is present, there are two conceptually different possibilities. All coordinates can be (linearly) coupled to the same bath:

$$\hat{H}_{I,lin}^{(a)} = \sum_i g_i\hat{B}_i\sum_\alpha\hat{Q}_\alpha \tag{1.62}$$

or each coordinate can be coupled to an independent bath:[104, 105]

$$\hat{H}_{I,lin}^{(b)} = \sum_{i,\alpha} g_i\hat{B}_{i,\alpha}\hat{Q}_\alpha. \tag{1.63}$$

For the sake of simplicity, in both equations g_i is set independent of α, meaning that all the coordinates are coupled to the bath(s) with the same spectral density. In the last equation, $\hat{B}_i$ acquires an α index to clarify that each α coordinate is coupled to its own bath, independently from other coordinates. The two options, each coordinate coupled to a different or to the same bath, are not equivalent and lead to qualitatively different results. Indeed, coupling all coordinates to the same bath (eq. 1.62) amounts to impose that, in their interaction with the bath, all coordinates move coherently in phase or, in other terms, amounts to impose that the single effective coordinate $\sum_\alpha \hat{Q}_\alpha$, linear combination of all coupled coordinates, is actually coupled to the bath. If the bilinear coupling is adopted, the two Hamiltonians in eq. 1.62 and 1.63 become:

$$\hat{H}^{(a)}_{I,bil} = \sum_i g_i \left(\hat{b}^\dagger_i \sum_\alpha \hat{d}_\alpha + \hat{b}_i \sum_\alpha \hat{d}^\dagger_\alpha \right) \tag{1.64}$$

$$\hat{H}^{(b)}_{I,bil} = \sum_{i,\alpha} g_i \left(\hat{b}^\dagger_{i,\alpha} \hat{d}_\alpha + \hat{b}_{i,\alpha} \hat{d}^\dagger_\alpha \right). \tag{1.65}$$

Once defined the interaction Hamiltonian, explicit expressions for the kinetic coefficients $\Gamma^{+/-}_{db,ac}$ are derived and used to build the Redfield relaxation tensor. For a system with two vibrational coordinates ($\hat{Q}_1 = \hat{d}^\dagger_1 + \hat{d}_1$ and $\hat{Q}_2 = \hat{d}^\dagger_2 + \hat{d}_2$) linearly coupled to two independent baths[8], the same derivation shown in sec. 1.3 leads to:

$$\begin{aligned}\Gamma^{+}_{db,ac} = &\frac{\pi}{\hbar^2} q^1_{db} q^1_{ac} \left[\mathcal{J}_1(\omega_{ac}) n(\omega_{ac}) + \mathcal{J}_1(\omega_{ca}) \left[n(\omega_{ca}) + 1 \right] \right] \\ &+ \frac{\pi}{\hbar^2} q^2_{db} q^2_{ac} \left[\mathcal{J}_2(\omega_{ac}) n(\omega_{ac}) + \mathcal{J}_2(\omega_{ca}) \left[n(\omega_{ca}) + 1 \right] \right]\end{aligned} \tag{1.66}$$

$$\begin{aligned}\Gamma^{-}_{db,ac} = &\frac{\pi}{\hbar^2} q^1_{db} q^1_{ac} \left[\mathcal{J}_1(\omega_{bd}) n(\omega_{bd}) + \mathcal{J}_1(\omega_{db}) \left[n(\omega_{db}) + 1 \right] \right] \\ &+ \frac{\pi}{\hbar^2} q^2_{db} q^2_{ac} \left[\mathcal{J}_2(\omega_{bd}) n(\omega_{bd}) + \mathcal{J}_2(\omega_{db}) \left[n(\omega_{db}) + 1 \right] \right]\end{aligned} \tag{1.67}$$

where the same Bose-Einstein distribution is used for the two baths since it depends only on the temperature, which of course is the same.
When the two coordinates are linearly coupled to the same bath[9], expressions for $\Gamma^{+}_{db,ac}$ and $\Gamma^{-}_{db,ac}$ read:

$$\begin{aligned}\Gamma^{+}_{db,ac} = &\frac{\pi}{\hbar^2} q^1_{db} q^1_{ac} \left[\mathcal{J}_1(\omega_{ac}) n(\omega_{ac}) + \mathcal{J}_1(\omega_{ca}) \left[n(\omega_{ca}) + 1 \right] \right] \\ &+ \frac{\pi}{\hbar^2} q^2_{db} q^2_{ac} \left[\mathcal{J}_2(\omega_{ac}) n(\omega_{ac}) + \mathcal{J}_2(\omega_{ca}) \left[n(\omega_{ca}) + 1 \right] \right] \\ &+ \frac{\pi}{\hbar^2} q^1_{db} q^2_{ac} \left[\mathcal{J}_{12}(\omega_{ac}) n(\omega_{ac}) + \mathcal{J}_{12}(\omega_{ca}) \left[n(\omega_{ca}) + 1 \right] \right] \\ &+ \frac{\pi}{\hbar^2} q^2_{db} q^1_{ac} \left[\mathcal{J}_{12}(\omega_{ac}) n(\omega_{ac}) + \mathcal{J}_{12}(\omega_{ca}) \left[n(\omega_{ca}) + 1 \right] \right]\end{aligned} \tag{1.68}$$

$$\begin{aligned}\Gamma^{-}_{db,ac} = &\frac{\pi}{\hbar^2} q^1_{db} q^1_{ac} \left[\mathcal{J}_1(\omega_{bd}) n(\omega_{bd}) + \mathcal{J}_1(\omega_{db}) \left[n(\omega_{db}) + 1 \right] \right] \\ &+ \frac{\pi}{\hbar^2} q^2_{db} q^2_{ac} \left[\mathcal{J}_2(\omega_{bd}) n(\omega_{bd}) + \mathcal{J}_2(\omega_{db}) \left[n(\omega_{db}) + 1 \right] \right] \\ &+ \frac{\pi}{\hbar^2} q^1_{db} q^2_{ac} \left[\mathcal{J}_{12}(\omega_{bd}) n(\omega_{bd}) + \mathcal{J}_{12}(\omega_{db}) \left[n(\omega_{db}) + 1 \right] \right] \\ &+ \frac{\pi}{\hbar^2} q^2_{db} q^1_{ac} \left[\mathcal{J}_{12}(\omega_{bd}) n(\omega_{bd}) + \mathcal{J}_{12}(\omega_{db}) \left[n(\omega_{db}) + 1 \right] \right].\end{aligned} \tag{1.69}$$

Noticeably, eqs. 1.66 and 1.67 contain only terms in which matrix elements of either $\hat{Q}_1$ or $\hat{Q}_2$ are present, while in eqs. 1.68 and 1.69 products of

8: In this case the system-bath interaction Hamiltonian reads:

$$\hat{H}^{(a)}_{I,lin} = \sum_i g_i \hat{B}_{i,1} \hat{Q}_1 + \sum_j f_j \hat{B}_{j,2} \hat{Q}_2$$

with i and j independently running on the coordinates of the two separate baths. In the most general case, two spectral densities (one for each molecular coordinate) are defined as:

$$\mathcal{J}_1(\omega) = \sum_i |g_i|^2 \delta(\omega - \omega_i)$$

$$\mathcal{J}_2(\omega) = \sum_j |f_j|^2 \delta(\omega - \omega_j).$$

9: Here

$$\hat{H}^{(b)}_{I,lin} = \sum_i \hat{B}_i \left(g_i \hat{Q}_1 + f_i \hat{Q}_2 \right).$$

Two additional spectral density functions have to be defined as:

$$\mathcal{J}_{12}(\omega) = \sum_i g_i f^*_i \delta(\omega - \omega_i)$$

$$\mathcal{J}_{21}(\omega) = \sum_i g^*_i f_i \delta(\omega - \omega_i)$$

and since g and f are real and positive for every bath oscillator, then

$$\mathcal{J}_{12}(\omega) = \mathcal{J}_{21}(\omega) = \sqrt{\mathcal{J}_1(\omega) \mathcal{J}_2(\omega)}.$$

matrix elements of $\hat{Q}_1$ and $\hat{Q}_2$ also appear, imposing a constraint in the motion on the two coordinates. Analogous expressions are found for the bilinear coupling Hamiltonians in eqs. 1.64 and 1.65. When each coordinate is coupled to an independent bath, they read:

$$\begin{aligned}\Gamma^{+}_{db,ac} = \frac{\pi}{\hbar^2}\Big[&d^1_{db}d^{1\dagger}_{ac}\mathcal{J}_1(\omega_{ac})n(\omega_{ac}) + d^{1\dagger}_{db}d^1_{ac}\mathcal{J}_1(\omega_{ca})\left[n(\omega_{ca})+1\right] \\ &+ d^2_{db}d^{2\dagger}_{ac}\mathcal{J}_2(\omega_{ac})n(\omega_{ac}) + d^{2\dagger}_{db}d^2_{ac}\mathcal{J}_2(\omega_{ca})\left[n(\omega_{ca})+1\right]\Big]\end{aligned} \tag{1.70}$$

$$\begin{aligned}\Gamma^{-}_{db,ac} = \frac{\pi}{\hbar^2}\Big[&d^1_{db}d^{1\dagger}_{ac}\mathcal{J}_1(\omega_{bd})n(\omega_{bd}) + d^{1\dagger}_{db}d^1_{ac}\mathcal{J}_1(\omega_{db})\left[n(\omega_{db})+1\right] \\ &+ d^2_{db}d^{2\dagger}_{ac}\mathcal{J}_2(\omega_{bd})n(\omega_{bd}) + d^{2\dagger}_{db}d^2_{ac}\mathcal{J}_2(\omega_{db})\left[n(\omega_{db})+1\right]\Big]\end{aligned} \tag{1.71}$$

whereas, when both coordinates are coupled to the same bath:

$$\begin{aligned}\Gamma^{+}_{db,ac} = \frac{\pi}{\hbar^2}\Big[&d^1_{db}d^{1\dagger}_{ac}\mathcal{J}_1(\omega_{ac})n(\omega_{ac}) + d^{1\dagger}_{db}d^1_{ac}\mathcal{J}_1(\omega_{ca})\left[n(\omega_{ca})+1\right] \\ &+ d^2_{db}d^{2\dagger}_{ac}\mathcal{J}_2(\omega_{ac})n(\omega_{ac}) + d^{2\dagger}_{db}d^2_{ac}\mathcal{J}_2(\omega_{ca})\left[n(\omega_{ca})+1\right] \\ &+ d^1_{db}d^{2\dagger}_{ac}\mathcal{J}_{12}(\omega_{ac})n(\omega_{ac}) + d^{1\dagger}_{db}d^2_{ac}\mathcal{J}_{12}(\omega_{ca})\left[n(\omega_{ca})+1\right] \\ &+ d^2_{db}d^{1\dagger}_{ac}\mathcal{J}_{12}(\omega_{ac})n(\omega_{ac}) + d^{2\dagger}_{db}d^1_{ac}\mathcal{J}_{12}(\omega_{ca})\left[n(\omega_{ca})+1\right]\Big]\end{aligned} \tag{1.72}$$

$$\begin{aligned}\Gamma^{-}_{db,ac} = \frac{\pi}{\hbar^2}\Big[&d^1_{db}d^{1\dagger}_{ac}\mathcal{J}_1(\omega_{bd})n(\omega_{bd}) + d^{1\dagger}_{db}d^1_{ac}\mathcal{J}_1(\omega_{db})\left[n(\omega_{db})+1\right] \\ &+ d^2_{db}d^{2\dagger}_{ac}\mathcal{J}_2(\omega_{bd})n(\omega_{bd}) + d^{2\dagger}_{db}d^2_{ac}\mathcal{J}_2(\omega_{db})\left[n(\omega_{db})+1\right] \\ &+ d^1_{db}d^{2\dagger}_{ac}\mathcal{J}_{12}(\omega_{bd})n(\omega_{bd}) + d^{1\dagger}_{db}d^2_{ac}\mathcal{J}_{12}(\omega_{db})\left[n(\omega_{db})+1\right] \\ &+ d^2_{db}d^{1\dagger}_{ac}\mathcal{J}_{12}(\omega_{bd})n(\omega_{bd}) + d^{2\dagger}_{db}d^1_{ac}\mathcal{J}_{12}(\omega_{db})\left[n(\omega_{db})+1\right]\Big]\,.\end{aligned} \tag{1.73}$$

Extension to the case with three vibrational modes is straightforward, explicit expressions for the $\Gamma^{+/-}_{db,ac}$ coefficients are reported in appendix A.

The dimension of the non-adiabatic problem increases very fast with the number of vibrational modes, reaching the order of $\sim 10^2$ and $\sim 10^3$ for two and three explicit coordinates, respectively. Performing a full Redfield dynamics (i.e., accounting for all the $\mathcal{R}_{ab,cd}$ terms of the relaxation tensor) over such large systems is computationally too demanding. In order to speed up the calculation without affecting the accuracy, the basis is truncated neglecting all states higher in energy than the most populated states upon coherent excitation and whose initial population is lower than a fixed value[94, 95] (here 10^{-6}). Moreover, for the system with two coordinates, the pseudo non-secular approximation[76] is adopted (i.e. only $\mathcal{R}_{ab,cd}$ terms for which $|\omega_{ab} - \omega_{cd}| \leq \alpha$ are accounted for, with $\alpha = 0.01$ eV) and the secular approximation (i. e. only terms for which $|\omega_{ab} - \omega_{cd}| = 0$ survive) is applied when three coordinates are introduced.

Fig. 1.8 shows results obtained for DCM with two coupled modes *linearly* coupled with two *independent baths* (eq. 1.63). A *constant* spectral density is used ($\gamma = 5$ ps^{-}1, same spectral density for the two coordinates; other model parameters are reported in table 1.2, the total number of vibrational quanta is fixed to $M = 16$). Results obtained for a single coupled mode (same as in fig. 1.4) are also shown as a reference. A reduced amplitude of the vibrational coherent oscillations with respect to the single mode case signals the reduced relaxation energy associated with each mode (panels **b** and **c**). Nevertheless, the energy relaxation is basically unaffected by the

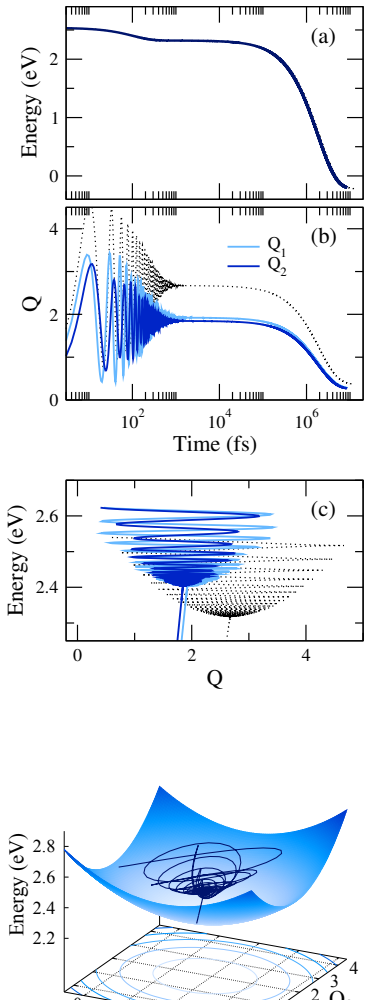

Figure 1.8: Relaxation dynamics of DCM calculated accounting for two coupled vibrational modes, each mode being independently coupled to a dissipative bath (coupling model in eq. 1.63). The black dotted lines show results obtained for a single coupled mode (same as in Fig. 1.4). (**a**) Time-evolution of the system energy. (**b**) Time evolution of Q_1 and Q_2 (light and dark blue lines, respectively).(**c**) System energy plotted against the coordinates. Bottom panel: same quantities ad in panel **c** displayed in 3D. The curve reports the system non-adiabatic trajectory, the surface, shown only for reference purposes, corresponds to the 2D adiabatic potential energy surface of the excited state.

Table 1.2: Model parameters entering the multimode Hamiltonian 1.61 for DCM and other relevant dyes (all quantities in eV).

		z_0	$-\tau$	ε_1	$\hbar\omega_1$	ε_2	$\hbar\omega_2$	ε_3	$\hbar\omega_3$
DCM	1 mode	1.14	0.88	0.456	0.172	-	-	-	-
	2 modes	1.14	0.88	0.195	0.154	0.261	0.19	-	-
	3 modes	1.14	0.88	0.12	0.146	0.152	0.17	0.184	0.2
$C_{16}H_{33}Q$-3CNQ	1 mode	-0.25	0.47	0.17	0.14	-	-		
	2 modes	-0.25	0.47	0.08	0.13	0.09	0.15	-	-
Nile Red	1 mode	0.88	0.95	0.33	0.14	-	-		
	2 modes	0.88	0.95	0.15	0.135	0.18	0.145	-	-
DANS	1 mode	1.32	0.72	0.3	0.17	-	-		
	2 modes	1.32	0.72	0.12	0.15	0.18	0.19	-	-

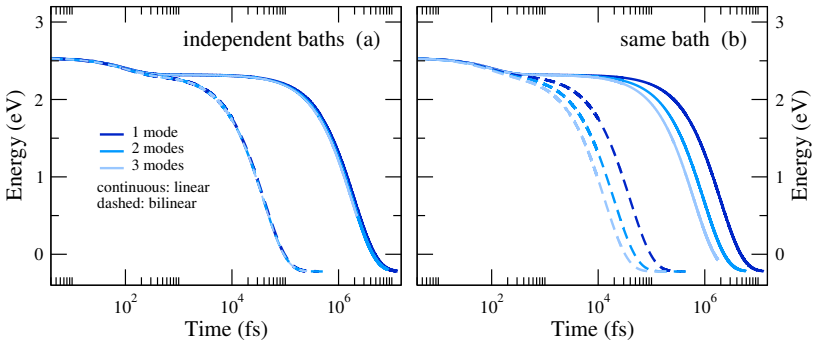

Figure 1.9: Relaxation dynamics of coherently excited DCM with up to three vibrational modes. Continuous and dashed lines report results obtained with linear and bilinear system bath coupling, respectively. In panel **a** each mode is couple to its own independent bath, while in panel **b** all the coordinates are coupled to the same bath. Constant spectral density is used ($\gamma = 5\ \mathrm{ps}^{-1}$).

presence of more than a single coordinate (panel **a**). This notable result is however only obtained if each coordinate is coupled to an independent bath.

Figure 1.9 compares the results obtained coupling each coordinate with its own independent bath with the ones obtained when they are all coupled to the same bath, also including results for three coupled coordinates (parameters in table 1.2 and $M = 12$). While panel **a** confirms that when the relaxation on each coordinate is independent the decay rates do not depend on the number of coupled modes explicitly accounted for, panel **b** clearly shows that when they are coupled with the same bath the relaxation rate towards the ground state increases with the number of coupled modes with a characteristic time t that scales as t/m. Dashed lines in figure 1.9 show that this result holds true also when bilinear coupling is used.

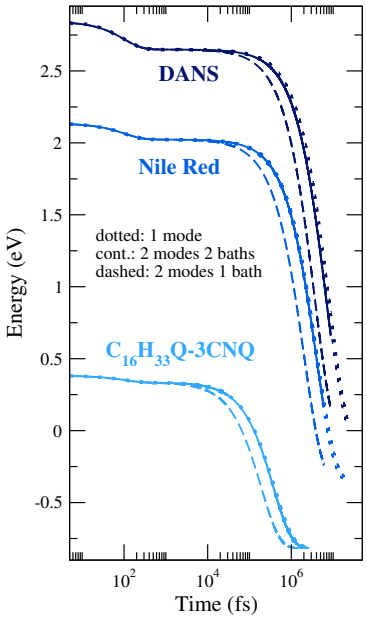

Figure 1.10: Relaxation dynamics of three DA dyes (parameters in table 1.2, structures in figure 1.1) with linear coupling and constant spectral density. Time evolution of the system energy. Dotted lines: model with a single vibrational mode. Continuous lines: model with two modes coupled to two independent baths. Dashed lines: model with two modes coupled to the same bath.

Similar results as for DCM are obtained for other DA dyes (figure 1.10 shows results obtained with linear coupling and constant spectral density): the separation between the two relaxation regimes proves to be solid for this class of dyes, together with the fact that in multimode systems each vibrational degree of freedom has to be coupled to its own relaxation bath in order to have a reliable effective model.

It is worth mentioning that the same model discussed here was investigated in a series of papers by the Domcke group in the context of ultrafast electron transfer processes.[74, 106–108] The results obtained there for the multimode case contrast sharply with the results shown above, with the relaxation calculated for the multimode case being much faster than for the case of a single coordinate. While Domcke and coworkers adopted the bilinear coupling, it has been explicitly verified that the discrepancy survives even when linear coupling is used and it is actually due to the

different investigated regimes. In this work, the focus is on relaxation in DA dyes, in an effort to address their spectroscopic behavior. DA dyes are characterized by large τ values (~ 1 eV), much larger than vibrational relaxation energies and vibrational frequencies. In these conditions, as discussed above, vibrational and electronic relaxations occur in different time windows. On the opposite, Domcke and coworkers were interested in ultrafast electron transfer, occurring for strong coupling and very poor conjugation, with τ never exceeding the vibrational frequency and typically small z_0 values. In this regime, the electronic and vibrational relaxation concur, making the details of the vibrational coupling relevant and defining a substantially different picture with respect to the case of DA dyes.

1.5 Calculation of optical spectra

Among all the properties of a DA dye that can be calculated having this dynamical model at hand, in the context of this thesis optical responses are for sure the most interesting ones. While linear absorption might be somehow trivial, the dynamical nature of the approach opens the remarkable possibility to calculate time resolved emission spectra. In both cases, molecular optical spectra can be calculated as the Fourier transform of the time-correlation function of the dipole moment $C_{\mu\mu}(t) = \langle \hat{\mu}(t)\hat{\mu}(0)\rangle$. The correlation function is evaluated as $C_{\mu\mu}(t) = Tr\{\hat{\mu}\hat{\Omega}(t)\}$, where $\hat{\Omega}(t)$ is the so-called spectral generating function, whose time evolution obeys the same Liouville-von Neumann equation as the density matrix.[109]

1.5.1 Absorption

Following Mukamel[109], the generating function for the absorption spectrum is defined at $t = 0$ as $\Omega^{abs}(0) = \hat{\mu}|\phi_1\rangle\langle\phi_1|$, where ϕ_1 is the molecular ground state. Top panel of figure 1.11 shows the time-evolution of the absorption dipole correlation function for DCM: since the Liouville-von Neumann dynamics does not describe energy dissipation, the correlation functions oscillate without damping. To avoid numerical instabilities, spectra are then calculated as the real part of the Fourier transform of an artificially damped correlation function, $C_{\mu\mu}(t)\exp[-t/a]$. Of course, the resolution of calculated spectra can be arbitrary tuned through the parameter a (the faster the damping, the broader the bands), and they can be virtually infinitely resolved as the model does not account for any source of inhomogeneous broadening. Panel **a** of figure 1.11 shows that when the spectra are sufficiently resolved ($a = 50$ fs) increasing the number of coupled modes leads to more structured vibronic band, as expected, but when spectra are broader ($a = 6$ fs, panel **b**) accounting for a single effective coordinate is enough to obtain realistic band-structures.

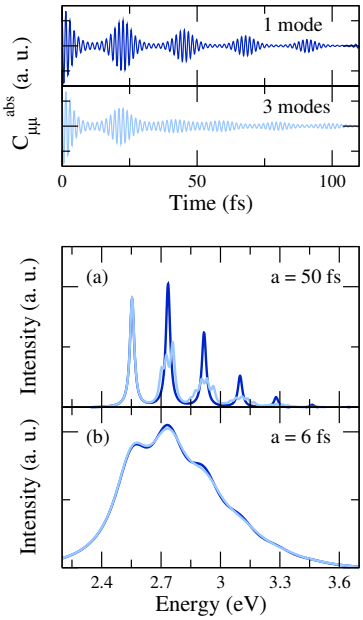

Figure 1.11: Absorption spectra of DCM. Top panel: dipole-dipole correlation functions $C^{abs}_{\mu\mu}(t)$ damped with $a = 50$ fs for the model with one and three vibrational modes (dark and light blue respectively). Bottom panels: real part of the Fourier transforms of the dipole-dipole correlation function damped with $a = 50$ fs (**a**) and $a = 6$ fs (**b**).

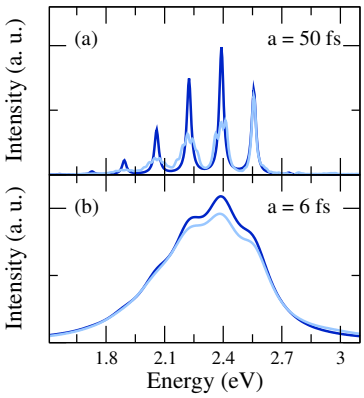

Figure 1.12: Emission spectra at $t' = 1$ ps (steady state limit) of DCM. Real part of the Fourier transforms of the relevant correlation functions damped with $a = 50$ fs (**a**) and $a = 6$ fs (**b**). Results for one (dark blue) and three (light blue) coupled vibrational modes. Main dynamics carried out with linear system-bath coupling and constant spectral density ($\gamma = 5$ ps^{-1}).

1.5.2 Time-resolved emission

Time-resolved emission spectra can be calculated along similar lines. The system is coherently excited at time 0 and then it is allowed to evolve freely (as per eq. 1.27) up to time t' (main dynamics). At this point, the density

matrix is frozen and multiplied by the dipole moment operator to give the initial ($t = t'$) generating function $\hat{\Omega}^{fluo}(0, t') = \hat{\mu}\hat{\sigma}(t')$[95]. Once again, the time evolution of the generating function is evaluated following the Liouville-von Neumann equation, while the time correlation function of the dipole moment is calculated as $C^{fluo}_{\mu\mu}(t-t', t') = Tr\{\hat{\mu}\hat{\Omega}^{fluo}(t-t', t')\}$. The real part of the Fourier transform in the $t - t'$ domain of the dipole correlation function gives the emission spectrum at time t' after coherent excitation. Once again, the time correlation function is damped with an exponential decay before taking the Fourier transform. When t' is sufficiently long, the time-resolved spectrum coincides with the steady-state fluorescence spectrum: in figure 1.12 it can be seen how at $t' = 1$ ps (i. e. at the end of the first fast vibrational relaxation) emission comes from the Kasha state and the fluorescence spectrum is basically the mirror image of absorption, with the 0-0 transition in common.

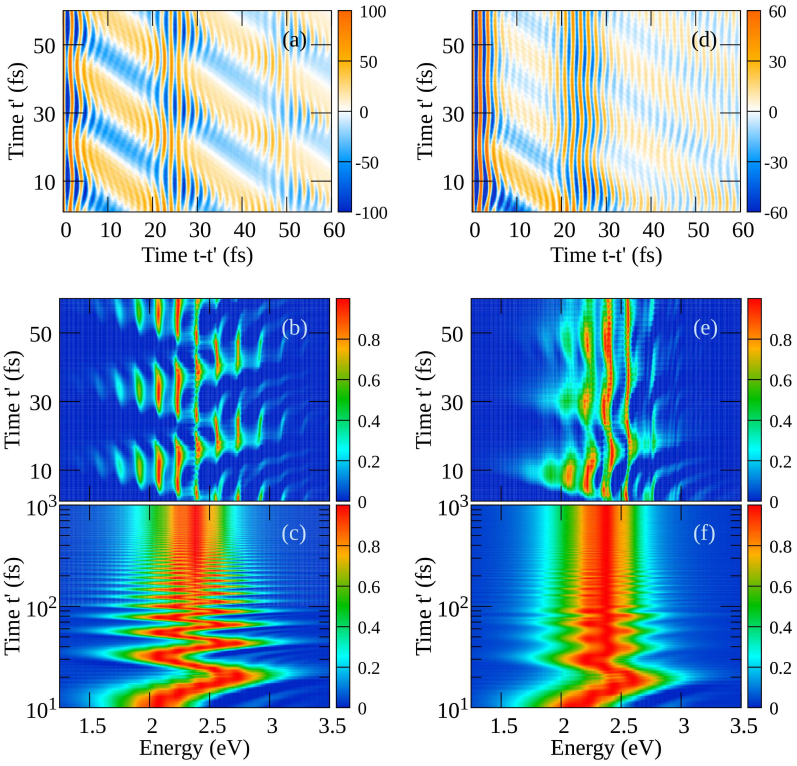

Figure 1.13: Time resolved emission spectra for DCM with one (left panels) and three (right panels) vibrational modes. Time evolution (t-t') of the time dependent (t') emission dipole correlation function damped with $a = 50$ fs (panels **a** and **d**). Normalized real parts of the corresponding Fourier transforms over the $t - t'$ domain (panels **b** and **e**). Longer time evolution of the emission spectra broadened with $a = 6$ fs (panels **c** and **f**). Main dynamics carried out with linear system-bath coupling and constant spectral density ($\gamma = 5$ ps^{-1}).

A more intriguing scenario emerges when looking at early time emission, as shown in figure 1.13 where (normalized) emission spectra are reported as a function of t'. In left panels results for DCM with a single vibrational mode are reported. Panel **a** shows the damped dipole correlation function $C^{fluo}_{\mu\mu}(t - t', t') \exp[-t/a]$ with $a = 50$ fs. In panel **b** the real parts of the corresponding Fourier transforms are reported. At early times emission comes from "hot" states and the spectrum shifts to the red and to the blue with a period of ~ 22 fs (~ 0.18 eV, the excited state vibrational frequency) following the coherent motion on Q (cfr. figure 1.5). With such resolved bands ($a = 50$ fs) it can be seen how the shift of the spectrum is not due to a shift in the energy of the eigenstates, that are actually fixed, but rather to a transfer of oscillator strength among the fixed transitions. This oscillation in the position of the spectrum is due to the coherent nature of the motion and it damps as coherence is progressively lost, as it can be seen in panel **c**, where spectra reported in panel **b** are broadened ($a = 6$

fs) and shown up to longer times. At the end of the vibrational relaxation the coherent oscillation is no longer observed and the spectrum stabilizes at steady state emission. Right panels report the same quantities for the system with three vibrational modes. The same features emerge, with the difference that having now three coupled modes with three different frequencies the overall coherent oscillation observed in the spectrum position is less prominent.

1.6 Conclusions

The relaxation of a photoexcited molecule can only be understood connecting the microscopic quantum mechanical model for the molecule to a macroscopic thermodynamic reservoir, thus entering the fascinating world of open quantum systems. Refined quantum mechanical models are available for isolated molecular systems, that describe the molecular properties in great detail and whose accuracy is only limited by the available computational capabilities. However, the coupling between the molecule and the reservoir is more delicate. The first step is the separation of the system from the bath variables. Often in the literature vibrational degrees of freedom are all clamped within the bath. While useful in several respects, these models cannot capture the vibrational dynamics, so that they do not apply to model vibrational or vibronic spectra and, not addressing vibrational relaxation, they do not allow to follow the initial steps of the relaxation dynamics. Moreover, in many cases, and specifically for the DA dyes of interest in this context, molecular vibrations are strongly coupled to the electronic system and affect in a specific way the system behavior with major effects on the molecular polarity and (hyper)polarizability. Explicitly accounting for the few strongly coupled vibrations via their inclusion in the system ensures for a proper treatment of their major role. The residual coupling to the bath will then address weakly coupled vibrational modes, as well as environmental effects and specifically those related to non-polar solvation.

In this chapter, the relaxation dynamics of a photoexcited DA dye described by an essential state model has been addressed exploiting the Redfield approach to open quantum systems, with special focus on how the details of the model (which is phenomenological in nature) affect the relaxation pathway. In particular, linear and bilinear system-bath coupling have been compared, together with the case of a constant and a Debye spectral density.

The most intriguing result is that two relaxation regimes are always observed for the molecular system: a very fast vibrational relaxation to the Kasha state, followed by a (orders of magnitude) slower decay from the excited electronic state towards the ground state. This solid result is in line with the general spectroscopic rule that emission occurs from the vibrationally relaxed excited state, since vibrationally hot states are too short-lived with respect to radiative and non-radiative decay rates.

The bilinear system-bath coupling (often improperly referred to as the rotating wave approximation, RWA) neglects some relaxation channels out of all the possible channels included in the more general linear coupling model. This approximation is only reliable as long as the system closely resembles a harmonic oscillator (here, in the case of the vibrational

relaxation). In strongly anharmonic systems, or when several electronic states are non-adiabatically coupled, the relaxation channels arbitrarily closed in the RWA do play a role and their exclusion results in a faster decay towards the ground state. Since the two couplings require the same computational cost, the more general linear coupling is preferred and will be used hereinafter.

Another, possibly more delicate, issue is the choice of the spectral density. An important task in this field would be the definition, via independent estimates, of reliable spectral densities for molecular systems embedded in realistic environments. Approaches of this kind are available for models where all vibrational degrees of freedom are clamped in the bath,[110–112] but nowadays strategies to evaluate spectral densities relevant to models where the vibrational coordinates are coupled to the bath are not available.

Working with multimode molecular models, an important lesson has been learned: each molecular mode must be coupled to an independent reservoir to prevent the unphysical coupling of the two motions due to their interaction with a common bath. In other terms, by assuming that several vibrational modes are coupled to the same bath, one imposes that a specific linear combination of the molecular modes is actually coupled to the bath, thus introducing a predefined decay pathway. Interestingly, when the coupling is properly introduced accounting for independent decay pathways for each coordinate, the decay dynamics is independent of the number of coupled modes, provided that the total strength of electron-vibration coupling is maintained constant. This is an important result, as it allows to safely reduce the relaxation dynamics in a multimode system to the much simpler calculation of the dynamics of a molecular system with a single effective coordinate. However, this result only holds true provided that all modes have a similar coupling to the electronic system and the electronic energy gaps are much larger than typical vibrational frequencies, as it is the case for DA dyes.

In conclusion, we have explored in detail the different approximations introduced in a model for the relaxation of an excited CT dipolar chromophore, exploiting a simple molecular model relevant to DA dyes where only two electronic states are considered, coupled to a few effective vibrational coordinates that, in turn, are coupled to a bath. This preliminary and fundamental study defines safe guidelines for the definition of relaxation models. The knowledge and confidence gained in this chapter set a firm basis to investigate more complex systems. Specifically, in the context of this thesis, the topic of a DA dye in a polar environment will be addressed in chapter 2 and small molecular aggregates and multichromophoric systems for energy transfer in chapter 4.

Single molecule relaxation in polar environments: liquid and solid state solvation

2

Organic electronics relies on molecular functional materials that are exploited in several devices including organic light emitting devices (OLEDs), organic photovoltaics (OPV), luminescent solar concentrators, photodetectors etc.[1, 2] Organic-based devices are low-cost, are composed of abundant elements and offer an opportunity for easy recycling, while exploiting the enormous tunability of molecular properties by synthetic approaches. The interaction between functional molecules and the local environment, if properly mastered, offers a powerful tool to optimize the materials the specific applications. Indeed, the unique properties of molecules of interest for advanced applications (e. g. large absorption or emission features in the visible-near IR regions, large non-linear optical responses, multistability and charge transport) are related to the presence of extended π-conjugated backbones which are responsible for the large (hyper)polarizability of functional molecules, and hence for their large responsivity to any perturbation due to the local environment.

Solvatochromism, the solvent dependence of spectral properties of a dye, is the easiest demonstration of the responsivity of π-conjugated molecules to the local environment. Solvatochromism is well understood: the first models date back to the work of Liptay[113] and more recently Reichardt[64] and Ratner,[114] while the Lippert-Mataga plots,[115] relating the absorption and emission frequencies of a dye to the dielectric properties of the solvent, are a well established tool to extract useful information on the permanent dipole moment of polar molecules in the ground and excited state. Several computational strategies have been devised to address solvation phenomena that either rely on a continuum dielectric model[116–119] for the solvent or on atomistic descriptions.[120] Both strategies should be considered with care as for the electronic component of solvation,[121, 122] yet they offer reliable approaches to polar solvation.

Solid state solvation (SSS) is much less investigated and understood. Its relevance to OLED was early recognized by Forrest and coworkers who exploited the large dependence of the emission color of a dye on the polarity of the environment to tune the color of phosphorescent OLED[123] and to create white-OLEDs.[124] Green et al.[125] exploited SSS in solar light concentrators, tuning the dielectric properties of the polymeric matrix with the addition of camphor (a small polar dopant) to optimize the absorption properties of a dye dispersed in the matrix and hence the efficiency of the solar concentrator. Doping organic matrices with camphor,[126] ethylene glycols[127] or other small molecules[128] was also proposed to improve the efficiency of organic solar cells, with limited success.[129] The importance of matrix effects, and hence of SSS, in the third generation of OLED was early recognized.[130] In these

The work presented in this chapter is published in *Mater. Horiz., 10,* 4172-4182, **2023**, where additional details on the preparation of the samples and on experimental set ups and measurements can be found.
Experimental data were recorded by Brunella Bardi in the host group at the University of Parma and by Andrea Lapini, Mariangela Di Donato and Alessandro Iagatti at the European Laboratory for Non-Linear Spectroscopy (LENS) in Florence, Italy.

devices, non-emissive triplet states are harvested via a mechanism called thermally activated delayed fluorescence (TADF) that relies on a tiny energy gap between the lowest energy singlet and triplet states and on a well-balanced mixing between charge transfer (CT) and local excited triplet states.[131, 132] The delicate TADF mechanism is largely affected by SSS,[133–136] indeed a smart matrix approach has been proposed to optimize the device performance via the concurrent optimization of the dye inside the matrix.[137] Several experimental and theoretical works were devoted to disentangle the subtle effects of the matrix in TADF-OLED: on one side the dielectric properties of the matrix are important, but for sure its rigidity also plays a role, altering the conformation of the emitter.[138, 139]

SSS has been discussed so far with reference to fluorescence, paying very little, if any, attention to environmental effects in absorption and vibrational spectra. However, when focusing on fluorescence, a delicate issue must be considered that makes SSS more complex and difficult to deal with than liquid solvation. The relevant degrees of freedom of liquid (low-viscosity) solvents relax in the first few picoseconds after the solute photoexcitation,[71, 136, 140] so that fluorescence (typically in the nanosecond timescale) occurs from the solute experiencing a fully relaxed environment. In frozen glassy solvents the environment is very rigid as to fully hinder its relaxation.[141] But in polymeric or in small molecule matrices at room temperature the situation is much less clear cut. Of course the molecules cannot freely tumble inside a matrix, however the matrix is not fully frozen. As discussed in polymeric matrices,[142] polar groups can rotate around C-C bonds and other groups may librate in timescales that are strongly dependent on the environment.

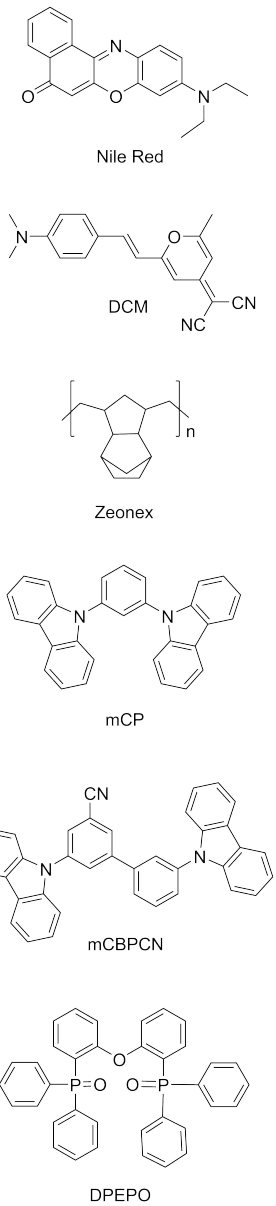

Figure 2.1: Structures of the two dyes (DCM and Nile Red) used as polarity sensors and of the four matrices of interest (zeonex, mCP, mCBPCN ans DPEPO).

The dynamical behavior of the matrix is of enormous relevance to control the physics of actual devices.[129, 139, 143, 144] Just as an example, camphor is often added to the matrices to increase their dielectric constant.[125, 126, 138, 145] However, as demonstrated by a careful analysis,[146] the camphor molecule readjusts quickly inside the matrix, with typical relaxation times in the picosend time window, so that the matrix behaves like a liquid polar environment. Experimental data on the dielectric response of small molecule matrices are scanty[147] and even less is known about their dynamical behavior, with main results relying on molecular dynamics simulations.[143, 148]

In this chapter a detailed study is carried out with the aim of unveiling the static and dynamical dielectric properties of some of the most common amorphous organic matrices used in optoelectronic devices. The approach exploits dipolar dyes as microscopic polarity probes: the study of the spectroscopic properties of the dye dispersed in these media with steady state and time-resolved techniques allows to gain important information about the equilibrium polarity and dynamical behavior of the materials. Specifically, DCM and Nile Red (hereinafter NR) are used as polarity probes and zeonex, mCP, mCBPCN and DPEPO are the four investigated organic amorphous matrices (molecular structures in figure 2.1). The main focus of this chapter will be on the theoretical modeling that supports the interpretation of steady state and time-resolved experiments.

The essential state model for a dipolar dye used in chapter 1 has already been extended to account for polar solvation.[15] Here, the model is adapted to the case of solid state solvation and parametrized against

steady state absorption and emission spectra. Afterwards, the relaxation of the polar environment is included in the relaxation model set up in chapter 1. To this aim, polar solvation dynamics is treated classically, presenting the challenging task of coupling a quantum and a classical system.

The chapter is structured as follows: in section 2.1 the analysis of steady state spectra is carried out. An introduction to solvatochromism is proposed (2.1.1), together with the extension of the essential state model to liquid solvation (2.1.2). Steady state spectra in solid matrices are then addressed (2.1.3). Section 2.2 is devoted to relaxation dynamics, introducing polar solvation dynamics in the Redifeld master equation (2.2.1). The model is validated in solution (2.2.2) and then applied to simulate relaxation in amorphous matrices (2.2.3). Section 2.3 concludes the chapter.

2.1 Steady state spectra in liquid solvents and solid matrices

2.1.1 Solvatochromism

Solvatochromism is the dependence on the environment of the spectroscopic properties of a molecule. When a polar dye enters a polar medium (either liquid or solid), the medium polarizes in response to the dipole moment of the dye generating a local electric field, dubbed as the reaction field. Two contributions to the reaction field must be considered, a contribution related to the electronic polarizability of the medium molecules, and a contribution related to their conformational and rotational degrees of freedom. The first contribution is traced back to the medium refractive index at optical frequencies. Since the refractive index is roughly invariant in different organic media, to a first approximation, its contribution to the solvatochromism can be disregarded.[17] To be more specific, the medium polarizability largely and non-trivially affects the photophysics of a dye when going from gas phase to an organic medium (the refractive index changing from 1 to ~ 1.4),[135] but the effect is roughly the same in all common organic media, so that the large variation of spectral properties in different solvents or matrices can be safely ascribed to the rotational and conformational motion of the medium molecules.

In a low viscosity liquid, the medium molecules are free to tumble and in presence of a polar dye, they reorient to generate at the solute location a reaction field F_R proportional to the solute dipole moment $\langle\hat{\mu}\rangle$:[17, 64, 113]

$$F_R = r\langle\hat{\mu}\rangle \tag{2.1}$$

where r increases with the solvent polarity. This reaction field in turn stabilizes both the ground and the excited state of the solute, but by different amounts if the permanent dipole moment of the ground state μ_g is different from the permanent dipole moment of the excited state μ_e, thus generating a dependence of the transition frequencies over r, i. e. over the polarity of the environment, as illustrated in figure 2.2.

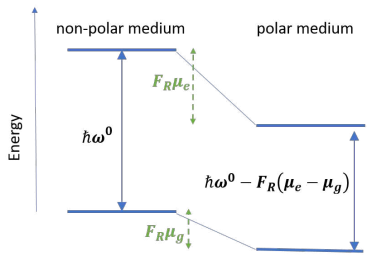

Figure 2.2: A sketch of polar solvation effects on transition energies. The concept is the same for absorption and steady state fluorescence spectra (ω^0 represents either the absorption or fluorescence energy of the dye in a non-polar environment): the energy of the excited and of the ground state is lowered by an amount $F_R\mu_e$ and $F_R\mu_g$, respectively, so that the transition energy is lowered by $F_R(\mu_e - \mu_g)$. For absorption processes, $F_R = r\mu_g$, in either liquid or solid matrices. As for steady state fluorescence, in liquid solvents $F_R = r\mu_e$, with the same solvent-specific r value as in absorption. In solid matrices the picture for steady state fluorescence is more complex, as discussed in this chapter.

The absorption transition is a vertical process, occurring while the slow degrees of freedom of the medium stay frozen and $F_R = r\mu_g$. The energy of the excited state is then lowered due to the interaction with the environment by $-F_R\mu_e = -r\mu_g\mu_e$ and the energy of the ground state is lowered by $-F_R\mu_g = -r\mu_g\mu_g$, so that absorption transition frequency as a function of the medium polarity reads:

$$\hbar\omega_{abs} = \hbar\omega^0_{abs} - r\mu_g(\mu_e - \mu_g) \tag{2.2}$$

where $\hbar\omega^0_{abs}$ is the absorption frequency in non-polar media.

Upon excitation, the permanent dipole moment of the solute changes and the surrounding molecules rearrange around the new charge distribution of the excited state. In a low viscosity environment like a liquid solvent, just a few picoseconds are needed for the solvent molecules to rearrange in response to the new molecular polarity.[71] Steady state fluorescence, typically occurring in the nanosecond timescale, therefore comes from a state where the excited dye is experiencing a reaction field equilibrated over the excited state permanent dipole moment $F_R = r\mu_e$. Along the same line that gave eq. 2.2, the progressive shift of the fluorescence band with the solvent polarity can be estimated as:

$$\hbar\omega_{fluo} = \hbar\omega^0_{fluo} - r\mu_e(\mu_e - \mu_g) \tag{2.3}$$

where $\hbar\omega^0_{fluo}$ is the fluorescence frequency in non-polar media. If $\mu_e > \mu_g$ (as it is the case for Nile Red and DCM[15] and as illustrated in figure 2.2) the reaction field stabilizes the excited state more than the ground state, generating both in absorption and in emission a red shift that increases upon increasing the solvent polarity. Moreover, since F_R is larger when the medium is equilibrated over the excited state, solvatochromism is more pronounced in emission than in absorption, resulting in an increasing Stokes shift (i. e. the difference in energy between absorption and emission maxima) with solvent polarity. On the other hand, if $\mu_g > \mu_e$ the ground state is more stabilized, so that both absorption and emission frequencies move to the blue with respect to a non-polar medium and solvatochromism is more pronounced in absorption. The two scenarios are referred to as *direct* and *inverse* solvatochromism, respectively.[64]

2.1.2 DA dye in liquid solvents

Figure 2.3 shows experimental Raman, absorption and emission spectra of DCM (panels **a**, **b** and **c**) and NR (panels **g**, **h** and **i**) dissolved in four solvents of increasing polarity, from carbon tetrachloride (CCl_4) to dimethylsulfoxide (DMSO). As mentioned in the previous section, both dyes have a polar ground state, with a permanent dipole moment μ_g smaller than the very large excited state dipole moment μ_e associated to the CT nature of the excited state.[15] The progressive red shifts in the absorption spectra clearly point to a solvent polarity that increases in the order CCl_4, $CHCl_3$, DMF and DMSO. Absorption spectra of NR (panel **h**) show a larger solvatochromism than DCM (panel **b**), in line with NR having a larger ground state permament dipole moment than DCM.[15, 149] Finally, the progressive broadening of the absorption band with increasing solvent polarity is ascribed to the inhomogenous broadening induced by thermal disorder on the reaction field.[15, 17]

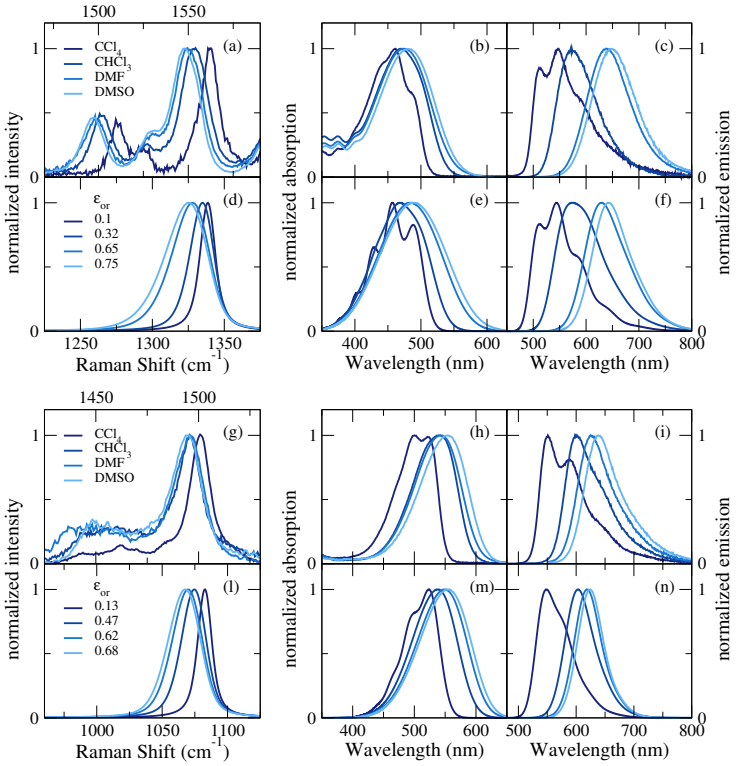

Figure 2.3: Steady state spectra for DCM (panels **a-f**) and NR (panels **g-n**) in liquid solvents. From left to right Raman spectra, absorption and fluorescence spectra are reported. Panels **a-c**, **g-i** show measured spectra and panels **d-f**, **l-n** the calculated ones. Molecular parameters are reported in table 2.1, solvent relaxation energies ε_{or} are reported in the legends.

Vibrational solvatochromism, recently proposed as a powerful tool to monitor the local medium polarity,[150] has been extensively investigated in polar donor-acceptor dyes.[151–153] It relies on the polarizability of the dye: upon increasing the solvent polarity, the charge distribution on the dye changes, towards an increased dipole moment. Vibrational frequencies are extremely responsive even to small variations of the charge distribution in the molecule and move to the red (in the hypothesis of linear electron-vibration coupling). The non-resonant Raman spectra of DCM (panel **a**) are more sensitive to the polarity than those of NR (panel **g**), but for both systems, they support the same polarity scale as absorption spectra. Much as for absorption, the Raman bands also broaden in polar media.[153]

After excitation, in a few picoseconds the solvent molecules rearrange around the excited state and fluorescence (nanosecond timescale) occurs from a state where the reaction field is equilibrated over μ_e. Therefore, the same polarity scale as observed in absorption is recovered, with the polarity increasing in the order CCl_4, $CHCl_3$, DMF and DMSO. As expected, solvatochromism is more pronounced in emission than in absorption ($\mu_e > \mu_g$, direct solvatochromism), and the solvatochromic shifts are larger for DCM (panel **c**) than NR (panel **i**) since $\mu_e^{DCM} > \mu_e^{NR}$.

Solvation model

The essential state model for a DA dye described in chapter 1 is here extended to account for polar solvation. In particular, the interaction with the reaction field (hereinafter dubbed as F_{or}, conveniently defined in energy units) is added to the molecular Hamiltonian $\hat{H}_S$ in eq. 1.39 to give the total Hamiltonian:[1]

1: The dipole moment operator is defined as $\hat{\mu} = \mu_0\hat{\rho}$, where μ_0 is the dipole moment associated with the zwitterionic state and $\hat{\rho}$ is the ionicity operator. F_{or} is therefore defined as the reaction field times μ_0.

$$\hat{H}_{tot} = \hat{H}_S - F_{or}\hat{\rho} + \frac{F_{or}^2}{4\varepsilon_{or}} \tag{2.4}$$

where the second term in the right-hand side describes the interaction between the field (or, to be specific, the field component parallel to the molecular dipole moment) and the solute molecule, and the last term accounts for the elastic restoring force with ε_{or} measuring the solvent relaxation energy. ε_{or} enters as a solvent-dependent parameter and its value increases with increasing polarity. Polar solvation is related to the slow, typically overdamped, motion of polar solvent molecules around the solute. Accordingly, its kinetic energy is neglected and F_{or} is treated as a classical coordinate.

A grid of F_{or} values is defined, and in each point of the grid the Hamiltonian in eq. 2.4 is written, as done in chapter 1, on the vibronic basis obtained as the direct product of the two electronic states times the first M eigenstates of the harmonic oscillator that describes the vibrational coordinate. The F_{or}-dependent Hamiltonians are diagonalized and, following a well established procedure,[15] the F_{or}-dependent non-adiabatic vibronic eigenstates and energies are used to calculate F_{or}-dependent steady state spectra exploiting sum over states expressions. In particular, absorption and Raman spectra are calculated as:

$$Abs(\omega; F_{or}) \propto \omega \sum_{i>1} |\mu_{i1}(F_{or})|^2 \exp\left(-\frac{(\omega_{i1}(F_{or}) - \omega)^2}{2\sigma^2}\right) \tag{2.5}$$

$$R(\omega, F_{or}) \propto \mathcal{I}m \sum_{i>1} \frac{1}{\omega_{i1}(F_{or}) - \omega - i\Gamma} \left(\sum_{j>1} \frac{2\mu_{1j}(F_{or})\mu_{ji}(F_{or})}{\omega_{j1}(F_{or})}\right) \tag{2.6}$$

where i and j run on the F_{or}-dependent eigenstates (i=1 being the ground state) and $\omega_{ij}(F_{or})$ and $\mu_{ij}(F_{or})$ are the frequency and transition dipole moment for the $j \rightarrow i$ transition. A Gaussian lineshape with standard deviation σ is assigned to each transition for absorption spectra, while a Lorentzian lineshape with half width at half maximum Γ is used for Raman spectra. In the following $\sigma = 0.055$ eV and $\Gamma = 0.0005$ eV are used. Finally, the spectra of the solvated dye are calculated averaging the F_{or}-dependent spectra over the field temperature-dependent Boltzmann distribution relevant to the ground state.
Along similar lines, F_{or}-dependent steady state fluorescence spectra are calculated as:

$$Fluo(\omega, F_{or}) \propto \omega^3 \sum_{i<f} |\mu_{if}(F_{or})|^2 \exp\left(-\frac{(\omega_{if}(F_{or}) - \omega)^2}{2\sigma^2}\right) \tag{2.7}$$

where the fluorescent state f (the Kasha state) is identified as the first eigenstate of the electronically excited manifold and the thermal average is performed over the Boltzmann distribution relevant to the Kasha state. As it will be discussed in greater detail in the next section, this approach works well for fluorescence spectra in liquid (non-viscous) solvents, where the relaxation time of the solvents ensures the full equilibration of the solvent around the excited solute before fluorescence takes place.

	z_0	$-\tau$	ε_v	$\hbar\omega_v$
DCM	1.14	0.88	0.456	0.172
NR	0.88	0.95	0.33	0.14

Table 2.1: Molecular model parameters for DCM and NR (all quantities in eV).

Simulated steady state Raman, absorption and fluorescence spectra for DCM (panels **d**, **e** and **f**) and NR (panels **l**, **m** and **n**) are reported in figure 2.3. They compare very well with experiment, confirming the reliability

of the model and of its parametrization (molecular parameters, same used in chapter 1, are reported in table 2.1; solvent relaxation energies ε_{or} are reported in the legends). Simulated vibrational spectra only account for a single effective vibrational mode, therefore a punctual comparison with experimental Raman frequencies is meaningless, yet the progressive red-shift and broadening of the vibrational band upon increasing the solvent polarity is well reproduced. Indeed, the model captures well the complex evolution with solvent polarity of frequencies and bandshapes of absorption, fluorescence and vibrational spectra only accounting for the 4 fixed molecular parameters and adjusting the solvent relaxation energy. While μ_0 (the dipole moment associated with the zwitterionic state) would introduce an additional parameter, it is irrelevant here since absolute absorption intensities are not addressed.

2.1.3 DA dye in organic amorphous matrices

With the final aim of studying the dynamics in organic amorphous matrices (as relevant to OLED devices) in this section the experimental solvatochromic behavior of steady state spectra in matrices is investigated and a model for solid state solvation is built.

A strange solvatochromic behavior

In figure 2.4 experimental Raman, absorption and emission spectra are reported for DCM (panels **d**, **e**, **f**) and NR (panels **l**, **m**, **n**) dispersed in four different amorphous organic matrices (zeonex, mCP, mCBPCN and DPEPO), together with the spectra collected in different liquid solvents (same spectra as in figure 2.3). By comparing *absorption* spectra in liquid solvents and in matrices, a polarity scale for the matrices can be

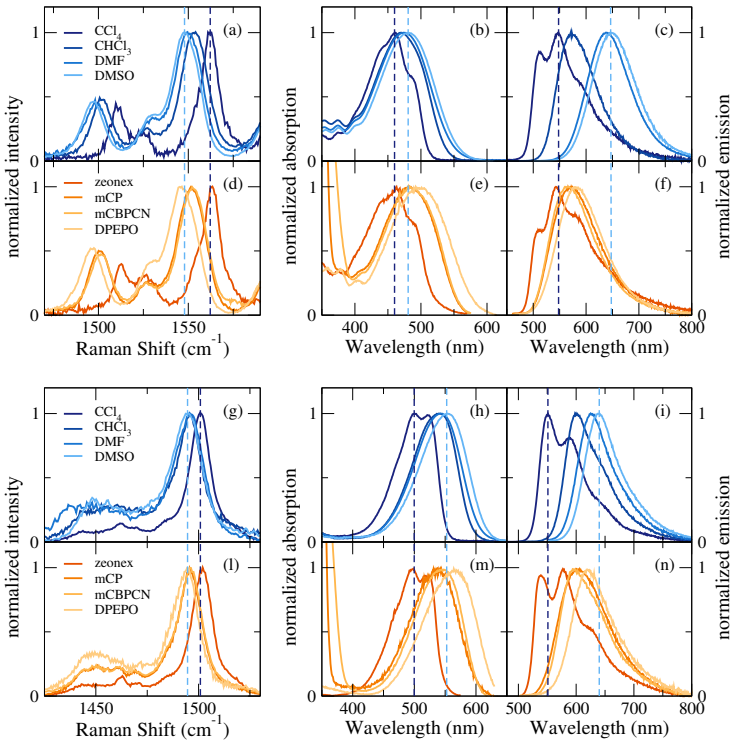

Figure 2.4: Experimenatal steady state spectra for DCM (panels **a**-**f**) and NR (panels **g**-**n**) collected in liquid solvents and in matrices. From left to right Raman spectra, absorption and fluorescence spectra are reported. Absorption spectra in matrices are measured as fluorescence excitation spectra. The vertical dashed lines show, as a guide for the eye, the positions of the band maxima measured in CCl_4 and DMSO.

defined: zeonex is non polar as CCl_4, mCP and mCBPCN have similar polarity as DMSO, while DPEPO is even more polar than DMSO. In solid matrices, the molecular units or the polymeric fragments are not moving freely, however, during the formation of the matrix, it is likely that polar molecules and/or polar groups arrange themselves around a polar dye generating again a reaction field proportional to the dipole moment of the dye. Once again, matrices containing polar molecules or polar groups are expected to generate a sizable reaction field $F_R \propto r\mu_g$. Non-resonant Raman spectra support the same polarity scale: once again, zeonex behaves like CCl_4, mCP and mCBPCN have similar polarity, being slightly less polar than DMSO, and DPEPO is as polar as or possibly slightly more polar than DMSO.

However, looking at *fluorescence* spectra collected in solid matrices (panels **f** and **n**), a surprise is found: the polarity scale defined upon comparison with emission spectra in polar solvents is different respect to the one established in absorption. In particular, zeonex, a non-polar matrix, behaves like CCl_4, as expected, but the other matrices look much less polar than they are in absorption. Just as the most striking example, Raman and absorption spectra suggest that DPEPO is as polar as or possibly slightly more polar than DMSO, but in emission DPEPO looks much less polar than DMSO. This is a clear indication that the matrix cannot fully readjust in response to the dye photoexcitation in the time-window of relevance to fluorescence. On the other hand, in the same timescale, the matrix is not fully rigid, as demonstrated by the sizable Stokes shifts observed in polar matrices.

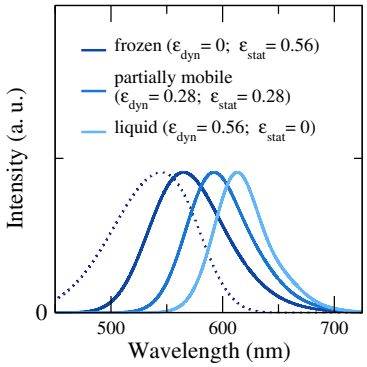

Figure 2.5: Calculated emission spectra for NR in a frozen, liquid and partially mobile environment. Absorption (calculated using $\varepsilon_{tot} = 0.56$ eV) is reported as a dotted line.

		ε_{or}	ε_{dyn}	ε_{stat}
DCM	zeonex	0.10	0.10	0.0
	mCP	0.65	0.20	0.45
	mCBPCN	0.70	0.15	0.55
	DPEPO	0.90	0.20	0.70
NR	zeonex	0.08	0.08	0.0
	mCP	0.50	0.40	0.10
	mCBPCN	0.56	0.28	0.28
	DPEPO	0.79	0.39	0.40

Table 2.2: Total relaxation energy ε_{or} (relevant to Raman and absorption spectra) and its partitioning in the static and dynamical components (relevant to emission) for DCM and Nile Red in zeonex, mCP, mCBPCN and DPEPO (all quantities in eV).

Model for solid state solvation

The same model adopted to simulate steady state DCM and NR spectra in solution also works for absorption and vibrational spectra in matrices, in the hypothesis that the matrix is equilibrated to the ground state molecular polarity of the dyes. Emission spectra are more delicate. Indeed, it is not possible to reproduce experimental emission spectra neither considering a liquid environment, i. e. assuming a complete relaxation of the environment around the excited dye before emission takes place, nor considering the environment completely frozen at the ground state equilibrium. In the first hypothesis the red shift would be too large, while in the second case it would be too small with respect to the experiment (see figure 2.5). Experimental data suggest that the molecules of the matrix are partially free to readjust around the excited dye as demonstrated by the finite Stokes shift, but the relaxation is hindered, so that the matrix molecules cannot fully relax before emission takes place. Following a recently proposed approach,[139] steady state fluorescence spectra can be simulated partitioning the relaxation energy estimated from the analysis of vibrational and absorption spectra into a dynamical component that describes the degrees of freedom that relax before emission takes place (up to the order of few nanoseconds) and a static component that relaxes on much longer timescales, if ever. A reaction field and a corresponding relaxation energy are assigned to the two components so that the Hamiltonian that describes the dye inside a

matrix reads:

$$\hat{H}_{tot}^{SSS} = \hat{H}_S - F_{stat}\hat{\rho} + \frac{F_{stat}^2}{4\varepsilon_{stat}} - F_{dyn}\hat{\rho} + \frac{F_{dyn}^2}{4\varepsilon_{dyn}}. \tag{2.8}$$

Steady state emission spectra are finally calculated considering the Boltzmann distribution relevant to the ground state over F_{stat} and the one relevant to the excited state over F_{dyn}. This partitioning is somewhat rough, but leads to a simple and effective approach to steady state fluorescence in semirigid environments. The position of the absorption spectrum only depends on the total amount of coupling $\varepsilon_{or} = \varepsilon_{stat} + \varepsilon_{dyn}$, while the position of the emission spectrum depends also on the relative magnitude of the two relaxation energies. Figure 2.5 shows how when the total relaxation energy is equally partitioned between the static and dynamical component (therefore simulating a partially mobile environment), the emission spectrum falls midway between emission in a completely frozen ($\varepsilon_{dyn} = 0$) and a completely mobile ($\varepsilon_{stat} = 0$) environment.

In figure 2.6 calculated Raman, absorption and emission spectra for DCM (panels **d**, **e**, **f**) and Nile Red (panels **l**, **m**, **n**) in the four investigated matrices are reported, together with experimental spectra (the same shown in figure 2.4). Molecular parameters are the same as in liquid solvents (table 2.1); total relaxation energies used to calculate absorption and Raman spectra and their partitioning in the static and dynamical contributions for the calculation of fluorescence spectra are reported in table 2.2.

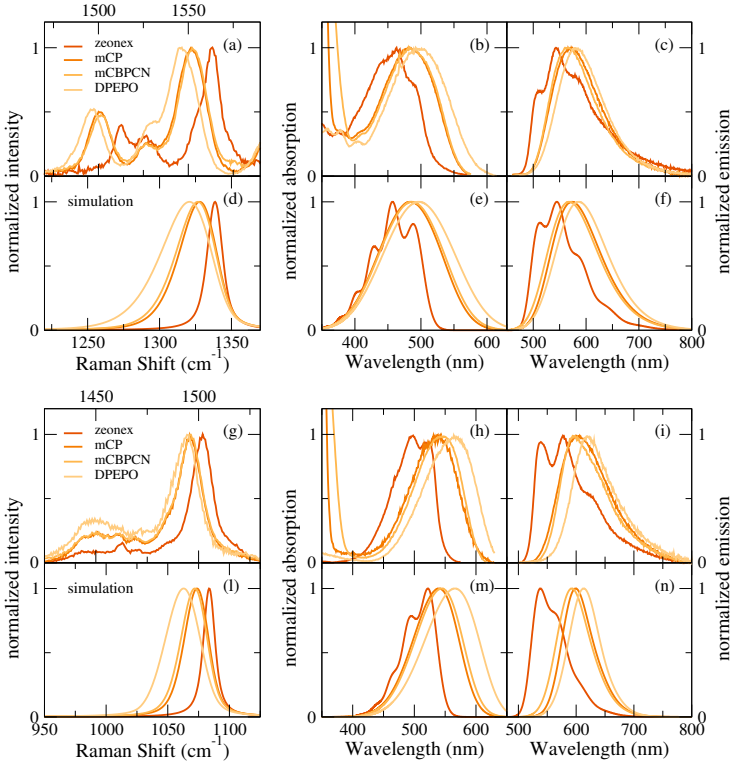

Figure 2.6: Steady state spectra for DCM (panels **a-f**) and NR (panels **g-n**) in matrices. From left to right Raman spectra, absorption and fluorescence spectra are reported. Panels **a-c**, **g-i** show measured spectra and panels **d-f**, **l-n** the calculated ones. Molecular parameters are reported in table 2.1, solvent relaxation energies and their partitioning in the static and dynamical components are reported in table 2.2.

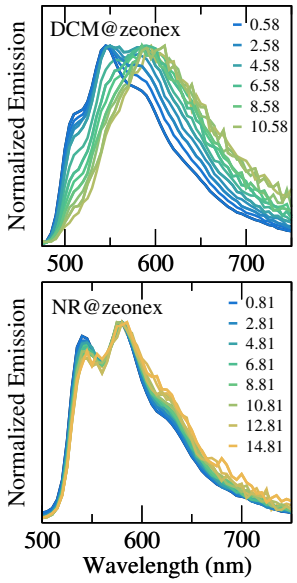

Figure 2.7: Time-resolved emission spectra of DCM (top panel) and NR (bottom panel) in zeonex. Legends report time in nanoseconds. Details on the experimental set up in ref.[72].

2.2 Relaxation dynamics in polar environments

The analysis of steady state spectra described in the previous section gives important hints about the behavior of molecular amorphous matrices. Primarily, experimental data suggests that these materials are neither completely frozen nor completely free to move and to reorient around the excited dye (at least not within the typical fluorescence lifetimes of few nanoseconds) and a theoretical model has been set up to support this physical interpretation. However, to fully understand solid state solvation, and in particular to get information about the matrix relaxation timescales, a time-resolved analysis is in order. Nile Red is chosen for the time-resolved studies because of its rigidity. DCM has a flexible molecular structure and it is expected to undergo a geometrical relaxation with a characteristic time that might compete with the relaxation of the environment. The emerging picture would therefore be compromised since disentangling the contributions to the Stokes shift related to the relaxation of the environment and to the conformational relaxation of the dye is practically impossible. Figure 2.7 shows how even in zeonex (i. e. a non polar environment, where solvatochromic effects are not expected) the time-resolved emission spectra of DCM present a significant red-shift, ascribed to the relaxation of the internal conformational coordinate. Conversely, this red shift is not observed for Nile Red (bottom panel in figure 2.7). DCM is a good and reliable polarity sensor as long as the interest is on the equilibrium polarity of the matrix, as tested by absorption and Raman spectra, but its flexibility makes it an unreliable probe for the dielectric dynamics. On the other hand, the rigidity of Nile Red ensures for the relaxation of the environment to be the only degree of freedom present in the system.

From the theoretical perspective, the relaxation model developed in chapter 1 has to be extended to account for the interaction with the classical reaction field F_{or}. Once validated in solution, the model will be used to address relaxation dynamics in solid matrices.

2.2.1 The quantum-classical Redfield-Smoluchowski master equation

An explicit and fully quantum mechanical treatment of the concurrent relaxation of a photoexcited molecule and of the surrounding environment is an impractical task due to the huge amount of degrees of freedom that would require. Since it is related to rotational and conformational motion, an appealing possibility is to treat the reaction field as a classical coordinate. Care has to be taken though, since the approach entails the delicate problem of combining a classical and a quantum systems. Here, a quantum classical Liouville equation based approach originally proposed to address energy transfer in solution[154] is exploited. Specifically, the Redfield relaxation model settled in chapter 1 (with linear system-bath coupling and constant spectral density) is adopted for the relaxation of the dye. The relaxation of the solvent, that enters the model as a classical overdamped coordinate, is described by the Smoluchowski equation.[154, 155] Following ref. [154], the quantum classical Redfield-Smoluchowski

master equation is obtained:

$$\begin{aligned}\frac{\partial}{\partial t}\sigma_{ab}(F_{or};t) =& -i\omega_{ab}\sigma_{ab}(F_{or};t) + \sum_{cd}\mathcal{R}_{ab,cd}\sigma_{cd}(F_{or};t)\\ &- \frac{F_{or}}{i\hbar}\sum_{c}\left(\rho_{ac}\sigma_{cb}(F_{or};t) - \sigma_{ac}(F_{or};t)\rho_{cb}\right)\\ &- \frac{\varepsilon_{or}}{\tau_l}\sum_{c}\left(\rho_{ac}\frac{\partial\sigma_{cb}(F_{or};t)}{\partial F_{or}} + \frac{\partial\sigma_{ac}(F_{or};t)}{\partial F_{or}}\rho_{cb}\right)\\ &+ \frac{1}{\tau_l}\frac{\partial}{\partial F_{or}}\left(F_{or}\sigma_{ab}(F_{or};t) + k_BT2\varepsilon_{or}\frac{\partial}{\partial F_{or}}\sigma_{ab}(F_{or};t)\right)\end{aligned} \tag{2.9}$$

where $\sigma_{ab}(F_{or};t)$ is the F_{or}-dependent density matrix element written on the basis of the eigenstates of the molecular Hamiltonian $\hat{H}_S$ in eq. 1.39 (the Hamiltonian for $F_{or} = 0$, i. e. a non-polar environment) and ρ_{ij} are the matrix elements of the ionicity operator. The first line in the above equation describes the Liouvillian dynamics (ω_{ab} is the frequency of the $b \rightarrow a$ transition) and the Redfield relaxation ($\mathcal{R}_{ab,cd}$ are the terms of the Redfield relaxation tensor as defined in section 1.1.3). The second and third lines describe the effect of the solvent on the solute and *vice versa*, respectively, and the last line accounts for the Smoluchowski dynamics of the solvent (k_B is the Boltzmann constant and T the temperature). The longitudinal relaxation time τ_l is the only parameter needed to describe the environment relaxation. It is characteristic of the environment and the values for common organic solvents are known.[71]

A well known problem of coupled quantum-classical dynamics is due to the third line in eq. 2.9, that breaks the positivity of the density matrix.[156–158] Moreover, when mixing quantum and classical dynamics, problems may arise with the dynamics not obeying detailed balance. To address these issues, the off-diagonal matrix elements of the ionicity operator $\hat{\rho}$ in the second and third line of eq. 2.9 are neglected. The approximation is somewhat crude, but it works well for the molecular relaxation process investigated here, as demonstrated by the analysis of time-resolved spectra collected in liquid solvents (see below). The master equation then becomes:

$$\begin{aligned}\frac{\partial}{\partial t}\sigma_{ab}(F_{or};t) =& -i\tilde{\omega}_{ab}(F_{or})\sigma_{ab}(F_{or};t) + \sum_{cd}\mathcal{R}_{ab,cd}\sigma_{cd}(F_{or};t)\\ &- \frac{\varepsilon_{or}}{\tau_l}\frac{\partial\sigma_{ab}(F_{or};t)}{\partial F_{or}}(\rho_{aa}+\rho_{bb})\\ &+ \frac{1}{\tau_l}\frac{\partial}{\partial F_{or}}\left(F_{or}\sigma_{ab}(F_{or};t) + k_BT2\varepsilon_{or}\frac{\partial}{\partial F_{or}}\sigma_{ab}(F_{or};t)\right).\end{aligned} \tag{2.10}$$

Quite interestingly, the frequency of the $b \rightarrow a$ transition involved in the Liouvillian dynamics described in this equation acquires a F_{or}-dependency accounting for solvatochromic effects:

$$\tilde{\omega}_{ab}(F_{or}) = \omega_{ab} - \frac{F_{or}}{\hbar}(\rho_{aa} - \rho_{bb}). \tag{2.11}$$

2.2.2 Validating the model: relaxation in liquid solvents

In this section, eq. 2.10 is used to simulate the relaxation dynamics of Nile Red in liquid organic solvents upon impulsive excitation and the results are validated against time-resolved pump probe experiments.

The system at equilibrium consists in a collection of molecules, each one experiencing a different reaction field, distributed according to the Boltzman law. To simulate an impulsive excitation over such a system (i. e. to prepare the initial state for the dynamics), the F_{or}-dependent Hamiltonian for the solvated molecule in eq. 2.4 is diagonalized on a grid of F_{or} values to obtain the F_{or}-dependent energies and eigenstates $|\psi_i(F_{or})\rangle$. The equilibrium solvent distribution is calculated as

$$w(F, t = 0) = e^{-\frac{E_1(F_{or})}{k_B T}} \tag{2.12}$$

where $E_1(F_{or})$ is the F_{or}-dependent ground state (the only populated state at the equilibrium). Upon impulsive excitation, the solvent distribution is unaffected, but for each value of the field F_{or}, the molecule is driven in the coherent state

$$|\Psi^*(F_{or})\rangle = \sum_{i=2}^{N} |\psi_i(F_{or})\rangle\langle\psi_i(F_{or})|\hat{\mu}|\psi_1(F_{or})\rangle. \tag{2.13}$$

Each $|\Psi^*(F_{or})\rangle$ is then rotated on the basis of the eigenstates of the F_{or}-independent molecular Hamiltonian in eq. 1.39 and finally the initial state for the dynamics is obtained as: [2]

$$\hat{\sigma}(F_{or}, 0) = w(F_{or}, 0)|\Psi'^*(F_{or})\rangle\langle\Psi'^*(F_{or})| \tag{2.14}$$

2: In the initial state prepared in this way the quantum and the classical parts are entangled, indeed it is not possible to write it as a direct product of a density matrix $\hat{\sigma}$ and a classical distribution w since $\hat{\sigma}$ acquires a dependence over F_{or}.

where $|\Psi'^*(F_{or})\rangle$ are the F_{or}-dependent coherent states rotated on the F_{or}-independent basis. The density matrix is normalized, $Tr_S\{\int dF_{or}\hat{\sigma}(F_{or}, t)\} = 1$, and the expectation value of a generic operator $\hat{A}$ (possibly F_{or}-dependent) is evaluated as:

$$\langle\hat{A}(t)\rangle = Tr_S\left\{\int dF_{or}\hat{A}(F_{or})\hat{\sigma}(F_{or}, t)\right\} \tag{2.15}$$

where $Tr_S\{\cdot\}$ is the trace over the system degrees of freedom.[159]

The relaxation of the coherently excited state is evaluated integrating eq. 2.10 with the Short-Iterative-Arnoldi algorithm with a time-step of 1.5 fs and with a Krylov space of dimension of 20. A full Redfield approach is adopted, meaning that all the terms of the four dimensional Redfield tensor $\mathcal{R}_{ab,cd}$ are accounted for. Temperature is set to 298 K and a constant spectral density is used with $\gamma = 5$ ps^{-1}.

Figure 2.8 shows results for NR in chloroform ($\varepsilon_{or} = 0.47$ eV, $\tau_l = 0.28$ ps). Panels **a**, **b** and **c** report the time evolution of the energy of the molecule, $\langle\hat{Q}\rangle$ and $\langle F_{or}\rangle$, respectively, where $\langle F_{or}\rangle$ is calculated as $Tr_S\{\int dF_{or}\hat{\sigma}(F_{or}, t)F_{or}\}$. Panels **d** and **e** show the evolution of the distribution of the solvation coordinate calculated as $w(F_{or}, t) = Tr_S\{\hat{\sigma}(F_{or}, t)\}$. In panel **a** the energy decay obtained for $F_{or} = 0$ (i. e. for the molecule in a non-polar solvent) is reported as a black dashed line for reference. In polar solution, the energy of the initial state is a bit lower (~ 0.1 eV) because of the stabilization due to the interaction with the polar solvent

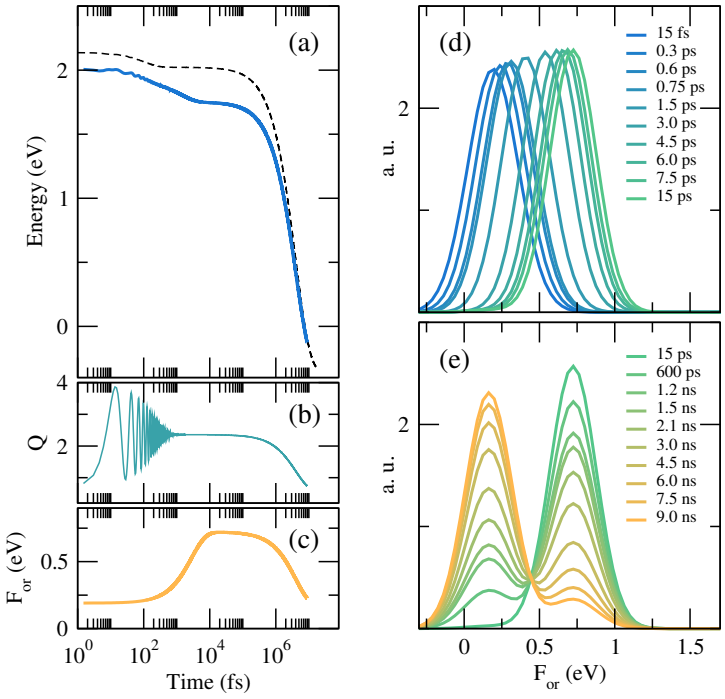

Figure 2.8: Relaxation dynamics of coherently excited NR in $CHCl_3$ ($\varepsilon_{or} = 0.47$ eV, $\tau_l = 0.28$ ps). Linear system bath coupling and constant spectral density are used ($\gamma = 5$ ps^{-1}). (**a**) time evolution of the energy of the system, the black dashed line shows the result obtained for $F_{or} = 0$ (same as in chapter 1, figure 1.10). Time evolution of $\langle\hat{Q}\rangle$ and $\langle F_{or}\rangle$ (**b** and **c**, respectively) and evolution of the solvent distribution $w(F_{or}, t)$ (**d** and **e**, times indicated in the legends).

and most notably an energy decay due to the equilibration of the solvent around the excited state appears in the picosecond timewindow that is not present in a non-polar environment. At first, the system relaxes from the initial coherent state to the Kasha state with a characteristic time of 100 fs. The motion is initially coherent, as demonstrated by the oscillations of $\langle\hat{Q}\rangle$ in panel **b**, but by the time population is completely transferred to the Kasha state coherence is lost, as reflected in the damping of the oscillations. The solvent then equilibrates around the Kasha state with its characteristic time of $\tau_l = 2.8$ ps, as it can be seen in panels **c** and **d**, where the solvent distribution shifts to higher fields and becomes slightly narrower. Subsequently, the system starts its slow (~ 4 ns characteristic time) and incoherent run towards the ground state, with the solvent distribution developing a bimodal shape as long as both the ground and Kasha states are populated.

Following the same approach exposed in chapter 1, time-resolved emission spectra are calculated and compared to experiment. The emission spectrum at time t' after the impulsive excitation is calculated defining the initial generating function as $\hat{\Omega}^f(F_{or}; t - t', t') = \hat{\mu}\hat{\sigma}(F_{or}; t')$, where $\hat{\sigma}(F_{or}; t')$ is the system reduced density matrix at time t' obtained integrating equation 2.10. Time evolution of $\hat{\Omega}^f(F_{or}; t - t', t')$ is evaluated according to equation 2.9 (where the whole $\hat{\rho}$ operator is used). Same temperature and dimension of the Krylov space are used as in the main dynamics and 0.15 fs is used as time integration step. The dipole-dipole correlation function is obtained as $C^f_{\mu\mu}(t-t', t') = \langle\hat{\mu}(t-t')\hat{\mu}(t')\rangle = Tr_S\left\{\int dF_{or}\hat{\mu}'\hat{\Omega}^f(F_{or}; t - t', t')\right\}$ where $\hat{\mu}'$ is the lower triangle of the dipole moment operator, that allows to extract only the emission contribution. The emission spectrum at t' is finally obtained as the power spectrum of the Fourier transform of $C^f_{\mu\mu}(t - t', t')$ over the $t - t'$ domain (damped with an exponential decay $e^{-t/a}$; $a = 30$ fs is used here). Since the generating function has to be propagated just for a short time compared to τ_l, to speed up the calculation in this propagation

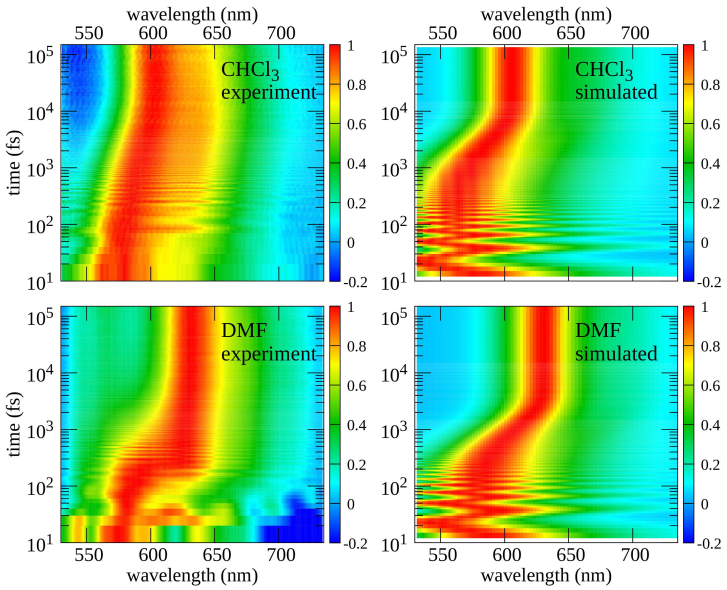

Figure 2.9: Left panels: experimental pump-probe maps showing the time evolution of the stimulated emission signal (positive sign) for NR in $CHCl_3$ (top) and DMF (bottom). Right panels: relative simulated time-resolved emission spectra (molecular parameters in table 2.1; in $CHCl_3$ ε_{or} = 0.47 eV and τ_l =2.8 ps, in DMF ε_{or} = 0.62 eV and τ_l =0.91 ps). Details on the experimental set up in ref.[72].

the environment can be considered frozen.

Color maps in right panels of figure 2.9 show the (normalizad) time-resolved emission spectra calculated for NR dissolved in $CHCl_3$ (τ_l = 2.8 ps) and DMF (τ_l = 0.91 ps). Same model parameters (including the solvent relaxation energies) adopted to simulate steady state spectra (figure 2.3) are used. The time evolution of emission spectra is related to the concurrent relaxation of the photoexcited molecule and or the surrounding solvent. Within the first few hundreths of fs clear signatures related to the coherent vibrational oscillations are observed, as in figure 1.13 in chapter 1. The subsequent red shift is related to the reorganization of the solvent around the solute excited state (occurring precisely with the characteristic relaxation times of the solvents). It is worth to point out that in this theoretical approach no approximation regarding the separation of these two motions is introduced, but everything is treated in a unique framework. Reliable results are therefore obtained also for systems where solvation dynamics is fast and totally or partially (as in DMF) intertwined with the fast vibrational internal conversion.

Experimantally, the time evolution of the emission spectrum is followed observing the stimulated emission signal in an Ultra Short pump-probe (US-pp) experiment (more details are reported in ref.[72]). The agreement with experimental data (reported in the left panels of figure 2.9) is impressive and validates the theoretical approach. It is worth to highlight that for simulations in liquid solvents no adjustable parameters enter the dynamics: once a specific dye in a specific solvent is chosen, the molecular parameters, together with the solvent relaxation energy ε_{or}, are fixed by the analysis of steady state spectra, while the solvent relaxation time is taken from literature. The main discrepancy between simulations end experiments is observed in the very early time, where the coherent oscillations are very pronounced in the simulations and much less prominent in experimental spectra. This minor discrepancy is traced back to the main approximation of the molecular model that accounts for a single effective vibrational mode coupled to the electronic degrees of freedom. In the actual molecule, several vibrations with different

frequencies are coupled to the electronic system, somewhat suppressing the signal due to coherent oscillations (as proven in figure 1.13, chapter 1, where TRES for a system with one and three coupled modes are compared).

2.2.3 Amorphous matrices: how do they move?

After the validation of the model *via* the analysis of time-resolved emission spectra in liquid solvent, dynamical behavior of amorphous matrices is now addressed. At variance with liquid solvents, relaxation times for solid matrices are not known and *via* a careful simulation of time-resolved spectra this important information will be extracted for the first time. The time window that can be investigated extends up to ~ 15 ns, being clearly limited by the fluorescence lifetime of Nile Red.

The model for time-resolved emission spectra can be extended to account for the interaction with the two separate static and dynamical components of the reaction field in eq. 2.8. The presence of two classical fields makes the calculation very demanding, therefore to address the very long times (>ns) needed to simulate spectra in matrices further approximations are required. Specifically, the first 1.5 ps of the main dynamics is calculated exactly as in section 2.2.2 for liquid solvents: the initial coherent excitation is simulated following eq. 2.13, full Redfield tensor is used, dimension of Krylov space 20, time integration step 1.5 fs, temperature 298 K and $\gamma = 5$ ps^{-1}. This allows to observe the oscillations of the spectrum in the first hundreds of femtoseconds. The second part of the dynamics (from 1.5 ps on) is calculated adopting the Bloch approximation and evolving just the populations. The calculation significantly speeds up since just the N diagonal elements of the density matrix have to be evolved and not the N^2 elements. This approximation is reliable since coherences are completely suppressed after 1.5 ps. Moreover, evolving just the populations in the Bloch approximation allows to drastically reduce the dimension of the Krylov space required by the SIA algorithm from 20 to only 3.

The straightforward extension of the dynamical model for TRES in solution to the Hamiltonian in eq. 2.8 is too rough to address the complex relaxation phenomena that governs time-resolved emission in solid matrices. In particular, it is not possible to reproduce the expetimental data considering a constant τ_l for the dynamical component of the reaction field, suggesting that motion in matrices occurs in a different way with respect to a liquid environment. The partially hindered motion of the molecules in the solid amorphous phase is likely to originate several relaxation degrees of freedom, each one with its characteristic τ_l. Most probably, there is a distribution of relaxation times, and as a first attempt to describe this complex scenario a *time-dependent relaxation time* is introduced, as to account for the different timescales associated to the different degrees of freedom of the solid matrices.[142] Specifically, the following form for the relaxation time is adopted:

$$\tau_l(t) = a + b\left(1 - e^{-ct}\right) \tag{2.16}$$

where a, b and c are adjustable parameters. This function describes an initial relaxation time a that increases in time (with a velocity governed by c) up to the $a + b$ value, representing an environment that, in response

to the stimulus related to the molecular excitation, moves initially with velocity $1/a$ and progressively slows down to $1/(a+b)$.

Best fit to experimental data are obtained setting $a = 100$ ps, $b = 14.9$ ns and $c = 0.0007$ ps^{-1} for DPEPO and $a = 20$ ps, $b = 5$ ns and $c = 0.001$ ps^{-1} for mCBPCN. An additional adjustment is needed for mCBPCN: experimental data suggest the presence of an initial very fast (<1 ps) relaxation, most probably related to the vibrational relaxation of CN groups. To reproduce this feature, for the first 300 fs a relaxation time of 500 fs is considered, that is then switched off. In a first approximation, this is equivalent to splitting the dynamical coordinate in two: F_{dyn1} with $\tau_l = 500$ fs and F_{dyn2} with $\tau_l(t)$.

Color maps in figure 2.10 show the comparison between experimental and simulated time-resolved emission for NR in mCBPCN and DPEPO, while the rightmost panels show the measured and simulated time evolution of the maximum of the emission spectrum. To explore such a wide time window, different experimental techniques are exploited: a Long Range and an Ultra Short pump-probe set up (LR-pp and US-pp, respectively) are used to detect the stimulated emission signal up to 1.5 ns and time-resolved emission is recorded up do 15 ns with the time-correlated single-photon counting (TCSPC) technique, more details in ref.[72]. The results of the simulations compare impressively well with experimental data in the whole accessible 15 fs - 15 ns time window, demonstrating that the model is robust and yields reliable information about the dielectric dynamics of amorphous matrices. The major discrepancy is again observed in the subpicosecond window, where the molecular model, accounting for a single coupled vibrational mode, amplifies coherent oscillations.

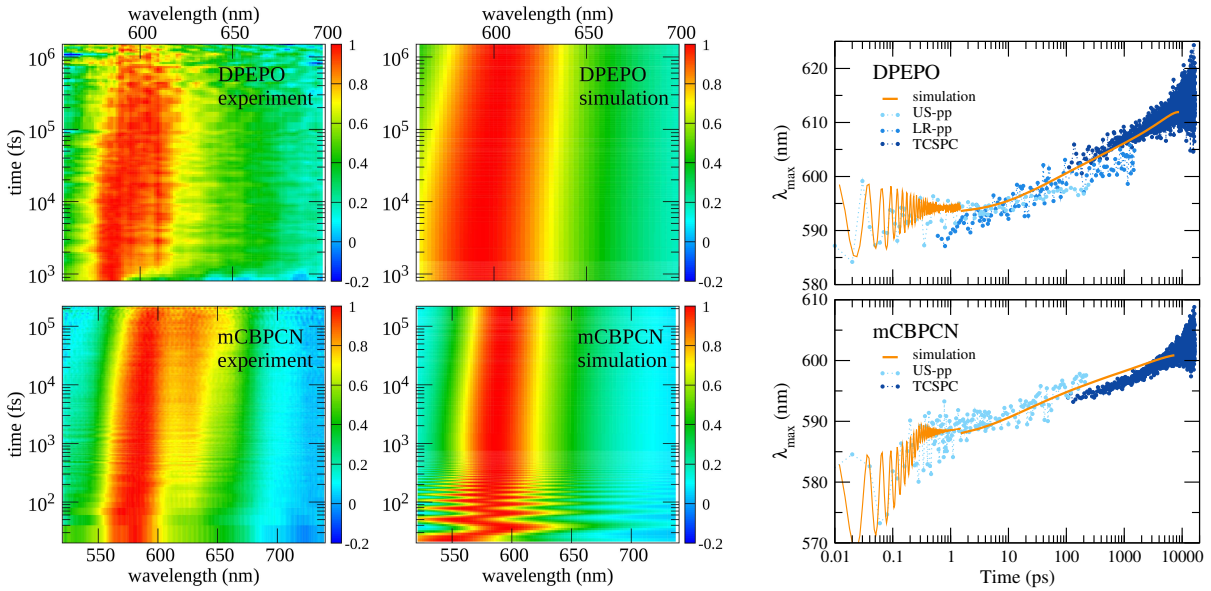

Figure 2.10: Left panels: stimulated emission signal (positive sign) for NR in DPEPO (top, LR-pp pump-probe set up) and mCBPCN (bottom, US-pp pump-probe set up). Central panels: relative simulated time-resolved emission spectra (molecular parameters in tables 2.1 and 2.2, time-dependent relaxation times as defined in the main text). Right panels: time evolution of the maximum of the emission spectra. Bluish dots refer to experimental data collected with different techniques (as per legends), the orange line shows simulated results. For better comparison, simulated spectra are red shifted by 2.5 nm for DPEPO (top panels) and by 6 nm for mCBPCN (bottom panels). Details on the experimental set ups in ref.[72].

As a definitive proof that the observed dynamical Stokes shift is due to the mobility of the environment, measurements at low temperature are performed, where matrices are expected to be completely frozen. As expected, figure 2.11 shows how at 77 K the dynamical Stokes shift is negligible if compared to the room temperature case.

The results conclusively suggest that at room temperature these materials do move at least up to ~ 15 ns, with DPEPO being much more sluggish than mCBPCN. Moreover, relaxation dynamics in matrices proves to be inherently more complex than in a liquid environment, as demonstrated by the impossibility to reproduce experimental data accounting for a single constant longitudinal relaxation time.

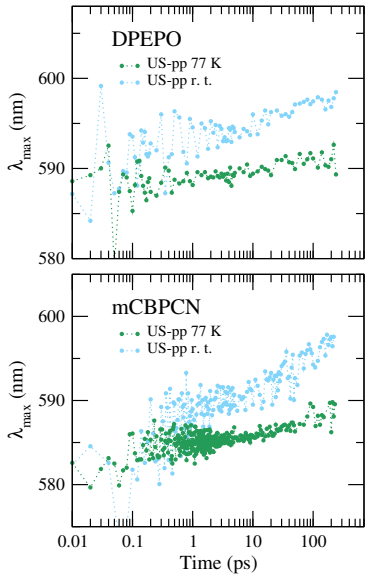

Figure 2.11: Time evolution of the maximum of the emission spectrum for NR in DPEPO (top panel) and mCBPCN (bottom panel) at room temperature (cyan dots) and at 77 K (green dots).

2.3 Conclusions

Understanding how optical properties of an organic dye are affected when the dye is dispersed in a matrix is crucial for the optimization of materials for optoelectronic devices like OPV, OLED or organic solar concentrators. However, while solvatochromism is well recognized in low viscosity solvents, solid state solvation is still far less understood. Here an extensive experimental and theoretical study of SSS in presented, where two commercial solvatochromic dyes are used to characterize the static and dynamical dielectric response of several amorphous matrices of interest for OLED applications. When discussing the dielectric behavior of a medium, the timescales of relevant processes are decisive. In solid state solvation care has to be taken when distinguish between the dielectric properties that define the spectral responses of the dye at equilibrium, i.e. absorption and Raman spectra, and those related to emission spectra, occurring from an out of equilibrium state. In the first case, the dynamical behavior of the environment is irrelevant, while for emission spectra its dielectric dynamics is of paramount importance. A deep understanding of the subtleties of environmental effect is therefore crucial.

The electronic degrees of freedom of the environment, associated to the medium polarizability, are related to the medium refractive index at optical frequencies.[17, 121] Relevant degrees of freedom, typically in the UV region, instantaneously readjust during the excitation of the dye. They are responsible for large effects on the molecular spectral properties when going from gas phase to an organic medium. However, the marginal variability of the refractive index in common organic media makes it very difficult to appreciate the role of the environmental electronic polarizability when comparing spectra collected in condensed phases. In other terms, when discussing solvatochromism, the most relevant effect is due to the rearrangement of polar molecules or polar groups around a polar solute.

These orientational degrees of freedom are much slower than the degrees of freedom of the dye in the visible or IR regions, so that, during the electronic or vibrational excitation of the dye, they are essentially frozen in the configuration equilibrated to the charge distribution of the dye in the ground state. To measure the static polarity of the environment, polar dyes, like DCM or NR, are good microscopic polarity probes: comparing their absorption or vibrational spectra with those measured in liquid solvents of different polarity offers a reliable polarity scale for

solid matrices. In particular absorption and Raman spectra of the above mentioned dyes in the four investigated matrices indicate that at the equilibrium zeonex is non-polar (as CCl_4), mCP and mCBPCN have similar polarity as DMSO and DPEPO is slightly more polar.

After photoexcitation of a solvatochromic dye, the orientational degrees of freedom of the medium, equilibrated to the ground state charge distribution of the dye, start to reorganize to respond to the large variation of the charge distribution in the excited state. The dynamics of this rearrangement is very different in media of different nature. In non-viscous liquid solvents, the solvent equilibrates in few picoseconds, [71] and steady state fluorescence occurs from a dye surrounded by the solvent equilibrated to the excited state charge distribution.[155, 160] This relaxation is responsible for the large Stokes shifts observed for polar molecules in polar solvents. In glassy solvents at cryogenic temperatures, the solvent relaxation is hindered, leading to virtually infinite relaxation times, and the Stokes shifts due to polar solvation vanish, even in highly polar solvents.[141]

The situation is more delicate in solid matrices: the frequency of steady state fluorescence spectra depends in an intricate way on the matrix polarity and on its dynamics and the scale of polarity defined by steady state emission is different with respect to the one defined in absorption. Consequently, solid state solvation (typically discussed with reference to fluorescence spectra[123–125]) requires a detailed understanding of the dielectric relaxation of the matrix. Nile Red is chosen as a reliable probe for the dielectric relaxation due to its rigidity, so that the relaxation of the molecular conformational degrees of freedom does not interfere with the matrix dynamic. Time-resolved spectra in mCBPCN and DPEPO show that both these matrices rearrange in the whole accessible time-window (ranging from 15 fs to 15 ns, being clearly limited by NR fluorescence lifetime) without reaching equilibrium.

In this intriguing scenario, a theoretical model is developed both to support the physical interpretation of the experimental data and to gain some insights on the nature of these subtle phenomena. The essential state model for a dipolar chromophore is extended to account for polar solvation introducing the interaction with an electric field F coupled to the electronic degrees of freedom of the dye and treated as a classical coordinate. The model is then adapted to solid state solvation, where the separation of the reaction field F in a static and a dynamical contribution is necessary to reproduce in a unified picture both absorption and steady state emission spectra.

The model is extended to address time-resolved emission. Relaxation of the polar environment, described with the Smoluchowski equation, is included in the Redfield relaxation model for the dipolar dye presented in chapter 1, leading to a mixed quantum-classical master equation. The approach is validated in liquid solvent, where literature data about solvent relaxation times are available and hence no additional fitting parameters are needed. On this solid basis, the simulation of time-resolved spectra of NR in mCBPCN and DPEPO gives a first reliable estimate of relevant relaxation times. Indeed, a single relaxation time is not enough to describe the matrix relaxation and a time-dependent relaxation time must be introduced, meaning that the motion in solid

matrices is not just slower than in liquid solvents, but has a different nature.

In conclusion, a joint experimental and theoretical study is presented that validates a reliable and effective approach to address the intricate topic of solid state solvation, encompassing a wide range of spectral properties. Experimental data, supported and elucidated by a detailed theoretical model, definitely demonstrate that the dielectric relaxation in polar amorphours matrices is not fully frozen and definitely occurs on timescales that extend above 10 ns, with an overall sluggish relaxation of DPEPO if compared with mCBPCN. The approach is easily generalized to other types of matrices or media offering a useful characterization tool to exploit solid state solvation towards optimized optoelectronic devices.

Part II

The Frenkel-Holstein Hamiltonian: from aggregates to squaraine crystals

3

This chapter opens the second part of this thesis, dedicated to molecular aggregates. Intermolecular interactions drive the collective behavior of materials and play a pivotal role in defining the properties of molecular aggregates, films and crystals. Charge generation and transport, energy transfer, photophysical properties, exciton dynamics are just a few phenomena governed by intermolecular interactions. Jelley and Scheibe independently observed the aggregation-induced appearence of an intense red-shifted band in the absorption spectrum of aggregates of pseudoisocyanine chloride[161, 162] in seminal works that opened a novel research field. Relying on the Frenkel and Davydov exciton theory for molecular crystals,[163–165] McRae and Kasha developed a unified theory[166–168] to explain the peculiar and diverse photophysics of molecular aggregates, with the crucial classification of red-shifted superradiant J-aggregates and blue-shifted non emissive H-aggregates (where the shift is intended as the shift of the absorption spectrum of the aggregate with respect to the absorption of the isolated monomer). In its original formulation, Kasha theory only accounts for electronic degrees of freedom and intermolecular interactions are treated as purely electrostatic interactions. As extensively reviewed by Hestand and Spano,[169] the theory has been further developed to include intramolecular vibronic coupling, typically described by the Frenkel-Holstein Hamiltonian, and charge transfer intermolecular interactions, revealing an incredibly rich and variegated array of possibilities beyond the original Kasha model.

In the first part of this chapter, Kasha theory and its extension to account for intramolecular vibronic coupling is presented, focusing on the vibronic shape of absorption spectra of ideal H- and J-aggregates. Aggregates of non-parallel molecules are then addressed. In particular, a detailed discussion on the interplay between nearest neighbor and next-nearest neighbor interactions in the definition of the vibronic features of absorption spectra is proposed.

Among the most interesting and intriguing families of molecules whose aggregates, thin films and crystals are fervently studied, squaraines certainly represent a remarkable case. As it will be further discussed in chapter 5, squaraine aggregates and thin films often provide challenging case studies pushing forward theoretical research. Squaraines are π-conjugated dyes constituted by a central electron acceptor unit derived from the squaric acid and two variously decorated side branches acting as energy donor groups arranged in a quadrupolar D-A-D structure.[170, 171] The great variability of possible decoration patterns offered by organic synthesis makes the squaraine scaffold an ideal playground for the engeneering of functional molecules for several applications in different fields encompassing organic optoelectronics,[6–11] bioimaging[3, 4], xerography[172] and photodynamic therapy.[5]

SQIB (2,4-bis[4-(*N*,*N*-diisobutylamino)-2,6-dihydroxyphenyl]squaraine) is a prototypical anilino squaraine decorated with branched isobutyl

Part of the work presented in this chapter was carried out during a stay at Temple University, Philadelphia (PA), under the supervision of prof. Frank Spano.

alkyl side chains. SQIB thin films are easily grown from solution or by vapor phase deposition and have been investigated for photovoltaic applications.[30–37] Two SQIB polymorphs are known: a monoclinic $P2_1/c$ phase and an orthorhombic $Pbcn$ phase. Both phases have been experimentally characterized[30, 32, 33, 173] and the selective growth of crystalline thin films of the two polymorphs has been engineered by controlling deposition conditions such as the nature and temperature of the templating substrate and post-deposition annealing treatments.[31] In the second part of the chapter, the Frenkel-Holstein Hamiltonian is used to simulate polarized absorbance spectra of thin films of both polymorphs supporting the interpretation of experimental data and getting insights on the physics of these systems.

The chapter is structured as follows: in section 3.1 Kasha theory for ideal H- and J-aggregates is briefly exposed, together with the effects of the inclusion of intramolecular vibronic coupling. In section 3.2 aggregates of non-parallel molecules are investigated, with a particular focus on the role played by next-nearest neighbor interactions in affecting the vibronic structure of the absorption spectrum. Section 3.3 is then devoted to the simulation of polarized absorption spectra of thin films of the SQIB orthorhombic and monoclinic phases. Section 3.4 finally concludes the chapter.

3.1 Vibronic signatures of ideal H and J aggregates

3.1.1 Kasha theory

Kasha theory[166–168] considers Coulomb coupling as the only source of intermolecular interaction and, in its simplest formulation, accounts for a single excited state for each molecule. Since electrons are localized on the molecular sites, a convenient basis to describe the aggregate is obtained as the direct product of molecular states. As sketched in figure 3.1, for a system of N-coupled chromophores the aggregate ground state $|G\rangle$ is trivially defined as the state where each molecule is in its ground state g, while state $|n\rangle$ (with n ranging from 1 to N) represent a state where the n-th molecule is in the excited state e, all other molecules remaining in the ground state g. The Heitler-London approximation is then invoked,[165, 174] that in the hypothesis of small coupling considers only interactions among degenerate states. Only the subspace of the N local excitations $\{|n\rangle\}$ is therefore considered, and on this basis the Frenkel exciton Hamiltonian reads:

$$H = E_M + \sum_{m,n} J_{m,n} |m\rangle\langle n|. \tag{3.1}$$

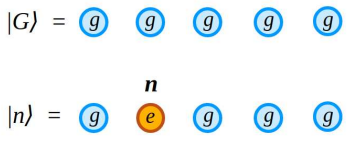

Figure 3.1: Sketches of the aggregate ground state $|G\rangle$ and of the local excited state $|n = 2\rangle$ for a linear chain of 5 molecules, each circle representing a molecular site.

The site excitation energy E_M is defined as $E_M = E_M^0 + D$, where E_M^0 is the energy of the $S_0 \rightarrow S_1$ transition of the isolated molecule and D is the gas-to-crystal shift, representing a correction to the gas-phase excitation energy of the monomer due to non-resonant interactions with the other molecules of the aggregate. As mentioned above, the resonant intermolecular interactions $J_{m,n}$ are typically evaluated as the Coulomb

interaction between the transition dipole moments on molecule n and m. In the simplest flavour of Kasha theory, they are treated in the point dipole approximation. Accordingly:

$$J_{m,n} = \frac{\vec{\mu}_n \vec{\mu}_m - 3(\vec{\mu}_n \cdot \hat{r})(\vec{\mu}_m \cdot \hat{r})}{4\pi\varepsilon r^3} \tag{3.2}$$

where $\vec{\mu}_n$ is the transition dipole moment for the $S_0 \rightarrow S_1$ transition on the n-th molecule, $\vec{r} = r\hat{r}$ is the vector connecting the two point dipoles (r being the magnitude and $\hat{r}$ the versor) and ε is the dielectric constant of the medium. Considering the two limiting geometries (dubbed as side-by-side and head-to-tail arrangements) sketched in figure 3.2 (where each ellipse represents a molecule with the transition dipole moment oscillating along the long molecular axis), eq. 3.2 gives for in-phase oscillating dipoles a positive Coulomb coupling in the former case and a negative coupling in the latter.

If periodic boundary conditions are applied, solutions of the Hamiltonian 3.1 are wavelike excitons:

$$|k\rangle = \frac{1}{\sqrt{N}} \sum_n e^{ikn} |n\rangle \tag{3.3}$$

where k is the wave vector $k = 0, \pm 2\pi/N, \pm 4\pi/N, \ldots, \pi$, with $k = 0$ and $k = \pi$ defining the states where all local transition dipole moments oscillate in-phase and out-of-phase, respectively, as sketched in figure 3.2. A selection rule in optical spectroscopy states that only states at $k = 0$ are active. States at $k = 0$ actually bear all oscillator strength, with a total transition dipole moment from the ground state scaling as $\sqrt{N}\vec{\mu}$ (where $\vec{\mu}$ is the transition dipole moment of the monomer).[167] For all other k values, contributions with opposite sign cancel out giving a vanishing total transition dipole moment. The energy associated with the k-th eigenstate is:

$$E_k = E_M + J_k \tag{3.4}$$

with

$$J_k = \sum_n J_{m,n} \cos\left[k(n-m)\right] \tag{3.5}$$

where the sum is independent of m due to the periodic boundary conditions. Often, only nearest-neighbor coupling J_C is accounted for (a good approximation for linear aggregates). In this case, the dispersion relation reads:

$$E_k = E_M + 2J_C \cos(k) \tag{3.6}$$

defining a band with a width $W = |J_{k=0} - J_{k=\pi}| = 4|J_C|$.

Eq. 3.6 highlights the role of the sign of the Coulomb coupling in the definition of the electronic band structure of the aggregate and hence of its photophysics. Figure 3.3 shows in panel **a** the dispersion relation for positive and negative J_C (blue and red curves, respectively), where filled circles mark the bright states at $k = 0$. In a so-called H-aggregate[175–183] (often associated with a side-by-side geometry) a positive interaction $J_C > 0$ sets the bright state at $k = 0$ at the band top and the dark state at $k = \pi$ at the band bottom. This shows up with an absorption spectrum blue-shifted with respect to the monomer and a suppressed emission (according to the Kasha rule, emission comes from the lowest energy excited state[184], that for H-aggregates is a dark $k = \pi$ state). On the

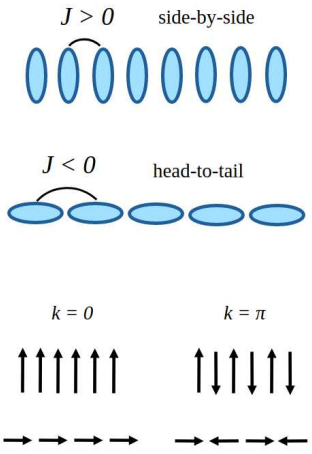

Figure 3.2: Top: side-by-side and head-to-tail arrangements of molecules, interacting respectively with a positive and negative Coulomb coupling. Bottom: in-phase ($k = 0$) and out-of-phase ($k = \pi$) combination of transition dipoles for the two arrangements shown above.

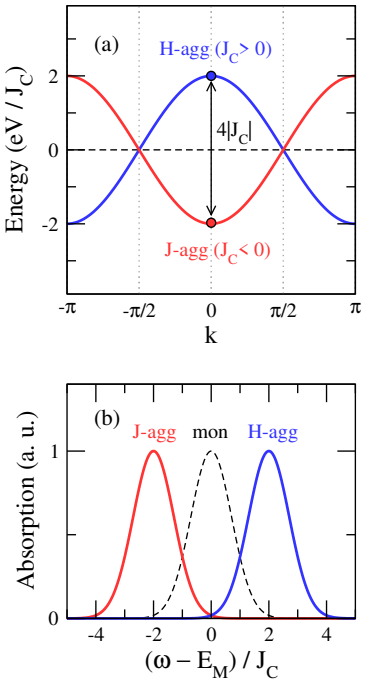

Figure 3.3: (**a**) Dispersion relations for a linear H-aggregate ($J_C > 0$ blue curve) and J-aggregate ($J_C < 0$, red curve). Filled circles mark the bright ($k = 0$) states. Black dashed line indicates E_M, set as the zero of the energy scale. (**b**) Absorption spectra of the isolated monomer (black dashed line), H-aggregate (blue line) and J-aggregate (red line). Gaussian bandshapes with standard deviation $\sigma = J_C$ are assigned to every transition.

contrary, a negative interaction $J_C < 0$ (often associated with a head-to-tail geometry) defines a so-called J-aggregate[161, 185–189], where the bright state at $k = 0$ is located at the band bottom, resulting in a red-shifted absorption spectrum with respect to the monomer and an emission radiative rate (that scales as the the square of the transition dipole moment) enhanced by a factor of N with respect to the monomer (a feature usually referred to as superradiance).

Relying on the Kasha model, aggregates are classified as H- and J-aggregates with reference to the absorption spectrum being blue- and red-shifted with respect to the monomer. In particular, if $D = 0$ the absorption spectrum of a H- and J-aggregate is respectively blue- and red-shifted with respect to the monomer by $2|J_C|$ (as reported in panel **b** of figure 3.3). This, however, can lead to ambiguous scenarios, for example, if the gas-to-crystal shift D is larger than the shift due to the Coulomb coupling J_C ($|D| > 2|J_C|$). Actually, the world of molecular aggregation offers a much more diversified landscape with respect to the guidelines offered by Kasha theory,[169] whose main limitations arise from neglecting vibronic coupling and limiting intermolecular interactions to the purely electrostatic Coulomb coupling within the framework of the Heitler-London approximation. In the next section, intramolecular vibronic coupling is introduced, showing how vibronic signatures arising from intermolecular interactions display different features in H- and J-aggregates and constituite a much more reliable signature for the type of aggregation than the spectral shifts.[169, 190]

3.1.2 Accounting for vibronic effects

The Frenkel-Holstein Hamiltonian

In the landscape of molecular aggregates, a prominent role is played by π-conjugated molecules because of the great variety of aggregation patterns driven by π-stack interactions. In the majority of π-conjugated molecules, the $S_0 \rightarrow S_1$ electronic transition is coupled to few nuclear coordinates, like the symmetric vinyl stretching mode or the aromatic-quinoidal stretching mode in ring systems. The intramolecular vibronic coupling has a great impact on the monomer spectra, where it is responsible for the vibronic progression in absorption and emission bands. Vibronic coupling in the isolated molecule is typically modeled collapsing all coupled nuclear coordinates into a single effective harmonic coordinate Q with frequency ω_{vib}, generally in the $\sim 0.15 - 0.18$ eV range (here and hereinafter in this chapter $\hbar$ is set to 1). The two electronic states S_0 and S_1 are therefore assigned two harmonic potential energy curves along the nuclear coordinate, mutually shifted by ΔQ. The vertical excitation $S_0 \rightarrow S_1$ energy can be written as $\omega_{00} + \lambda^2\omega_{vib}$, where ω_{00} is the energy difference between the two minima and $\lambda^2\omega_{vib}$ is the nuclear relaxation energy, as shown in figure 3.4. The amount of vibronic coupling is determined by the dimensionless Huang-Rys factor λ^2, that defines the number of vibrational quanta in the relaxation energy.

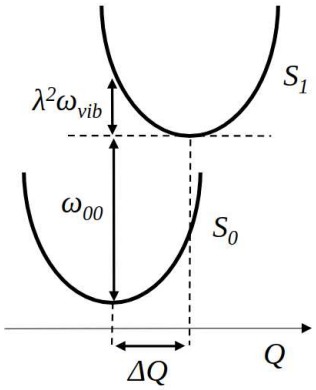

Figure 3.4: Displaced potential energy curves along the nuclear coordinate Q for the ground S_0 and excited S_1 states for a single molecule.

Assuming that the only populated state at thermal equilibrium at room temperature is the lowest energy state of the S_0 manifold (i. e. the state bearing no vibrational quanta), the absorption spectrum of a single molecule shows a vibronic progression where each vibronic peak (labelled

as $0\tilde{\nu}$) correspond to the transition between the ground state and the S_1 state bearing $\tilde{\nu}$ vibrational quanta. The vibronic peaks are spaced by ω_{vib} and their intensities are dictated by the Poissonian distribution defined by the Frank-Condon factors:

$$|\langle\tilde{\nu}|0\rangle|^2 = \frac{e^{-\lambda^2}\lambda^{2\tilde{\nu}}}{\tilde{\nu}!}. \tag{3.7}$$

Eq. 3.7 can be used to derive the ratio between the 00 and 01 vibronic peak intensities, that results to be $I_{00}/I_{01} = 1/\lambda^2$. The first two peaks have therefore the same intensity when $\lambda^2 = 1$.

Intramolecular vibronic coupling can be introduced in the aggregate Hamiltonian in eq. 3.1 to obtain the celebrated Frenkel-Holstein (FH) Hamiltonian:[25–29]

$$\begin{aligned} H_{FH} =& \tilde{\omega}_{00} + \sum_{m,n} J_{m,n}|m\rangle\langle n| + \omega_{vib}\sum_n b_n^\dagger b_n \\ &+ \omega_{vib}\sum_n \{\lambda(b_n^\dagger + b_n) + \lambda^2\}|n\rangle\langle n| \end{aligned} \tag{3.8}$$

where, in analogy with eq. 3.1, the site excitation energy is defined as $\tilde{\omega}_{00} = \omega_{00} + D$, with ω_{00} defined as in figure 3.4 and D being the gas-to-crystal shift. The bosonic operators $b_n^\dagger$ and b_n create and annihilate, respectively, a vibrational quantum in the S_0 harmonic potential and the last term in eq. 3.8 represents the shift of the S_1 potential.

To calculate absorption spectra the transition dipole moment operator is defined as:

$$\hat{\vec{M}} = \sum_n \vec{\mu}_n\{|G\rangle\langle n| + |n\rangle\langle G|\} \tag{3.9}$$

where $\vec{\mu}_n$ is the transition dipole moment of the isolated n-th molecule and $|G\rangle$ and $|n\rangle$ are the aggregate ground state and local excites states as defined in section 3.1.1. Absorption spectra (normalized on the number of molecules) are hence obtained as:

$$A(\omega) = \frac{1}{N|\vec{\mu}|^2}\sum_i |\langle G|\hat{\vec{M}}|i\rangle|^2 S(\omega - \omega_i) \tag{3.10}$$

where $|i\rangle$ are the eigenstates of the FH Hamiltonian with energies ω_i and $S(\omega - \omega_i)$ is a function defining the bandshape associated to each transition. Following Fulton and Gouterman,[191] in eq. 3.10 the ω_i dependence of the oscillator strength $\omega_i|\langle G|\hat{\vec{M}}|i\rangle|^2$ is dropped thus defining the so-called "reduced" absorption spectrum, referred to in this chapter simply as the absorption spectrum. This is done to recover the sum rule that states that the total oscillator strength must be conserved. The sum rule is naturally recovered when releasing the Heitler-London approximation.[174] However, when looking at narrow spectral windows, as it is the case in this chapter, the inclusion of the ω_i dependence of the oscillator strength yields negligible deviations with respect to the reduced spectrum.

The multiparticle basis set

Different basis sets can be adopted to represent the Frenkel-Holstein Hamiltonian in eq. 3.8. In the very strong coupling regime ($W \gg \lambda^2\omega_{vib}$) the wisest choice is the exciton-phonon representation, where both electronic and nuclear degrees of freedom are represented as wavelike delocalized excitations.[28, 169, 192] In the weak to intermediate coupling regime ($W \tilde{\leq} \lambda^2\omega_{vib}$) an accurate representation is obtained exploiting the so-called multiparticle basis set.[169, 190, 193] In this context, a particle is defined as a localized excitation of whatever nature, i. e. either a vibronic excitation or a purely vibrational one. Since the Heitler-London approximation is adopted,[165, 174] a single local vibronic excitation is present, so that a m-particles state is a state where one chromopore is vibronically excited and $m-1$ chromophores carry a purely vibrational excitation. A two-particles state, for example, is indicated as $|n, \tilde{\nu}; n', \nu\rangle$, where the chromophore n bears a vibronic excitation with $\tilde{\nu}$ vibrational quanta in the S_1 potential well (with $\tilde{\nu} \geq 0$, where the equality describes a purely electronic excitation) and chromophore n' bears a purely vibrational excitation with ν vibrational quanta (with $\nu > 0$). If $\nu = 0$, the state clearly reduces to the one-particle state $|n, \tilde{\nu}\rangle$. Figure 3.5 shows sketches of a one-particle and a two-particles state for a linear chain of chromophores.

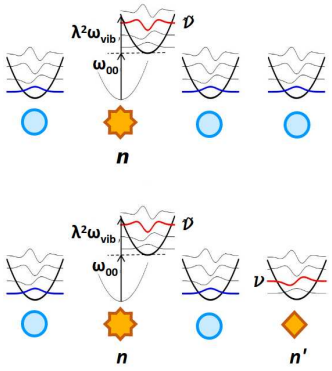

Figure 3.5: Top: one-particle state with a vibronic excitation on chromophore n bearing $\tilde{\nu} = 2$ vibrational quanta. Bottom: two-particles state with a vibronic excitation on chromophore n bearing $\tilde{\nu} = 2$ vibrational quanta and a purely vibrational excitation on chromophore n' bearing $\nu = 1$ vibrational quantum.

The approach is very versatile and allows to effectively reduce the dimension of the basis set by including only the relevant states for the system at hand. Generally, only states with a fixed total number of vibrational quanta are accounted for, such that $\tilde{\nu} + \sum_i \nu_i \leq \nu_{max}$, with i running over the vibrational particles. The ν_{max} needed to reach convergence depends on λ^2 and increases for strongly vibronically coupled systems, but normally does not exceed 6-7. For very weak intermolecular coupling ($W \ll \lambda^2\omega_{vib}$) one particle states are sufficient for an accurate description, and with increasing coupling strength, states with a higher number of particles can be progressively introduced. Moreover, if only nearest neighbor coupling is considered, purely vibrational particles can be restricted to reside on chromophores $n \pm 1$ (being n the vibronically excited chromophore).

Vibronic signatures

As for the isolated molecule, the inclusion of vibronic coupling generates a progression of states among which the total oscillator strength is redistributed. In particular, for an aggregate in the weak coupling regime ($W < \lambda^2\omega_{vib}$) a series of bands appears at higher energies with respect to the purely electronic band reported in figure 3.3, spaced approximately by one vibrational quantum. Useful hints on the role that intramolecular vibronic coupling has in reshaping the structure of the exciton bands in aggregates can be obtained treating the resonant intermolecular Coulomb coupling in the Hamiltonian 3.8 as a perturbation.[194] Clearly, the results obtained with the perturbative treatment are only reliable in the limit of weak coupling, and significant deviations emerge for increasing coupling strength ($W \gg \lambda^2\omega_{vib}$). A first result is that the exciton bandwidth is renormalized due to vibronic coupling according to the Huang-Rys factor λ^2 as $We^{-\lambda^2}$. The same perturbative treatment leads also to the celebrated

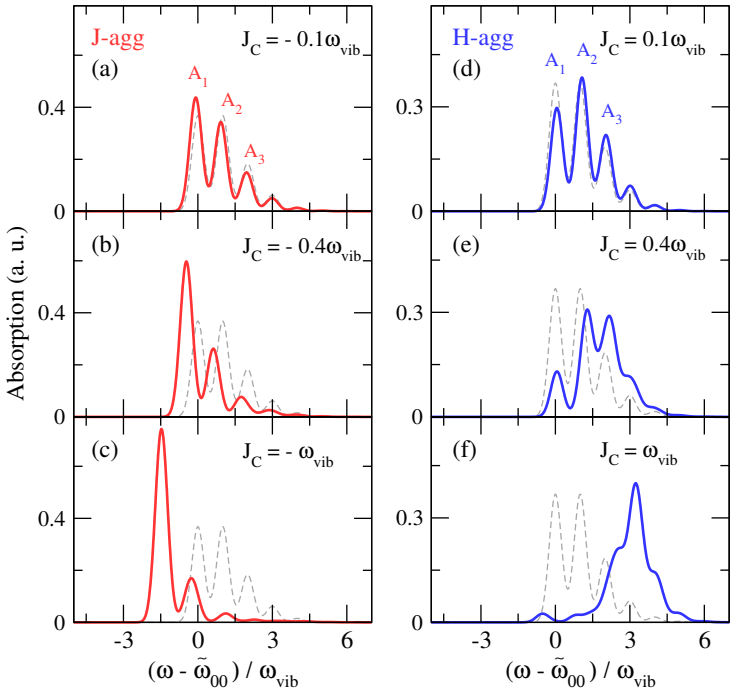

Figure 3.6: Absorption spectra for J- and H-aggregates for increasing $|J_C|$ (panels **a**, **b**, **c** and **d**, **e**, **f**, respectively). A linear chain of 10 molecules is considered, periodic boundary conditions are adopted. $\lambda^2 = 1$, monomer absorption is reported as a gray dashed line. Up to two particles states are used, fixing $v_{max} = 6$. A gaussian bandshape is assigned to every transition with a standard deviation of $\sigma = 0.35\omega_{vib}$.

ratio rule,[169, 190, 194] that gives an expression for the ratio between the intensity of the first and the second transition of the vibronic progression (dubbed as A_1 and A_2 respectively):

$$R_{abs} = \frac{I_{A_1}}{I_{A_2}} \approx \frac{\left[1 - e^{-\lambda^2} G(0;\lambda^2) J_{k=0}/\omega_{vib}\right]^2}{\lambda^2 \left[1 - e^{-\lambda^2} G(1;\lambda^2) J_{k=0}/\omega_{vib}\right]^2} \tag{3.11}$$

with

$$G(v_t;\lambda^2) = \sum_{u \neq v_t} \frac{\lambda^{2u}}{u!(u - v_t)}. \tag{3.12}$$

For $\lambda^2 < 3.26$ (i. e. for all significantly coupled vibrational modes in organic molecules), $G(1;\lambda^2) < G(0;\lambda^2)$. In this regime, for $J_{k=0} < 0$ (J-aggregates) the ratio is higher than in the isolated monomer ($R_{abs} > 1/\lambda^2$) and increases with increasing exciton coupling, while for $J_{k=0} > 0$ (H-aggregates) the ratio is lower than in the isolated monomer ($R_{abs} < 1/\lambda^2$) and decreases with increasing exciton coupling.

Figure 3.6 shows how the absorption spectrum varies with the strength of the exciton coupling. The numerical results are obtained for a linear aggregate of 10 chromophores where only nearest neighbor interactions J_C are included and periodic boundary conditions are applied. A basis set including up to two-particles states is used, with a maximum number of vibrational quanta fixed to $v_{max} = 6$. The Huang-Rys factor is set to $\lambda^2 = 1$ as to make more evident the deviations from the vibronic progression of the isolated monomer absorption (reported for reference as a gray dashed line). Panels **a**, **b** and **c** show how for a J-aggregate the spectrum progressively red-shifts with increasing $|J_C|$ and concurrently the ratio between the first two vibronic peaks I_{A_1}/I_{A_2} increases. Opposedly, for a H-aggregate the spectrum progressively blue-shifts with increasing $|J_C|$ and the ratio I_{A_1}/I_{A_2} decreases. Together with the changes in intensity of the vibronic peaks with respect to the monomer, excitonic coupling

also slightly perturbs their regular spacing. The effect is more evident in H-aggregates.

3.2 Davydov splitting and vibronic signatures of the Davydov components: the role of next-nearest neighbor interactions

3.2.1 The electronic picture

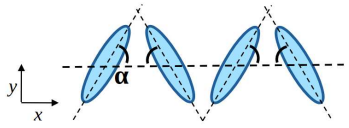

Figure 3.7: Sketch representation of a linear chain of non-parallel molecules. Dashed horizontal line indicates the aggregate long axis (x direction in the defined reference frame).

In the previous section, ideal linear aggregates where all the molecules are translationally equivalent and aligned in the same direction have been considered. In this geometry, all transition dipole moments are parallel and a single molecule is present in each unit cell so that a single band is formed, with only one optically allowed state at $k = 0$. However, if local transition dipole moments are non-parallel, as for example in figure 3.7, the presence of two molecules per unit cell gives rise to two bands, so that two $k = 0$ states are optically allowed.[164, 166]

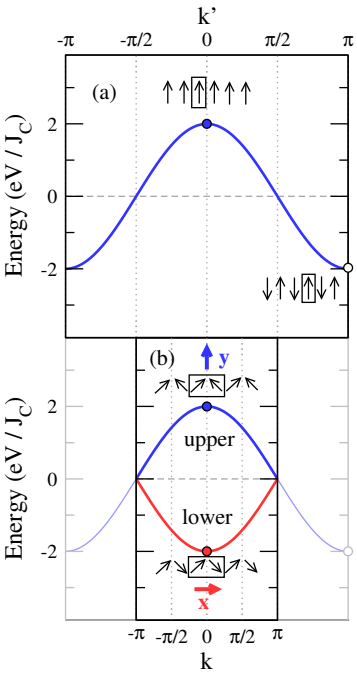

Figure 3.8: (**a**) Dispersion relation for a linear side-by-side arrangement of transition dipole moments with a single molecule per unit cell for $J_C > 0$ (H-aggregate). (**b**) Dispersion relation for a linear arrangement of non-parallel transition dipole moments with two molecules per unit cell for $J_C > 0$. Polarization on the two bright transitions are indicated with the blue and red arrows. In both panels the horizontal gray dashed line indicates E_M, set as the zero of the energy scale. Black boxes indicate the unit cells. Filled circles mark the bright states, in (**a**) the empty circle marks the dark $k' = \pi$ state.

The specific case of a linear chain with two symmetrically equivalent molecules per primitive unit cell is considered here. In each primitive unit cell the two translationally non-equivalent molecules are tilted by an angle α, as in figure 3.7. Doubling the dimension of the unit cell implies halving the Brillouin zone, with the new wavevector $k = 2k'$, where k' is the wavevector of the ideal aggregate with a single molecule per unit cell. If intermolecular interactions are retained and only the orientation of the molecules is changed as to have two molecules per unit cell, the electronic band structure of the aggregate stay unchanged but the band in k' folds in the new Brillouin zone originating 2 bands, as depicted in figure 3.8 for the case of $J_C > 0$. The two bands are commonly referred to as the upper (U) and lower (L) band with reference to their energy. Two optically active states at $k = 0$ are now present. For the system in figure 3.7, with $J_C > 0$, the state belonging to the upper band has a transition dipole moment proportional to $\vec{\mu}_1 + \vec{\mu}_2$ ($\vec{\mu}_1$ and $\vec{\mu}_2$ being the two molecular transition dipole moments within the unit cells) and it is therefore polarized perpendicular to the aggregate long axis (y direction according to the reference frame defined in figure 3.7) with an oscillator strength proportional to $|\vec{\mu}_1 + \vec{\mu}_2|^2$. The active state belonging to the lower band has instead a transition dipole moment proportional to $\vec{\mu}_1 - \vec{\mu}_2$ and therefore a polarization along the aggregate axis (x direction) and an oscillator strength proportional to $|\vec{\mu}_1 - \vec{\mu}_2|^2$.

The two orthogonally polarized transitions originating from the non parallel alignment of the molecular transition dipole moments are called the two Davydov components of the absorption spectrum, and the energy difference between the maxima of the two components is called the Davydov splitting.[30, 31, 164, 169, 195–200] The relative intensity of the two Davydov components is determined by the vectorial sum and difference between $\vec{\mu}_1$ and $\vec{\mu}_2$, and therefore depends on the angle α: if $\alpha = 45°$ the two components have the same oscillator strength, if $\alpha > 45°$ the y-polarized component is more intense and *vice versa* if $\alpha < 45°$ the more intense is the x-polarized one.

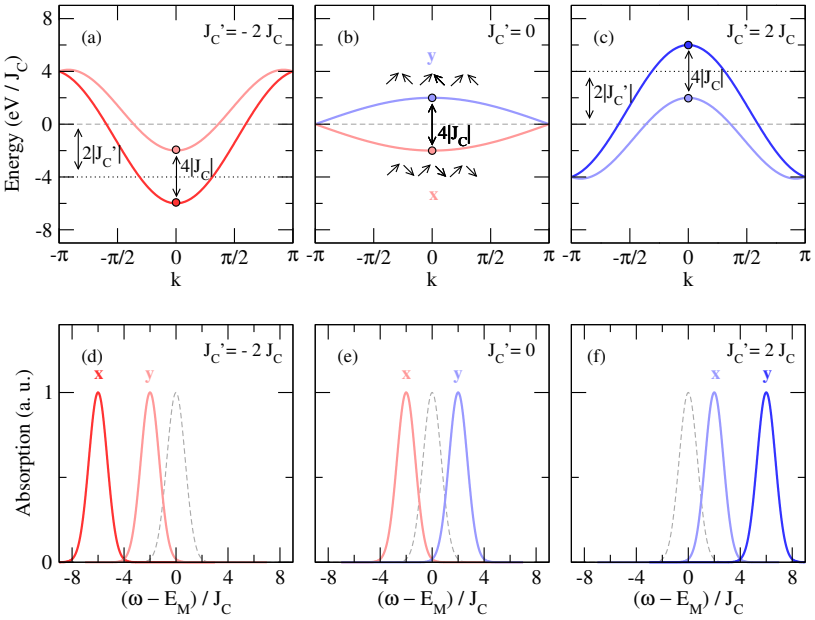

Figure 3.9: Band structures for linear aggregates with two non-parallel molecules per unit cell, including both nearest neighbor (J_C) and next-nearest neighbor (J'_C) coupling for $J_C > 0$ and $J'_C = -2J_C$ (**a**), $J'_C = 0$ (**b**) and $J'_C = 2J_C$ (**c**). Horizontal gray dashed lines mark the position of E_M, set as the zero of energy. Bottom panels report relative polarized absorption spectra obtained assigning a gaussian bandshape with $\sigma = J_C$ to each transition.

The sign of J_C is crucial in aggregates with parallel transition dipole moments since it defines the H- or J-ness nature of the aggregate. For non-parallel transition dipole moments, the distinction between H- and J-aggregates fades. The sign of J_C still determines the energy ordering of the bands, but since both the states at $k = 0$ are bright, its spectroscopic consequences are less prominent. Specifically, if $J_C > 0$ the higher and lower energy transitions are polarized along y and x, respectively, the opposite being true for $J_C < 0$. If there is a clear dominance of one of the two components in the absorption spectrum, the aggregate is however still referred to as a H-type/H-like or J-type/J-like aggregate depending on the position of the dominant peak. The two limiting cases of ideal side-by-side H-aggregate and head-to-tail J-aggregate are recovered for $\alpha = 90°$ and $\alpha = 0°$, respectively.

So far a system with two molecules per unit cell have been discussed, only accounting for nearest neighbor coupling. Accounting only for nearest neighbor interactions is usually a good approximation for linear aggregates, but sometimes also next-nearest neighbor interactions are sizable and can even prevail over the nearest neighbor ones.[201] The band structure in figure 3.8 is replicated in panel **b** of figure 3.9. Panel **e** in the same figure shows the absorption spectrum along the two polarization directions with monomer absorption falling exactly in between. The angle α is set to 45° as to have the two polarized components with the same intensity. These results are now compared with results obtained accounting for next-nearest neighbor interactions.

In addiction to the nearest neighbor coupling J_C between two translationally inequivalent molecules, the next-nearest neighbor coupling J'_C between translationally equivalent molecules is now introduced. If next-nearest neighbor interactions J'_C are included, the band structure undergoes significant changes. In the case of two non-parallel molecules per unit cell the dispersion relation in eq. 3.5 become for the two bands

(dubbed as 1 and 2):

$$J_{k,1} = \sum_n J_{m,n} \cos\left[k'(n-m)\right] \tag{3.13}$$

$$J_{k,2} = \sum_n J_{m,n} \cos\left[(k'-\pi)(n-m)\right]. \tag{3.14}$$

Considering nearest neighbor J_C and next-nearest neighbor J'_C interactions, eqs. 3.13 and 3.14 become:

$$J_{k,1} = 2J_C \cos(k') + 2J'_C \cos(2k') \tag{3.15}$$

$$J_{k,2} = 2J_C \cos(k'-\pi) + 2J'_C \cos\left[2(k'-\pi)\right] \tag{3.16}$$

so that at $k = 0$ the free exciton shifts with respect to the monomer site energy E_M are $J_{k=0,1} = 2\left(J'_C + J_C\right)$ and $J_{k=0,2} = 2\left(J'_C - J_C\right)$. A positive nearest neighbor coupling $J_C > 0$ defines the $J_{k,1}$ band as the upper band and $J_{k,2}$ band as the lower band setting the y-polarized and the x-polarized states as the upper and lower Davydov components, respectively, and *vice versa* for $J_C < 0$. The free exciton shifts of the upper and lower bright states are dubbed as J_U and J_L. Interestingly, the Davydov splitting $J_U - J_L = 4|J_C|$ only depends on J_C, while J'_C affects the position of the two components with respect to E_M, with the central frequency $(J_U - J_L)/2$ being shifted by $2J'_C$. It follows that if $|J'_C| > |J_C|$ both the components can be (depending on the sign of J'_C) either red-shifted or blue-shifted with respect to E_M, as shown in figure 3.9, where panels **a**, **b** and **c** show the band structure of an aggregate with $J'_C = -2J_C$, $J'_C = 0$ and $J'_C = 2J_C$, respectively, with $J_C > 0$. Panels **d**, **e** and **f** show relative polarized absorption spectra, setting the monomer excitation energy E_M to zero. The monomer normalized absorption spectrum is shown as a gray dashed line in the figure.

3.2.2 Vibronic signatures

As for ideal aggregates with parallel transition dipole moments, vibronic coupling affects the bandshapes of absorption spectra. The same perturbative treatment that lead to eq. 3.11 gives:

$$R_{abs}^{U/L} \approx \frac{\left[1 - e^{-\lambda^2} G(0;\lambda^2) J_{U/L}/\omega_{vib}\right]^2}{\lambda^2 \left[1 - e^{-\lambda^2} G(1;\lambda^2) J_{U/L}/\omega_{vib}\right]^2} \tag{3.17}$$

where the H- or J-like nature of the vibronic signatures of the two components is determined by the spectral shifts J_U and J_L. When $|J'_C| < |J_C|$, J_U and J_L have opposite signs and define a blue-shifted component displaying a H-like vibronic structure and a red-shifted component with a J-like vibronic structure. Instead, if $|J'_C| > |J_C|$ and $J'_C < 0$ both J_U and J_L are negative and give rise to two red-shifted J-like components, while for $J'_C > 0$ both J_U and J_L are positive and originate two blue-shifted H-like components. For $|J'_C| = |J_C|$ the system crosses a so called "null point" where, depending on the sign of J'_C, either the upper or the lower component has a vanishing spectral shift, that shows up with an unaltered vibronic structure with respect to the monomer. Once again, since the ratio rule in eq. 3.17 is based on a perturbative treatment, it is strictly

valid in the the weak coupling regime. Deviations in the positions of the null points may arise for increasing exciton coupling.

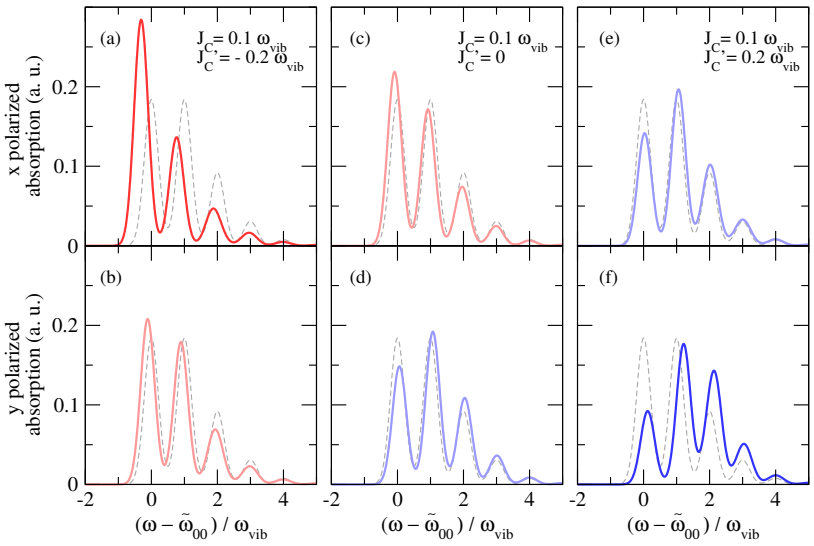

Figure 3.10: Absorption spectra for linear aggregates of 10 non parallel molecules (5 unit cells) accounting for nearest neighbor (J_C) and next-nearest neighbor (J_C') coupling (values used are specified in the panels) and intramolecular vibronic coupling. ω_{vib} is taken as unity. Periodic boundary conditions are adopted and gaussian lineshapes are used with $\sigma = 0.25\omega_{vib}$.

Figure 3.10 shows numerical results for a linear aggregate of 10 molecules (5 unit cells) arranged as in figure 3.7 with $\alpha = 45°$ and with periodic boundary conditions. States with up to three-particles are included in the basis set imposing $\nu_{max} = 5$. J_C is positive and set to $0.1\omega_{vib}$ while J_C' is set to $-2J_C$ in panels **a** and **b**, $J_C' = 0$ in panels **c** and **d** and $J_C' = 2J_C$ in panels **e** and **f**. Top panels show the x-polarized lower component and bottom panels show the y-polarized upper component of the relevant aggregate. As in figure 3.6, λ^2 is set to 1 and monomer absorption is reported in gray dashed line. Panels **c**-**d** shows the more typical case of a J-like and a H-like component, while in panels **a**-**b** and **e**-**f** two J-like and H-like components can be respectively observed.

Results in figure 3.10 confirm is that the H- or J-like nature of the Davydov components is determined by their free exciton shift and not by their relative energy ordering. In the majority of cases the lower (upper) component displays J-like (H-like) features, but depending on the weight of next-nearest neighbor interactions cases may occur where both components share the same nature.

3.3 SQIB crystals: an interesting case study

In this section, the Frenkel-Holstein Hamiltonian is applied to the case of crystalline thin films grown in the orthorhombic and monoclinic phases of SQIB (2,4-bis[4-(*N*,*N*-diisobutylamino)-2,6-dihydroxyphenyl] squaraine, molecular structure in figure 3.11). The crystallographic parameters of the two polymorphs are reported in table 3.1. The monoclinic (orthorhombic) phase has two (four) symmetrically equivalent non-parallel molecules per unit cell, supporting Davydov splitting. Crystalline thin films of both polymorphs have been characterized *via* polarization resolved spectromicroscopy techniques and imaging Mueller matrix ellipsometry[30–33] offering an interesting case study in the Davydov landscape. Polarized absorbance spectra are simulated to support the interpretation of experimental data and to obtain insights on the structure of the Davydov

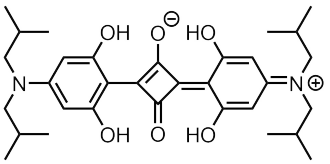

Figure 3.11: Molecular structure of SQIB (2,4-bis[4-(*N*,*N*-diisobutylamino)-2,6-dihydroxyphenyl]squaraine).

Table 3.1: Unit cell parameters for SQIB single crystals, taken from ref.[30].

polymorph	a (Å)	b (Å)	c (Å)	β (°)	Z
monoclinic	6.1979(2)	16.4874(6)	15.4762(5)	111.248(2)	2
orthorhombic	15.0453(8)	18.2202(10)	10.7973(6)	90	4

components. An interesting picture emerges, with the monoclinic phase displaying two H-like components and the orthorhombic phase representing one of the very rare cases in which three Davydov components are clearly observed.

SQIB molecular parameters entering the Hamiltonian 3.8 are extracted from the absorption spectrum of the isolated molecule in chloroform and are fixed to $\omega_{00} = 1.91$ eV, $\omega_{vib} = 0.15$ eV and $\lambda^2 = 0.12$. In the crystal packing of both polymorphs, intermolecular distances between nearest neighbor molecules are shorter than the dimension of the molecules themselves, making the point dipole approximation inadequate. Therefore, the couplings $J_{m,n}$ entering eq. 3.8 are calculated from transition atomic charges obtained *via* Mulliken population analysis (MPA). A single point TDDFT calculation is performed using the Gaussian 16 package on the gas phase monomer in the geometry extracted from the crystal structure. The functional CAM-B3LYP is used and def2-TZVP is chosen as basis set. The atomic MPA transition charges relevant to the transition towards the first singlet excited state S_1 are then used to evaluate the $J_{m,n}$ interaction as follows:

$$J_{m,n} = \frac{1}{4\pi\varepsilon_0\varepsilon}\sum_{i,j}\frac{q^t_{i,m}q^t_{j,n}}{|r_{i,n} - r_{j,m}|} \tag{3.18}$$

where i and j run over the atoms of chromophore n and m, respectively, $q^t_{i,m}$ is the MPA transition charge on atom i on molecule m and $r_{i,m}$ is the corresponding position. Finally, ε_0 is the vacuum permittivity and ε is the dielectric constant of the medium.

The Frenkel-Holstein Hamiltonian in eq. 3.8 is represented with the multiparticle basis with up to two-particles states. Performing a complete multiparticle calculation over a portion of a crystal is impossible due to the dimension of the basis set. Translational symmetry is therefore exploited working in the subspace at $k = 0$.

For a crystal with N molecules per unit cell there are N purely electronic states at $k = 0$ defined as:

$$|n\rangle_{k=0} = \frac{1}{\sqrt{A}}\sum_{\alpha=1}^{A}|n_\alpha\rangle \tag{3.19}$$

where n ranges from 1 to N and α runs over the unit cells (A being the total number of cells). The state $|n_\alpha\rangle$ therefore represents a state where the excitation resides on the n-th molecule of the α-th unit cell and all other molecules in the crystal are in the ground state. Equation 3.19 is easily extended to one-particle states:

$$|n,\tilde{\nu}\rangle_{k=0} = \frac{1}{\sqrt{A}}\sum_{\alpha=1}^{A}|n_\alpha,\tilde{\nu}\rangle \tag{3.20}$$

where $\tilde{\nu}$ is the number of vibrational quanta in the excited state of

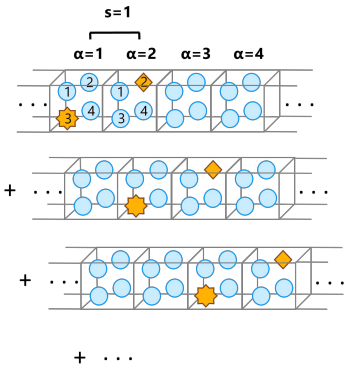

Figure 3.12: Representation of a 2-particles state at $k = 0$ in a monodimensional array of unit cells, each unit cell accomodating 4 molecules. Blue circles represent molecules in their ground state, yellow stars molecules in a vibronic excited state and yellow diamonds molecules with a purely vibrational excitation. The represented state is $|n = 3, \tilde{\nu}; n' = 2_{s=1}, \nu\rangle_{k=0}$.

chromophore n_α. A two-particles state in the $k = 0$ space is defined as:

$$|n, \tilde{\nu}; n'_s, \nu\rangle_{k=0} = \frac{1}{\sqrt{A}} \sum_{\alpha=1}^{A} |n_\alpha, \tilde{\nu}; n'_{\alpha+s}, \nu\rangle \tag{3.21}$$

where both n and n' range from 1 to N and s is an integer number (ranging from 0 to $A - 1$) defining the distance between the unit cell that accomodates the vibronic excitation and the one accomodating the purely vibrational one. $|n_\alpha, \tilde{\nu}; n'_{\alpha+s}, \nu\rangle$ indicates a state where chromophore n in the α-th unit cell is vibronically excited, and a pure vibrational excitation is on chromophore n' in the $(\alpha + s)$-th cell. Clearly if $s = 0$, $n \neq n'$. The states where the pair of vibronic and vibrational particles is rigidly translated are combined to give the $k = 0$ state $|n, \tilde{\nu}; n'_s, \nu\rangle_{k=0}$. A sketch of a two particle state in a monodimensional array of unit cells with 4 molecules per cell is shown in figure 3.12, where blue circles represent molecules in their ground state and yellow stars and squares represent vibronically and vibrationally excited molecules, respectively. To further reduce the dimension of the basis, s is restricted to range from $-s_{max}$ to $+s_{max}$. To treat a three-dimensional lattice A and s_{max} are defined along the three crystallographic directions a, b and c. In the following $A_a = A_b = A_c = A$ and $s_{max_a} = s_{max_b} = s_{max_c} = s_{max}$. Periodic boundary conditions are adopted and A, s_{max} and the maximum of total vibrational excitation $\nu_{max} = \tilde{\nu} + \nu$ are set high enough as to ensure convergence.

3.3.1 The orthorhombic polymorph: observing three Davydov components

The orthorhombic polymorph (unit cell parameters in table 3.1, structure in figure 3.13) crystallizes adopting a cofacial herringbone packing with a π-stacking along the c-axis, where consecutive molecules are alternatively rotated as shown in the middle panel of figure 3.13. Crystalline thin films of the orthorhombic polymorph grow with the (110) surface (or $(1\bar{1}0)$ and mirror faces) parallel to the substrate. The (110) face is represented in figure 3.13 with the cyan plane as to indicate the orientation of the unit cell and of the molecules with respect to the exposed surface of the film. Films are composed of large platelets-like crystalline domains with dimensions of the order of $\sim 200\mu$m.[30–33] Intermolecular charge transfer interactions between donor and acceptor moieties of nearby molecules can be disregarded in view of the packing geometry.

Since there are four molecules in the unit cell, it is not possible to gain information about the orientation of the Davydov components relying on the simple consideration of summing and subtracting the transition dipole moment vectors. Symmetry considerations help to address the issue. The isolated SQIB molecule belongs to the D_{2h} point group, with the $S_0 \rightarrow S_1$ transition having B_{1u} symmetry (the z-axis is oriented along the long molecular axis). In the crystal, each molecule lie on a center of inversion, acquiring a site symmetry C_i: the $S_0 \rightarrow S_1$ transition belongs to the A_u representation in this group. In the $Pbcn$ space group the 4 A_u transitions recombine to give 4 states with symmetry A_u, B_{1u}, B_{2u} and B_{3u}. The state with symmetry A_u is optically inactive, while the other three are mutually orthogonal and polarized along the a, b and c crystallographic directions, respectively. The component polarized along

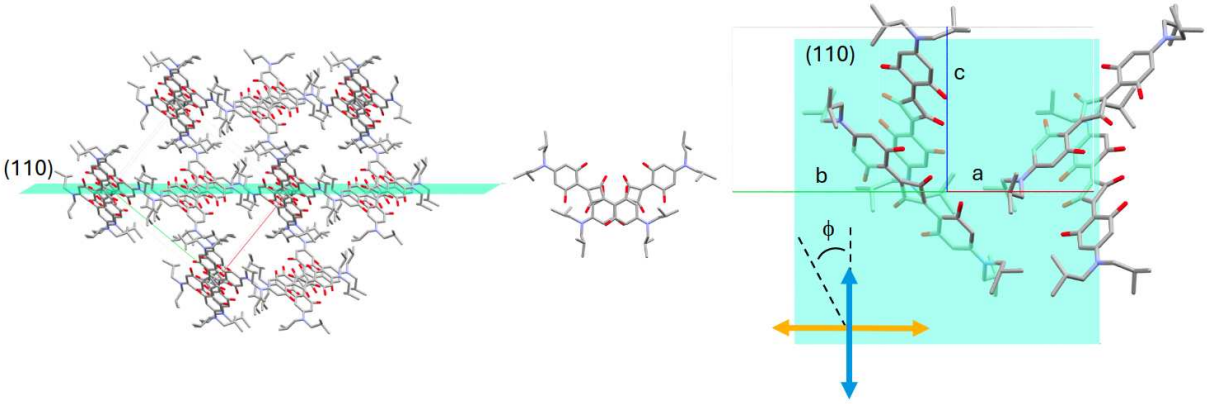

Figure 3.13: SQIB orthorhombic polymorph. Molecular packing and relative orientation of the unit cell with respect to the exposed surface of the film (i. e. the (110) face, indicated with the cyan plane). The arrows in the right panel indicate the orientation of the projected Davydov components onto the film surface. Adapted from ref.[30].

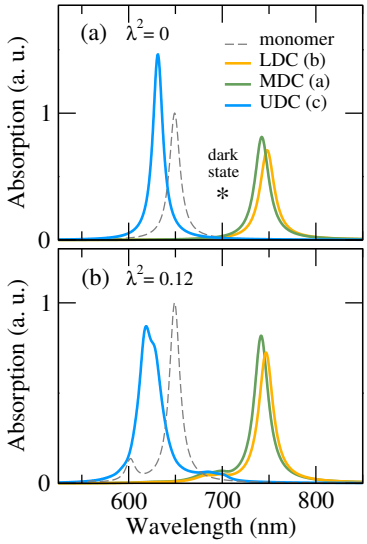

Figure 3.14: Simulated polarized absorption spectra for the SQIB orthorhombic polymorph along the three orthogonal crystallographic directions a, b and c. Simulated monomer spectrum is reported in gray dashed line as a reference. Panel (**a**) shows results obtained with the purely electronic Hamiltonian (i. e. the Huang-Rys factor λ^2 is set to 0) and panel (**b**) results obtained with the total FH Hamiltonian with $\lambda^2 = 0.12$. Lorentzian lineshapes with hwhm=0.02 eV are used.

c is completely projected on the surface of the film, being the c-axis parallel to the exposed (110) face, while the other two components are both projected along the orthogonal direction.

The orthorhombic phase of SQIB is a rare case of a crystal supporting three distinct Davydov components. Strict symmetry requirements have to be satisfied in order to display this very peculiar feature. Specifically, the molecule must crystallize in a space group of the family of the point groups D_2 or D_{2h}, with 4 (or more) molecules per unit cell. Few molecules are known fulfilling these requirements: solid benzene,[202] 9-cyanoantracene[203] and paracetamol,[204] but the lucky combination of the crystallographic packing and orientation of the exposed surface of the film makes orthorhombic SQIB the first case in which all three components are experimentally accessible and have been detected.[30–33]

Coulomb couplings $J_{m,n}$ are calculated following eq. 3.18 and are shielded with a dielectric constant of $\varepsilon = 4$. The gas-to-crystal shift D is set to -0.2 eV. Periodic boundary conditions are used fixing $A = 7$ and up to two-particle states are included in the basis set fixing $s_{max} = 1$, meaning that in all the crystallographic directions the purely vibrational excitation can reside at most one unit cell away from the cell accomodating the vibronic excitation. The total number of vibrational quanta is fixed to $v_{max} = 3$. A Lorentzian bandshape is assigned to each transition.

Figure 3.14 shows calculated absorption spectra polarized along the three crystallographic directions. In panel **a** the result of a purely electronic simulation ($\lambda^2 = 0$) is reported, showing the lower component (LDC) at 1.65 eV (748 nm) polarized along b, the very close in energy middle component (MDC) at 1.67 eV (742 nm) polarized along a and the upper component (UDC) at 1.96 eV (630 nm) polarized along c. Moreover, a dark state is calculated at 1.77 eV (700 nm), marked in the figure with a black star. Unfortunately, the dark state is not accessible neither in one nor two photon absorption experiments. Both LDC and MCD are red-shifted with respect to monomer absorption, while UDC is slightly blue-shifted. The result is in very good agreement with experimental data reported in ref.[32], with the additional information about the location of the dark state. Note that in figure 3.14 the results are reported

accounting also for the gas-to-crystal shift D, but even neglecting it the relative shifts of the components with respect to monomer absorption stay unchanged, with the upper component being blue-shifted and the middle and lower components being red-shifted. This is confirmed by the vibronic signatures that emerge when vibronic coupling is introduced ($\lambda^2 = 0.12$). Panel **b** shows how LDC and MCD display J-like vibronic signatures, while UDC displays prominent H-like features.

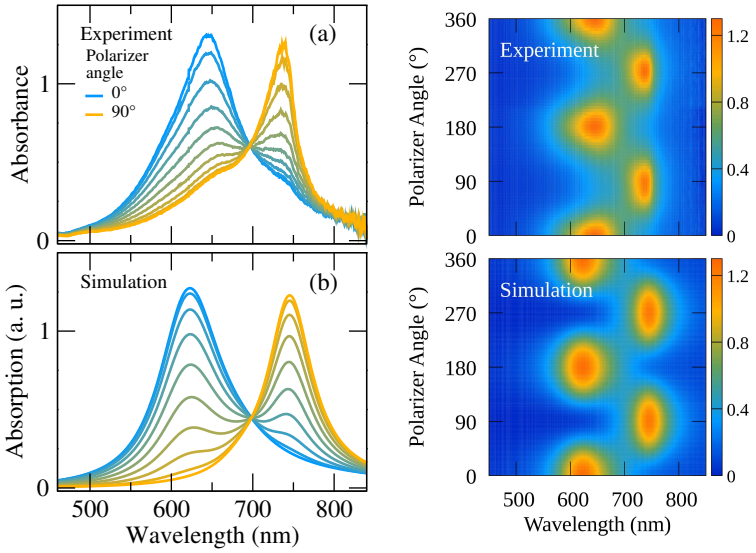

Figure 3.15: Top panels: experimental polarized absorbance spectra of the orthorhombic SQIB polymorph thin film. Bottom panels: corresponding simulated polarized absorption spectra. In the left panels selected spectra are reported. The polarizer is rotated by 10° for every spectrum, ranging from $\phi = 0°$ (blue line, polarization aligned to the crystallographic c axis) to $\phi = 90°$ (yellow line, polarization aligned to the projection of a and b onto the (110) plane). Right panels show the maps for a complete 360° rotation of the polarization, where the colors code the spectrum intensity. Experimental data adapted from ref.[31].

Figure 3.15 shows experimental polarized absorbance spectra and corresponding simulated absorption spectra. In panel **a**, selected experimental spectra are reported where the sample is rotated with respect to the polarization of incident light over 90° in steps of 10°, with the starting point 0° fixed to the direction in which the upper peak displays its maximum intensity (experimental data adapted from ref.[31]). Panel **b** shows simulated polarized spectra for the oriented system with the polarization angle ϕ defined as in the right panel of figure 3.13, with $\phi = 0°$ coinciding with the crystallographic c direction. Bandwidths are taken as fitting parameters, specifically a half width at half maximum of 0.135 eV is assigned to all transitions belonging to the UDC manifold and 0.072 eV to all transitions belonging to the MDC and LDC manifolds. When $\phi = 0°$ the UDC is captured and the MDC and LDC are completely extinct, while for $\phi = 90°$ the projected MDC and LDC are detected (even if they are not resolved due to their quasi degeneracy) and UDC is completely extinct. Complete extinction of the components is not observed in experimental data, a result most likely due to some degree of orientational disorder. A clear isosbestic point due to the orthogonality of the projected components is observed both in experiment and simulation. Color maps to the right of figure 3.15 show the entire series of data and the corresponding simulation where the polarization angle of incident light is varied over 360° and the color scale codes for the spectrum intensity. These panels show how the data set collected from $\phi = 0°$ to $\phi = 90°$ is symmetric and reverse with respect to the one collected from $\phi = 90°$ to $\phi = 180°$, and of course the whole data set is symmetric with respect to a rotation of 180°. The excellent agreement between theory and experiment supports the physical interpretation of the spectroscopic features of this very interesting system, where Coulomb excitonic coupling generates three mutually orthogonal Davydov components.

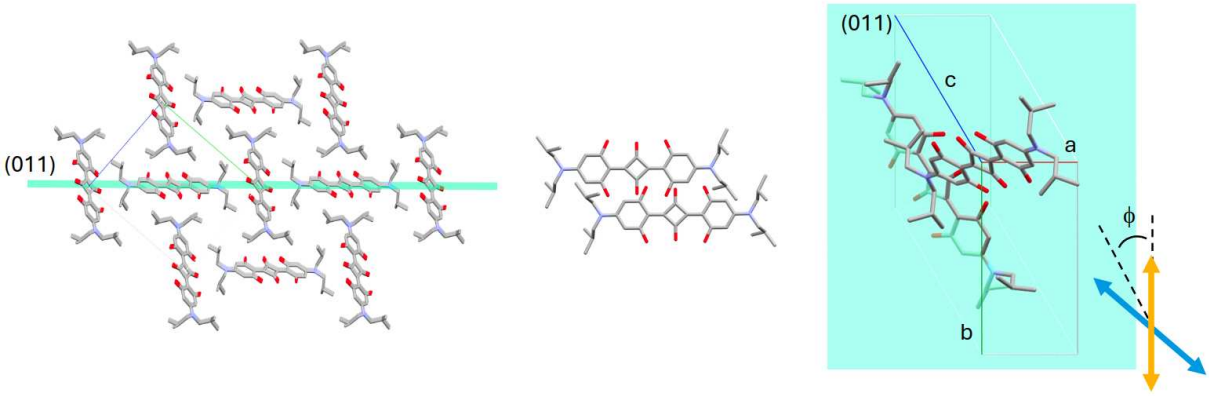

Figure 3.16: SQIB monoclinic polymorph. Molecular packing and relative orientation of the unit cell with respect to the exposed surface of the film (i. e. the (011) face, indicated with the cyan plane). The arrows in the right panel indicate the orientation of the projected Davydov components onto the film surface. Adapted from ref.[30].

3.3.2 The monoclinic polymorph: two H-like components

The monoclinic polymorph (unit cell parameters in table 3.1) adopts a herringbone packing in the bc plane and a slipped π-stacking along the a-axis. Molecular packing is shown in figure 3.16. The slip along the π-stack displayed in the central panel of figure 3.16 allows to neglect (at least in a first approximation) possible intermolecular charge transfer interactions. Crystalline thin films of the monoclinic polymorph grow with the (011) surface (or $(0\bar{1}1)$ and mirror faces) parallel to the substrate (cyan plane in figure 3.16).[30, 31]

The orientations of the two Davydov components can be obtained as the sum and difference of the transition dipole moments of the two molecules within a unit cell, as discussed in section 3.2.1, considering the transition dipole moment of each molecule oriented along the long molecular axis. One of the components is oriented along the crystallographic b axis (i. e. perpendicular to the stack direction), with the other lying in the orthogonal plane. When projected onto the surface of the film (the (011) face) the two components form an angle of 55.2°, as shown by the two arrows in the right panel of figure 3.16.

When deposited on a substrate, the monoclinic phase typically forms sunflower-like structures with sub-μm crystalline domains, making the spectroscopic characterization of the films a challenging task.[30] Elongated crystallites with dimension of the order of 10-20 μm, allowing for the measurement of polarized absorbance spectra with spectro-microscopy techniques, have been obtained *via* organic molecular beam deposition on the (001) surface of KCl at 120 °C.[31]

Figure 3.17 shows the results of the calculation, together with the comparison with experimental data. The dielectric constant is set to $\varepsilon = 2$ and the gas-to-crystal shift to $D = 0$ eV. Periodic boundary conditions are adopted with $A = 9$, while $s_{max} = 2$ and $v_{max} = 3$. Panel **a** of figure 3.17 shows the result of a purely electronic calculation ($\lambda^2 = 0$). In agreement with the prediction based on the orientation of the molecules within the unit cell, two Davydov components are found, the lower one (LDC) oriented along the **b** direction and the upper one (UDC) lying in the orthogonal plane.

Notably, both components are blue-shifted with respect to monomer absorption. In line with results discussed in section 3.2.2, when vibronic coupling is introduced ($\lambda^2 = 0.12$) a H-like vibronic structure is found for both components, as it can be seen in panel **b**.

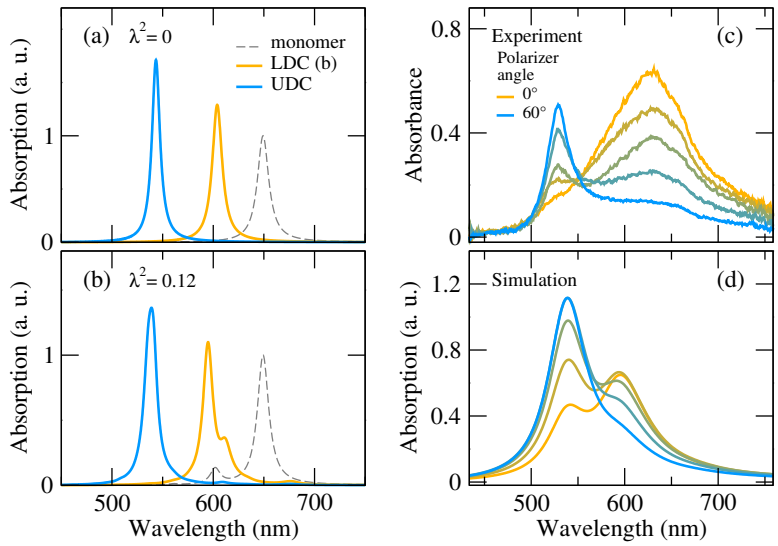

Figure 3.17: Left panels: simulated polarized absorption spectra for the SQIB monoclinic polymorph along the *b* crystallographic direction (yellow line) and in the orthogonal plane (blue line). Simulated monomer spectrum is reported in gray dashed line as a reference. Panel (**a**) shows results of a purely electronic calculation ($\lambda^2 = 0$) and panel (**b**) results including vibronic coupling ($\lambda^2 = 0.12$). Lorentzian lineshapes with hwhm=0.02 eV are used. Panel (**c**): experimental polarized absorbance spectra of the monoclinic SQIB polymorph thin film. The sample has been rotated with respect to the polarization of incident light over 60° in steps of 15°; the starting point 0° is fixed as the direction in which the lower peak displays its maximum intensity (adapted from ref.[31]). Panel (**d**): corresponding simulated polarized absorption spectra. Lorentzian lineshapes with hwhm=0.1 eV are used.

Panel **c** shows experimental polarized absorbance spectra where the sample has been rotated with respect to the polarization of incident light over 60° in steps of 15°, where the starting point 0° is fixed as the direction in which the lower peak displays its maximum intensity (experimental data adapted from ref.[31]). Panel **d** shows simulated polarized spectra orienting the system as in the experimental film and defining the polarization angle ϕ as in the right panel of figure 3.16, with $\phi = 0°$ coinciding with the crystallographic *b* direction. Due to the non orthogonality of the projection of the two components on the surface of the film a complete extinction of the components is never observed (nor simulated) in the reported range of polarization angle. When $\phi = 0°$ the lower component is captured plus a contribution coming from the projection of the upper component on the polarization direction, the other way around for $\phi = 60°$. The non orthogonality of the projected components is also responsible for the absence of an isosbestic point. Overall, experimental data are fairly well reproduced, with some minor discrepancy. In experimental spectra the lower component is much broader than in simulated spectra. Of course in the simulation the bandwidth is an adjustable parameter, but playing with the bandwidths does not improve the agreement with the experiment. The very broad experimental feature is most probably due to either orientational or energetic disorder or both, none of which is taken into account in the model. Moreover, the relative intensities of the two components is not precisely reproduced. This, together with the underestimate of the Davydov splitting of 20%, might be an indication that a certain degree of intermolecular charge transfer along the π-stack (neglected in the present model) could be present affecting these features. Notwithstanding, the physics of the system is well captured, providing the significant and solid result (hard to see experimentally but clearly confirmed by the simulations) of two H-like Davydov components.

3.4 Conclusions

The classification of molecular aggregates in the two families of H- and J-aggregates finds its roots in the Kasha theory, where H-aggregates, often associated with a side-by-side arrangement of the molecules interacting *via* a positive Coulomb coupling, are non fluorescent and display a blue-shifted absorption spectrum with respect to the monomer and J-aggregates, associated with a head-to-tail geometry, have a red-shifted absorption and are strongly emissive.

The relative position of the monomer and aggregate absorption spectra, however, does not depend only on the electrostatic excitonic coupling, but is also sensitive to several other factors not accounted for by the Kasha model, among which mean field effects,[85, 86, 171, 205, 206] ultraexcitonic couplings[174, 207] and possible intermolecular charge transfer interactions.[208] In this variegated scenario, vibronic signatures originated by intramolecular vibronic coupling proves a more reliable signature of the type of aggregation than the spectral shifts.[169, 190] Specifically, for increasing excitonic coupling, the relative ratio between the first and second peaks in the vibronic progression increases in J-aggregates and decreases in H-aggregates.

A plethora of different shades is encountered between the two limiting cases of ideal H- and J-aggregates, starting from aggregates and crystals in which a non-parallel alignment of molecules shows up with in the presence of a Davydov splitting between the two (or possibly more) bright transitions in the absorption spectrum (also dubbed as Davydov components). In the definition of the vibronic features of the Davydov components the interplay between nearest neighbor and next-nearest neighbor interactions plays a non trivial role. Most often, nearest neighbor interactions are stronger and (in a system with two molecules per unit cell) the lower (upper) Davydov component is red-(blue-)shifted with respect to the monomer and display a J-like (H-like) vibronic structure. However, if next-nearest neighbor interactions are sizable, both components can be either red-shifted and exhibit J-like signatures or both can be blue-shifted with H-like signatures, depending on the sign of next-nearest neighbor coupling. More generally, the vibronic structure of a Davydov component depends on its free exciton spectral shift and not on the relative energy ordering with respect to the other components.

Thin films of the orthorhombic and monoclinic SQIB polymorphs are studied as interesting materials for applications in organic photovoltaics.[30–37] A theoretical investigation based on the Frenkel-Holstein Hamiltonian accounting for intermolecular Coulomb couplings is provided to support experimental data available in literature and significant insights on the structure of the Davydov components are found. The orthorhombic polymorph in fact offers the rare possibility to observe three Davydov components, while the monoclinic phase represents an example of a system with two blue-shifted H-like components. A satisfactory agreement between experiments and simulations is obtained for the monoclinic phase, where minor discrepancies could be cured by a refinement of the model accounting for a small degree of intermolecular charge transfer among nearby molecules along the π-stack and a certain degree of energetic and orientational disorder. For the orthorhombic polymorph,

experimental data are almost quantitatively reproduced, with the additional information about the positioning of a dark state experimentally inaccessible both in one- and two-photon absorption.

A comprehensive approach to exciton delocalization and energy transfer

4

Resonance energy transfer (RET) and exciton delocalization play a prominent role in defining the spectral features and more generally the behavior of molecular materials.[169, 209–214] The two phenomena do not require delocalized electrons among involved molecules, but are driven by classical electrostatic intermolecular interactions. Useful phenomenological models have been proposed and are widely applied to address the two phenomena, namely the Förster model for energy transfer[215, 216] and the exciton model (already discussed in detail in chapter 3) for energy delocalization.[164, 211, 212] While the two models were proposed independently, both rely on the same main approximations: (a) only states with one excited molecule are accounted for, (b) electrostatic intermolecular interactions are treated in the dipolar approximation.

The first approximation applies to systems where excitation energies are larger than interaction energies. It has been discussed quite extensively with reference to molecular aggregates,[174, 217] where it is responsible for the apparent deviations from the sum rules of the oscillator and rotational strengths. In aggregates of polar molecules,[85, 86, 206, 218] relaxing this approximation leads to an offset of the excitation energies that, in some cases, may overcome the exciton splitting leading to the puzzling observation of non-fluorescent J-aggregates or of fluorescent H-aggregates. The same approximation is much less discussed in RET systems, and will be addressed below.

The second approximation applies when intermolecular distances are much larger than molecular dimensions, and is therefore poor in most cases. However it is often adopted, as it allows to express intermolecular interactions in terms of experimentally accessible quantities, i. e. the transition dipole moments. Several strategies have been adopted to relax the dipolar approximation, ranging from the use of the extended dipole approximation[219] to transition density approximations.[220–222] The most striking effects of the dipolar approximation are observed in RET, where it imposes that only optically bright states are involved in RET processes, a limitation that is overcome when the dipolar approximation is released.[219, 223, 224]

Molecular vibrations add further complexity to the picture. Their role in defining the bandshape of optical spectra of molecular aggregates is well understood (as already discussed in details in chapter 3). Moreover, vibronic coupling is responsible for the appearence of the nominally forbidden emission of H-aggregates as a weak and largely red-shifted band.[85, 169, 174, 190, 225] In RET systems, the role of molecular vibrations was traditionally relegated to the broadening of absorption and fluorescence spectra, then favoring the Förster overlap.[226] More recently, molecular vibrations in RET were explicitly addressed[227–235] to account for subtle effects, including coherent oscillations, and a major role of vibrational states has been observed.[62, 230] In either molecular

The work presented in this chapter is published in *J. Chem. Theory Comput.*, *19*(2), 436-447, **2023**.

aggregates or RET systems, the explicit inclusion of molecular vibrations is highly non-trivial as the adiabatic approximation breaks down and a fully quantum non-adiabatic approach to the coupled electron-vibration problem must be adopted.

The essential state model for a dipolar dye discussed in chapters 1 and 2 has been succesfully extended to treat intermolecular electrostatic interactions in molecular aggregates [84–86, 207] as well as in energy transfer pairs.[94] In this chapter it is shown that the essential state approach offers a unified framework to describe both energy transfer and exciton delocalization in molecular aggregates, while releasing the two major approximations of the Förster and exciton models. Molecular homo- and etero-dimers are then explicitly addressed. The Redfield-based dynamical model developed in chapter 1 is applied to these systems addressing the energy fluxes after photoexcitation, thus solving in an elegant way the tricky issue of recognizing the fluorescent state and hence opening the path to calculate time-resolved emission spectra of aggregates and RET systems.

The chapter is organized as follows: in section 4.1 the essential state model for the supramolecular assembly is presented, making a clear connection between the exciton and Förster models. In section 4.2 the dynamical model introduced in chapter 1 is briefly discussed and adapted to the new supramolecular Hamiltonian. Section 4.3 shows the results for homodimers (4.3.1) and heterodimers (4.3.2), as well as for asymmetric dimers (4.3.3). Section 4.4 concludes the chapter.

4.1 The supramolecular model

As mentioned above, the systems of interest in this chapter are dimers of dipolar dyes. Each dye is described by the two state Hamiltonian presented in chapter 1 (eq. 1.39).[1] Briefly, two diabatic basis states $|N\rangle$ and $|Z\rangle$ (corresponding to the two main resonance structures DA and D^+A^-, respectively) are separated by an energy gap $2z$ and are mixed by a matrix element $-\tau$ to give a ground $|G\rangle$ and an excited state $|E\rangle$. An effective dimensionless molecular vibration $\hat{Q} = \hat{d}^\dagger + \hat{d}$ with frequency $\hbar\omega_v$ is introduced to account for the different geometry of the molecule in the two basis states, with the relaxation energy ε_v measuring the strength of the electron-vibration coupling. Accepted model parameters for Nile Red (NR) and DANS, the two dyes investigated in this chapter (molecular structures in figure 1.1, chapter 1), are reported in table 4.1.[15, 84]

1: The molecular Hamiltonian (eq. 1.39) reads:

$$\begin{aligned}\hat{H}_{mol} = &-\tau\hat{o} + 2z\hat{\rho} \\ &- \sqrt{\hbar\omega_v\varepsilon_v}\left(\hat{d} + \hat{d}^\dagger\right)\hat{\rho} \\ &+ \hbar\omega_v\left(\hat{d}^\dagger\hat{d} + \frac{1}{2}\right)\end{aligned}$$

with the electronic operators $\hat{o}$ and $\hat{\rho}$ defined as:

$$\begin{aligned}\hat{\rho} &= |Z\rangle\langle Z| \\ \hat{o} &= |N\rangle\langle Z| + |Z\rangle\langle N|.\end{aligned}$$

	z	$-\tau$	ε_v	$\hbar\omega_v$
NR	0.88	0.95	0.33	0.14
DANS	1.32	0.72	0.3	0.17

Table 4.1: Molecular model parameters for NR and DANS (all quantities in eV).

4.1.1 ESM for aggregates of dipolar dyes

To investigate in the same theoretical framework both energy delocalization and RET, we consider a pair of molecules that only interact via electrostatic forces. The dimer is then described in terms of the four electronic basis states obtained as the direct product of the two electronic states relevant to the two molecules: $|N_1, N_2\rangle$, $|N_1, Z_2\rangle$, $|Z_1, N_2\rangle$ and $|Z_1, Z_2\rangle$. In line with the Mulliken approximation,[236] the electrostatic interactions involving neutral states are neglected. Accordingly, electrostatic intermolecular interactions in the dimer are described by V that

measures the electrostatic interaction energy between the two molecules when both are in the zwitterionic state. In other terms, V only affects the energy of the $|Z_1, Z_2\rangle$ state. The Hamiltonian for the molecular dimer reads:

$$\hat{H}_{dimer} = \hat{H}_1 + \hat{H}_2 + V\hat{\rho}_1\hat{\rho}_2 \tag{4.1}$$

where $\hat{H}_{1(2)}$ is the molecular Hamiltonian in eq. 1.39, as relevant to the molecular site 1(2) and, more generally, the pedices specify operators relevant to each one of the two molecules. Explicit expressions for V require the definition of the electrostatic model. If the dipolar approximation is considered, V is fully defined by the permanent dipole moments $\mu_{0,i}$ of the two molecules in the zwitterionic state and their relative orientation. Typical values of $\mu_{0,i}$ range between 10 and 30 D[15, 84, 237, 238]. For aligned molecules, V values are then of the order of few eV for typical intermolecular distances of ~ 4-5 Å, similar values being obtained upon relaxing the dipolar approximation.[84] Of course, for RET pairs much larger intermolecular distances must be considered, leading to smaller V values.

The two states $|G\rangle$ and $|E\rangle$ obtained diagonalizing the Hamiltonian of the isolated molecule correspond to the ground and excited states typically accounted for, on each molecule, in either the exciton model (that applies when the two molecules are equivalent or almost so) or in the Förster model (that applies when the two molecules are distinctively different). At variance with either the exciton model or the Förster model, however, in the essential state model (eq. 4.1) the nature of the ground and of the excited state in each molecule (i.e., the amount of mixing between $|N\rangle$ and $|Z\rangle$) varies as the result of the interaction with the nearby molecule. In this view, eq. 4.1 accounts for the molecular polarizability, which is disregarded in either the standard exciton or Förster models.

4.1.2 Connection with the standard exciton and Förster models

The Hamiltonian for the molecular pair in eq. 4.1 is very simple, yet it describes both energy delocalization and RET. To understand the relation among the models, following ref. [85], the dimer Hamiltonian in eq. 4.1 is rewritten on the adiabatic basis defined by the four electronic states $|G_1, G_2\rangle$, $|G_1, E_2\rangle$, $|E_1, G_2\rangle$ and $|E_1, E_2\rangle$, with the $|G\rangle$ and $|E\rangle$ states defined on each molecule as:

$$\begin{aligned} |G_i\rangle &= \sqrt{1-\bar{\rho}_i}|N_i\rangle + \sqrt{\bar{\rho}_i}|Z_i\rangle \\ |E_i\rangle &= \sqrt{\bar{\rho}_i}|N_i\rangle - \sqrt{1-\bar{\rho}_i}|Z_i\rangle \end{aligned} \tag{4.2}$$

where $\bar{\rho}_i = \langle G_i|\hat{\rho}_i|G_i\rangle$ is the ground state expectation value of the ionicity operator on each molecule.

The electronic part of Hamiltonian in eq. 4.1 can be rewritten as:

$$\begin{aligned} \hat{H}^{el}_{dimer} &= 2z_1\hat{\rho}_1 - \tau_1\hat{\sigma}_{x,1} + 2z_2\hat{\rho}_2 - \tau_2\hat{\sigma}_{x,2} + V\hat{\rho}_1\hat{\rho}_2 \\ &= 2z_1\left(\frac{1}{2} - \frac{\hat{\sigma}_{z,1}}{2}\right) - \tau_1\hat{\sigma}_{x,1} + 2z_2\left(\frac{1}{2} - \frac{\hat{\sigma}_{z,2}}{2}\right) - \tau_2\hat{\sigma}_{x,2} \\ &+ V\left(\frac{1}{2} - \frac{\hat{\sigma}_{z,1}}{2}\right)\left(\frac{1}{2} - \frac{\hat{\sigma}_{z,2}}{2}\right) \end{aligned} \tag{4.3}$$

where, for each molecule, the following operators are defined:

$$\hat{\sigma}_x = \begin{pmatrix} 0 & 1 \\ 1 & 0 \end{pmatrix}, \quad \hat{\sigma}_z = \begin{pmatrix} 1 & 0 \\ 0 & -1 \end{pmatrix}, \tag{4.4}$$

$$\hat{\rho} = \begin{pmatrix} 0 & 0 \\ 0 & 1 \end{pmatrix} = \left(\frac{1}{2} - \frac{\hat{\sigma}_z}{2} \right). \tag{4.5}$$

To rotate the Hamiltonian in eq. 4.3 on the adiabatic basis for the dimer the Paulion operators $\hat{p}_i^\dagger$ and $\hat{p}_i$ are introduced, that transform the i-th site from $|G_i\rangle$ to $|E_i\rangle$ and from $|E_i\rangle$ to $|G_i\rangle$, respectively. These operators are related to the operators in eq. 4.5 as:[85, 207]

$$\hat{\sigma}_{z,i} = (1 - 2\bar{\rho}_i)\left(1 - 2\hat{p}_i^\dagger \hat{p}_i\right) - 2\sqrt{\bar{\rho}_i(1-\bar{\rho}_i)}\left(\hat{p}_i^\dagger + \hat{p}_i\right) \tag{4.6}$$

$$\hat{\sigma}_{x,i} = 2\sqrt{\bar{\rho}_i(1-\bar{\rho}_i)}\left(1 - 2\hat{p}_i^\dagger \hat{p}_i\right) + (1 - 2\bar{\rho}_i)\left(\hat{p}_i^\dagger + \hat{p}_i\right) \tag{4.7}$$

By plugging eqs. 4.6 and 4.7 into eq. 4.3 and neglecting constant terms, the following expression is obtained:

$$\begin{aligned}
\hat{H}^{el}_{dimer} = & \left[2(1-2\bar{\rho}_1)(z_1 + M\bar{\rho}_2) + 4\tau_1\sqrt{\bar{\rho}_1(1-\bar{\rho}_1)}\right]\hat{n}_1 \\
& + \left[2(1-2\bar{\rho}_2)(z_2 + M\bar{\rho}_1) + 4\tau_2\sqrt{\bar{\rho}_2(1-\bar{\rho}_2)}\right]\hat{n}_2 \\
& + \left[2\sqrt{\bar{\rho}_1(1-\bar{\rho}_1)}(z_1 + M\bar{\rho}_2) - \tau_1(1-2\bar{\rho}_1)\right]\left(\hat{p}_1^\dagger + \hat{p}_1\right) \\
& + \left[2\sqrt{\bar{\rho}_2(1-\bar{\rho}_2)}(z_2 + M\bar{\rho}_1) - \tau_2(1-2\bar{\rho}_2)\right]\left(\hat{p}_2^\dagger + \hat{p}_2\right) \\
& + V\sqrt{\bar{\rho}_1(1-\bar{\rho}_1)}\sqrt{\bar{\rho}_2(1-\bar{\rho}_2)}\left(\hat{p}_1^\dagger \hat{p}_2 + \hat{p}_1 \hat{p}_2^\dagger\right) \\
& + V(1-2\bar{\rho}_1)(1-2\bar{\rho}_2)\hat{n}_1\hat{n}_2 \\
& + V\sqrt{\bar{\rho}_1(1-\bar{\rho}_1)}\sqrt{\bar{\rho}_2(1-\bar{\rho}_2)}\left(\hat{p}_1^\dagger \hat{p}_2^\dagger + \hat{p}_1 \hat{p}_2\right) \\
& + V(1-2\bar{\rho}_1)\sqrt{\bar{\rho}_2(1-\bar{\rho}_2)}\left(\hat{p}_2^\dagger + \hat{p}_2\right)\hat{n}_1 \\
& + V(1-2\bar{\rho}_2)\sqrt{\bar{\rho}_1(1-\bar{\rho}_1)}\left(\hat{p}_1^\dagger + \hat{p}_1\right)\hat{n}_2
\end{aligned} \tag{4.8}$$

where the exciton number operator $\hat{n}_i = \hat{p}_i^\dagger \hat{p}_i$ counts the excitations on the i-th molecular site and $M = V/2$.

The Hamiltonian in eq. 4.8 is equivalent to the Hamiltonian in eq. 4.1 for any choice of $\bar{\rho}_1$ and $\bar{\rho}_2$ values. However if $\bar{\rho}_1$ and $\bar{\rho}_2$ are chosen no that the $|G_i\rangle$ and $|E_i\rangle$ states coincide with the actual ground and excited states of the two molecules in the dimer (i.e., feeling the potential generated by the other molecule), the third and fourth lines in eq. 4.8 vanish:

$$\begin{cases} 2\sqrt{\bar{\rho}_1(1-\bar{\rho}_1)}(z_1 + M\bar{\rho}_2) - \tau_1(1-2\bar{\rho}_1) = 0 \\ 2\sqrt{\bar{\rho}_2(1-\bar{\rho}_2)}(z_2 + M\bar{\rho}_1) - \tau_2(1-2\bar{\rho}_2) = 0 \end{cases} \tag{4.9}$$

thus getting:

$$\begin{cases} \bar{\rho}_2 = \frac{\tau_1(1-2\bar{\rho}_1)}{2M\sqrt{\bar{\rho}_1(1-\bar{\rho}_1)}} - z_1/M \\ \bar{\rho}_1 = \frac{\tau_2(1-2\bar{\rho}_2)}{2M\sqrt{\bar{\rho}_2(1-\bar{\rho}_2)}} - z_2/M \end{cases} \tag{4.10}$$

With this special choice of the basis states, the single molecule terms entering eq. 4.8 reduce to the first two lines, that account for the excitation energy of the two molecules in the electrostatic environment of the dimer. By plugging $\bar{\rho}_2$ and $\bar{\rho}_1$ from eq. 4.10 in the first and second line of eq. 4.8, respectively, one obtain:

$$\hat{H}^{el}_{mf} = \left[\frac{\tau_1}{\sqrt{\bar{\rho}_1(1-\bar{\rho}_1)}}\right]\hat{n}_1 + \left[\frac{\tau_2}{\sqrt{\bar{\rho}_2(1-\bar{\rho}_2)}}\right]\hat{n}_2 \tag{4.11}$$

where $\bar{\rho}_i$ is the ionicity on the i-th molecule that self-consistently depends on itself (as a result of electron-vibration coupling) and on the ionicity of the nearby molecule (as a result of electrostatic intermolecular interactions):[85, 207]

$$\bar{\rho}_i = \frac{1}{2}\left(1 - \frac{\tilde{z}_i}{\sqrt{\tilde{z}_i^2 + \tau_i^2}}\right) \tag{4.12}$$

with

$$\begin{aligned} \tilde{z}_1 &= z_1 + V\bar{\rho}_2 - \varepsilon_{v,1}\bar{\rho}_1 \\ \tilde{z}_2 &= z_2 + V\bar{\rho}_1 - \varepsilon_{v,2}\bar{\rho}_2 \end{aligned} \tag{4.13}$$

In other terms, the Hamiltonian in eq. 4.11 is the mean field Hamiltonian describing the two molecules each one responding to the potential generated by the other.
As for the vibrational part, the ground state equilibrium position for each oscillator varies with the ionicity on the relevant molecule:

$$\bar{Q}_i = \langle G_i|\hat{Q}_i|G_i\rangle = \sqrt{\frac{2\omega_{v,i}}{\hbar}}\frac{g_i}{\omega^2_{v,i}}\bar{\rho}_i \tag{4.14}$$

where $g_i = \sqrt{\hbar\omega_{v,i}\varepsilon_{v,i}}$. It is convenient to move the origin of each vibrational coordinate to its equilibrium position, via a Lang-Firsov transformation of the vibrational operators:[85, 239]

$$\hat{\tilde{Q}}_i = \hat{Q}_i - \bar{Q}_i = \sqrt{\frac{\hbar}{2\omega_v}}\left(\hat{\tilde{a}}^\dagger_i + \hat{\tilde{a}}_i\right) \tag{4.15}$$

$$\hat{\tilde{P}}_i = \hat{P}_i = i\sqrt{\frac{\hbar\omega_v}{2}}\left(\hat{\tilde{a}}^\dagger_i - \hat{\tilde{a}}_i\right) \tag{4.16}$$

where displaced bosonic creation and annihilation operators $\hat{\tilde{a}}^\dagger_i, \hat{\tilde{a}}_i$ are introduced[85].

The complete Hamiltonian in eq. 4.1 is finally rewritten on the mean field basis as:

$$\hat{H}_{dimer} = \hat{H}_{mf} + \hat{H}_{exc} + \hat{H}_{uex} \tag{4.17}$$

where:

$$\begin{aligned} \hat{H}_{mf} &= \sum_{i=1}^{2}\Delta\mathscr{E}_{CT,i}\,\hat{n}_i + \sum_{i=1}^{2}\hbar\omega_{v,i}\left(\hat{\tilde{a}}^\dagger_i\hat{\tilde{a}}_i + \frac{1}{2}\right) \\ &- \sum_{i=1}^{2} g_i(\hat{\tilde{a}}^\dagger_i + \hat{\tilde{a}}_i)\left[(1-2\bar{\rho}_i)\hat{n}_i + \sqrt{\bar{\rho}_i(1-\bar{\rho}_i)}(\hat{p}^\dagger_i + \hat{p}_i)\right] \end{aligned} \tag{4.18}$$

$$\hat{H}_{exc} = V\sqrt{\bar{\rho}_1\bar{\rho}_2(1-\bar{\rho}_1)(1-\bar{\rho}_2)}\left(\hat{p}_1^\dagger\hat{p}_2 + \hat{p}_2^\dagger\hat{p}_1\right) \tag{4.19}$$

$$\begin{aligned}\hat{H}_{uex} &= V\sqrt{\bar{\rho}_1\bar{\rho}_2(1-\bar{\rho}_1)(1-\bar{\rho}_2)}\left(\hat{p}_1^\dagger\hat{p}_2^\dagger + \hat{p}_2\hat{p}_1\right)\\ &+ V(1-2\bar{\rho}_1)(1-2\bar{\rho}_2)\hat{n}_1\hat{n}_2\\ &+ V(1-2\bar{\rho}_1)\sqrt{\bar{\rho}_2(1-\bar{\rho}_2)}\left(\hat{p}_2^\dagger + \hat{p}_2\right)\hat{n}_1\\ &+ V(1-2\bar{\rho}_2)\sqrt{\bar{\rho}_1(1-\bar{\rho}_1)}\left(\hat{p}_1^\dagger + \hat{p}_1\right)\hat{n}_2\end{aligned} \tag{4.20}$$

$\hat{H}_{mf}$ collects the on-site terms, accounting for the mean field transition energies of the dyes, $\Delta\mathscr{E}_{CT,i} = \tau_i/\sqrt{\bar{\rho}_i(1-\bar{\rho}_i)}$, for the two displaced harmonic oscillators and (in the second row) for the linear electron-phonon coupling. $\hat{H}_{exc}$ and $\hat{H}_{uex}$, containing terms proportional to V, are due to intermolecular electrostatic interactions. Specifically, $\hat{H}_{exc}$ accounts for the exciton hopping term, i.e. the term mixing $|G_1, E_2\rangle$ and $|E_1, G_2\rangle$ states, that is responsible for energy delocalization in aggregates and for energy transfer in RET systems. $\hat{H}_{uex}$ collects all the terms that are not accounted for in the exciton or Förster model and are therefore dubbed as *ultaexcitonic*.[207] In the first line a term appears mixing the ground state $|G_1, G_2\rangle$ with the state where both molecules are excited $|E_1, E_2\rangle$. The second line describes an exciton-exciton interaction term, and the last two lines group two additional ultraexcitonic terms that mix states which differ by one exciton.

When the excitation energies are large, the ultraexcitonic terms have minor effects and, in this limit, the only relevant term is $\hat{H}_{exc}$, accounting for the exciton migration. This term is proportional to $V\sqrt{\bar{\rho}_1\bar{\rho}_2(1-\bar{\rho}_1)(1-\bar{\rho}_2)}$ and, in the dipolar approximation, it describes the interaction between the transition dipole moments of the two molecules. In other terms, if the dipolar approximation is adopted and ultraexcitonic terms are neglected, the model in eq. 4.1 boils down to the standard exciton model if the two molecules are equal, or to the Förster model if they are different.

Equations 4.17 - 4.20 make clear how the essential state model is more general than both the Förster and the standard exciton model, naturally accounting for all the ultraexcitonic terms and for site energies that readjust in response to the electrostatic potential generated by the other molecule, thus accounting for the molecular polarizability.

The Hamiltonian in eq. 4.17 is useful to understand the connection between the proposed model and either the exciton or the Förster models. However, working on the original diabatic basis is more expedient for the numerically exact solution of the complete problem. In the following, the more practical form of the dimer Hamiltonian in eq. 4.1 is used, represented on the basis obtained as the direct product of the 4-dimensional electronic Hilbert space $|N_1, N_2\rangle, |Z_1, N_2\rangle, |N_1, Z_2\rangle, |Z_1, Z_2\rangle$ times the two Fock spaces associated with the two molecular vibrational coordinates. To make the approach numerically tractable, the vibrational basis is truncated so that the sum of the vibrational quanta associated with the two molecules does not exceed a fixed threshold M, high enough to ensure convergence on properties of interest (in this chapter M=14, for a grand total of 420 basis states). Numerical diagonalization of the resulting Hamiltonian gives numerically exact vibronic eigenstates $|\phi_a\rangle$ of the complete Hamiltonian in eq. 4.1 (or equivalently in eq. 4.17), without

reducing the basis set to the single exciton manifold, as usually done in the exciton model or in standard treatments of RET.

4.2 The dynamical model

To follow in real time RET and exciton delocalization, the open quantum system approach presented in chapter 1 is adopted here with reference to the dimer Hamiltonian in eq. 4.1. Brielfly, each vibrational coordinate is coupled to a thermal bath simulated by an infinite number of quantum harmonic oscillators.[240] The total Hamiltonian reads:

$$\hat{H}_{tot} = \hat{H}_{dimer} + \hat{H}_{dimer-bath} + \hat{H}_{bath} \tag{4.21}$$

$$\hat{H}_{dimer-bath} = \sum_{i} \sum_{\alpha=1}^{2} g_i \hat{B}_{i,\alpha} \hat{Q}_{\alpha} \tag{4.22}$$

$$\hat{H}_{bath} = \sum_{i} \sum_{\alpha=1}^{2} \hbar\omega_i \left(\hat{b}^{\dagger}_{i,\alpha} \hat{b}_{i,\alpha} + \frac{1}{2} \right) \tag{4.23}$$

where α runs over the two molecular units and $\hat{B}_{i,\alpha} = \hat{b}^{\dagger}_{i,\alpha} + \hat{b}_{i,\alpha}$ is the i-th bath coordinate coupled to the α-th supramolecular vibration, with i ranging from one to infinity, covering all possible bath frequencies. The α-dependence acquired by the bath coordinates means that each molecular vibration $\hat{Q}_{\alpha}$ is coupled to an independent harmonic bath.[104, 105, 240, 241] The coupling constants g_i define the strength of the system-bath coupling and therefre the bath spectral density $\mathcal{J}(\omega) = \sum_i |g_i|^2 \delta(\omega - \omega_i)$, that for the sake of simplicity is set independent from α, meaning that all vibrational degrees of freedom couple with the same strength to the bath.

The proposed model is general and applies to pairs of identical or different molecules, as to simulate excitonic or RET pairs, respectively. However, for molecular homodimers the high degree of degeneracy leads to divergent dynamics. To overcome this problem, two slightly different frequencies $\omega_{v,1}$ and $\omega_{v,2}$ could be assigned to the two molecules. However, this would artificially lower the symmetry of the dimeric system, heavily affecting its physics. A viable alternative to deal with homodimers recasts the system Hamiltonian in eq. 4.1 in terms of the symmetrized vibrational coordinate operators $\hat{Q}_+$ and $\hat{Q}_-$:

$$\hat{Q}_+ = \frac{1}{\sqrt{2}} \left(\hat{Q}_1 + \hat{Q}_2 \right), \qquad \hat{Q}_- = \frac{1}{\sqrt{2}} \left(\hat{Q}_1 - \hat{Q}_2 \right) \tag{4.24}$$

with the relevant bosonic operators $\hat{d}^{(\dagger)}_{\pm} = (\hat{d}^{(\dagger)}_1 \pm \hat{d}^{(\dagger)}_2)/\sqrt{2}$ ($\hat{d}^{(\dagger)}_{1/2}$ being the bosonic operators associated to the two molecular coordinates). The two coordinates have vibrational frequencies $\omega_{v,\pm}$, relaxation energies $\varepsilon_{v,\pm}$ and are coupled to the electrons *via* the symmetrized ionicity operators

$\hat{\rho}_{\pm} = (\hat{\rho}_1 \pm \hat{\rho}_2)/\sqrt{2}$. The symmetrized Hamiltonian reads:

$$\begin{aligned}\hat{H}_{symm} =& -\tau_1\hat{\sigma}_1 + 2z_1\hat{\rho}_1 - \tau_2\hat{\sigma}_2 + 2z_2\hat{\rho}_2 \\ & - \sqrt{\hbar\omega_{v,+}\varepsilon_{v,+}}\left(\hat{d}_+ + \hat{d}_+^\dagger\right)\hat{\rho}_+ - \sqrt{\hbar\omega_{v,-}\varepsilon_{v,-}}\left(\hat{d}_- + \hat{d}_-^\dagger\right)\hat{\rho}_- \\ & + \hbar\omega_{v,+}\left(\hat{d}_+^\dagger\hat{d}_+ + \frac{1}{2}\right) + \hbar\omega_{v,-}\left(\hat{d}_-^\dagger\hat{d}_- + \frac{1}{2}\right).\end{aligned} \tag{4.25}$$

By assigning slightly different values for $\omega_{v,+}$ and $\omega_{v,-}$, the numerical divergence problem is solved without affecting the symmetry of the system.

Using either eq. 4.1 or eq. 4.25 to describe the system, the system-bath Hamiltonian in eq. 4.22 leads to the following expressions for the kinetic coefficients $\Gamma^+_{db,ac}$ and $\Gamma^-_{db,ac}$ entering eq. 1.28 in chapter 1 for the definition of the Redfield relaxation tensor read:

$$\begin{aligned}\Gamma^+_{db,ac} =& \frac{\pi}{\hbar^2} q_{db}^{1/+} q_{ac}^{1/+} \left[\mathcal{J}(\omega_{ac})n(\omega_{ac}) + \mathcal{J}(\omega_{ca})\left(n(\omega_{ca})+1\right)\right] \\ & + \frac{\pi}{\hbar^2} q_{db}^{2/-} q_{ac}^{2/-} \left[\mathcal{J}(\omega_{ac})n(\omega_{ac}) + \mathcal{J}(\omega_{ca})\left(n(\omega_{ca})+1\right)\right]\end{aligned} \tag{4.26}$$

$$\begin{aligned}\Gamma^-_{db,ac} =& \frac{\pi}{\hbar^2} q_{db}^{1/+} q_{ac}^{1/+} \left[\mathcal{J}(\omega_{bd})n(\omega_{bd}) + \mathcal{J}(\omega_{db})\left(n(\omega_{db})+1\right)\right] \\ & + \frac{\pi}{\hbar^2} q_{db}^{2/-} q_{ac}^{2/-} \left[\mathcal{J}(\omega_{bd})n(\omega_{bd}) + \mathcal{J}(\omega_{db})\left(n(\omega_{db})+1\right)\right]\end{aligned} \tag{4.27}$$

where $q_{db}^{1/+(2/-)}$ and $q_{ac}^{1/+(2/-)}$ are the db and ac matrix elements of the vibrational operators $\hat{Q}_{1/+(2/-)}$ and $n(\omega)$ is the Bose-Einstein distribution function.

Since evolving the full Redfield master equation (eq. 1.26, chapter 1) is computationally cumbersome, the secular approximation is adopted in this chapter, only accounting for the $\mathcal{R}_{ab,cd}$ terms with $|\omega_{ab} - \omega_{cd}| = 0$.

4.3 Results

NR and DANS (structures in figure 1.1, relevant model parameters in table 4.1) are taken as reference systems, representative of the large family of push-pull dyes.[15] Molecular Hamiltonians for different dyes will have slightly different parameters, but the differences are marginal and do not alter the main picture. In the following the molecular system is coupled to a quantum bath at 300K. The spectral density is set to a constant value $\mathcal{J}(\omega) = \hbar^2\gamma/\pi$,[91, 93–95] setting γ =5 ps^{-1}. The master equation is solved using the Short-Iterative-Arnoldi (SIA) algorithm[24, 99] with 1 fs time integration step.

4.3.1 Molecular dimers

As for molecular dimers, the Hamiltonian in eq. 4.25 is used. Model parameters relevant to NR in table 4.1 are adopted, but setting $\hbar\omega_{v,+}$ = 0.15 eV and $\hbar\omega_{v,-}$ = 0.13 eV. The electrostatic intermolecular interaction between the two molecules in the zwitterionic state, V, is varied from −1.2 to 1.2 eV. The interaction J entering the exciton model measures

instead the interaction between the transition dipole moments and is related to V by $J = V\rho(1-\rho)$ (see discussion following eq. 4.19). For NR $\rho \sim 0.16$, so that, in the chosen V interval J ranges from ~ -0.16 to 0.16 eV, in line with typical values for molecular aggregates. At time $t = 0$, the system undergoes an impulsive excitation, and the initial state for the dynamics is prepared as:[78, 94, 95, 240]

$$|\Psi^*(t=0)\rangle \propto \sum_{a=2}^{N} |\phi_a\rangle\langle\phi_a|\hat{\mu}|\phi_1\rangle \tag{4.28}$$

where a runs over the excited eigenstates of $\hat{H}_{dimer}$ ($|\phi_1\rangle$ being the ground state) and $\hat{\mu} = \hat{\mu}_1 + \hat{\mu}_2$ is the dimer dipole moment operator for the chosen geometry. As done in chapter 1 for the multimode systems, the basis is truncated neglecting states lying at higher energy than the most populated states reached upon coherent excitation, and whose initial population is lower than 10^{-6}.[94, 95, 240]

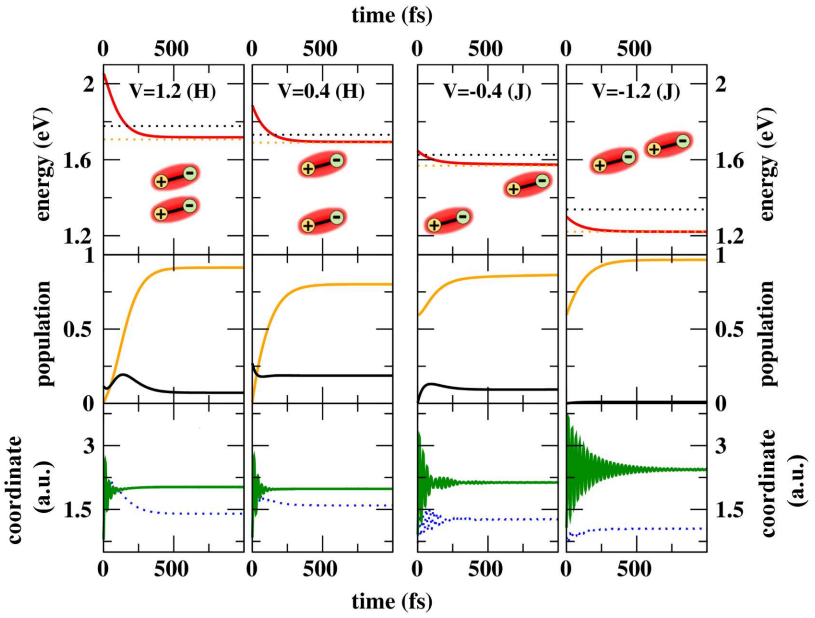

Figure 4.1: Results for dimers of NR. Each column shows results obtained for the V value listed in the topmost panel (eV units). Top panels: time evolution of the system energy (red). For reference, the energy of the lowest vibronic eigenstate in S_1 and S_2 manifolds are shown as orange and black dotted lines, respectively. The sketches in the upper panels schematically show the geometrical arrangement of the molecular permanent dipoles. Middle panels: time evolution of the populations of the lowest vibronic eigenstate in S_1 and S_2 manifolds (orange and black lines, respectively). Bottom panels: time evolution of $\langle\hat{Q}_+\rangle$ and ΔQ_- (green line and blue dotted line, respectively).

Figure 4.1 shows relevant results. Each column refers to an aggregate pair with a different V value. Top panels show the time evolution of the energy of the system (red lines) along with the energies of the lowest vibronic eigenstates in the S_1 and S_2 manifolds (orange and black dotted lines, respectively), whose population is shown in the middle panels. Bottom panels show time evolution of $\langle\hat{Q}_+\rangle$ (green lines) and the standard deviation along $\hat{Q}_-$, $\Delta Q_- = \sqrt{\langle\hat{Q}_-^2\rangle}$ (blue dotted lines). As it is well known, in J- and H-aggregates the optically allowed transitions go towards the first and second electronic excited state, respectively.[166, 169] Accordingly, for negative V values (J-dimers), the initial excitation brings the system in the first excited electronic manifold (namely S_1, see also figure 4.2 panel **d**, where the green dot marks the initial state of the dynamics). On the opposite, for positive V values (H-dimers) the most populated initial state belongs to the second electronic excited manifold, S_2 (see also figure 4.2 panel **b**). In either case, the initially populated state is the vertical state, lying higher in energy than the lowest eigenstate in the relevant S_1 or S_2 manifold. A fast relaxation is always observed in

the first ~100 fs that transfers the population from the initially populated states to the lowest state of the S_1 manifold, the so-called Kasha's state.

It is worth to point out that the adopted relaxation model with the two (supra)molecular coordinates coupled to two independent baths allows for the uncorrelated motion of the relevant degrees of freedom, or, in other terms, it allows for energy dissipation driven by either the $\hat{Q}_+$ or $\hat{Q}_-$ coordinate. This is important because it allows for energy relaxation among states with different symmetry, a phenomenon that would be strictly forbidden if both molecular coordinates were coupled to a single bath (or, equivalently, if only the $\hat{Q}_+$ coordinate was coupled).

After an initial very fast relaxation on the timescale of ~ 0.1-0.5 ps, once the system reaches the Kasha's state,[240] the dynamics slows down dramatically with relaxation times in the nanosecond window. The different timescales of the two processes ensures that, in this case, emission occurs from a thermally equilibrated Kasha's state, as best demonstrated by the residual thermal population of the lowest eigenstate in the S_2 manifold observed at long times for $V = 1.2$, 0.4 and -0.4 eV (middle panels of figure 4.1).

An initial regime of coherent vibrational oscillations of $\langle \hat{Q}_+ \rangle$ is observed in all dimers (bottom panels in figure 4.1, green lines). Quite interestingly, the coherence lives longer in J-dimers, and particularly so in J-dimers with large V. In these systems in fact the dynamics in the S_1 manifold is marginally perturbed by the presence of S_2 states (see also figure 4.2 panel **d**). On the opposite, in H-dimers the vibrational coherence is quickly lost due to the interfering relaxation towards states in the S_1 manifold (see also figure 4.2 panel **b**). The expectation value $\langle \hat{Q}_- \rangle$ vanishes by symmetry along the whole dynamics. Yet, its standard deviation ΔQ_- shows a qualitatively different behavior for J- and H-aggregates. This is best appreciated by data reported in figure 4.2. The color maps show the adiabatic potential energy surfaces (PES) of the S_1 state of two dimers (the grey surface in panel **b** shows the PES for the S_2 states). In the adiabatic approximation, the vibrational kinetic energy is neglected and the vibrational coordinates become classical variables: the PES show the energy of the relevant state, calculated upon varying the two classical coordinates Q_+ and Q_-. More specifically, top panels (**a** and **b**) show

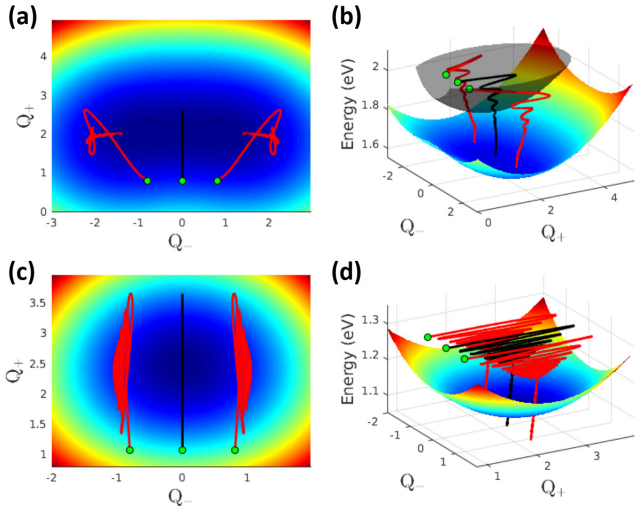

Figure 4.2: Vibrational trajectories calculated for NR dimers Top panels refer to a H-dimer ($V = 1.2$ eV), bottom panels refer to a J-dimer ($V = -1.2$ eV). The colored surfaces show the adiabatic potential energy surface of S_1 and in panel (b) the gray surface refer to the adiabatic potential energy surface of S_2. The black lines show the evolution of the system energy as a function of $\langle \hat{Q}_+ \rangle$ and $\langle \hat{Q}_- \rangle$. The red lines show the evolution of the system energy as a function of $\langle \hat{Q}_+ \rangle$ and $\pm\Delta Q_-$. In all trajectories, green dots mark the starting point ($t = 0$). Note the different energy scale in panels b and d.

results for a H dimer with $V = 1.2$ eV and bottom panels (**c** and **d**) refer instead to a J dimer with $V = -1.2$ eV. The PES relevant to the J-dimer with $V = -1.2$ eV has a single minimum and ΔQ_- is roughly constant as expected for a quasi-harmonic oscillator. On the opposite, the H-dimer with $V = 1.2$ eV has a largely anharmonic PES with two well developed minima. In this case, large $\hat{Q}_-$ fluctuations drive the system to visit the two minima, suggesting a tendency towards energy localization.

Adopting the same approach as in chapter 1, optical absorption spectra of the dimer are calculated as the real part of the Fourier transform (FT) of the damped dipole-dipole correlation function $C^{abs}_{\mu\mu}(t) = \langle\hat{\mu}(t)\hat{\mu}(0)\rangle \cdot \exp[-t/a] = Tr\{\hat{\mu}\hat{\Omega}_{abs}(t)\}\exp[-t/a]$, where the absorption generating function, $\Omega_{abs}(t=0) = \hat{\mu}|\phi_1\rangle\langle\phi_1|$, evolves according to the Liouville-von Neumann (unitary) equation.[91, 109, 240, 242, 243] Time-resolved fluorescence spectra are calculated as the FT of the damped dipole-

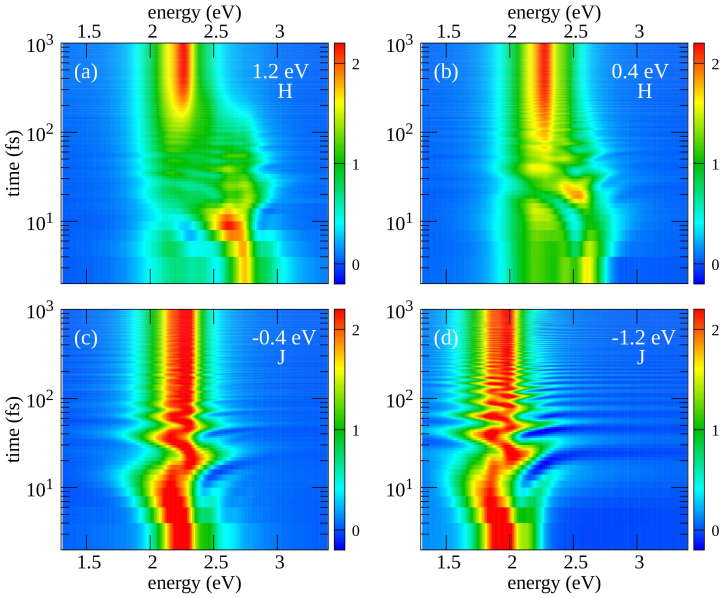

Figure 4.3: Time-resolved emission spectra for NR dimers (same parameters as in figure 4.1, values of the electrostatic intermolecular interaction V are indicated in the panels). The dipole-dipole correlation function is damped with $a = 7$ fs. At each time, spectra are normalized to unit area.

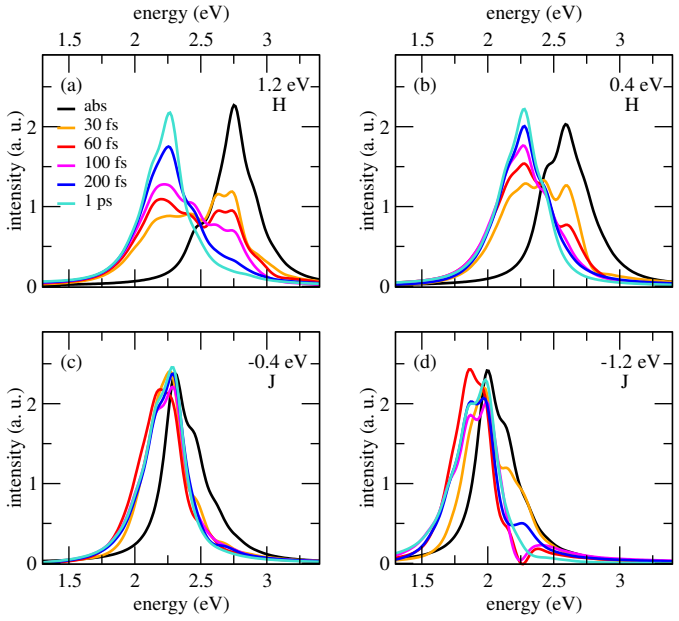

Figure 4.4: Absorption (black lines) and time-resolved emission spectra (colored lines) at selected times t' (as indicated in the legend) for the four investigated NR dimers. Emission spectra extracted form figure 4.3.

dipole correlation function $C_{\mu\mu}^{fluo}(t;t') = Tr\{\hat{\mu}\hat{\Omega}_{fluo}(t;t')\}\exp[-t/a]$, where the fluorescence generating function is $\hat{\Omega}_{fluo}(0;t') = \hat{\mu}\hat{\sigma}(t')$, being $\sigma(t')$ the reduced density matrix of the system at time t'.[95, 240] To avoid spurious signals, absorption spectra are calculated using the upper triangle of the dipole moment operator and emission spectra are calculated using the lower triangle.[54]

Figure 4.3 shows emission spectra for the four investigated dimers as a function of time t'. Spectra at selected t' times are shown in figure 4.4 along with absorption spectra, reported in black. In both figures spectra are normalized to unit area. In H-dimers (panels **a** and **b**) the time-resolved fluorescence shows a bimodal behavior: at very early time, emission largely comes from the second electronic manifold S_2, the same state populated upon absorption with a large transition dipole moment. As time goes on, while the system is coherently oscillating along the vibrational coordinates, the population is transferred to the first excited state S_1 leading to a much weaker and largely red-shifted emission. Normalized spectra are shown, but H-dimer emission is at least one order of magnitude weaker than for J-aggregates. Specifically, the weak long-time emission from the electronically dark S_1 state in H-aggregate is due to a vibronic coupling mechanism, with the emission occurring towards the ground state with a vibrational quantum in the antisymmetric $\hat{Q}_-$ mode.[169] Interestingly, in the H-aggregate with $V = 0.4$ eV a shoulder is clearly seen in the long-time emission superimposed to the 0-0 absorption band (figure 4.4 panel **b**). This signal is due to the residual thermal population of the (optically allowed) lowest state in the S_2 manifold (see middle panels in figure 4.1).

Time evolution of the emission spectra of the J-aggregates is less prominent: since the Kasha state coincides with the bright state reached upon absorption, all the dynamics lives in the same electronic state. The emission spectrum oscillates in time as long as vibrational coherence survives in the system and by the end of the vibrational relaxation (~ 1 ps) the emission spectrum is essentially the mirror image of the absorption spectrum, as expected (figure 4.4 panels **c** and **d**). In large J-aggregates, a sizable increase of the intensity of the 0-0 absorption peak vs the 0-1 peak upon increasing V would be expected,[190] as a result of delocalization of the exciton on several molecules, that would imply a reduced effective

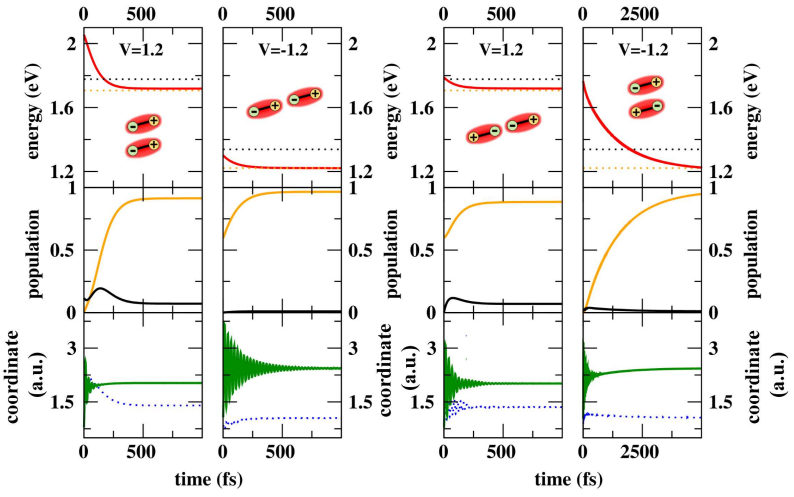

Figure 4.5: Results for dimers of NR with different relative orientations of the monomers (sketches of the dimeric geometries are shown in the top panels; left panels are taken from figure 4.1). Top panels: time evolution of the system energy (red). For reference, the energy of the lowest vibronic eigenstates in S_1 and S_2 manifolds are shown as orange and black dotted lines, respectively. Middle panels: time evolution of the populations of the lowest vibronic eigenstate in S_1 and S_2 manifolds (orange and black lines, respectively). Bottom panels: time evolution of $\langle\hat{Q}_+\rangle$, and of ΔQ_- (green and blue dotted lines, respectively).

electron-vibration coupling. This phenomenon is not observed in the dimers investigated here, where the exciton can never spread on more than two molecules.

Up to now, systems of aligned molecules have been considered. As already discussed, a positive electrostatic interaction sets the in-phase combination $|G_1E_2\rangle + |E_1G_2\rangle$ at higher energy than the out-of-phase one $|G_1E_2\rangle - |E_1G_2\rangle$, and *vice versa* for a negative interaction. For two molecules oriented in the same direction (non-centrosymmetric dimers), the bright state reached upon light absorption is the in-phase combination. On the other hand, for molecules oriented in opposite directions (centrosymmetric dimers) the out-of-phase combination becomes the bright state. The rightmost part of figure 4.5 shows results for centrosymmetric dimers (in the leftmost part, results also shown in figure 4.1 are reported for reference). More specifically, the systems in the first and third column have the same Hamiltonian (positive electrostatic interactions $V = 1.2$ eV), but the coherent excitation populates S_2 in the non-centrosymmetric system (first column) and S_1 in the centrosymmetric one (third column), as it can be seen from the populations reported in the middle panels. Moreover, the expectation value of $\hat{Q}_+$ shows how in the centrosymmetric dimer the coherence is maintained for a longer time with respect to the non-censtrosymmetric system, since excited state dynamics occurs in the same electronic manifold. The same considerations apply to the systems with negative interactions (second and fourth column, $V = -1.2$ eV). Here the slower relaxation of the centrosymmetric system is due to the higher energy difference between S_1 and S_2.

4.3.2 Resonance Energy Transfer

DANS and NR form a good RET pair, with a sizable overlap between the emission spectrum of DANS, acting as the energy donor $\mathscr{D}$, and the absorption spectrum of NR, acting as the energy acceptor $\mathscr{A}$. Hereinafter, for the sake of clarity, $\mathscr{D}$ and $\mathscr{A}$ indices will be used to refer to the two molecules. To address RET, the system is initially prepared in a state where only the energy donor $\mathscr{D}$ is coherently excited, inserting in eq. 4.28 the dipole moment operator relevant to the energy donor $\hat{\mu}_{\mathscr{D}}$.

Figure 4.6 shows results obtained for the DANS-NR RET pair with different values of the electrostatic intermolecular interaction V. In the left panel, the energy of the system is reported as a function of time, in the right panels $\langle \hat{Q}_{\mathscr{D}}(t) \rangle$ and $\langle \hat{Q}_{\mathscr{A}}(t) \rangle$ are shown as continuous and dashed lines, respectively. For $V \leq 0.05$ eV, the initial vibrational relaxation brings the system in the lowest vibronic eigenstate of the excited energy donor manifold within the first few hundreds of femtoseconds, as seen from the initial energy drop, as well as in the time evolution of $\langle \hat{Q}_{\mathscr{D}} \rangle$, where after some initial oscillations the coordinate stabilizes at the equilibrium geometry of the excited donor. From there, the energy flows towards the energy acceptor $\mathscr{A}$ through an incoherent process that can take several picoseconds to reach completion (as reflected by $\langle \hat{Q}_{\mathscr{A}} \rangle$) depending on the interaction strength V. When V increases ($V > 0.05$ eV), the system enters the strong coupling regime, with RET occuring in the same time window as the vibrational relaxation of $\mathscr{D}$. For $V = 0.1$ eV no clear distinction between the two processes is observed any more, as demonstrated by the single energy drop in the left panel of figure 4.6 (blue line). RET clearly

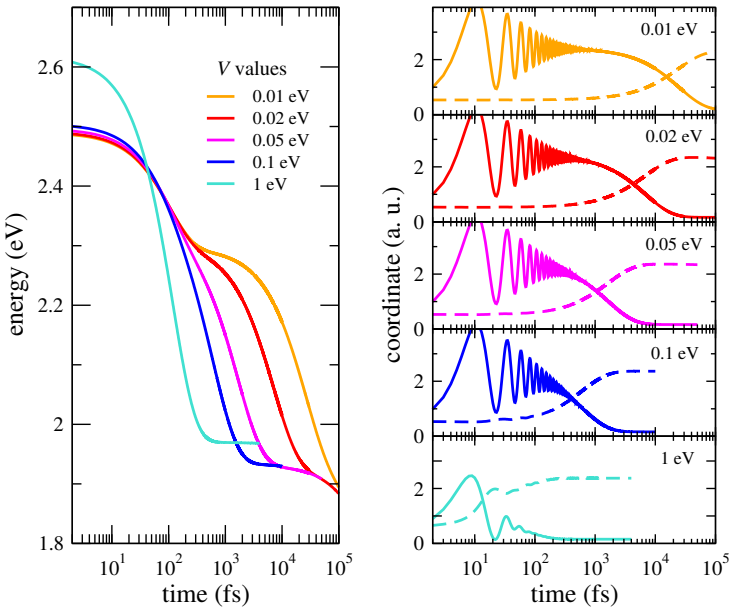

Figure 4.6: RET dynamics for a DANS - NR pair (molecular parameters in table 4.1) for different values of the electrostatic intermolecular interaction V. Left panel: time-evolution of the system energy; right panels: time evolution of $\langle \hat{Q}_{\mathcal{D}} \rangle$ (continuous lines) and $\langle \hat{Q}_{\mathcal{A}} \rangle$ (dashed lines).

starts while $\langle \hat{Q}_{\mathcal{D}} \rangle$ is still coherently oscillating, meaning that energy is partially transferred also from *hot* donor states. For even larger coupling (V = 1 eV), RET is even faster and the system enters a coherent transfer regime, as shown by the induced oscillations on $\langle \hat{Q}_{\mathcal{A}} \rangle$.

The model applies in a very wide range of intermolecular interaction strenghts, providing a consistent and unified picture of RET both in the weak (as described in the Förster model) and strong coupling regime. By treating at the same time vibrational relaxation, RET and the relaxation towards the ground state, without imposing any artificial separation on the time scales of the different phenomena and accounting for both forward and backward RET, the presented model reliably simulates the dynamics of the system irrespective of the coupling strength. Accordingly, vibrational relaxation of the excited donor and the simultaneous energy transfer towards the acceptor can be addressed in the case of very strong intermolecular coupling, as well as energy transfer and relaxation of the donor towards its ground state in the case of very weak coupling.

RET rates can be extrapolated from the dynamical simulations *via* an exponential fit of the time-dependent $\mathcal{DA}^*$ state population, i. e. the state where the acceptor is in its Kasha state (eigenstate 106 in all investigated

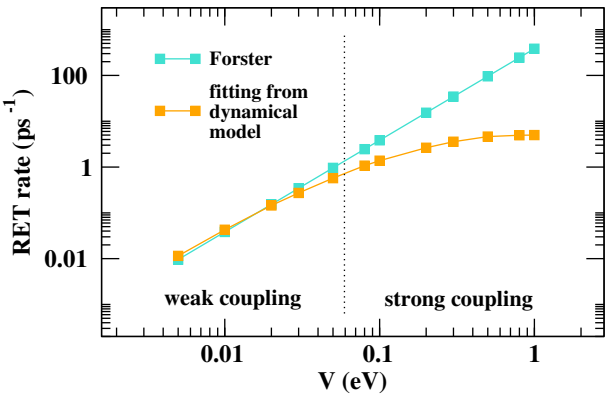

Figure 4.7: RET rates estimated for the DANS-NR pair as a function of the electrostatic interaction V. Cyan symbols refer to estimates obtained in the Förster model; results obtained from an exponential fit of the results of the dynamical simulations are reported in orange.

cases), with the equation:

$$f(t) = a_1 - a_2 \exp(-a_3 t) \tag{4.29}$$

where a_3 is the rate of interest.

In figure 4.7 rates obtained from the dynamical simulations (fitting parameters reported in table 4.2) are compared with those obtained in the Förster approximation. In the Förster model, RET occurs from the relaxed excited donor with a rate constant:

$$k_{FRET} = \frac{1}{\hbar^2 c} |J_{\mathcal{DA}}|^2 \mathcal{S} \tag{4.30}$$

where $\mathcal{S} = \int_0^\infty d\tilde{\nu} F_{\mathcal{D}}(\tilde{\nu}) A_{\mathcal{A}}(\tilde{\nu})$ is the spectral overlap between the fluorescence spectrum of the isolated donor ($F_{\mathcal{D}}$) and the absorption spectrum of the isolated acceptor ($A_{\mathcal{A}}$) (both in cm^{-1} and normalized to unit area), while $J_{\mathcal{DA}}$ is the electrostatic intermolecular interaction between the states involved in the RET process. The transition dipole moments for the *isolated* energy donor and acceptor are proportional to $\sqrt{\bar{\rho}_{\mathcal{D}}(1-\bar{\rho}_{\mathcal{D}})}$ and $\sqrt{\bar{\rho}_{\mathcal{A}}(1-\bar{\rho}_{\mathcal{A}})}$, respectively, so that, as discussed in section 4.1.2, $J_{\mathcal{DA}} = V\sqrt{\bar{\rho}_{\mathcal{D}}\bar{\rho}_{\mathcal{A}}(1-\bar{\rho}_{\mathcal{D}})(1-\bar{\rho}_{\mathcal{A}})}$. Results in figure 4.7 are obtained setting $\mathcal{S} = 3.45 \cdot 10^{-4}$ cm. In the weak coupling regime (up to $V \sim 0.05$ eV) the dynamical model agrees well with Förster prediction. Indeed, in this regime the RET process has characteristic times of $\sim 1 - 10$ ps, at least an order of magnitude slower than typical vibrational relaxation rates. On the other hand, in the strong coupling regime, the time scale separation between vibrational relaxation and RET, as imposed in the

V [eV]	a_1	a_2	a_3 [ps^{-1}]
0.005	0.906	0.908	0.0115
0.01	0.951	0.959	0.0427
0.02	0.985	1.011	0.145
0.03	0.992	1.038	0.272
0.05	0.995	1.078	0.573
0.08	0.996	1.126	1.071
0.1	1.000	1.153	1.378
0.2	1.010	1.223	2.634
0.3	1.011	1.250	3.576
0.5	1.007	1.254	4.628
0.8	1.005	1.250	4.944
1.0	1.004	1.244	4.985

Table 4.2: Fitting parameters for the extraction of the RET rates shown in figure 4.7.

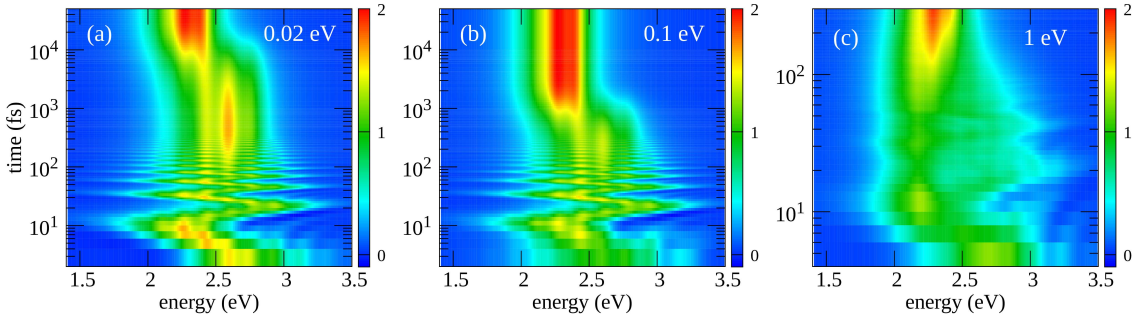

Figure 4.8: Time-resolved emission spectra for the DANS-NR RET pair with different values of the electrostatic intermolecular interaction $V = 0.02$, 0.1 and 1 eV (panels **a**, **b** and **c**, respectively). The dipole-dipole correlation function is damped with $a = 7$ fs. At each time, spectra are normalized to unit area.

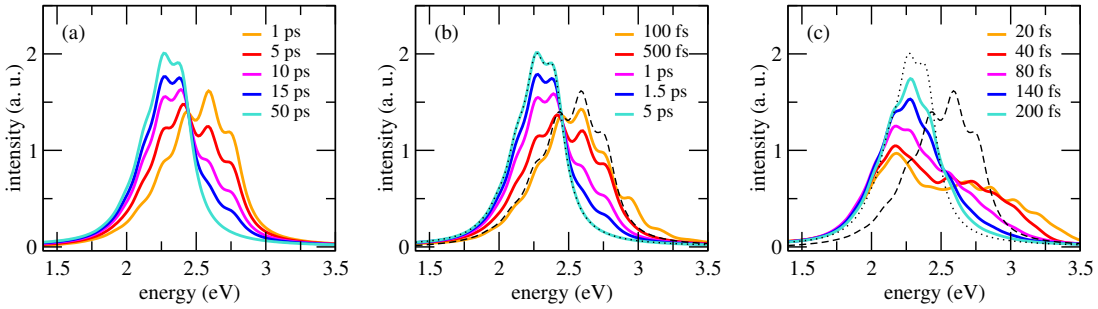

Figure 4.9: Time-resolved emission spectra at selected times (as indicated in the legends) for the DANS-NR RET pair with $V = 0.02$, 0.1 and 1 eV (panels **a**, **b** and **c**, respectively). Spectra are extracted form figure 4.3. Spectra at 1 ps and 50 ps from panel **a** are reported in dashed and dotted black lines, respectively, in panels **b** and **c** as a reference for the steady state emission of the donor and the acceptor.

$z_{\mathcal{D}}$ [eV]	a_1	a_2	a_3 [ps^{-1}]
1.250	0.980	0.978	0.0788
1.270	0.983	0.970	0.7476
1.282	0.994	1.158	2.4072
1.291	0.998	1.227	4.2802
1.303	0.998	1.222	4.1777
1.315	0.994	1.060	0.4430
1.320	0.992	1.038	0.2721
1.326	0.989	1.015	0.1528
1.332	0.985	0.992	0.1053
1.338	0.987	1.000	0.0850
1.344	0.977	0.967	0.0828
1.356	0.975	0.927	0.2083
1.359	0.986	1.020	0.6398
1.373	0.999	1.255	3.8222
1.385	0.999	1.260	4.0085
1.396	0.996	1.213	3.2061
1.409	0.996	1.082	0.5737
1.419	0.991	1.021	0.1697

Table 4.3: Fitting parameters for the extraction of the RET rates shown in figure 4.10.

Förster model, breaks down and sizable deviation from Förster rates are observed: while Förster rates grow as $|J_{\mathcal{DA}}|^2$ reaching unrealistically high values, the rates obtained from the dynamical simulations tend to the value of ~ 5 ps^{-1} (~ 200 fs), as limited by the vibrational relaxation.

Figure 4.8 shows time-resolved emission spectra calculated for the DANS-NR pair for $V = 0.02$, 0.1 and 1 eV using the same machinery described in section 4.3.1. Figure 4.9 shows emission spectra at selected times (in the legends) for the same systems. For weak coupling ($V = 0.02$ eV, panel **a** in both figures 4.8 and 4.9) emission initially comes from the (excited) donor and oscillates in time following its coherent vibrational relaxation, reaching the steady state emission well before 1 ps. Hence, the spectrum smoothly evolve from the steady state $\mathcal{D}$ emission to the steady state $\mathcal{A}$ emission. Indeed, after ~ 50 ps, only the $\mathcal{A}$ spectrum survives. In panels **b** and **c** of figure 4.9 steady state emission of the donor and the acceptor are also reported for reference as black dashed and dotted lines, respectively. Specifically, emission of the weakly coupled system (panel **a**) at 1 ps and 50 ps are respectively used as steady state emission of the donor and acceptor. For $V = 0.1$ eV (panels **b**) RET starts before the complete relaxation of the donor towards its Kasha state, as proven by the fact that the spectrum never coincides with steady state $\mathcal{D}$ emission (black dashed line) and in 5 ps the whole population is transferred to the acceptor. For stronger coupling ($V = 1$ eV, panels **c**), the situation is different. The whole process occurs very fast (~ 200 fs) and energy is transferred to the acceptor from the *hot* states of the donor during the very first coherent vibrational oscillations. Moreover, the spectra cannot be considered as the simple sum of $\mathcal{D}$ and $\mathcal{A}$ spectra: in the strong coupling regime, the interaction between the two dyes heavily affects their properties. The spectra are therefore strongly perturbed, and, even after RET completion, the spectrum does not match the steady state spectrum of $\mathcal{A}$.

While the Förster model leads to the correct V-dependence of the RET rates at least in the weak coupling regimes, it does not allow to appreciate subtle phenomena related to the details of the vibronic spectrum. The bottom panel of figure 4.10 shows the variation of RET rates calculated for a system with $V = 0.03$ eV and where the $z_{\mathcal{D}}$ parameter is varied

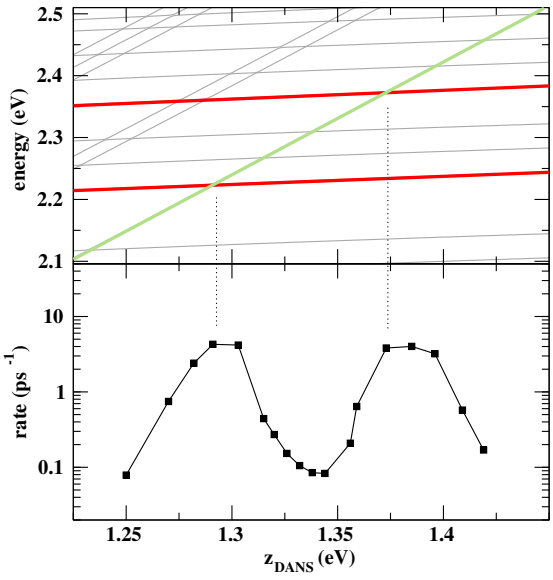

Figure 4.10: Vibronic energies (top panel) and RET rate (bottom panel) as a function of $z_{\mathcal{D}}$ for the DANS-NR pair with V=0.03 eV. In the top panel, thicker curves highlight the energies of the most important states involved in the dynamics, namely the Kasha's state for the excited energy donor $\mathcal{D}^*$ (green) and the excited energy acceptor $\mathcal{A}^*$ with two and three vibrational excitations (red).

(simulating, e.g., the effect of a local electric field), as to affect the alignment of vibronic states. A non-monotonous behavior is observed, with two orders of magnitude variations of the rates (fitting parameters reported in table 4.3). To understand the physical origin of this phenomenon, in the top panel of the same figure the $z_{\mathcal{D}}$-dependence of relevant vibronic energies is reported. RET rates are particularly large when the energy of the long-lived Kasha's state of $\mathcal{D}$ (green line), the states from where RET occurs in the weak coupling regime, crosses states in the manifold relevant to the excited $\mathcal{A}$ with either two or three vibrational excitations (red lines), the states that mainly receive the energy. A very clear energy resonance effect is observed affecting the RET rates and highlighting the prominent role of vibronic state alignment, fully in line with recent experimental results.[62, 230]

4.3.3 The RET-exciton crossover

The presented model, that naturally encompasses energy delocalization in homodimers and energy transfer in heterodimers, can be exploited to address the crossover regime. A first observation is that in aggregates a paramount role is played by the sign of the intermolecular interaction, V, that distinguishes J- and H-aggregates. On the opposite, the sign of V does not enter the Förster rate equation. This qualitative difference is easily understood: when energy delocalizes between two equivalent molecules, the sign of the interaction defines the relative energy of the in-phase and out-of-phase combinations of the two states where the excitation resides on either molecule. When the molecules are not equivalent, instead, the order of the excited states is governed by the energy difference between the two local excitations, the contribution from intermolecular interactions being marginal in most cases.

To investigate the crossover regime, increasingly asymmetric dimers are considered, adopting the Hamiltonian in eq. 4.1 and NR parameters in table 4.1, but assigning a different z value to one of the two molecules. The asymmetry is then defined by $\Delta z_{12} = z_2 - z_1$ (where z_1 is kept fixed, while increasing z_2). The global population of the states with the excitation residing on molecule 1 is chosen as the relevant observable and is defined as:

$$\begin{aligned}\hat{P}_{M_1^*} =& \bar{\rho}_1 |N_1\rangle\langle N_1| + (1-\bar{\rho}_1)|Z_1\rangle\langle Z_1| \\ &- \sqrt{\bar{\rho}_1(1-\bar{\rho}_1)}(|N_1\rangle\langle Z_1| + |Z_1\rangle\langle N_1|)\end{aligned} \tag{4.31}$$

where $\bar{\rho}_1 = \langle\phi_1|Z_1\rangle\langle Z_1|\phi_1\rangle$ and $|\phi_1\rangle$ is the ground state of the dimer Hamiltonian. Figure 4.11 shows the time-evolution of $\langle P_{M_1^*}\rangle$ calculated for asymmetric NR dimers with different Δz_{12} values and with positive and negative interactions and different values of $|V|$.

When a large V value is considered ($|V| = 0.8$ eV), its sign makes a difference only for small asymmetry parameter, where basically the system behaves as an aggregate, with almost perfect delocalization $P_{M_1^*} \sim 0.5$. In this case the delocalization is slightly favored for negative V. For larger asymmetry, the system behaves as a RET pair, with the excitation localizing on the molecule with the lowest excitation energy, acting as the energy acceptor. The sign of V in this case only affects

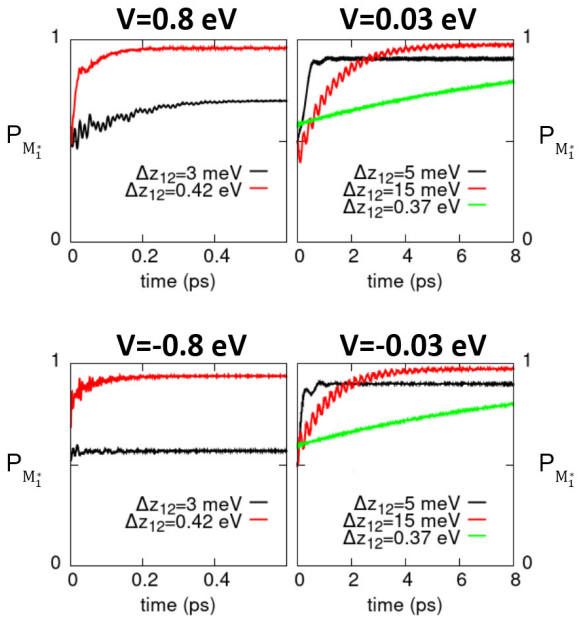

Figure 4.11: Results for NR asymmetric dimers (molecular parameters in table 4.1, with the z value of molecule 2 increased by an amount Δz_{12}). Time evolution of the global population of molecule 1 ($P_{M_1^*}$, lower lying energy molecule) for different V values and Δz_{12}.

the very early time dynamics, when the relative phase of states with the excitation on either sites is relevant. For smaller V ($V = 0.03$ eV in the figure) the exciton delocalization regime is not regained, except for vanishing asymmetry.

4.4 Conclusions

Electrostatic interactions drive energy fluxes in assemblies of either nonequivalent or equivalent molecules. Well-established approaches to describe energy fluxes are available and proved successful, namely the Förster model for RET and the exciton model for energy delocalization. However, both models only rely on a limited basis, that only comprises states with a single excitation, and then only apply in the weak intermolecular coupling regime. The interplay between energy fluxes and molecular vibrations leads to some interesting but complex physics that requires a non-adiabatic approach to the coupled electron-vibration problem. Against this background, the simple model in eq. 4.1 unifies RET between different molecules and energy delocalization among identical molecular units, explicitly accounting for molecular vibrations. If the dipolar approximation is used and ultraexcitonic terms are neglected, the proposed model maps either into the standard exciton model (for equivalent molecules) or into the Förster model (for different molecules). Explicitly accounting for energy dissipation, by coupling the supramolecular system to an external bath, allows to follow the time-evolution of the system as needed to calculate time-dependent properties and spectra.

The proposed model is applied to both J and H molecular dimers. Particularly interesting results are obtained for H-aggregates where the lowest excited state is a dark state that, despite being optically inactive, is populated as a result of the system relaxation. This demonstrates that a reliable model for energy dissipation properly describes how the system transfers population between states with different symmetry. At

the same time, however, the overall symmetry of the system is preserved, as demonstrated e.g. by the exact vanishing, along the whole relaxation trajectory, of the expectation value of the antisymmetric vibrational coordinate, $\langle \hat{Q}_- \rangle$.

The subtle interplay between electronic and vibrational degrees of freedom is responsible in H-aggregates for a fast decoherence of vibrational motion. Another important result is obtained again for H-aggregates. In particular, the PES relevant to the lowest excited state shows a double minimum, pointing to an intrinsic instability of the dimer towards symmetry breaking (i.e., excitation energy localization). Of course, localization is only possible in the presence of the coupling to a slow coordinate (e.g., a polar solvent). The proposed model confirms this result: the relaxation dynamics of the dimer occurs along the ridge that separates the two minima, thus excluding any localization. However, large fluctuations of the system are observed, showing how the system equally visits the regions of the two minima. This dynamical effect (similar to the well-known dynamic Jahn-Teller effect[78]) requires additional studies of optical spectra of these systems, to single out experimental signatures of the phenomenon.

Resonance energy transfer is then addresses: the model applies in the weak-coupling regime, where, in line with the Förster model, RET occurs from the relaxed $\mathcal{D}^*$ state, but it also describes the strong coupling regime, where the transfer is effective well before the complete $\mathcal{D}^*$ relaxation. In this regime, RET rates obtained from a fitting of the dynamical simulation results differ from those obtained with the Förster theory.

The model naturally lends itself to address increasingly asymmetric dimers. In particular, in the strong coupling regime and for small asymmetries Δz_{12}, a negative V value favors energy delocalization, thus making the dimer behave like an aggregate. Further increasing the asymmetry Δz_{12}, the dimer becomes a RET pair.

The firm basis set on this chapter opens the way to several possible future steps, the most challenging and interesting being the inclusion of the effects due to a polar environment (e.g., a polar solvent). Indeed, the photophysics of supramolecular assemblies can be strongly affected by the interactions with the surroundings.[244, 245] Moreover, having a fully dynamical picture of symmetry breaking induced by solvation effects in photoexcited dimers and RET among aggregates would be of paramount importance in the development of new functional materials.[246]

Chiral squaraine aggregates: chiroptical spectra beyond the exciton model

5

Squaraine dyes are a well known and widely investigated family of organic chromophores with unique spectral properties.[170, 247–256] They are characterized by a rigid inner core, the squaraine ring, with a strong electron affinity and, typically, two equivalent electron-donating groups are attached to the inner core in a centrosymmetric D-A-D structure. So called quadrupolar DAD (or ADA) dyes are often unstable towards symmetry breaking either in the excited state (class I quadrupolar dyes) or in the ground state (class III quadrupolar dyes), a phenomenon that shows up most clearly in fluorescence or absorption solvatochromism, respectively.[170] Squaraines are the most famous representatives of the elusive family of quadrupolar dyes of class II, and resist symmetry breaking in either the ground or excited state, as a result of a strong conjugation among the D and A molecular moieties. They show intense, narrow and marginally solvatochromic absorption and fluorescence bands, typically in the red portion of the spectrum, that can be moved to the near infrared region by a judicious choice of the D groups.[11, 257–260] Moreover, at roughly twice the energy of linear absorption, a state is found, dark to linear absorption, but with a large (resonantly enhanced) two photon cross-section.[170] Squaraine dyes are investigated and exploited for NLO applications,[248] bioimaging,[261] biosensing[262] and photodynamic therapy.[263, 264] Another interesting applicative field for squaraine dyes is found in solar cells,[265–267] where most interesting results are obtained with squaraine aggregates that show an amazing panchromatic absorbance spectrum.[260, 268–275]

Squaraine aggregates are fascinating systems, attracting interest not just for their panchromatic spectrum, but also for amplified NLO responses,[276] and for large chiral responses.[6, 277, 278] Modeling squaraine aggregates is challenging as the intertwined role of electrostatic (ES) intermolecular interactions, intra and intermolecular charge transfer (CT) and disorder must be taken into account. In a series of papers, [169, 206, 274, 279] Spano and Collison first proposed that the panchromatic absorption spectrum of squaraine aggregates is due to intermolecular CT interactions, a hypothesis recently supported by detailed spectroscopic measurements in squaraine crystals.[280] The same hypothesis was very recently challenged in a paper where linear absorption and pump-probe spectra of squaraine aggregates are discussed in the framework of a disordered exciton model.[281]

In this complex and intriguing scenario, in this chapter chiroptical properties of a series of chiral squaraine aggregates are addressed. Specifically, a family of anilino squaraine dyes decorated with chiral pendants bearing alkyl chains of different length is investigated and theoretical modeling is exploited in an attempt to unveil the physics underlying the observed peculiar experimental features. The dyes aggregate in solution forming chiral superstructures that, depending on the length of the terminal

The work presented in this chapter is published in *J. Mater. Chem. C, 11,* 8307-8321, **2023**, where additional details on the experimental characterization can be found, together with a Molecular Dynamics study of the structure of the aggregates.

alkyl chain, show distinctively different behavior. Aggregates of dyes decorated with alkyl chains with intermediate length (from C6 to C10) show two features in absorbance spectra: the first one at 500-550 nm is located to the blue with respect to the monomer absorption (at 640 nm) and the second one, in the 700-800 nm spectral region, is strongly red-shifted vs the monomer absorption. Quite interestingly, a bisignated signal appears in the CD spectrum in correspondence of both features. In aggregates formed by dyes with either shorter (C3-C5) or longer (C11, C12, and C16) pendants, instead, the features at long wavelength become extremely weak and almost disappear.

This complex experimental scenario will be discussed adopting an essential state model (ESM) approach,[170] describing each squaraine dye in terms of three basis states, leading to a molecular model that reliably describes the spectral properties of the isolated dye.[170, 282] A first model for the aggregate, the ESM-ES, is then built accounting just for ES interactions among the dyes, much as in the standard exciton model. ESM-ES results are compared with the ones obtained with the standard exciton model. The pictures emerging from the two models are qualitatively similar, suggesting that the experimental data can be accounted for in terms of the coexistence of H- and J-aggregates in the system.

Following the original suggestion from Spano and Collison,[169, 206, 274, 279] the model is then extended to also account for intermolecular CT interactions (ESM-CT model). In such a picture, the highly non-trivial problem of calculating CD spectra in an aggregate with electrons delocalized among different molecular units has to be faced. Towards this aim, the spinless-Fermion approximation adopted by Spano and Collison is released and the explicit expression for the rotational strengths in aggregates with delocalized electrons originally proposed in ref.[283] is exploited. In the ESM-CT approach, the experimental observation of two features in absorption spectra and two exciton couplets in CD spectra can be rationalized accounting for a single aggregate structure, an appealing result, as it does not require the somewhat ad hoc hypothesis of two families of aggregates. However, the model cannot describe the behavior of systems with short or very long alkylic chains that show a single dominant feature either in absorption or CD spectra.

While a firm conclusion on the structure of the chiral aggregates of squaraine dyes is hardly reached, the discussion sets the basis for a thorough understanding of the physics of chiral aggregates. In any case, the origin of the two bands as related to a Davydov splitting can be excluded, strongly suggesting that the panchromatic spectrum seen in squaraine films implies the presence of more subtle phenomena.

The chapter is structured as follows: in section 5.1 an overview of available experimental data is given and in section 5.2 the essential state model for an isolated quadrupolar dye is briefly presented. In section 5.3 the aggregation problem is addressed accounting for purely electrostatic intermolecular interactions (ESM-ES approach), together with a comparison with the results obtained with the exciton model. In section 5.4 the model is extended to intermolecular charge transfer (ESM-CT approach) and, finally, section 5.5 concludes the chapter.

5.1 Experimental data

The different proline-derived squaraine dyes (ProSQs, molecular structure in panel **c** of figure 5.1), which differ in the terminal alkyl chain length (C3 to C12 and C16), were investigated for their aggregation behavior in poor solvent titration experiments. Experimental absorbance and CD spectra of colloidal (*S*,*S*)-ProSQ aggregates having an alkyl chain length of C5, C10 and C12 in varying ratios of the poor solvent methanol-water mixture are plotted in figure 5.1. These compounds are representative for

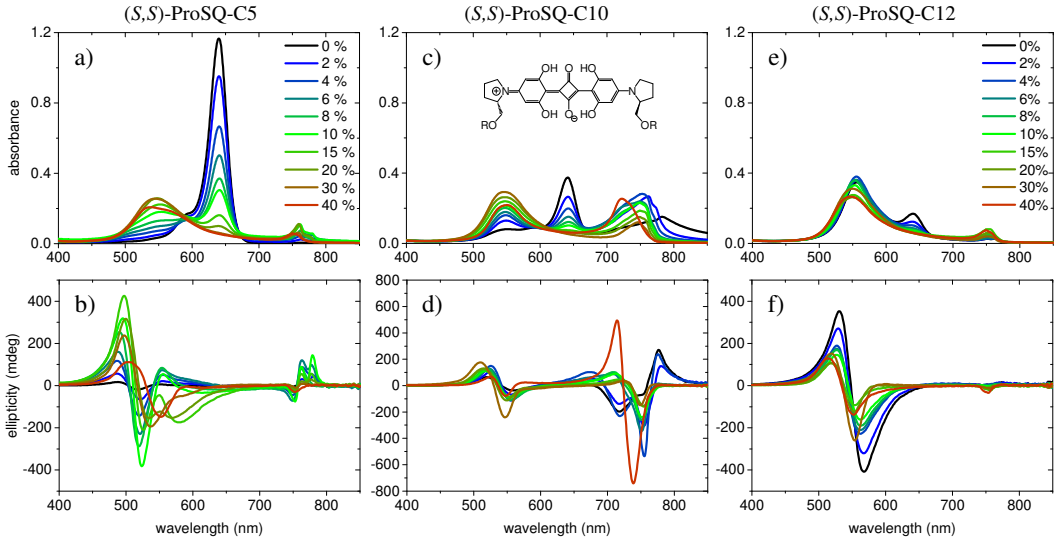

Figure 5.1: Experimental UV/Vis absorbance spectra (top row) and corresponding ellipticity spectra (bottom row) for selected (*S*,*S*)-ProSQ compounds with varying alkyl chain lengths: C5 in **a** and **b**, C10 in **c** and **d**, and C12 in **e** and **f**. The inset in **c** sketches the molecular structure were R denotes the varying alkyl chain. The legend indicates the volume-percentage of water in the methanol-water mixture used as bad solvent (good solvent being chloroform) and applies for all plots.

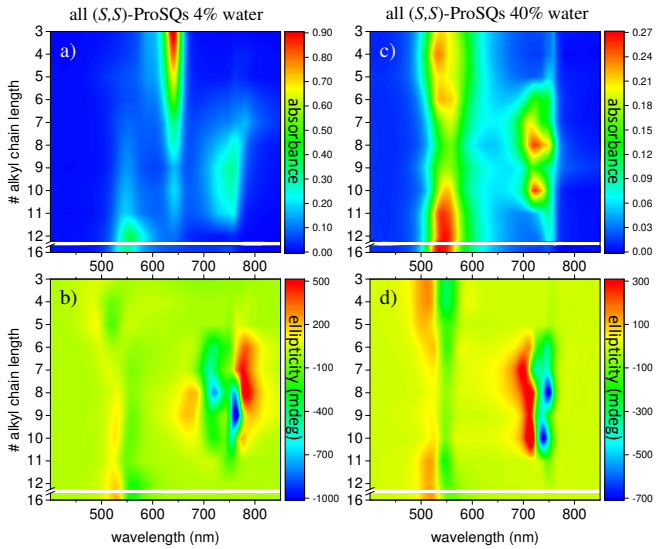

Figure 5.2: UV/Vis absorbance spectra (top row) and corresponding ellipticity spectra (bottom row) in a 2D representation of all (*S*,*S*)-ProSQ compounds with varying alkyl chain lengths (C3 to C12 and C16) for two selected volume-percentages of water in the methanol-water mixture: 4 % in **a** and **b** and 40 % in **c** and **d**.

Experimental data presented in section 5.1 and in appendix B were recorded by Marvin F. Schumacher and Dr. Jennifer Zablocki in the lab of prof. Arne Lützen, University of Bonn.

the different aggregation regimes, data for the entire series of molecules are reported in appendix B. The C10 compound has an intermediate alkyl chain length and expresses two pronounced aggregate absorbance bands with two corresponding bisignate CD bands (panels **c** and **d**). These aggregate absorbance bands are blue- and red-shifted with respect to the monomer absorbance band peaking at 640 nm. Both for the C5 and the C12 compounds, the blue-shifted aggregate absorbance and CD features are largely dominant (panels **a** and **b**, and **e** and **f**, respectively). The overall aggregation tendency increases with increasing chain length, which is indicated by the reduction of the molecular absorbance band already in the initial pure methanol solvent. Therefore, the predominant expression of blue-shifted spectral features is neither simply correlated with alkyl chain length nor with aggregation tendency. The dissolved monomers do not have a corresponding CD feature since the stereogenic carbon atoms are located on the pyrrolidine rings carrying the alkyl chains, and is not conjugated with the chromophoric squaraine backbone. The circular dichroism of the aggregate arises from the chiral arrangement of the squaraine backbones directed by the chiral alkyl chains.

The two-dimensional representation of absorbance and CD spectra for all (*S*,*S*)-ProSQ compounds for two selected methanol-water mixing ratios are shown in figure 5.2 to give a better impression of the different aggregation regimes. For a lower water fraction of 4 vol% (panels **a** and **b**) there is a dominant blue-shifted bisignate CD response for both the shorter (C3 to C5) and the longer (C11, C12, C16) alkyl chain compounds, while the intermediate alkyl chain length (C6 to C10) compounds form more pronounced red-shifted bisignate CD response. Interestingly, the red-shifted CD signatures are not smoothly bisignate in shape but express more detailed spectral features. For a higher water fraction of 40 vol% (panels **c** and **d**) nearly no molecular dissolved compounds are left. The bisignate blue-shifted CD response for the shorter and longer alkyl chain compounds gains signal strength and maintains the signs of the band, while the red-shifted CD features of the intermediate alkyl chain length compounds become less detailed and the bisignate shape becomes more evident, with an inverted sign with respect to panel **b**.

5.2 Model for the isolated molecule

All molecules of interest have the same chromophoric core, and only differ for the different length of the alkyl pendants. The spectral properties of the isolated molecules in the visible region are not affected by the length of the pendants, as best recognized looking at the absorption spectrum, where the monomer absorption is seen in all cases as a narrow band at 640 nm. The chiral groups, while instrumental to guide the aggregate into chiral supramolecular structures, do not affect the spectral properties of the non-aggregated molecules, that do not show any CD response. The model for the isolated molecule can therefore be defined and parametrized only accounting for the main chromophoric part.

Low-energy spectral properties of squaraine dyes are well-captured by an essential state model (ESM) that only accounts for three electronic states.[170, 282] The three basis (diabatic) states correspond to the main resonating structures, a neutral (DAD) state, $|N\rangle$, and two degenerate

zwitterionic states (D^+A^-D and DA^-D^+) $|Z_1\rangle$ and $|Z_2\rangle$. The zwitterionic states are separated from the neutral state by an energy gap $2z_0$ and are coupled to the neutral state by a mixing matrix element $-\tau$. Vibronic coupling is marginally relevant in squaraines, so that, in view of the complexity of the aggregation problem, it is not addressed. Polar solvation will not be discussed either, as it does not affect the spectral properties of squaraines that have and maintain a centrosymmetric (hence non-polar) structure both in the ground and excited states.[170] The molecular Hamiltonian reads:

$$\hat{h} = 2z_0\hat{\rho} - \tau\hat{\sigma} \tag{5.1}$$

with

$$\begin{aligned} \hat{\rho} &= \sum_{k=1,2} |Z_k\rangle\langle Z_k| \\ \hat{\sigma} &= \sum_{k=1,2} (|N\rangle\langle Z_k| + |Z_k\rangle\langle N|) \end{aligned} \tag{5.2}$$

Finally, the molecular dipole moment is aligned along the long molecular axis and its magnitude is measured by the operator:

$$\hat{d} = \mu_0(|Z_1\rangle\langle Z_1| - |Z_2\rangle\langle Z_2|) \tag{5.3}$$

where μ_0 is the equal and opposite permanent dipole moment associated with the zwitterionic forms, $|Z_1\rangle$ and $|Z_2\rangle$.

Accounting for symmetry helps to understand the photophysics of squaraines:[170, 256] the two zwitterionic states can in fact be mixed into a symmetric $|Z_+\rangle$ and an antisymmetric $|Z_-\rangle$ combination. The $|N\rangle$ and $|Z_+\rangle$ states are mixed into a ground $|g\rangle$ and a symmetric excited $|e\rangle$ state, while $|Z_-\rangle$ stays unmixed, as sketched in figure 5.3. The lowest energy excitation $|g\rangle \rightarrow |Z_-\rangle$ is active in one-photon absorption, while the higher energy excitation $|g\rangle \rightarrow |e\rangle$ is seen in two-photon absorption. The model parameters for squaraines can be fixed to best reproduce the position of one and two photon absorption band. Specifically, the one and two photon transition energies $\hbar\omega_c$=1.93 eV and $\hbar\omega_e$=3.04 eV, respectively,[282] allow to fix τ= 1.04 eV and z_0=0.4 eV. Finally, the experimental transition dipole moment, μ_c=12.5 D[282] fixes μ_0=20.83 D. This corresponds to a dipole length $a \sim 4.33$ Å, that is assigned as the effective length of each D-A arm (see figure 5.4). The parametrization of the electronic Hamiltonian against solution data ensures that it implicitly accounts for the effect of the medium refractive index:[17] the marginal variability of the refractive index in common organic solvents and, more generally, in organic media, allows to adopt environment independent model parameters to describe dyes in organic media.[17, 135, 284]

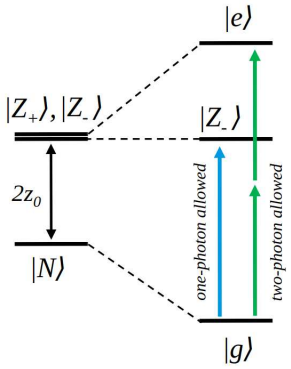

Figure 5.3: Diabatic (left) and adiabatic (right) states for a quadrupolar dye.

5.3 Simulations of the spectral properties of aggregates: the ESM-ES approach

The alkyl pendant and the chiral groups play a fundamental and specific role in guiding the geometry of the supramolecular assemblies formed upon aggregation in poor solvents. This specific role is recognized in the distinctively different spectral properties of the aggregates formed

by dyes with alkyl chains of different length (figures 5.1, 5.2), and by the opposite sign of the CD spectra collected from aggregates formed by enantiomeric species. As stated above, the tendency to aggregate is amplified in systems with longer chains. Specifically, signatures of aggregation are seen already in pure methanol solvent for pendants longer than C7, while for C16 only the aggregated form is observed. In any case, the spectral properties of the aggregates in the visible region are dominated by the chromophoric cores and their interactions.

As it was done in chapter 4 for dipolar dyes, the essential state model for quadrupolar dyes proposed in the previous section is here extended to aggregates accounting for electrostatic (ES) intermolecular interactions (ESM-ES approach). In the same spirit as in chapter 4 (where the topic is discussed in details), a comparison with the results of the simpler exciton model is also proposed.

5.3.1 The exciton model

As extensively discussed in chapter 3, the exciton (or Kasha) model[190, 212] is widely and successfully applied to describe linear spectral properties of molecular aggregates. Briefly, the basic assumption of the exciton model is that electrons are localized on each molecular unit, so that only ES intermolecular interactions are accounted for and are usually dealt with in the dipolar approximation. In the standard version of the exciton model, molecules are described in terms of a single excited state with frequency ω_c, so that the number of states bearing a single excitation is equal to N, the number of molecules in the aggregate. Finally, the interactions between non-degenerate states are neglected, so that the exciton Hamiltonian is defined on the N degenerate states bearing a single excitation. As highlighted in chapter 4, this approximation amounts to neglect the molecular polarizability.[85, 174, 207] In other terms, when the molecules are brought together in the aggregate, the exciton model neglects any interaction with the surrounding molecules apart from the exciton delocalization. This is a good approximation for poorly polarizable molecules or, equivalently, when the excitation energy is much larger than intermolecular interactions, but is expected to fail for aggregates of largely polarizable molecules with low-lying excitations, like squaraines.[85, 86, 174, 206, 207, 285]

As stated above, electrostatic intermolecular interactions are typically introduced in the dipolar approximation so that the interaction between the two states where either molecule i or j is in the excited state reads:

$$J_{ij} = \frac{\mu_c^2}{4\pi\varepsilon_0\eta^2 d_{ij}^3} G_{ij} \tag{5.4}$$

where μ_c is the transition dipole moment of the isolated dye, ε_0 is the vacuum dielectric constant, η is the medium refractive index and G_{ij} is a purely geometric factor that only depends on the distance and relative orientation of the transition dipole moments on the two molecules:

$$G_{ij} = \vec{e}_i \cdot \vec{e}_j - 3(\vec{e}_i \cdot \vec{e}_{ij})(\vec{e}_j \cdot \vec{e}_{ij}) \tag{5.5}$$

where $\vec{e}_i$ is the unit vector parallel to the dipole moment on molecule i and $\vec{e}_{ij}$ is the unit vector associated with the $i-j$ direction.

To address absorption spectra, transition dipole moments must be calculated from the ground state (the state where all molecules are not excited) and the ϕ_k eigenstates. To do so, the total dipole moment operator is defined as the vectorial sum of the molecular dipole moment operators, so that the transition dipole moment and the rotational strength for the k-th exciton transition are easily expressed on the basis of the transition dipole moments on each dye and their relative orientation and positions.[286] Since in the exciton model the dimension of the relevant subspace is equal to N (the number of dyes in the aggregates) very large aggregates, easily up to thousands dyes, can be addressed.

5.3.2 The ESM-ES Hamiltonian

ESMs for polar and multipolar dyes lend themselves quite naturally to address ES intermolecular interactions in molecular aggregates, releasing the main approximations of the exciton model.[84, 85, 207, 276, 287] Specifically, modeling aggregates of DAD dyes the dipolar approximation is released and each molecule is described in terms of a ground and two excited states. More interestingly, however, since intermolecular interactions are defined on the diabatic basis, the resulting model fully accounts for the molecular polarizability, allowing the charge distribution on each dye to readjust in response to the ES potential generated by the surrounding molecule.[85, 174, 207, 287] As in the exciton model[190, 212], in this section the overlap between frontiers molecular orbitals of different molecules is neglected, so that electrons are fully localized on each squaraine unit and intermolecular interactions are just ES in origin. The basis set relevant to the aggregate is then the direct product of the three basis states of each dye, for a grand-total of 3^N states. This limits the dimension of aggregates that can be reasonably dealt with to ~ 9. The Hamiltonian for the aggregate reads:

$$\hat{H} = \sum_i \hat{h}_i + \sum_{i>j} \sum_{p,q} V_{ip,jq} \hat{q}_{i,p} \hat{q}_{j,q} \tag{5.6}$$

where the first term is the sum of the molecular Hamiltonians in eq. 5.1, with i running on the molecules. The second term accounts for ES intermolecular interactions, with i and j running on the molecules, and p and q on the three sites (D, A, D) of each molecule. The three operators measuring the charge on each site of the i-th molecule are:

$$\begin{aligned} \hat{q}_{i,1} &= |Z_1^i\rangle\langle Z_1^i| \\ \hat{q}_{i,2} &= -|Z_1^i\rangle\langle Z_1^i| - |Z_2^i\rangle\langle Z_2^i| \\ \hat{q}_{i,3} &= |Z_2^i\rangle\langle Z_2^i|. \end{aligned} \tag{5.7}$$

Finally, the ES interaction between unit charges residing on site p of molecule i and site q of molecule j is

$$V_{ip,jq} = \frac{1}{4\pi\varepsilon_0\eta^2} \frac{1}{|\vec{r}_{ip} - \vec{r}_{jq}|} \tag{5.8}$$

where $\vec{r}_{ip}$ is the vector that defines the position of the i,p site and η is the effective refractive index, accounting for the medium refractive index and for the screening due to electrons not explicitly accounted for in the model.

5.3.3 Calculation of absorption and CD spectra

To calculate absorption spectra in either the exciton or the ESM-ES model, the dipole moment operator for the aggregate $\hat{\vec{D}}$ is defined as the vectorial sum of molecular dipole moments $\hat{\vec{d}}_n$. The transition dipole moment from the ground state $|\psi_0\rangle$ to state $|\psi_i\rangle$ is finally obtained as needed to calculate the linear absorption spectrum following the sum over states expression:

$$Abs(\omega) = \frac{1}{N}\hbar\omega \sum_i e^{-\frac{\hbar\omega-\hbar\omega_i}{2\sigma^2}} |\langle\psi_i|\hat{\vec{D}}|\psi_0\rangle|^2 \tag{5.9}$$

where N is the number of molecules in the aggregate and $\hbar\omega_i$ is the energy of the $|\psi_0\rangle \rightarrow |\psi_0\rangle$ transition A Gaussian bandshape with standard deviation σ is assigned to each transition. $\sigma = 0.04$ eV is used in this chapter.

The rotational strength, defining the intensity and sign of each feature in the CD spectrum, is:

$$R_i = \Im\{\langle\psi_0|\hat{\vec{M}}|\psi_i\rangle \cdot \langle\psi_i|\hat{\vec{D}}|\psi_0\rangle\} \tag{5.10}$$

where $\Im\{...\}$ takes the imaginary part and $\hat{\vec{M}}$ is the magnetic dipole moment operator. Since for both the exciton and the ESM-ES model electrons are localized on each molecular unit, following Condon[288, 289] the rotational strength can be evaluated as:

$$R_i \propto \sum_{m\neq n} (\vec{r}_n - \vec{r}_m) \cdot \langle\psi_0|\hat{d}_n|\psi_i\rangle \wedge \langle\psi_i|\hat{d}_m|\psi_0\rangle \tag{5.11}$$

where $\vec{r}_m$ is the position vector of the m-th molecular site. CD spectra are then calculated as:

$$CD(\omega) = \frac{1}{N} \sum_i e^{-\frac{\hbar\omega-\hbar\omega_i}{2\sigma^2}} R_i. \tag{5.12}$$

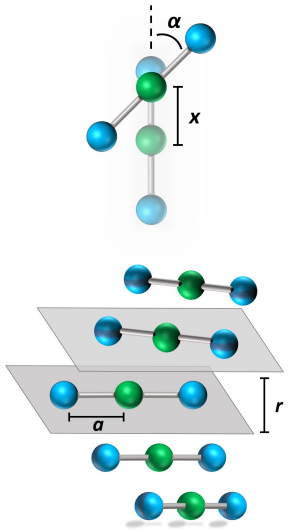

Figure 5.4: Schematic representation of the aggregate geometry. The blue and green spheres represent the electron donor (D) and acceptor (A) sites, respectively. Geometrical parameters are shown: a is the length of the D-A arm, r is the interplanar distance, x is the displacement along the long molecular axis, α is the angle formed by adjacent molecules. Positive and negative α describes left and right handed helices, respectively.

5.3.4 Results

Experimental hints about the structure and dimension of the aggregates are unfortunately lacking. An extensive MD study by L. Grisanti[290] suggested that the chromophoric cores may arrange in helical structures. Figure 5.4 shows a schematic view of the adopted aggregate geometry with the definition of the main geometrical parameters: a is the length of the D-A arm, r the distance between adjacent molecular planes, α the rotation angle between adjacent molecules, and x the displacement of the dyes along the long molecular axis.

The color maps in Fig. 5.5 show absorption and CD spectra calculated for aggregates of N=2, 4 and 8 molecules with the ESM-ES Hamiltonian,

with r=3.5 Å, α=20° (left-handed helix) and variable x (a is fixed to 4.33 Å, as explained in section 5.2). Results for different geometries and different values for η^2, reported in appendix C, demonstrate that different aggregate geometries lead to marginally different spectra, yet maintaining the general picture unaffected.

Comparing results for 4 and 8 sites, the spectra become cleaner, as expected, due to the progressive reduction of finite size effects. Moreover, the splitting between the positive and negative peaks in the CD spectrum reduces when going from 4 to 8 sites, an effect that is more pronounced at small x. Nevertheless, the overall picture is only marginally altered and the main qualitative features of a large aggregate are already captured

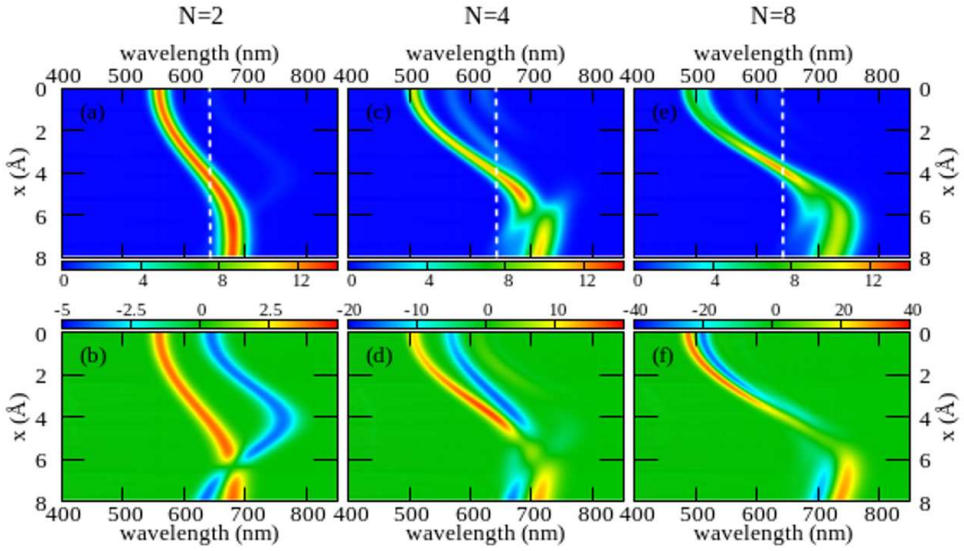

Figure 5.5: Spectral properties of squaraine aggregates described in the ESM-ES approach (model Hamiltonian in eq. 5.6). Molecular parameters: z_0=0.4 eV, τ=1.04 eV, a=4.33 Å. Results are shown for aggregates of 2, 4 and 8 molecules with r=3.5 Å and α=20°. The color maps show the absorption intensity (top panels) and the CD intensity (bottom panels) plotted against the wavelength (horizontal axis) upon varying x (vertical axis). All intensities, in arbitrary units, are normalized to the number of molecules. Notice the different scale adopted for the CD intensity in the three bottom panels to account for the superlinear amplification of CD intensity with aggregate size.

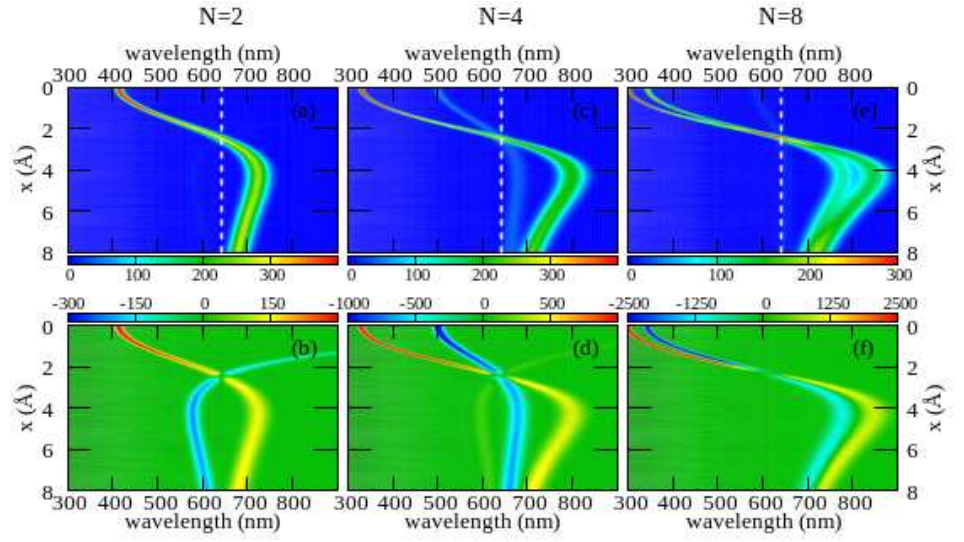

Figure 5.6: Results for aggregates of 2, 4 and 8 molecules obtained in the standard exciton model for the same geometries as in figure 5.5 and setting the molecular parameters entering the model as ω_c=1.93 eV, μ_c=12.5 D (values from ref.[282]). Same quantities as in figure 5.5 are shown. All intensities, in arbitrary units, are normalized to the number of molecules.

for N=4. On the opposite, the dimer leads to a qualitatively different picture. The dimeric model qualitatively captures the behavior of linear absorption, where a single band largely dominates the spectrum, located to the blue of the monomer absorption for small x (H-aggregate geometry) and progressively moving to the red at larger x (J-aggregate geometry). However, the situation changes when looking at CD spectra. In all cases, a bisignated feature appears: at small x, the positive CD feature is observed at higher frequency (shorter wavelength, as expected for a left-handed H-aggregate), while at large x (when moving to a J-aggregate structure) the sign of the CD doublet reverses.[217] The CD signal for the dimer is qualitatively different from the one obtained for longer aggregates. For a dimer in fact the positive and negative CD signatures are seen at the frequencies of the upper and lower exciton states, so that the distance between the two peaks amounts to twice the exciton coupling. In bigger aggregates, instead, the exciton couplet involves nearby states close in energy to either the highest energy states in the exciton band (H-aggregates) or to the lowest energy states in the exciton band (J-aggregates). Therefore, the distance between the positive and negative peaks is not a measure of the exciton splitting in aggregates with $N > 2$.[217] A lesson is learned here: dimeric models work reasonably well to describe linear absorption spectra, but they are misleading when applied to CD spectra. Another interesting observation concerns the intensity of the spectra. Absorption and CD intensities in Fig. 5.5 are normalized to the number of sites. As expected, the normalized absorption intensity is roughly constant upon increasing the aggregate length. On the opposite, the normalized intensity of the CD signals increases fast with N, a result that could explain the very large chiroptical responses reported recently for annealed thin films of proline-derived squaraines with C16 alkyl chain (ProSQ-C16).[278]

It is instructive to compare results from ESM-ES model in figure 5.5 with the results obtained for the same geometries in the standard exciton model in figure 5.6. The two sets of results share some similarity, with a single main absorption peak and a single main bisignated signature in CD spectra. Moreover, as expected, in both models the absorption peak is located to the blue of the monomer absorption for superimposed or almost so molecules (small x in figure 5.4, H-like aggregates) while it is located to the red of the monomer absorption for largely displaced molecules (large x in figure 5.4, J-like aggregates). However, some important differences between the two models can be pointed out. In the exciton model the switch from H- to J-aggregate behavior occurs for $x \sim 2.5$Å, while much larger values are needed in the ESM-ES model ($x \sim 6$Å). In the exciton model, the molecular polarizability is disregarded, so that the position of the absorption band vs the monomer absorption is determined only by the sign of the intermolecular electrostatic interactions, positive for H-aggregates (blu-shifted absorption) and negative for J-aggregates (red-shifted absorption). Since, as recently discussed,[217, 291] for fixed helicity the sign of the CD doublet depends on the sign of intermolecular interactions, in the exciton model the sign of the bisignated signature in the CD spectrum reverses precisely at the same x value where the absorption band cohincides with the monomer absorption (i. e. intermolecular interactions equal to zero, the crossing point from H- to J-behavior). The situation is more complex in the ESM-ES model, where the molecular polarizability is fully accounted for so that the charge distribution on

each molecular unit rearranges in response to the presence of surrounding molecules. Accordingly, the reference absorption frequency of the monomer does not coincide with the one observed for the isolated dye and the position of the absorption peak of the aggregate cannot be only ascribed to the sign of the interaction. Just for the sake of simplicity, let's focus on the dimer case (left panels of figure 5.5): the sign of the CD spectrum reverses at $x \sim 6$Å, unambiguously suggesting that the sign of the intermolecular interaction is positive for $x < 6$Å, and negative for $x > 6$Å. This apparently contrasts with the observation of a red-shifted absorption in the region of x comprised between 4 and 6 Å. Indeed this is the strange region of *non-fluorescent J-aggregates* (or *red-shifted H-aggregates*) corresponding to a region where the blue-shift associated with repulsive intermolecular interactions is overcompensated by the red-shift of the monomer absorption as due to the rearrangement of the charge distribution occurring in each polarizable molecule in response to the electric potential generated by the surrounding molecules.[86, 206, 207, 292] How ESMs relax the approximations of the exciton model accounting for the molecular polarizability is discussed in details in chapter 4.

As noticed above, both the exciton model and the ESM-ES model predict for the dimer a bisignated CD signal whose positive and negative peaks are close to the position of the two Davydov components, so that the CD spectrum is centered at the position of the monomer absorption. For larger aggregates instead, the main CD features are seen in the close proximity of the main absorption band, so that the CD bisignated signal is centered either to the blue or to the red of the monomer absorption in H- or J-aggregates, respectively.[217] These results teach another important lesson: as long as electrons stay localized in each molecular unit, a single main bisignated CD signal is expected for each aggregate geometry. In the hypothesis of localized electrons, the experimental observation of two bisignated peaks in squaraine aggregates therefore rules out the possibility that the red and blue spectral features observed in absorption spectra are related to two Davydov components, that would imply a single bisignated signal in the CD spectrum. This is an important observation as it excludes at least one of the possible scenarios invoked to explain the spectra of squaraine films.[273]

Having a general picture of the spectral properties of an aggregate of squaraine dyes described in the ESM-ES approach, experimental data can be addressed. The observation of two spectral features in both absorption and CD spectra can be rationalized within ESM-ES as due to the formation of large aggregates (at least larger than dimers) where structures with $x = 6 - 8$ Å, responsible for the feature in the red region of the spectrum, coexists with structures with $x \sim 2$ Å, responsible for the spectral feature at ~ 500 nm. Quite interestingly, the feature in the red portion of the spectrum is located very close to the region where the simulated CD feature changes its sign, possibly explaining the large variability of the experimental CD spectrum in this region. Of course, the different intensities of the two spectral features in the aggregates formed by dyes with different side chains could be rationalized in terms of different relative amounts of the two aggregates in the different systems.

5.4 Introducing intermolecular charge resonance: the ESM-CT approach

5.4.1 The ESM-CT Hamiltonian

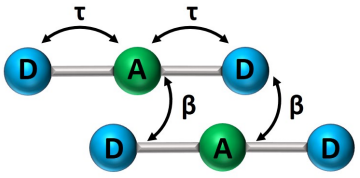

Figure 5.7: A sketch of intramolecular (τ) and intermolecular (β) charge resonance interactions, shown as double-sided arrows, for a pair of adjacent molecules.

In recent years, squaraine aggregates have been extensively investigated by Collison and Spano,[169, 206, 272, 274, 279] who ascribed the fairly complex absorbance spectra of (non-chiral) squaraine films to the presence of charge transfer (CT) interactions among adjacent molecules. Specifically, a sizable overlap between two D-A pairs in nearby molecules, as schematically shown in figure 5.7, was proposed to justify the experimental observations. The films of (non-chiral) anilino squaraines with linear terminal alkyl chains investigated by Collison and Spano show two bands in the absorption spectrum, one to the blue and one to the red of the monomer absorption band, much as in the case investigated here, even if with much broader bandshapes. It is therefore interesting to see if a model accounting for intermolecular CT interactions (ESM-CT) does also apply to the colloidal suspensions of chiral proline-derived squaraine aggregates of interest in this chapter.

The Hamiltonian for N molecules is constructed as a modified Hubbard Hamiltonian accounting on each molecule for three sites (D-A-D) and four electrons. The Hamiltonian reads:[283]

$$\begin{aligned}\hat{H} \;=\; & \sum_{i,p} \varepsilon_p \hat{n}_{ip} + \frac{U}{2} \sum_{i,p} \hat{n}_{ip}(\hat{n}_{ip} - 1) + \frac{1}{2} \sum_{ip,jq} V_{ip,jq} \hat{q}_{ip} \hat{q}_{jq} \\ & - \frac{\tau}{\sqrt{2}} \sum_i \left(\hat{b}_{i1,i2} + \hat{b}_{i2,i1} + \hat{b}_{i2,i3} + \hat{b}_{i3,i2} \right) \\ & - \frac{\beta}{\sqrt{2}} \sum_i \left(\hat{b}_{i2,(i+1)1} + \hat{b}_{(i+1)1,i2} + \hat{b}_{i3,(i+1)2} + \hat{b}_{(i+1)2,i3} \right)\end{aligned} \tag{5.13}$$

where i, j run on the N molecules (apart from the last term, where the sum is truncated at $N-1$), and p, q run on the three sites on each molecule. The operator that counts the electrons on the p site of the i-th molecule is $\hat{n}_{i,p} = \sum_\sigma a^\dagger_{i,p,\sigma} a_{i,p,\sigma}$, where $a_{i,p,\sigma}$ and $a^\dagger_{i,p,\sigma}$ annihilate and create, respectively, an electron with spin σ on relevant site. The auxiliary hopping operator is also defined $\hat{b}_{ip,jq} = \sum_\sigma a^\dagger_{i,p,\sigma} a_{j,q,\sigma}$ that destroys an electron on site j, q and creates an electron on site i, p. The energy of the p site on each molecule is ε_p, while U (site-independent for the sake of simplicity) is the energy required to put two electrons on the same site. The intra and intermolecular electron hopping are described by τ and β, respectively. Finally, ES interactions are described by the last term in the first row: the operators measuring the charge on each site are $\hat{q}_{i,p} = 2 - \hat{n}_{i,p}$ for p=1,3 (D sites) and $\hat{q}_{i,p} = \hat{n}_{i,p}$ for p=2 (A site) and $V_{ip,jq}$ is defined as in Eq. 5.8.

The ESM-CT must describe exactly the same physics as the ESM-ES in section 5.3 when $\beta = 0$, provided that model parameters are properly selected. States with D sites bearing a negative charge or A sites bearing a positive charge or where sites bear double charges (D^{2+} or A^{2-}) are excluded setting their energy virtually to infinite. On-site energies are defined as $\varepsilon_p = -\Delta$ for p=1,3 (D sites) and $\varepsilon_p = +\Delta$ for p =2 (A site). For direct comparison with essential state models, the energy difference

between D^+A^-D and DAD configurations is $2z_0 = 2\Delta - U - V$, where

$$V = V_{i1,i2} = V_{i2,i3} = \frac{1}{4\pi\varepsilon_0\eta^2 a} \tag{5.14}$$

is the ES interaction energy between two charges on adjacent D and A sites in the same molecule. V therefore depends on the geometry of the molecule (specifically, on the length of the DA arm a), and for fixed ${}_0z$ and V, Δ is estimated as $\Delta = z - (U + V)/2$. This relation makes the numerical value of U irrelevant, readjusting Δ as to map exactly the Hamiltonian in eq. 5.13 over the ESM-ES Hamiltonian in eq. 5.6.

5.4.2 The real space basis and the bit representation

The definition of the basis relevant to the Hamiltonian in eq. 5.13 describing delocalized electrons in the aggregate is a delicate issue. If electrons can hop among different molecules, the number of states needed to describe the aggregate increases very fast with N, even when high energy states (with doubly charged sites or with negatively charged D or positively charged A) are discarded. In a dimer, accounting only for charge degrees of freedom (i. e. approximating the electrons as spinless fermions), the number of states increases from 9 in the case of localized electrons to 15.[279] However, 15 states are not enough if the electron spin is properly accounted for, leading to much larger basis. To account for spin degrees of freedom, the smallest basis is the valence-bond basis, that works on subspaces where the total spin quantum number S is conserved. Just as an example, figure 5.8 shows how a single diagram in the spinless fermion representation, corresponding to a specific charge distribution, actually corresponds to two valence bond-diagrams in the singlet states $S = 0$.

The valence bond basis is very convenient in terms of reduced dimension of the subspaces, but it has the main disadvantage of being non-

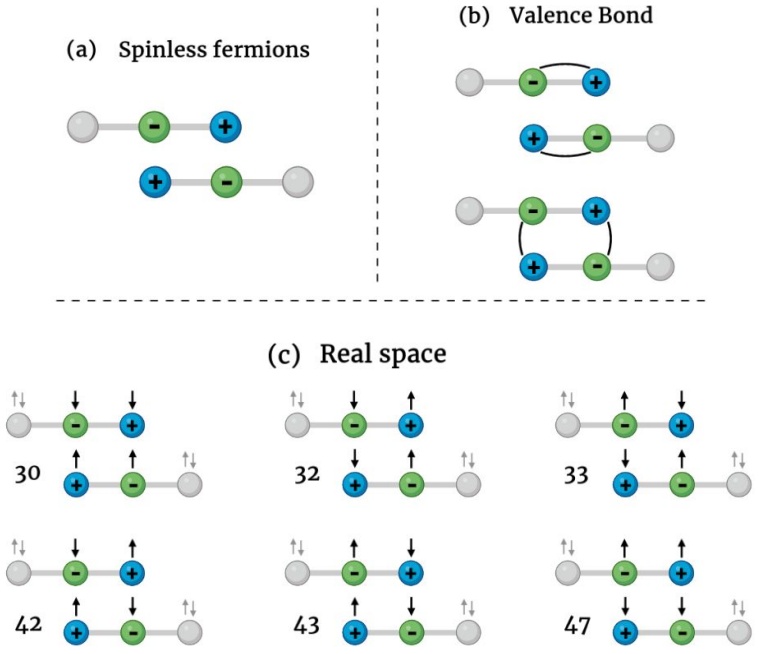

Figure 5.8: (**a**) Specific charge distribution for a dimer, corresponding to a single basis state in the spinless fermion approximation adopted in ref. [279]. (**b**) The two valence bond states corresponding to the same charge distribution as in (**a**) where the black lines mark two electrons paired in a singlet state, in the standard representation by Pauling. (**c**) The six real space diagrams corresponding to the charge distribution in (**a**), the numbers assigned to each diagram correspond to the labels in table 5.1.

1	1275	110111 110010
2	1467	110111 011010
3	1515	110101 111010
4	1530	010111 111010
5	1659	110111 100110
6	1719	111011 010110
7	1755	110110 110110
8	1767	111001 110110
9	1779	110011 110110
10	1782	011011 110110
11	1785	100111 110110
12	2295	111011 110001
13	2427	110111 101001
14	2487	111011 011001
15	2523	110110 111001
16	2535	111001 111001
17	2547	110011 111001
18	2550	011011 111001
19	2553	100111 111001
20	2679	111011 100101
21	2775	111010 110101
22	2805	101011 110101
23	3195	110111 100011
24	3255	111011 010011
25	3291	110110 110011
26	3303	111001 110011
27	3315	110011 110011
28	3418	011011 110011
29	3321	100111 110011
30	3435	110101 101011
31	3450	010111 101011
32	3483	110110 011011
33	3495	111001 011011
34	3507	110011 011011
35	3510	011011 011011
36	3513	100111 011011
37	3546	010110 111011
38	3555	110001 111011
39	3558	011001 111011
40	3561	100101 111011
41	3570	010011 111011
42	3675	110110 100111
43	3687	111001 100111
44	3699	110011 100111
45	3702	011011 100111
46	3705	100111 100111
47	3735	111010 010111
48	3765	101011 010111
49	3795	110010 110111
50	3798	011010 110111
51	3801	100110 110111
52	3813	101001 110111
53	3825	100011 110111

Table 5.1: The 53 diagrams composing the real space basis for a dimer. The first column numbers the diagrams, the second column is the integer number representative of each state, the third column is the corresponding bit representation.

orthonormal, leading to a somewhat cumbersome calculation of the matrix elements. The much simpler *real-space basis* is therefore adopted, where the $4N$ electrons are distributed on the different sites and only states with the total projection of the spin operator equal to zero S_z=0 are considered (i. e only states with an equal number of spins up and down). This leads to a much larger basis set than in valence bond, since it also includes S_z=0 components from triplet and higher spin states, but with the advantage of working with an orthonormal basis. Specifically, figure 5.8 shows that the spinless fermion state in panel (a) corresponds to 6 real space states in panel (c). With such a basis, the dimension scales from 53 states in a dimer, to 707 in a trimer and 10453 in a tetramer.

The bit representation is used to manipulate the real space basis, assigning 2 bits to each site, the first bit referring to a spin up and the second bit to a spin down. Of course 0/1 means that the specific spin state is void/occupied; 10 represent a state occupied by a spin up, 01 a site occupied by a spin down and 11 a site occupied by a spin up and a spin down. Considering a single squaraine, just as an example, the $|N\rangle$ state is represented as 110011, while $|Z_1\rangle$ is a singlet state, represented as a linear combination of 100111 and 011011. The string of bits representing a specific spin distribution (a basis state) is stored in the computer as an integer number. For a dimer, the real space basis is composed of 53 diagrams, listed in table 5.1.

5.4.3 Calculation of optical spectra: CD for delocalized electrons

The dipole moment operator, as needed to calculate absorption spectra, cannot be written as the sum of molecular dipoles due to intermolecular CT. Its definition, in terms of site charges and positions, is however very simple:

$$\hat{\vec{D}} = \sum_{ip} \hat{q}_{ip}\vec{r}_{ip} \tag{5.15}$$

The eigenstates of the Hamiltonian in eq. 5.13 can then be used to calculate transition dipole moments and hence absorbtion spectra with eq. 5.9.

Addressing CD spectra is much more delicate. The Condon approach[217, 286, 288, 289] only applies to aggregates where electrons are confined inside each molecular unit, therefore rotational strengths cannot be calculated with eq. 5.11, but the more general eq. 5.10 must be used. An explicit expression for both the electric dipole moment operator (given in eq. 5.15) and for the magnetic dipole moment operator is thus needed. The derivation of the magnetic dipole moment operator is non trivial.

The magnetic dipole is proportional to the total angular momentum:

$$\hat{\vec{M}} \propto -\hat{\vec{L}} = -\sum_k \hat{\vec{l}}_k \tag{5.16}$$

where k runs on all electrons and the angular momentum of electron k is related to its linear momentum $\hat{\vec{p}}_k$ by

$$\hat{\vec{l}}_k = \vec{r}_k \wedge \hat{\vec{p}}_k. \tag{5.17}$$

Finally the linear momentum can be obtained as

$$\hat{\vec{p}}_k = -\frac{i}{\hbar}[\hat{\vec{\mu}}_k, \hat{H}] \tag{5.18}$$

However, in a real-space description the properties of a single electron cannot be addressed. To overcome the problem the total linear momentum is directly evaluated. For the sake of clarity, only its x component is explicitly addressed:

$$\hat{P}_x = -\frac{i}{\hbar}[\hat{D}_x, \hat{H}] \tag{5.19}$$

where $\hat{D}_x$ is the x component of the total dipole moment, defined in eq. 5.15. The dipole moment operator commutes with all terms in the Hamiltonian in eq. 5.13 but the intra- and inter-molecular hopping terms. Accordingly:

$$\begin{aligned}\hat{P}_x = &\frac{i}{\hbar}t\sum_{i=1}^{N}[(x_{i2}-x_{i1})\hat{v}_{i1,i2}+(x_{i3}-x_{i2})\hat{v}_{i2,i3}] \\ &+\frac{i}{\hbar}\beta\sum_{i=1}^{N-1}\left[(x_{(i+1)1}-x_{i2})\hat{v}_{i2,(i+1)1}+(x_{(i+1)2}-x_{i3})\hat{v}_{i3,(i+1)2}\right]\end{aligned} \tag{5.20}$$

where the bond velocity is the antiHermitian operator

$$\hat{v}_{ip,jq} = \hat{b}_{ip,jq} - \hat{b}^{\dagger}_{ip,jq} = \hat{b}_{ip,jq} - \hat{b}_{jq,ip}. \tag{5.21}$$

The vectorial product $\hat{\vec{R}} \wedge \hat{\vec{P}}$ is not the total angular momentum in eq. 5.16. Indeed $\hat{\vec{L}}$ and hence the magnetic dipole operator is a one-electron operator, while $\hat{\vec{R}} \wedge \hat{\vec{P}}$ does contain both one-electron and two-electron terms. $\hat{\vec{L}}$ is therefore defined to the purpose selecting out of the $\hat{\vec{R}} \wedge \hat{\vec{P}}$ operator only the one-electron terms. Accordingly:

$$\begin{aligned}\hat{L}_x \;=\; &-\frac{i}{\hbar}t\sum_{i=1}^{N}\left[(z_{i2}-z_{i1})(y_{i1}\hat{b}_{i1,i2}-y_{12}\hat{b}_{i2,i1})+(z_{i3}-z_{i2})(y_{i2}\hat{b}_{i23}-y_3\hat{b}_{32})\right] \\ &-\frac{i}{\hbar}\beta\sum_{i=1}^{N-1}\Big[(z_{(i+1)1}-z_{i,2})(y_{i,2}\hat{b}_{i2,(i+1)1}-y_{(i+1)1}\hat{b}_{(i+1)1,i2}) \\ &+(z_{(i+1)2}-z_{i3})(y_{i3}\hat{b}_{i3,(i+1)2}-y_{(i+1)2}\hat{b}_{(i+1)2,i3})\Big] \\ &+\frac{i}{\hbar}t\sum_{i=1}^{N}\left[(y_{i2}-y_{i1})(z_{i1}\hat{b}_{i1,i2}-z_{12}\hat{b}_{i2,i1})+(y_{i3}-y_{i2})(z_{i2}\hat{b}_{i23}-z_3\hat{b}_{32})\right] \\ &+\frac{i}{\hbar}\beta\sum_{i=1}^{N-1}\Big[(y_{(i+1)1}-y_{i,2})(z_{i,2}\hat{b}_{i2,(i+1)1}-z_{(i+1)1}\hat{b}_{(i+1)1,i2}) \\ &+(y_{(i+1)2}-y_{i3})(z_{i3}\hat{b}_{i3,(i+1)2}-z_{(i+1)2}\hat{b}_{(i+1)2,i3})\Big].\end{aligned} \tag{5.22}$$

Analogous expressions for $\hat{L}_y$ and $\hat{L}_z$ can be obtained upon cyclic permutation of x, y, z indices. Remembering that $-\hat{\vec{L}} \propto \hat{\vec{M}}$, rotational strengths using eq. 5.10 can be calculated. CD spectra are then obtained according to eq. 5.12.

5.4.4 Results

The large dimension of the real space basis and the large number of matrices to be stored in the computer memory for the calculation of rotational strengths make ESM-CT calculations extremely demanding, limiting the dimension of the largest aggregate that could be addressed to 4 molecules. Nevertheless, the ESM-ES results shown in section 5.3.4 for aggregates of 4 and 8 molecules suggest that, while finite size effects are sizable, reliable information can already be obtained for 4 molecules. Figures 5.9 and 5.10 show ESM-CT spectra calculated for a dimer and a tetramer, respectively, with the same model parameters as in figure 5.5, but with intermolecular CT interactions switched on to $\beta = 0.2, 0.4$

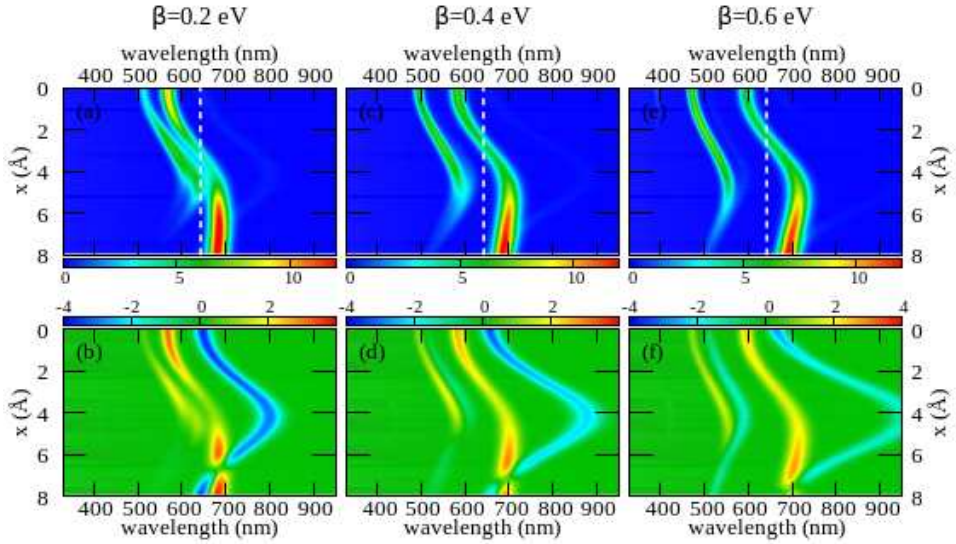

Figure 5.9: Spectral properties of a squaraine **dimer** described in the ESM-CT approach (model Hamiltonian in eq. 5.13). Same geometry and same molecular parameters as in figure 5.5. The color maps show the absorption intensity (top panels) and the CD intensity (bottom panels) plotted against the wavelength (horizontal axis) and x (vertical axis). Left panels refer to β=0.2 eV, middle panels to β=0.4 eV and right panels to β=0.6 eV.

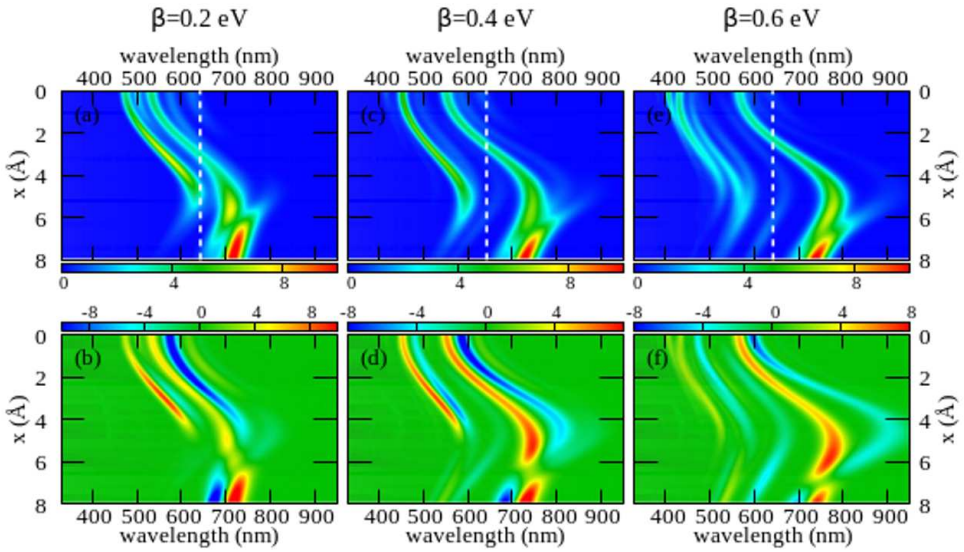

Figure 5.10: Spectral properties a squaraine **tetramer** described in the ESM-CT approach. Same geometry and same molecular parameters as in figure 5.9.

and 0.6 eV. Results for other aggregate geometries and other parameters values are shown in appendix C.

As first recognized by Collison and Spano,[279] when intermolecular CT interactions are accounted for, two major peaks appear in the absorption spectrum whose separation increases with increasing β. Indeed, two predominant bands are seen for a dimer (figure 5.9) but, upon increasing the number of molecules (figure 5.10), additional weak bands are also seen that could disappear in larger aggregates, being most probably related to finite size effects. Quite interestingly, two bisignate features appear in CD spectra in correspondence with the two main peaks seen in absorption (again the spectrum is somewhat more complex with additional small features appearing, most probably related to finite size effects). The superlinear increase of the intensity of CD signal, observed for the model with localized electrons, is also confirmed in the presence of intermolecular CT interactions.

Experimental results can now be discussed in the framework of the ESM-CT approach. Spectra collected for aggregates of dyes with pendants of intermediate size (C6, C7 or C10) could be roughly accounted for in terms of aggregates with β=0.4 eV and $x \sim$ 3-4 Å. So a single aggregate type can explain the observation of double features in both absorption and CD spectra. Simulating absorption and CD spectra accounting for a single form of aggregates is fairly appealing if compared with the need to postulate the presence of two different types of aggregates in the ESM-ES approach. However, the ESM-CT approach hardly applies to aggregates of dyes with short (C3, C5) or long (C11, C12, C16) chains. In these aggregates in fact the redmost feature observed in either absorption or CD spectra has a dramatically reduced intensity if compared with the blue-most features. In the model presented here, irrespective of the strength of the CT interaction and of the details of the aggregate geometry (see appendix C) it is not possible to simulate a spectrum where the redmost features have negligible intensity.

5.5 Conclusions

The extensive experimental and theoretical study on a large family of squaraine dyes presented in this chapter attempts to shed light on the structure of these fascinating systems showing astounding spectral features. The investigated proline-derived anilino squaraines have similar chemical structure, bearing a chiral terminal group in each one of the two D moieties. The only difference among the investigated dyes is the length of the alkyl pendant attached to each D moiety. These alkyl chains are not part of the chromophoric system but steer the aggregation pattern. Upon aggregation, induced in solution by poor solvent titration, the different compounds show distinctively different spectral properties, suggesting different aggregation behavior. Specifically, the tendency to aggregation increases with the length of the alkyl chains. On the contrary, the nature of formed aggregates, as demonstrated by the spectra, has a more complex and intriguing behavior. Specifically, dyes decorated with alkyl chains with intermediate length show in both absorption and CD spectra two distinct and intense features, one located at longer wavelength vs the monomer absorption the other one at shorter wavelengths. In aggregates

of dyes with very short or very long alkyl chains, instead, the spectral feature located at long wavelength loose intensity and becomes almost irrelevant, while the spectral position of the two features is basically the same in all samples.

The spectra of these colloidal suspensions of chiral aggregates, showing features appearing both to the blue and to the red of the monomer absorption, while much narrower, do share some similarity with the panchromatic spectra of squaraine films, then offering some useful hint about the origin of this technologically relevant and highly debated feature. Specifically, the consistent observation of two bisignated features in the CD spectrum of the aggregates here investigated, occurring at the frequencies of the red and blue-shifted absorption bands, allows to definitely exclude that the two signals are due to the two Davydov components of the relevant exciton, as expected in aggregates with oblique arrangement of the dyes. This conclusion can be very reasonably extended also to squaraine aggregates in films. Other alternative scenarios are presently considered in the literature to explain the observation of two peaks in the spectra of *non-chiral* anilino squaraine films. In the first scenario, the observation of the two peaks is ascribed to intermolecular CT interactions,[279] while an alternative view relies on the presence of disorder.[281] Of course, the aggregation behavior can be markedly different in aggregates obtained from different squaraine dyes, however the chiroptical responses of these proline-derived squaraine aggregates give precious additional information to shed light on this intriguing issue.

The lack of structural information for the investigated aggregates complicates the understanding of the picture. After a reasonable guess, supported by MD calculations,[290] two theoretical models are developed in order to unveil the physics underneath these such peculiar features. The essential state model for a quadrupolar dye is adopted to tackle the aggregation problem including purely electrostatic intermolecular interaction (ESM-ES approach) and it is hence extended to account for intermolecular charge transfer (ESM-CT approach). In the ESM-ES picture, experimental data can be roughly reproduced assuming the presence of H-aggregates for squaraines with short (C3-C5) and long (C11, C12 and C16) side chains and the simultaneous presence of both H- and J-aggregates for the intermediate chain length regime (C7-C10). On the other hand, the ESM-CT model elegantly allows to reproduce the double features observed both in absorption and CD spectra in the intermediate chain length regime considering only a single aggregate. However, neither the short nor the long side chain regimes, presenting a largely dominant blue-shifted feature, can be reproduced in this framework, suggesting that most probably in the specific case disorder is more important than intermolecular CT. However, due to the complexity of the calculation, the ESM-CT model could only be applied to systems not larger than a tetramer, leaving the doubt that finite size effects may alter the picture.

In conclusion, in this study a novel approach for the calculation of CD spectra of aggregates in the presence of intermolecular CT interactions is introduced, a highly non-trivial result. Other important lessons are learned: care must be taken when using dimeric models to describe larger aggregates. Even if they proved useful in some cases,[293] in general they

may be adequate to describe linear spectral properties of aggregates, but can fail for chiroptical properties. An impressive superlinear amplification of the CD response with the aggregate dimension that survives both in the presence or in the absence of intermolecular CT interactions is recognized. More work is certainly needed to gain a complete and unified picture of the whole series of chiral proline-derived squaraine aggregates investigated here, starting from a more detailed experimental structural characterization. While a firm conclusion is hardly reached, this extensive study gives important information on chiral responses of molecular aggregates beyond the exciton model.

Conclusions and future outooks

Different flavours of environmental effects in systems involving charge transfer chromophores have been discussed in this thesis.

In chapter 1 relaxation dynamics of a photoexcited dipolar dye is addressed. The Redfield approach to open quantum systems is exploited to couple the essential state model describing the dye to a bath of quantum harmonic oscillators. Details of the model, and in particular of the system-bath interaction, are extensively discussed, setting a firm basis to address more complex systems. In chapter 2 polar solvation and its relaxation dynamics are introduced *via* a mixed quantum-classical approach. The proposed model is then used to simulate time resolved emission spectra of a polar dye dissolved in liquid solvents and dispersed in amorphous organic matrices. Along these lines we unveiled the dielectric dynamical behavior of a couple of small molecule matrices, used in the fabrication of OLED. Specifically, for the first time we were able to estimate the timescale of the dielectric relaxation of these technologically relevant materials. The model opens the way to several future studies, starting from the investigation of symmetry breaking in quadrupolar chromophores and molecular dimers. Applying the model to the description of a slow conformational degree of freedom is also of extreme interest and on the to-do list. Collaborations are underway to apply this original modeling tool to single molecule spectrosocpy studies.

The realm of molecular aggregates and crystals is entered in the second part of the thesis. In chapter 3 the Frenkel-Holtstein Hamiltonian is used to obtain insights on the peculiar features of the Davydov components of the two polymorphs of SQIB, a relevant material for photovoltaic applications. In chapter 4 a clear connection between the standard exciton model and an essential state description of molecular aggregates is made, pointing out how essential state models release the main approximations introduced in the exciton model and allow to gain a unified picture of exciton delocalization and energy transfer, that are then simulated in real time exploiting the relaxation model set up in chapter 1. In chapter 5 chiroptical properties of a series of proline-derived squaraine aggregates are addressed, entering the debate about the physical origin of the panchromatic spectrum of squaraine aggregates and thin films. Effects of disorder and intermolecular charge transfer are investigated. Experimental data and theoretical results point to the need of including both phenomena in a unified framework. The work on aggregates will proceed along several lines. A collaboration just started to apply our models to films of near-IR suqraine dyes exploited in photodetector devices,[11] where both electrostatic and CT intermolecular interactions play a role. Chiral aggregates are also an important target of future work: understanding and simulating CD spectra offers important structural information. Moreover, circularly polarized luminescence is an important target, of interest for improving OLED efficiency as well as for background free microscopy techniques. Finally, a deep understanding of chiroptical properties of molecular systems has the potential to shed light on the fascinating and so far not understood phenomenon called chirality induced spin selectivity (CISS).

The effective models adopted in this thesis lend themselves to be paired with atomistic based approaches. *Ab initio* calculations can be exploited to parametrize the essential state models,[294] as well as for the evaluation of electrostatic (as done in chapter 3) and charge transfer intermolecular interactions in Frenkel-Holstein based Hamiltonians,[169, 295] while classical Molecular Dynamics simulations can be used to obtain hints about aggregate geometry, as done in chapter 5. This merging adds value to the approach, providing a general framework where different techniques concur to build a solid and exhaustive picture.

List of Publications

- Giavazzi, D.; Di Maiolo, F.; Painelli, A. The fate of molecular excited states: modeling donor-acceptor dyes, *Physical Chemistry Chemical Physics, 24* (9),5555-5563, **2022**.
- Bardi, B.; Giavazzi, D.; Ferrari, E.; Iagatti, A.; Di Donato, M.; Phan Huu, D. K. A.; Di Maiolo, F.; Sissa, C.; Masino, M.; Lapini, A.; Painelli, A. Solid state solvation: a fresh view, *Materials Horizons, 10* (10), 4172-4182, **2023**.
- Giavazzi, D.; Saseendrean, S.; Di Maiolo, F.; Painelli, A. A Comprehensive Approach to Exciton Delocalization and Energy Transfer, *Journal of Chemical Theory and Computation, 19* (2), 436-447, **2023**.
- Giavazzi, D.; Schumacher, M. F.; Grisanti, L.; Anzola, M.; Di Maiolo, F.; Zablocki, J.; Lützen, A.; Schiek, M.; Painelli A. A marvel of chiral squaraine aggregates: chiroptical spectra beyond the exciton model, *Journal of Materials Chemistry C, 11,* 8307-8321, **2023**.
- Bedogni, M.; Giavazzi, D.; Di Maiolo, F.; Painelli A. Shining Light on Inverted Singlet–Triplet Emitters, *Journal of Chemical Theory and Computation, 20* (2), 902-913, **2024**.
- Hu, W.-H.; Nüesch, F.; Giavazzi, D.; Jafarpour, M.; Hany, R.; Bauer, M. Squaraine Dyes for Single-Component Shortwave Infrared-Sensitive Photodiodes and Upconversion Photodetectors, *Advanced Optical Materials,* 2302105, **2023**.
- Di Maiolo, F.; Phan Huu, D. K. A.; Giavazzi, D.; Landi, A.; Racchi, O.; Painelli A. Shedding light on thermally-activated delayed fluorescence, *Chem. Sci.*, -, **2024**, invited submission.

Appendices

Kinetic coefficients $\Gamma^{+/-}_{db,ac}$ for a molecule with three coupled vibrational coordinates

A

Kinetic coefficients $\Gamma^{+/-}_{db,ac}$ entering eq. 1.28 for a molecule with three coupled coordinates ($\hat{Q}_1 = \hat{d}_1^\dagger + \hat{d}_1$, $\hat{Q}_2 = \hat{d}_2^\dagger + \hat{d}_2$ and $\hat{Q}_3 = \hat{d}_3^\dagger + \hat{d}_3$) are obtained following the same derivation shown in sec. 1.3.

When the three coordinates are *linearly* coupled to *three independent baths*[1], they read:

$$\begin{aligned}\Gamma^{+}_{db,ac} = &\frac{\pi}{\hbar^2} q^1_{db} q^1_{ac} \left[\mathcal{J}_1(\omega_{ac}) n(\omega_{ac}) + \mathcal{J}_1(\omega_{ca}) \left[n(\omega_{ca}) + 1\right]\right] \\ &+ \frac{\pi}{\hbar^2} q^2_{db} q^2_{ac} \left[\mathcal{J}_2(\omega_{ac}) n(\omega_{ac}) + \mathcal{J}_2(\omega_{ca}) \left[n(\omega_{ca}) + 1\right]\right] \\ &+ \frac{\pi}{\hbar^2} q^3_{db} q^3_{ac} \left[\mathcal{J}_3(\omega_{ac}) n(\omega_{ac}) + \mathcal{J}_3(\omega_{ca}) \left[n(\omega_{ca}) + 1\right]\right]\end{aligned} \tag{A.1}$$

$$\begin{aligned}\Gamma^{-}_{db,ac} = &\frac{\pi}{\hbar^2} q^1_{db} q^1_{ac} \left[\mathcal{J}_1(\omega_{bd}) n(\omega_{bd}) + \mathcal{J}_1(\omega_{db}) \left[n(\omega_{db}) + 1\right]\right] \\ &+ \frac{\pi}{\hbar^2} q^2_{db} q^2_{ac} \left[\mathcal{J}_2(\omega_{bd}) n(\omega_{bd}) + \mathcal{J}_2(\omega_{db}) \left[n(\omega_{db}) + 1\right]\right] \\ &+ \frac{\pi}{\hbar^2} q^3_{db} q^3_{ac} \left[\mathcal{J}_3(\omega_{bd}) n(\omega_{bd}) + \mathcal{J}_3(\omega_{db}) \left[n(\omega_{db}) + 1\right]\right].\end{aligned} \tag{A.2}$$

When the three coordinates are *linearly* coupled to *the same bath*[2], expressions for $\Gamma^{+}_{db,ac}$ and $\Gamma^{-}_{db,ac}$ read:

$$\begin{aligned}\Gamma^{+}_{db,ac} = &\frac{\pi}{\hbar^2} q^1_{db} q^1_{ac} \left[\mathcal{J}_1(\omega_{ac}) n(\omega_{ac}) + \mathcal{J}_1(\omega_{ca}) \left[n(\omega_{ca}) + 1\right]\right] \\ &+ \frac{\pi}{\hbar^2} q^2_{db} q^2_{ac} \left[\mathcal{J}_2(\omega_{ac}) n(\omega_{ac}) + \mathcal{J}_2(\omega_{ca}) \left[n(\omega_{ca}) + 1\right]\right] \\ &+ \frac{\pi}{\hbar^2} q^3_{db} q^3_{ac} \left[\mathcal{J}_3(\omega_{ac}) n(\omega_{ac}) + \mathcal{J}_3(\omega_{ca}) \left[n(\omega_{ca}) + 1\right]\right] \\ &+ \frac{\pi}{\hbar^2} q^1_{db} q^2_{ac} \left[\mathcal{J}_{12}(\omega_{ac}) n(\omega_{ac}) + \mathcal{J}_{12}(\omega_{ca}) \left[n(\omega_{ca}) + 1\right]\right] \\ &+ \frac{\pi}{\hbar^2} q^2_{db} q^1_{ac} \left[\mathcal{J}_{12}(\omega_{ac}) n(\omega_{ac}) + \mathcal{J}_{12}(\omega_{ca}) \left[n(\omega_{ca}) + 1\right]\right] \\ &+ \frac{\pi}{\hbar^2} q^2_{db} q^3_{ac} \left[\mathcal{J}_{23}(\omega_{ac}) n(\omega_{ac}) + \mathcal{J}_{23}(\omega_{ca}) \left[n(\omega_{ca}) + 1\right]\right] \\ &+ \frac{\pi}{\hbar^2} q^3_{db} q^2_{ac} \left[\mathcal{J}_{23}(\omega_{ac}) n(\omega_{ac}) + \mathcal{J}_{23}(\omega_{ca}) \left[n(\omega_{ca}) + 1\right]\right] \\ &+ \frac{\pi}{\hbar^2} q^1_{db} q^3_{ac} \left[\mathcal{J}_{13}(\omega_{ac}) n(\omega_{ac}) + \mathcal{J}_{13}(\omega_{ca}) \left[n(\omega_{ca}) + 1\right]\right] \\ &+ \frac{\pi}{\hbar^2} q^3_{db} q^1_{ac} \left[\mathcal{J}_{13}(\omega_{ac}) n(\omega_{ac}) + \mathcal{J}_{13}(\omega_{ca}) \left[n(\omega_{ca}) + 1\right]\right]\end{aligned} \tag{A.3}$$

$$\begin{aligned}\Gamma^{-}_{db,ac} = &\frac{\pi}{\hbar^2} q^1_{db} q^1_{ac} \left[\mathcal{J}_1(\omega_{bd}) n(\omega_{bd}) + \mathcal{J}_1(\omega_{db}) \left[n(\omega_{db}) + 1\right]\right] \\ &+ \frac{\pi}{\hbar^2} q^2_{db} q^2_{ac} \left[\mathcal{J}_2(\omega_{bd}) n(\omega_{bd}) + \mathcal{J}_2(\omega_{db}) \left[n(\omega_{db}) + 1\right]\right] \\ &+ \frac{\pi}{\hbar^2} q^3_{db} q^3_{ac} \left[\mathcal{J}_3(\omega_{bd}) n(\omega_{bd}) + \mathcal{J}_3(\omega_{db}) \left[n(\omega_{db}) + 1\right]\right] \\ &+ \frac{\pi}{\hbar^2} q^1_{db} q^2_{ac} \left[\mathcal{J}_{12}(\omega_{bd}) n(\omega_{bd}) + \mathcal{J}_{12}(\omega_{db}) \left[n(\omega_{db}) + 1\right]\right] \\ &+ \frac{\pi}{\hbar^2} q^2_{db} q^1_{ac} \left[\mathcal{J}_{12}(\omega_{bd}) n(\omega_{bd}) + \mathcal{J}_{12}(\omega_{db}) \left[n(\omega_{db}) + 1\right]\right]\end{aligned}$$

1: The system-bath interaction Hamiltonian is:

$$\hat{H}^{(a)}_{I,lin} = \sum_i g_i \hat{B}_{i,1} \hat{Q}_1 + \sum_j f_j \hat{B}_{j,2} \hat{Q}_2 + \sum_k h_k \hat{B}_{k,3} \hat{Q}_3$$

with i, j and k independently running on the coordinates of the three separate baths. Three spectral densities (one for each molecular coordinate) are now defined:

$$\mathcal{J}_1(\omega) = \sum_i |g_i|^2 \delta(\omega - \omega_i)$$
$$\mathcal{J}_2(\omega) = \sum_j |f_j|^2 \delta(\omega - \omega_j)$$
$$\mathcal{J}_3(\omega) = \sum_k |h_k|^2 \delta(\omega - \omega_k).$$

2: In this case

$$\hat{H}^{(b)}_{I,lin} = \sum_i \hat{B}_i \left(g_i \hat{Q}_1 + f_i \hat{Q}_2 + h_i \hat{Q}_3\right)$$

and additional spectral density functions are defined as:

$$\mathcal{J}_{12}(\omega) = \sum_i g_i f_i^* \delta(\omega - \omega_i)$$
$$\mathcal{J}_{21}(\omega) = \sum_i g_i^* f_i \delta(\omega - \omega_i)$$
$$\mathcal{J}_{23}(\omega) = \sum_i f_i h_i^* \delta(\omega - \omega_i)$$
$$\mathcal{J}_{32}(\omega) = \sum_i f_i^* h_i \delta(\omega - \omega_i)$$
$$\mathcal{J}_{13}(\omega) = \sum_i g_i h_i^* \delta(\omega - \omega_i)$$
$$\mathcal{J}_{31}(\omega) = \sum_i g_i^* h_i \delta(\omega - \omega_i)$$

and since g, f and h are real and positive for every bath oscillator:

$$\mathcal{J}_{12}(\omega) = \mathcal{J}_{21}(\omega) = \sqrt{\mathcal{J}_1(\omega)\mathcal{J}_2(\omega)}$$
$$\mathcal{J}_{23}(\omega) = \mathcal{J}_{32}(\omega) = \sqrt{\mathcal{J}_2(\omega)\mathcal{J}_3(\omega)}$$
$$\mathcal{J}_{13}(\omega) = \mathcal{J}_{31}(\omega) = \sqrt{\mathcal{J}_1(\omega)\mathcal{J}_3(\omega)}.$$

$$
\begin{aligned}
&+ \frac{\pi}{\hbar^2} q^2_{db} q^3_{ac} \left[\mathcal{F}_{23}(\omega_{bd}) n(\omega_{bd}) + \mathcal{F}_{23}(\omega_{db}) \left[n(\omega_{db}) + 1\right]\right] \\
&+ \frac{\pi}{\hbar^2} q^3_{db} q^2_{ac} \left[\mathcal{F}_{23}(\omega_{bd}) n(\omega_{bd}) + \mathcal{F}_{23}(\omega_{db}) \left[n(\omega_{db}) + 1\right]\right] \\
&+ \frac{\pi}{\hbar^2} q^1_{db} q^3_{ac} \left[\mathcal{F}_{13}(\omega_{bd}) n(\omega_{bd}) + \mathcal{F}_{13}(\omega_{db}) \left[n(\omega_{db}) + 1\right]\right] \\
&+ \frac{\pi}{\hbar^2} q^3_{db} q^1_{ac} \left[\mathcal{F}_{13}(\omega_{bd}) n(\omega_{bd}) + \mathcal{F}_{13}(\omega_{db}) \left[n(\omega_{db}) + 1\right]\right].
\end{aligned}
\tag{A.4}
$$

Analogous expressions are found for the *bilinear* coupling Hamiltonians in eqs. 1.64 and 1.65. When each coordinate is coupled to an *independent bath*, they read:

$$
\begin{aligned}
\Gamma^{+}_{db,ac} = \frac{\pi}{\hbar^2} \Big[& d^1_{db} d^{1\dagger}_{ac} \mathcal{F}_1(\omega_{ac}) n(\omega_{ac}) + d^{1\dagger}_{db} d^1_{ac} \mathcal{F}_1(\omega_{ca}) \left[n(\omega_{ca}) + 1\right] \\
&+ d^2_{db} d^{2\dagger}_{ac} \mathcal{F}_2(\omega_{ac}) n(\omega_{ac}) + d^{2\dagger}_{db} d^2_{ac} \mathcal{F}_2(\omega_{ca}) \left[n(\omega_{ca}) + 1\right] \\
&+ d^3_{db} d^{3\dagger}_{ac} \mathcal{F}_3(\omega_{ac}) n(\omega_{ac}) + d^{3\dagger}_{db} d^3_{ac} \mathcal{F}_3(\omega_{ca}) \left[n(\omega_{ca}) + 1\right] \Big]
\end{aligned}
\tag{A.5}
$$

$$
\begin{aligned}
\Gamma^{-}_{db,ac} = \frac{\pi}{\hbar^2} \Big[& d^1_{db} d^{1\dagger}_{ac} \mathcal{F}_1(\omega_{bd}) n(\omega_{bd}) + d^{1\dagger}_{db} d^1_{ac} \mathcal{F}_1(\omega_{db}) \left[n(\omega_{db}) + 1\right] \\
&+ d^2_{db} d^{2\dagger}_{ac} \mathcal{F}_2(\omega_{bd}) n(\omega_{bd}) + d^{2\dagger}_{db} d^2_{ac} \mathcal{F}_2(\omega_{db}) \left[n(\omega_{db}) + 1\right] \\
&+ d^3_{db} d^{3\dagger}_{ac} \mathcal{F}_3(\omega_{bd}) n(\omega_{bd}) + d^{3\dagger}_{db} d^3_{ac} \mathcal{F}_3(\omega_{db}) \left[n(\omega_{db}) + 1\right] \Big].
\end{aligned}
\tag{A.6}
$$

When the three coordinates are coupled to *the same bath*:

$$
\begin{aligned}
\Gamma^{+}_{db,ac} = \frac{\pi}{\hbar^2} \Big[& d^1_{db} d^{1\dagger}_{ac} \mathcal{F}_1(\omega_{ac}) n(\omega_{ac}) + d^{1\dagger}_{db} d^1_{ac} \mathcal{F}_1(\omega_{ca}) \left[n(\omega_{ca}) + 1\right] \\
&+ d^2_{db} d^{2\dagger}_{ac} \mathcal{F}_2(\omega_{ac}) n(\omega_{ac}) + d^{2\dagger}_{db} d^2_{ac} \mathcal{F}_2(\omega_{ca}) \left[n(\omega_{ca}) + 1\right] \\
&+ d^3_{db} d^{3\dagger}_{ac} \mathcal{F}_3(\omega_{ac}) n(\omega_{ac}) + d^{3\dagger}_{db} d^3_{ac} \mathcal{F}_3(\omega_{ca}) \left[n(\omega_{ca}) + 1\right] \\
&+ d^1_{db} d^{2\dagger}_{ac} \mathcal{F}_{12}(\omega_{ac}) n(\omega_{ac}) + d^{1\dagger}_{db} d^2_{ac} \mathcal{F}_{12}(\omega_{ca}) \left[n(\omega_{ca}) + 1\right] \\
&+ d^2_{db} d^{1\dagger}_{ac} \mathcal{F}_{12}(\omega_{ac}) n(\omega_{ac}) + d^{2\dagger}_{db} d^1_{ac} \mathcal{F}_{12}(\omega_{ca}) \left[n(\omega_{ca}) + 1\right] \\
&+ d^2_{db} d^{3\dagger}_{ac} \mathcal{F}_{23}(\omega_{ac}) n(\omega_{ac}) + d^{2\dagger}_{db} d^3_{ac} \mathcal{F}_{23}(\omega_{ca}) \left[n(\omega_{ca}) + 1\right] \\
&+ d^3_{db} d^{2\dagger}_{ac} \mathcal{F}_{23}(\omega_{ac}) n(\omega_{ac}) + d^{3\dagger}_{db} d^2_{ac} \mathcal{F}_{23}(\omega_{ca}) \left[n(\omega_{ca}) + 1\right] \\
&+ d^1_{db} d^{3\dagger}_{ac} \mathcal{F}_{13}(\omega_{ac}) n(\omega_{ac}) + d^{1\dagger}_{db} d^3_{ac} \mathcal{F}_{13}(\omega_{ca}) \left[n(\omega_{ca}) + 1\right] \\
&+ d^3_{db} d^{1\dagger}_{ac} \mathcal{F}_{13}(\omega_{ac}) n(\omega_{ac}) + d^{3\dagger}_{db} d^1_{ac} \mathcal{F}_{13}(\omega_{ca}) \left[n(\omega_{ca}) + 1\right] \Big]
\end{aligned}
\tag{A.7}
$$

$$
\begin{aligned}
\Gamma^{-}_{db,ac} = \frac{\pi}{\hbar^2} \Big[& d^1_{db} d^{1\dagger}_{ac} \mathcal{F}_1(\omega_{bd}) n(\omega_{bd}) + d^{1\dagger}_{db} d^1_{ac} \mathcal{F}_1(\omega_{db}) \left[n(\omega_{db}) + 1\right] \\
&+ d^2_{db} d^{2\dagger}_{ac} \mathcal{F}_2(\omega_{bd}) n(\omega_{bd}) + d^{2\dagger}_{db} d^2_{ac} \mathcal{F}_2(\omega_{db}) \left[n(\omega_{db}) + 1\right] \\
&+ d^3_{db} d^{3\dagger}_{ac} \mathcal{F}_3(\omega_{bd}) n(\omega_{bd}) + d^{3\dagger}_{db} d^3_{ac} \mathcal{F}_3(\omega_{db}) \left[n(\omega_{db}) + 1\right] \\
&+ d^1_{db} d^{2\dagger}_{ac} \mathcal{F}_{12}(\omega_{bd}) n(\omega_{bd}) + d^{1\dagger}_{db} d^2_{ac} \mathcal{F}_{12}(\omega_{db}) \left[n(\omega_{db}) + 1\right] \\
&+ d^2_{db} d^{1\dagger}_{ac} \mathcal{F}_{12}(\omega_{bd}) n(\omega_{bd}) + d^{2\dagger}_{db} d^1_{ac} \mathcal{F}_{12}(\omega_{db}) \left[n(\omega_{db}) + 1\right] \\
&+ d^2_{db} d^{3\dagger}_{ac} \mathcal{F}_{23}(\omega_{bd}) n(\omega_{bd}) + d^{2\dagger}_{db} d^3_{ac} \mathcal{F}_{23}(\omega_{db}) \left[n(\omega_{db}) + 1\right] \\
&+ d^3_{db} d^{2\dagger}_{ac} \mathcal{F}_{23}(\omega_{bd}) n(\omega_{bd}) + d^{3\dagger}_{db} d^2_{ac} \mathcal{F}_{23}(\omega_{db}) \left[n(\omega_{db}) + 1\right] \\
&+ d^1_{db} d^{3\dagger}_{ac} \mathcal{F}_{13}(\omega_{bd}) n(\omega_{bd}) + d^{1\dagger}_{db} d^3_{ac} \mathcal{F}_{13}(\omega_{db}) \left[n(\omega_{db}) + 1\right] \\
&+ d^3_{db} d^{1\dagger}_{ac} \mathcal{F}_{13}(\omega_{bd}) n(\omega_{bd}) + d^{3\dagger}_{db} d^1_{ac} \mathcal{F}_{13}(\omega_{db}) \left[n(\omega_{db}) + 1\right] \Big].
\end{aligned}
\tag{A.8}
$$

Chiral ProSQ-aggregates: additional UV/Vis absorbance and ellipticity spectra

B

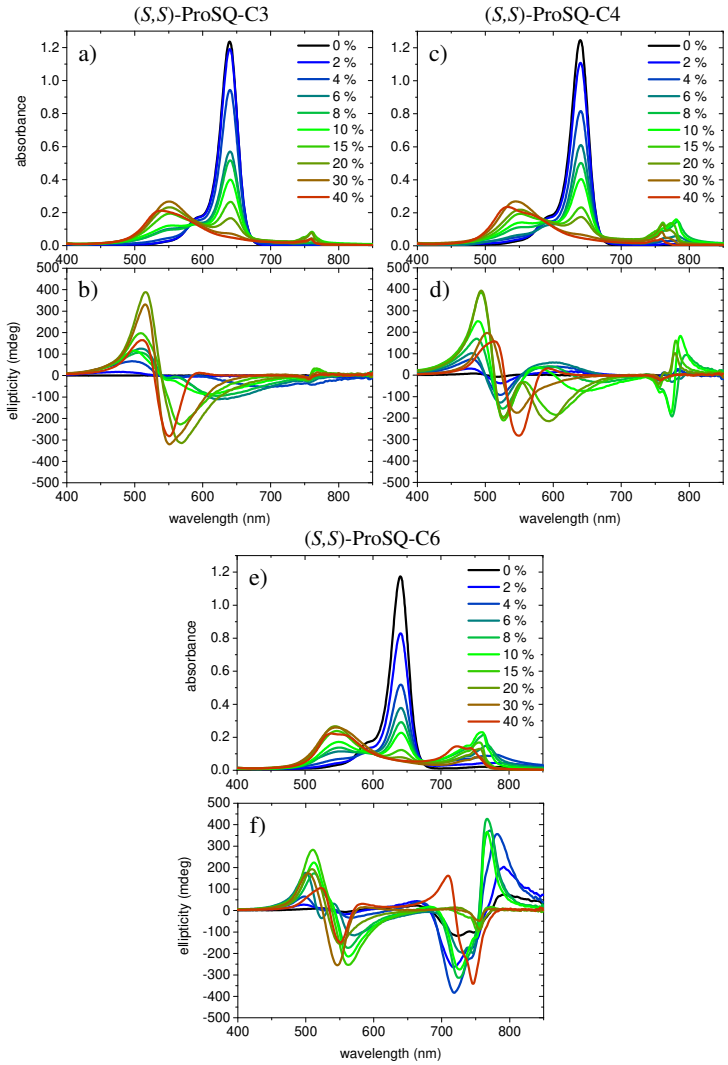

Figure B.1: Experimental UV/Vis absorbance spectra (**a**, **c** and **e**) and ellipticity spectra (**b**, **d** and **f**) for the(*S*,*S*)-ProSQ compounds with varying alkyl chains: C3 in **a** and **b**, C4 in **c** and **d**, and C6 in **e** and **f**. The legend indicates the volume-percentage of water in the methanol-water mixture used as bad solvent (good solvent being chloroform) and applies for all plots.

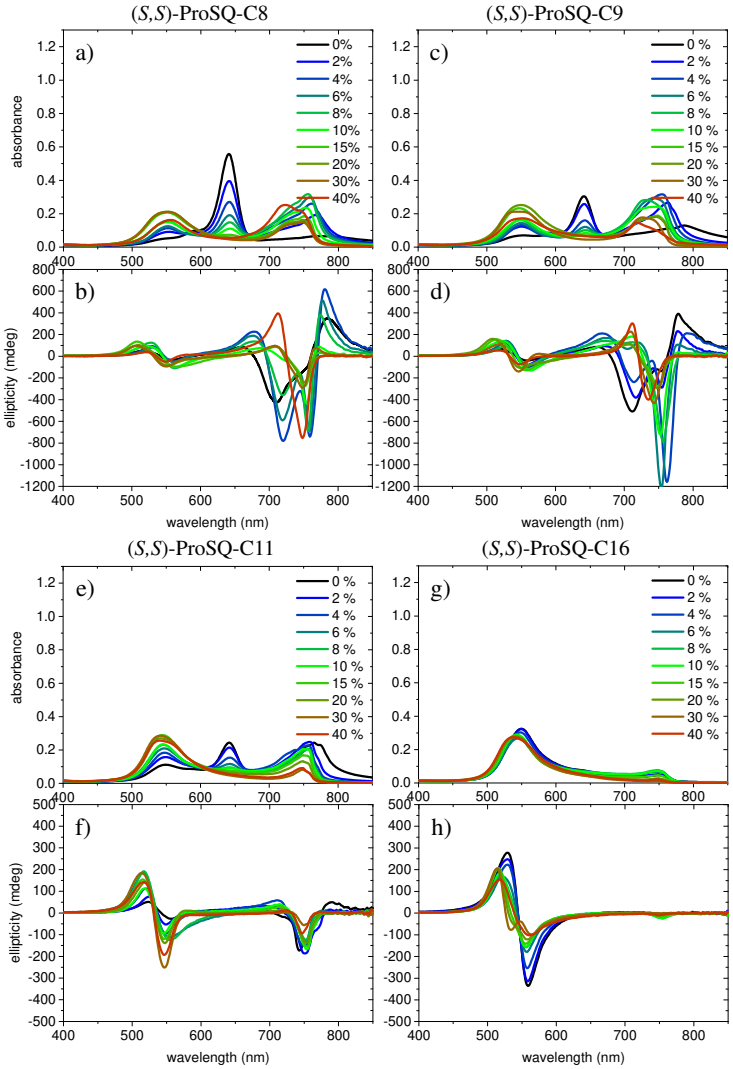

Figure B.2: Experimental UV/Vis absorbance spectra (**a**, **c**, **e** and **g**) and corresponding ellipticity spectra (**b**, **d**, **f** and **h**) for the(*S*,*S*)-ProSQ compounds with varying alkyl chain lengths: C8 in **a** and **b**, C9 in **c** and **d**, C11 in **e** and **f**, and C16 in **g** and **h**. The legend indicates the volume-percentage of water in the methanol-water mixture used as bad solvent (good solvent being chloroform) and applies for all plots.

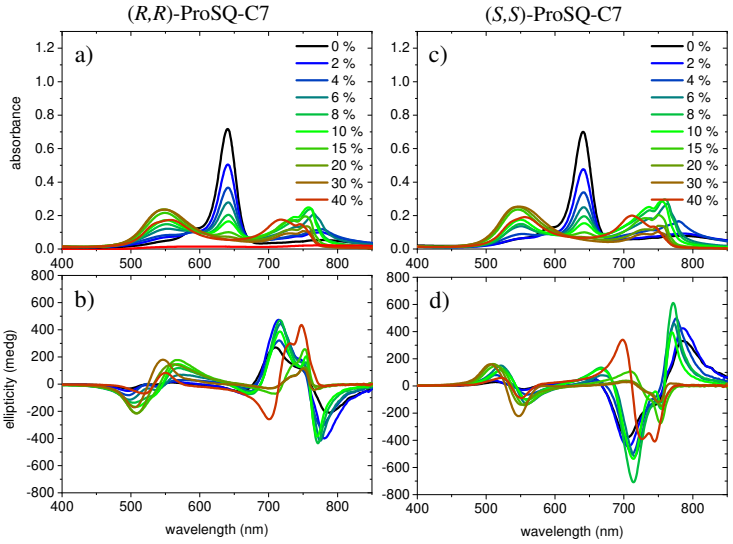

Figure B.3: Experimental UV/Vis absorbance spectra (**a** and **c**) and corresponding ellipticity spectra (**b** and **d**) for the (*R*,*R*)-ProSQ-C7 (**a**, **b**) and (*S*,*S*)-ProSQC7 compounds (**c**, **d**). The legend indicates the volume-percentage of water in the methanol-water mixture used as bad solvent (good solvent being chloroform) and applies for all plots.

Chiral ProSQ-aggregates: additional calculations

C

Additional results obtained with both the ESM-ES and ESM-CT Hamiltonians are reported in the following figures (absorption in the top panels and CD in the bottom panels). Molecular parameters (z, τ and a) together with the distance along the π-stack r are fixed as in chapter 5. Other parameters are varied (the number of molecules N, the angle α, the refractive index η, the displacement x and the amount of intermolecular charge transfer β; parameter values are specified in the figures).

The results show that the picture discussed in chapter 5, sections 5.3 and 5.4, is maintained in all the reasonable variation range of the parameters.

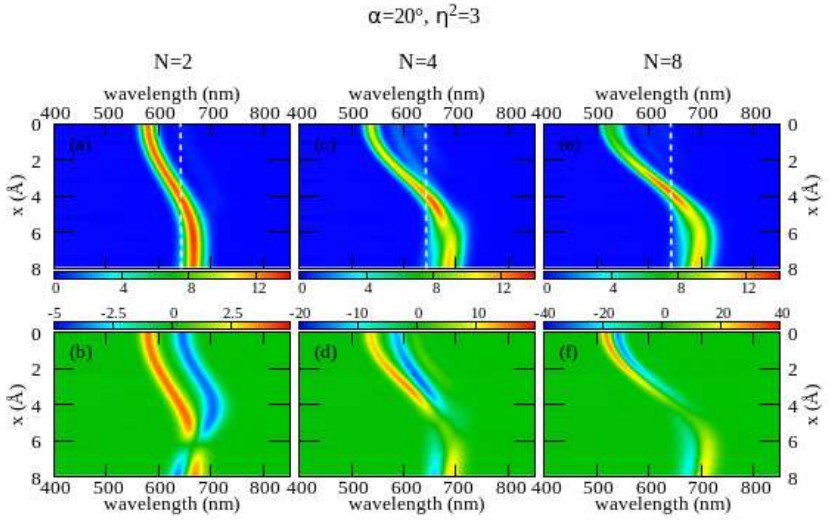

Figure C.1: ESM-ES: results for aggregates of 2, 4 and 8 molecules with the same molecular parameters as in figure 5.5, α=20° and $\eta^2 = 3$.

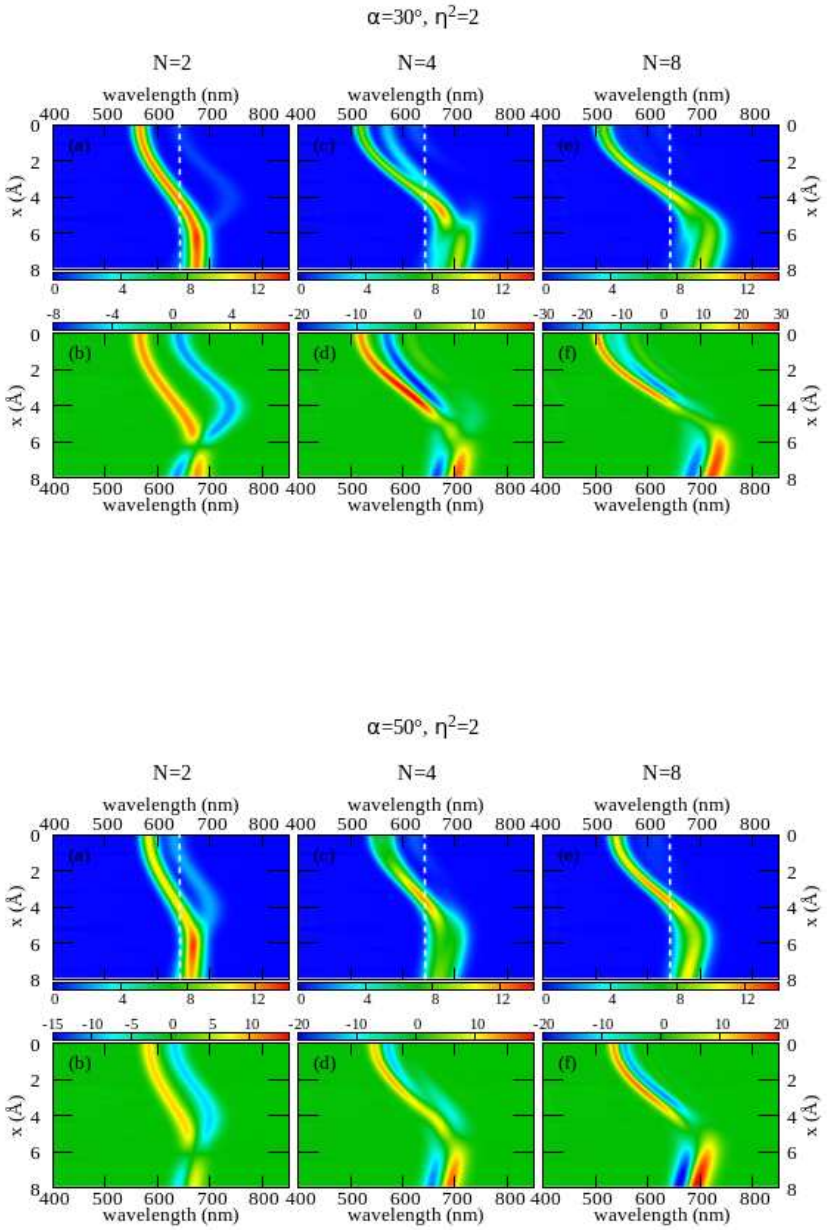

Figure C.2: ESM-ES: results for aggregates of 2, 4 and 8 molecules with the same molecular parameters as in figure 5.5, $\eta^2 = 2$ and α=30° (top panels) and α=50° (bottom panels).

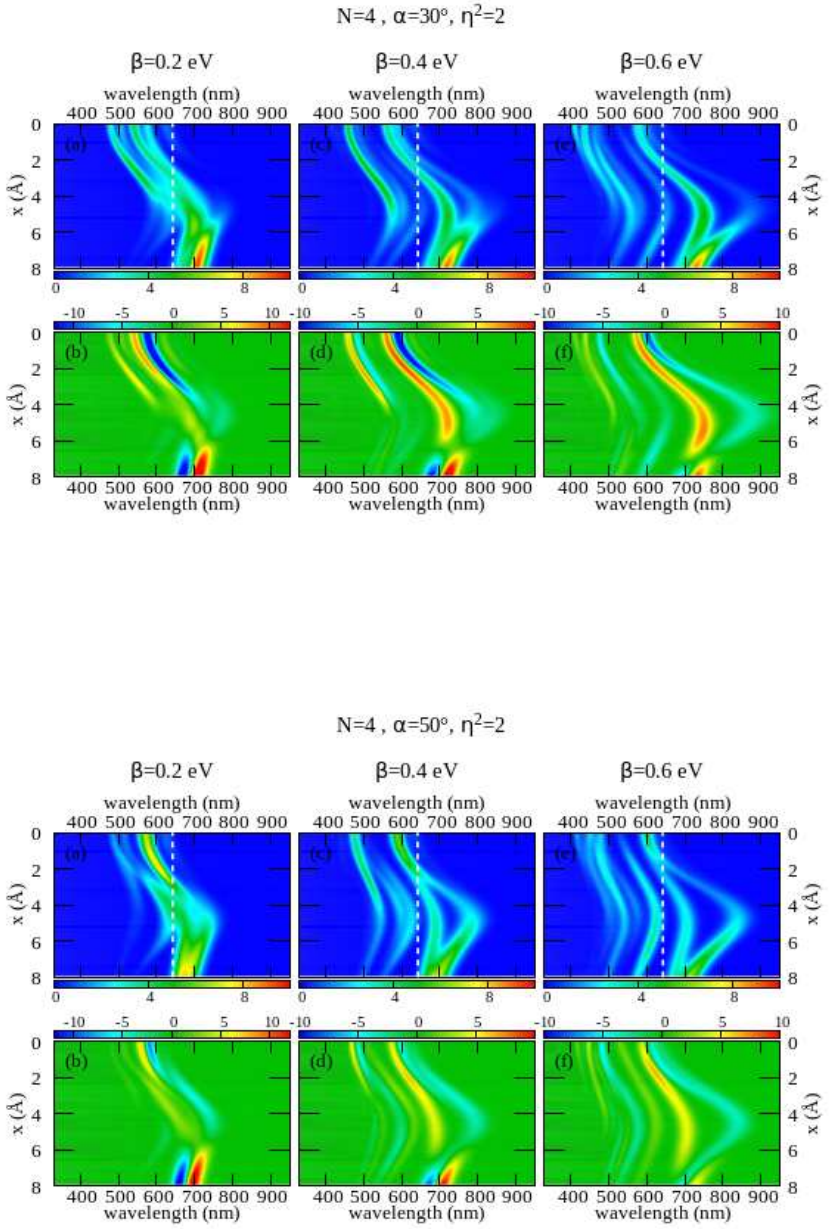

Figure C.3: ESM-CT: results for aggregates 4 molecules with the same molecular parameters as in figure 5.10 for β =0.2, 0.4 and 0.6 eV, η^2 = 2, α=30° (top panels) and α=50° (bottom panels).

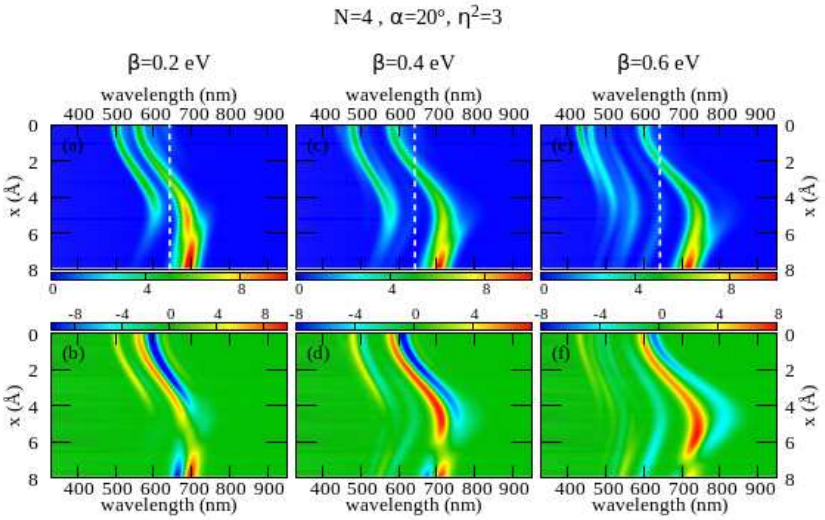

Figure C.4: ESM-CT: results for aggregates of 4 molecules with the same molecular parameters as in figure 5.10 for β =0.2, 0.4 and 0.6 eV, α=20° and η^2 = 3.

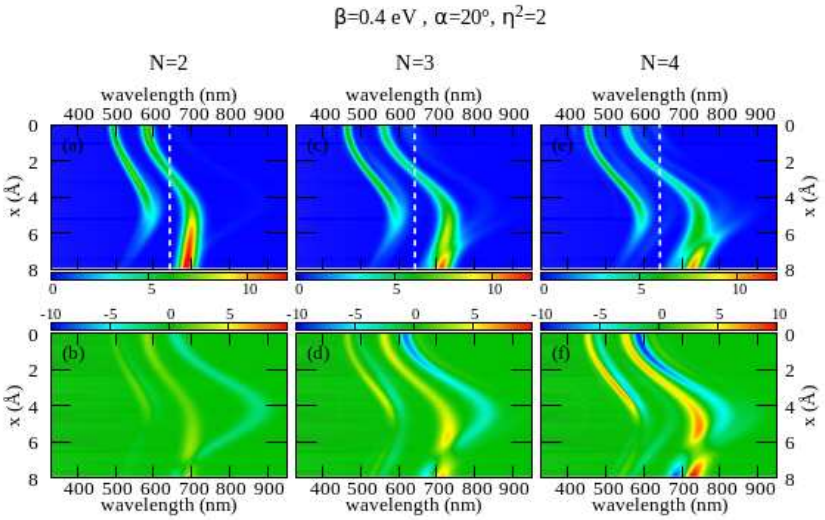

Figure C.5: ESM-CT: results for aggregates of 2, 3 and 4 molecules with the same molecular parameters as in figure 5.10 for β =0.4 eV, α=20° and η^2 = 2.

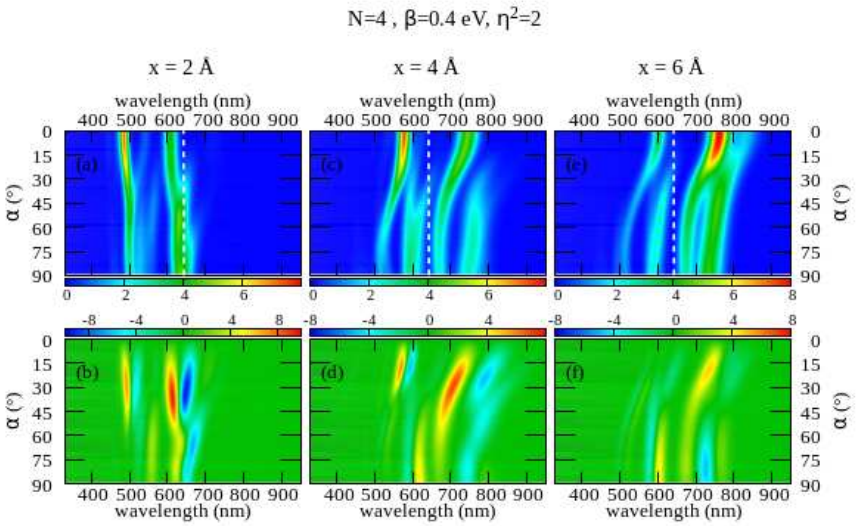

Figure C.6: ESM-CT: results as a function of the angle α for aggregates of 4 molecules with the same molecular parameters as in figure 5.10 for β =0.4 eV, η^2 = 2 ans different values of x =2, 4 and 6 Å.

Bibliography

[1] Ostroverkhova, O. Organic Optoelectronic Materials: Mechanisms and Applications, *Chemical Reviews*, *116* (22), 13279–13412, **2016-10**.

[2] Biscarini, F.; Coronado, E.; Painelli, A.; Yamashita, M. Materials for molecular electronics and magnetism, *Journal of Materials Chemistry C*, *9* (33), 10521–10523, **2021**.

[3] Yuan, L.; Lin, W.; Zheng, K.; He, L.; Huang, W. Far-red to near infrared analyte-responsive fluorescent probes based on organic fluorophore platforms for fluorescence imaging, *Chem. Soc. Rev.*, *42*, 622–661, **2013**.

[4] Jenkins, R.; Burdette, M. K.; Foulger, S. H. Mini-review: fluorescence imaging in cancer cells using dye-doped nanoparticles, *RSC Adv.*, *6*, 65459–65474, **2016**.

[5] Avirah, R. R.; Jayaram, D. T.; Adarsh, N.; Ramaiah, D. Squaraine dyes in PDT: from basic design to in vivo demonstration, *Org. Biomol. Chem.*, *10*, 911–920, **2012**.

[6] Schulz, M.; Mack, M.; Kolloge, O.; Lützen, A.; Schiek, M. Organic photodiodes from homochiral L-proline derived squaraine compounds with strong circular dichroism, *Phys. Chem. Chem. Phys.*, *19* (10), 6996–7008, **2017**.

[7] Brück, S.; Krause, C.; Turrisi, R.; Beverina, L.; Wilken, S.; Saak, W.; Lützen, A.; Borchert, H.; Schiek, M.; Parisi, J. Structure–property relationship of anilino-squaraines in organic solar cells, *Phys. Chem. Chem. Phys.*, *16*, 1067–1077, **2014**.

[8] Spencer, S.; Cody, J.; Misture, S.; Cona, B.; Heaphy, P.; Rumbles, G.; Andersen, J.; Collison, C. Critical Electron Transfer Rates for Exciton Dissociation Governed by Extent of Crystallinity in Small Molecule Organic Photovoltaics, *The Journal of Physical Chemistry C*, *118* (27), 14840–14847, **2014**.

[9] Mayerhöffer, U.; Deing, K.; Gruß, K.; Braunschweig, H.; Meerholz, K.; Würthner, F. Outstanding Short-Circuit Currents in BHJ Solar Cells Based on NIR-Absorbing Acceptor-Substituted Squaraines, *Angewandte Chemie International Edition*, *48* (46), 8776–8779, **2009**.

[10] Bagnis, D.; Beverina, L.; Huang, H.; Silvestri, F.; Yao, Y.; Yan, H.; Pagani, G. A.; Marks, T. J.; Facchetti, A. Marked Alkyl- vs Alkenyl-Substitutent Effects on Squaraine Dye Solid-State Structure, Carrier Mobility, and Bulk-Heterojunction Solar Cell Efficiency, *Journal of the American Chemical Society*, *132* (12), PMID: 20205468, 4074–4075, **2010**.

[11] Hu, W.-H.; Nüesch, F.; Giavazzi, D.; Jafarpour, M.; Hany, R.; Bauer, M. Squaraine Dyes for Single-Component Shortwave Infrared-Sensitive Photodiodes and Upconversion Photodetectors, *Advanced Optical Materials*, *n/a* (n/a), 2302105.

[12] Anderson, P. W. More Is Different: Broken symmetry and the nature of the hierarchical structure of science. *Science*, *177* (4047), 393–396, **1972**.

[13] Breuer, H.-P.; Petruccione, F., *The theory of open quantum systems*; Oxford University Press, USA: 2002.

[14] Painelli, A.; Terenziani, F. Optical Spectra of Push- Pull Chromophores in Solution: A Simple Model, *The Journal of Physical Chemistry A*, *104* (47), 11041–11048, **2000**.

[15] Boldrini, B.; Cavalli, E.; Painelli, A.; Terenziani, F. Polar Dyes in Solution: A Joint Experimental and Theoretical Study of Absorption and Emission Band Shapes, *J. Phys. Chem. A*, *106*, 6286–6294, **2002**.

[16] Painelli, A. Vibronic contribution to static NLO properties: exact results for the DA dimer, *Chemical Physics Letters*, *285* (5-6), 352–358, **1998**.

[17] Painelli, A. Amplification of NLO responses: vibronic and solvent effects in push-pull polyenes, *Chem. Phys.*, *245* (1), 185–197, **1999**.

[18] Barzoukas, M.; Blanchard-Desce, M. Molecular engineering of push–pull dipolar and quadrupolar molecules for two-photon absorption: A multivalence-bond states approach, *The Journal of Chemical Physics*, *113* (10), 3951–3959, **2000**.

[19] Terenziani, F.; Painelli, A.; Katan, C.; Charlot, M.; Blanchard-Desce, M. Charge Instability in Quadrupolar Chromophores: Symmetry Breaking and Solvatochromism, *Journal of the American Chemical Society*, *128* (49), PMID: 17147384, 15742–15755, **2006**.

[20] Albota, M. et al. Design of Organic Molecules with Large Two-Photon Absorption Cross Sections, *Science*, *281* (5383), 1653–1656, **1998**.

[21] Terenziani, F.; Sissa, C.; Painelli, A. Symmetry Breaking in Octupolar Chromophores: Solvatochromism and Electroabsorption, *The Journal of Physical Chemistry B*, *112* (16), PMID: 18376886, 5079–5087, **2008**.

[22] Lee, W.-H.; Lee, H.; Kim, J.-A.; Choi, J.-H.; Cho, M.; Jeon, S.-J.; Cho, B. R. Two-Photon Absorption and Nonlinear Optical Properties of Octupolar Molecules, *Journal of the American Chemical Society*, *123* (43), PMID: 11673997, 10658–10667, **2001**.

[23] Redfield, A. G. On the theory of relaxation processes, *IBM Journal of Research and Development*, *1* (1), 19–31, **1957**.

[24] Pollard, W. T.; Friesner, R. A. Solution of the Redfield equation for the dissipative quantum dynamics of multilevel systems, *The Journal of Chemical Physics*, *100* (7), 5054–5065, **1994**.

[25] Holstein, T. Studies of polaron motion: Part I. The molecular-crystal model, *Annals of Physics*, *8* (3), 325–342, **1959**.

[26] Fulton, R. L.; Gouterman, M. Vibronic Coupling. I. Mathematical Treatment for Two Electronic States, *The Journal of Chemical Physics*, *35* (3), 1059–1071, **2004**.

[27] Witkowski, A.; Moffitt, W. Electronic Spectra of Dimers: Derivation of the Fundamental Vibronic Equation, *The Journal of Chemical Physics*, *33* (3), 872–875, **2004**.

[28] Merrifield, R. E. Vibrational Structure of Molecular Exciton States, *The Journal of Chemical Physics*, *36* (9), 2519–2520, **2004**.

[29] Merrifield, R. E. Vibronic States of Dimers, *Radiation Research*, *20* (1), 154–158, **1963**.

[30] Balzer, F.; Kollmann, H.; Schulz, M.; Schnakenburg, G.; Lützen, A.; Schmidtmann, M.; Lienau, C.; Silies, M.; Schiek, M. Spotlight on Excitonic Coupling in Polymorphic and Textured Anilino Squaraine Thin Films, *Crystal Growth & Design*, *17* (12), 6455–6466, **2017**.

[31] Balzer, F.; Breuer, T.; Witte, G.; Schiek, M. Template and Temperature-Controlled Polymorph Formation in Squaraine Thin Films, *Langmuir*, *38* (30), PMID: 35858043, 9266–9277, **2022**.

[32] Funke, S.; Duwe, M.; Balzer, F.; Thiesen, P. H.; Hingerl, K.; Schiek, M. Determining the Dielectric Tensor of Microtextured Organic Thin Films by Imaging Mueller Matrix Ellipsometry, *The Journal of Physical Chemistry Letters*, *12* (12), PMID: 33739845, 3053–3058, **2021**.

[33] Balzer, F.; Abdullaeva, O. S.; Maderitsch, A.; Schulz, M.; Lützen, A.; Schiek, M. Nanoscale Polarization-Resolved Surface Photovoltage of a Pleochroic Squaraine Thin Film, *physica status solidi (b)*, *257* (3), 1900570, **2020**.

[34] Ryan, J. W.; Kirchartz, T.; Viterisi, A.; Nelson, J.; Palomares, E. Understanding the Effect of Donor Layer Thickness and a MoO_3 Hole Transport Layer on the Open-Circuit Voltage in Squaraine/C60 Bilayer Solar Cells, *The Journal of Physical Chemistry C*, *117* (39), 19866–19874, **2013**.

[35] Wei, G.; Wang, S.; Renshaw, K.; Thompson, M. E.; Forrest, S. R. Solution-Processed Squaraine Bulk Heterojunction Photovoltaic Cells, *ACS Nano*, *4* (4), PMID: 20359189, 1927–1934, **2010**.

[36] Chen, G.; Yokoyama, D.; Sasabe, H.; Hong, Z.; Yang, Y.; Kido, J. Optical and electrical properties of a squaraine dye in photovoltaic cells, *Applied Physics Letters*, *101* (8), 083904, **2012**.

[37] Cambarau, W.; Viterisi, A.; Ryan, J. W.; Palomares, E. Small molecule-based tandem solar cells with solution-processed and vacuum-processed photoactive layers, *Chem. Commun.*, *50*, 5349–5351, **2014**.

[38] Scholes, G. D.; Fleming, G. R.; Chen, L. X.; Aspuru-Guzik, A.; Buchleitner, A.; Coker, D. F.; Engel, G. S.; Van Grondelle, R.; Ishizaki, A.; Jonas, D. M., et al. Using coherence to enhance function in chemical and biophysical systems, *Nature*, *543* (7647), 647–656, **2017**.

[39] Maiuri, M.; Garavelli, M.; Cerullo, G. Ultrafast Spectroscopy: State of the Art and Open Challenges, *Journal of the American Chemical Society*, *142* (1), 3–15, **2020**.

[40] Conti, I.; Cerullo, G.; Nenov, A.; Garavelli, M. Ultrafast Spectroscopy of Photoactive Molecular Systems from First Principles: Where We Stand Today and Where We Are Going, *Journal of the American Chemical Society*, *142* (38), 16117–16139, **2020**.

[41] Giannetti, C.; Capone, M.; Fausti, D.; Fabrizio, M.; Parmigiani, F.; Mihailovic, D. Ultrafast optical spectroscopy of strongly correlated materials and high-temperature superconductors: a non-equilibrium approach, *Advances in Physics*, *65* (2), 58–238, **2016**.

[42] Morimoto, T.; Miyamoto, T.; Okamoto, H. Ultrafast Electron and Molecular Dynamics in Photoinduced and Electric-Field-Induced Neutral–Ionic Transitions, *Crystals*, *7* (5), 132, **2017**.

[43] Santoro, F.; Green, J. A.; Martinez-Fernandez, L.; Cerezo, J.; Improta, R. Quantum and semiclassical dynamical studies of nonadiabatic processes in solution: achievements and perspectives, *Phys. Chem. Chem. Phys.*, *23*, 8181–8199, **2021**.

[44] Mukamel, S., *Principles of nonlinear optical spectroscopy*; Oxford series in optical and imaging sciences; Oxford University Press: 1995, pp 358–359.

[45] Zurek, W. H. Decoherence, einselection, and the quantum origins of the classical, *Rev. Mod. Phys.*, *75*, 715–775, **2003**.

[46] Tafoya, S.; Large, S. J.; Liu, S.; Bustamante, C.; Sivak, D. A. Using a system's equilibrium behavior to reduce its energy dissipation in nonequilibrium processes, *Proceedings of the National Academy of Sciences*, *116* (13), 5920–5924, **2019**.

[47] Dovzhenko, D.; Lednev, M.; Mochalov, K.; Vaskan, I.; Rakovich, Y.; Karaulov, A.; Nabiev, I. Polariton-assisted manipulation of energy relaxation pathways: donor–acceptor role reversal in a tuneable microcavity, *Chem. Sci.*, *12*, 12794–12805, **2021**.

[48] Lindblad, G. On the generators of quantum dynamical semigroups, *Communications in Mathematical Physics*, *48* (2), 119–130, **1976**.

[49] Tanimura, Y. Numerically "exact" approach to open quantum dynamics: The hierarchical equations of motion (HEOM), *The Journal of Chemical Physics*, *153* (2), 020901, **2020**.

[50] Ishizaki, A.; Fleming, G. R. On the adequacy of the Redfield equation and related approaches to the study of quantum dynamics in electronic energy transfer, *The Journal of Chemical Physics*, *130* (23), 234110, **2009**.

[51] Chen, L.; Gelin, M. F.; Chernyak, V. Y.; Domcke, W.; Zhao, Y. Dissipative dynamics at conical intersections: simulations with the hierarchy equations of motion method, *Faraday Discussions*, *194*, 61–80, **2016**.

[52] Gelin, M. F.; Borrelli, R.; Chen, L. Hierarchical Equations-of-Motion Method for Momentum System–Bath Coupling, *The Journal of Physical Chemistry B*, *125* (18), 4863–4873, **2021**.

[53] Ikeda, T.; Scholes, G. D. Generalization of the hierarchical equations of motion theory for efficient calculations with arbitrary correlation functions, *The Journal of Chemical Physics*, *152* (20), 204101, **2020**.

[54] Palacino-González, E.; Gelin, M. F.; Domcke, W. Analysis of transient-absorption pump-probe signals of nonadiabatic dissipative systems: "Ideal" and "real" spectra, *The Journal of Chemical Physics*, *150* (20), 204102, **2019**.

[55] Gelin, M. F.; Palacino-Gonález, E.; Chen, L.; Domcke, W. Monitoring of Nonadiabatic Effects in Individual Chromophores by Femtosecond Double-Pump Single-Molecule Spectroscopy: A Model Study, *Molecules*, *24* (2), 231, **2019**.

[56] Rafiq, S.; Fu, B.; Kudisch, B.; Scholes, G. D. Interplay of vibrational wavepackets during an ultrafast electron transfer reaction, *Nature Chemistry*, *13* (1), 70–76, **2020**.

[57] Heshmatpour, C.; Malevich, P.; Plasser, F.; Menger, M.; Lambert, C.; Šanda, F.; Hauer, J. Annihilation Dynamics of Molecular Excitons Measured at a Single Perturbative Excitation Energy, *The Journal of Physical Chemistry Letters*, *11* (18), 7776–7781, **2020**.

[58] Rose, P. A.; Krich, J. J. Efficient numerical method for predicting nonlinear optical spectroscopies of open systems, *The Journal of Chemical Physics*, *154* (3), 034108, **2021**.

[59] Akhtar, P.; Caspy, I.; Nowakowski, P. J.; Malavath, T.; Nelson, N.; Tan, H.-S.; Lambrev, P. H. Two-Dimensional Electronic Spectroscopy of a Minimal Photosystem I Complex Reveals the Rate of Primary Charge Separation, *Journal of the American Chemical Society*, *143* (36), 14601–14612, **2021**.

[60] Higgins, J. S.; Lloyd, L. T.; Sohail, S. H.; Allodi, M. A.; Otto, J. P.; Saer, R. G.; Wood, R. E.; Massey, S. C.; Ting, P.-C.; Blankenship, R. E.; Engel, G. S. Photosynthesis tunes quantum-mechanical mixing of electronic and vibrational states to steer exciton energy transfer, *Proceedings of the National Academy of Sciences*, *118* (11), **2021**.

[61] Jang, S.; Jung, Y.; Silbey, R. J. Nonequilibrium generalization of Förster–Dexter theory for excitation energy transfer, *Chemical Physics*, *275* (1), Photoprocesses in Multichromophoric Molecular Assemblies, 319–332, **2002**.

[62] Policht, V. R.; Niedringhaus, A.; Willow, R.; Laible, P. D.; Bocian, D. F.; Kirmaier, C.; Holten, D.; Mančal, T.; Ogilvie, J. P. Hidden vibronic and excitonic structure and vibronic coherence transfer in the bacterial reaction center, *Science Advances*, *8* (1), **2022**.

[63] Nitzan, A., *Chemical dynamics in condensed phases : relaxation, transfer, and reactions in condensed molecular systems*; p. 384. Oxford University Press: Oxford, 2013.

[64] Reichardt, C. Solvatochromic Dyes as Solvent Polarity Indicators, *Chemical Reviews*, *94* (8), 2319–2358, **1994**.

[65] Marder, S. R.; Beratan, D. N.; Cheng, L.-T. Approaches for Optimizing the First Electronic Hyperpolarizability of Conjugated Organic Molecules, *Science*, *252* (5002), 103–106, **1991**.

[66] Marder, S. R.; Perry, J. W. Molecular materials for second-order nonlinear optical applications, *Advanced Materials*, *5* (11), 804–815, **1993**.

[67] Marder, S. R.; Kippelen, B.; Jen, A. K.-Y.; Peyghambarian, N. Design and synthesis of chromophores and polymers for electro-optic and photorefractive applications, *Nature*, *388* (6645), 845–851, **1997**.

[68] Castet, F.; Rodriguez, V.; Pozzo, J.-L.; Ducasse, L.; Plaquet, A.; Champagne, B. Design and Characterization of Molecular Nonlinear Optical Switches, *Accounts of Chemical Research*, *46* (11), 2656–2665, **2013**.

[69] Niko, Y.; Didier, P.; Mely, Y.; Konishi, G.-i.; Klymchenko, A. S. Bright and photostable push-pull pyrene dye visualizes lipid order variation between plasma and intracellular membranes, *Scientific Reports*, *6* (1), 18870, **2016**.

[70] Lee, W.-H.; Lai, J.-Z.; Hsu, Y.-H.; Cheng, F.-Y.; Luo, C.-L.; Huang, Y.-C.; Lin, T.-C.; Chien, F.-C. A two-photon fluorescence probe for cell membrane imaging under temporal-focusing multiphoton excitation microscopy (TFMPEM), *Chem. Commun.*, *57*, 13118–13121, **2021**.

[71] Horng, M. L. and Gardecki, J. A. and Papazyan, A. and Maroncelli, M. Subpicosecond Measurements of Polar Solvation Dynamics: Coumarin 153 Revisited, *J. Phys. Chem.*, *99* (48), 17311–17337, **1995**.

[72] Bardi, B.; Giavazzi, D.; Ferrari, E.; Iagatti, A.; Di Donato, M.; Phan Huu, D. K. A.; Di Maiolo, F.; Sissa, C.; Masino, M.; Lapini, A.; Painelli, A. Solid state solvation: a fresh view, *Mater. Horiz.*, *10*, 4172–4182, **2023**.

[73] Zwanzig, R. Ensemble Method in the Theory of Irreversibility, *The Journal of Chemical Physics*, *33* (5), 1338–1341, **2004**.

[74] Egorova, D.; Kühl, A.; Domcke, W. Modeling of ultrafast electron-transfer dynamics: multi-level Redfield theory and validity of approximations, *Chemical Physics*, *268* (1-3), 105–120, **2001**.

[75] Pisliakov, A. V.; Gelin, M. F.; Domcke, W. Detection of Electronic and Vibrational Coherence Effects in Electron-Transfer Systems by Femtosecond Time-Resolved Fluorescence Spectroscopy: Theoretical Aspects, *The Journal of Physical Chemistry A*, *107* (15), 2657–2666, **2003**.

[76] Balzer, B.; Stock, G. Modeling of decoherence and dissipation in nonadiabatic photoreactions by an effective-scaling nonsecular Redfield algorithm, *Chemical Physics*, *310* (1-3), 33–41, **2005**.

[77] Painelli, A. Vibronic contribution to static NLO properties: exact results for the DA dimer, *Chemical Physics Letters*, *285* (5), 352–358, **1998**.

[78] Sissa, C.; Delchiaro, F.; Di Maiolo, F.; Terenziani, F.; Painelli, A. Vibrational coherences in charge-transfer dyes: A non-adiabatic picture, *The Journal of Chemical Physics*, *141* (16), 164317, **2014**.

[79] Terenziani, F.; Painelli, A. Two-dimensional electronic-vibrational spectra: modeling correlated electronic and nuclear motion, *Physical Chemistry Chemical Physics*, *17* (19), 13074–13081, **2015**.

[80] Terenziani, F. and Painelli, A. and Girlando, A. and Metzger, R. M. From Solution to LangmuirBlodgett Films: Spectroscopic Study of a Zwitterionic Dye, *The Journal of Physical Chemistry B*, *108* (30), 10743–10750, **2004**.

[81] Painelli, A.; Terenziani, F. Multielectron Transfer in Clusters of Polar-Polarizable Chromophores, *Journal of the American Chemical Society*, *125* (19), 5624–5625, **2003**.

[82] Terenziani, F. and D'Avino, G. and Painelli A. Multichromophores for Nonlinear Optics: Designing the Material Properties by Electrostatic Interactions, *ChemPhysChem*, *8*, 2433–2444, **2007**.

[83] Terenziani, F.; D'Avino, G.; Painelli, A. Multichromophores for nonlinear optics: designing the material properties by electrostatic interactions, *ChemPhysChem*, *8* (17), 2433–2444, **2007**.

[84] Sanyal, S.; Sissa, C.; Terenziani, F.; Pati, S. K.; Painelli, A. Superlinear amplification of the first hyperpolarizability of linear aggregates of DANS molecules, *Physical Chemistry Chemical Physics*, *19* (36), 24979–24984, **2017**.

[85] Anzola, M.; Painelli, A. Aggregates of polar dyes: beyond the exciton model, *Phys. Chem. Chem. Phys.*, *23* (14), 8282–8291, **2021**.

[86] Zhong, C.; Bialas, D.; Spano, F. C. Unusual Non-Kasha Photophysical Behavior of Aggregates of Push–Pull Donor–Acceptor Chromophores, *The Journal of Physical Chemistry C*, *124* (3), 2146–2159, **2020**.

[87] Mulliken, R. S. Molecular Compounds and their Spectra. II, *Journal of the American Chemical Society*, *74* (3), 811–824, **1952**.

[88] Del Freo, L.; Painelli, A. Anharmonicity and NLO responses: an exact diagonalization study, *Chemical Physics Letters*, *338* (2-3), 208–216, **2001**.

[89] Borghi, G.-P.; Girlando, A.; Painelli, A.; Voit, J. Exact numerical diagonalization of one-dimensional interacting electrons non-adiabatically coupled to phonons, *EPL (Europhysics Letters)*, *34* (2), 127, **1996**.

[90] Del Freo, L.; Terenziani, F.; Painelli, A. Static nonlinear optical susceptibilities: Testing approximation schemes against exact results, *The Journal of Chemical Physics*, *116* (2), 755–761, **2002**.

[91] Roden, J.; Strunz, W. T.; Whaley, K. B.; Eisfeld, A. Accounting for intra-molecular vibrational modes in open quantum system description of molecular systems, *The Journal of Chemical Physics*, *137* (20), 204110, **2012**.

[92] Altland, A.; Simons, B. D., *Condensed Matter Field Theory*; Cambridge University Press: 2010.

[93] Klinduhov, N.; Boukheddaden, K. Vibronic Theory of Ultrafast Intersystem Crossing Dynamics in a Single Spin-Crossover Molecule at Finite Temperature beyond the Born–Oppenheimer Approximation, *The Journal of Physical Chemistry Letters*, *7* (4), 722–727, **2016**.

[94] Di Maiolo, F.; Painelli, A. Intermolecular Energy Transfer in Real Time, *Journal of Chemical Theory and Computation*, *14* (10), 5339–5349, **2018**.

[95] Di Maiolo, F.; Painelli, A. Dynamical disorder and resonance energy transfer: a novel quantum-classical approach, *Physical Chemistry Chemical Physics*, *22* (3), 1061–1068, **2020**.

[96] Kamiya, N. Quantum-to-classical reduction of quantum master equations, *Progress of Theoretical and Experimental Physics*, *2015* (4), 043A02, **2015**.

[97] Kühl, A.; Domcke, W. Multilevel Redfield description of the dissipative dynamics at conical intersections, *The Journal of Chemical Physics*, *116* (1), 263, **2002**.

[98] Thoss, M.; Wang, H.; Miller, W. H. Self-consistent hybrid approach for complex systems: Application to the spin-boson model with Debye spectral density, *The Journal of Chemical Physics*, *115* (7), 2991–3005, **2001**.

[99] Am-Shallem, M.; Levy, A.; Schaefer, I.; Kosloff, R. Three approaches for representing Lindblad dynamics by a matrix-vector notation, *arXiv preprint arXiv:1510.08634*, **2015**.

[100] Elsaesser, T.; Kaiser, W. Vibrational and Vibronic Relaxation of Large Polyatomic Molecules in Liquids, *Annual Review of Physical Chemistry*, *42* (1), 83–107, **1991**.

[101] Myers, A. B. Resonance Raman Intensities and Charge-Transfer Reorganization Energies, *Chemical Reviews*, *96* (3), 911–926, **1996**.

[102] Terenziani, F.; Painelli, A.; Comoretto, D. Solvation Effects and Inhomogeneous Broadening in Optical Spectra of Phenol Blue, *The Journal of Physical Chemistry A*, *104* (47), 11049–11054, **2000**.

[103] Painelli, A.; Terenziani, F. Push–pull chromophores: NLO responses, solvatochromism and vibrational spectra in a simple non-perturbative model, *Synthetic Metals*, *116* (1-3), 135–138, **2001**.

[104] Binder, R.; Burghardt, I. First-principles quantum simulations of exciton diffusion on a minimal oligothiophene chain at finite temperature, *Faraday Discuss.*, *221*, 406–427, **2020**.

[105] Di Maiolo, F.; Brey, D.; Binder, R.; Burghardt, I. Quantum dynamical simulations of intra-chain exciton diffusion in an oligo (para-phenylene vinylene) chain at finite temperature, *The Journal of Chemical Physics*, *153* (18), 184107, **2020**.

[106] Egorova, D.; Thoss, M.; Domcke, W.; Wang, H. Modeling of ultrafast electron-transfer processes: Validity of multilevel Redfield theory, *The Journal of Chemical Physics*, *119* (5), 2761–2773, **2003**.

[107] Egorova, D.; Domcke, W. Quantum dynamical simulations of ultrafast photoinduced electron-transfer processes, *Journal of Photochemistry and Photobiology A: Chemistry*, *166* (1-3), 19–31, **2004**.

[108] Egorova, D.; Domcke, W. Coherent vibrational dynamics during ultrafast photoinduced electron-transfer reactions: quantum dynamical simulations within multilevel Redfield theory, *Chemical Physics Letters*, *384* (1-3), 157–164, **2004**.

[109] Yan, Y. J.; Mukamel, S. Semiclassical dynamics in Liouville space: Application to molecular electronic spectroscopy, *J. Chem. Phys.*, *88* (9), 5735–5748, **1988**.

[110] Valleau, S.; Eisfeld, A.; Aspuru-Guzik, A. On the alternatives for bath correlators and spectral densities from mixed quantum-classical simulations, *The Journal of Chemical Physics*, *137* (22), 224103, **2012**.

[111] Pachón, L. A.; Brumer, P. Direct experimental determination of spectral densities of molecular complexes, *The Journal of Chemical Physics*, *141* (17), 174102, **2014**.

[112] Wang, X.; Ritschel, G.; Wüster, S.; Eisfeld, A. Open quantum system parameters for light harvesting complexes from molecular dynamics, *Physical Chemistry Chemical Physics*, *17* (38), 25629–25641, **2015**.

[113] Liptay, W. Electrochromism and Solvatochromism, *Angewandte Chemie International Edition in English*, *8* (3), 177–188, **1969**.

[114] Di Bella, S. and Marks, T. J. and Ratner, M. A. Environmental Effects on Nonlinear Optical Chromophore Performance. Calculation of Molecular Quadratic Hyperpolarizabilities in Solvating Media, *J. Am. Chem. Soc.*, *116* (10), 4440–4445, **1994**.

[115] Lakowicz, J. R., *Principles of Fluorescence Spectroscopy*; Springer US: 1999, p 698.

[116] Tomasi, J.; Mennucci, B.; Cammi, R. Quantum Mechanical Continuum Solvation Models, *Chem. Rev.*, *105*, 2999–3094, **2005**.

[117] Lunkenheimer, B.; Köhn Solvent Effects on Electronically Excited States Using the Conductor- Like Screening Model and the Second-Order Correlated Method ADC(2), *J. Chem. Theory Comput.*, *9*, 977–994, **2013**.

[118] Bjorgaard, J. A.; Kuzmenko, V.; Velizhanin, K. A.; Tretiak, S. Solvent effects in time-dependent self-consistent field methods. I. Optical response calculations, *The Journal of Chemical Physics*, *142* (4), 044103, **2015-01**.

[119] Guido, C. A.; Caprasecca, S. On the description of the environment polarization response to electronic transitions, *Int. J. Quantum Chem.*, *119* (1), e25711, **2019**.

[120] Vreven, T.; Morokuma, K. In *Chapter 3 Hybrid Methods: ONIOM(QM:MM) and QM/MM*, Spellmeyer, D. C., Ed.; Annual Reports in Computational Chemistry, Vol. 2; Elsevier: 2006, pp 35–51.

[121] Phan Huu, D. K. A.; Dhali, R.; Pieroni, C.; Di Maiolo, F.; Sissa, C.; Terenziani, F.; Painelli, A. Antiadiabatic View of Fast Environmental Effects on Optical Spectra, *Phys. Rev. Lett.*, *124*, 107401, **2020**.

[122] Dhali, R.; Phan Huu, D. K. A.; Terenziani, F.; Sissa, C.; Painelli, A. Thermally activated delayed fluorescence: A critical assessment of environmental effects on the singlet–triplet energy gap, *154* (13), 134112, **2021**.

[123] Bulović, V.; Shoustikov, A.; Baldo, M.; Bose, E.; Kozlov, V.; Thompson, M.; Forrest, S. Bright, saturated, red-to-yellow organic light-emitting devices based on polarization-induced spectral shifts, *Chemical Physics Letters*, *287* (3-4), 455–460, **1998-05**.

[124] Bulović, V.; Deshpande, R.; Thompson, M.; Forrest, S. Tuning the color emission of thin film molecular organic light emitting devices by the solid state solvation effect, *Chemical Physics Letters*, *308* (3-4), 317–322, **1999-07**.

[125] Green, A. P.; Butler, K. T.; Buckley, A. R. Tuning of the emission energy of fluorophores using solid state solvation for efficient luminescent solar concentrators, *Applied Physics Letters*, *102* (13), 133501, **2013-04**.

[126] Leblebici, S. Y.; Chen, T. L.; Olalde-Velasco, P.; Yang, W.; Ma, B. Reducing Exciton Binding Energy by Increasing Thin Film Permittivity: An Effective Approach To Enhance Exciton Separation Efficiency in Organic Solar Cells, *ACS Applied Materials & Interfaces*, *5* (20), 10105–10110, **2013-10**.

[127] Torabi, S.; Jahani, F.; Severen, I. V.; Kanimozhi, C.; Patil, S.; Havenith, R. W. A.; Chiechi, R. C.; Lutsen, L.; Vanderzande, D. J. M.; Cleij, T. J.; Hummelen, J. C.; Koster, L. J. A. Strategy for Enhancing the Dielectric Constant of Organic Semiconductors Without Sacrificing Charge Carrier Mobility and Solubility, *Advanced Functional Materials*, *25* (1), 150–157, **2014-10**.

[128] Liu, X.; Xie, B.; Duan, C.; Wang, Z.; Fan, B.; Zhang, K.; Lin, B.; Colberts, F. J. M.; Ma, W.; Janssen, R. A. J.; Huang, F.; Cao, Y. A high dielectric constant non-fullerene acceptor for efficient bulk-heterojunction organic solar cells, *Journal of Materials Chemistry A*, *6* (2), 395–403, **2018**.

[129] Sami, S.; Alessandri, R.; Broer, R.; Havenith, R. W. A. How Ethylene Glycol Chains Enhance the Dielectric Constant of Organic Semiconductors: Molecular Origin and Frequency Dependence, *ACS Applied Materials & Interfaces*, *12* (15), 17783–17789, **2020-03**.

[130] Méhes, G.; Goushi, K.; Potscavage, W. J.; Adachi, C. Influence of host matrix on thermally-activated delayed fluorescence: Effects on emission lifetime, photoluminescence quantum yield, and device performance, *Organic Electronics*, *15* (9), 2027–2037, **2014**.

[131] Dias, F. B.; Santos, J.; Graves, D. R.; Data, P.; Nobuyasu, R. S.; Fox, M. A.; Batsanov, A. S.; Palmeira, T.; Berberan-Santos, M. N.; Bryce, M. R.; Monkman, A. P. The Role of Local Triplet Excited States and D-A Relative Orientation in Thermally Activated Delayed Fluorescence: Photophysics and Devices, *Advanced Science*, *3* (12), 1600080, **2016**.

[132] Etherington, M. K.; Gibson, J.; Higginbotham, H. F.; Penfold, T. J.; Monkman, A. P. Revealing the spin–vibronic coupling mechanism of thermally activated delayed fluorescence, *Nature Communications*, *7* (1), 13680, **2016**.

[133] Samanta, P. K.; Kim, D.; Coropceanu, V.; Brédas, J.-L. Up-Conversion Intersystem Crossing Rates in Organic Emitters for Thermally Activated Delayed Fluorescence: Impact of the Nature of Singlet vs Triplet Excited States, *Journal of the American Chemical Society*, *139* (11), 4042–4051, **2017**.

[134] Mewes, J.-M. Modeling TADF in organic emitters requires a careful consideration of the environment and going beyond the Franck–Condon approximation, *Physical Chemistry Chemical Physics*, *20* (18), 12454–12469, **2018**.

[135] Phan Huu, D. K. A.; Saseendran, S.; Painelli, A. Effective models for TADF: the role of the medium polarizability, *J. Mater. Chem. C*, *10*, 4620–4628, **2022**.

[136] Gillett, A. J.; Pershin, A.; Pandya, R.; Feldmann, S.; Sneyd, A. J.; Alvertis, A. M.; Evans, E. W.; Thomas, T. H.; Cui, L.-S.; Drummond, B. H.; Scholes, G. D.; Olivier, Y.; Rao, A.; Friend, R. H.; Beljonne, D. Dielectric control of reverse intersystem crossing in thermally activated delayed fluorescence emitters, *Nature Materials*, *21* (10), 1150–1157, **2022**.

[137] Dos Santos, P. L.; Ward, J. S.; Bryce, M. R.; Monkman, A. P. Using Guest–Host Interactions To Optimize the Efficiency of TADF OLEDs, *The Journal of Physical Chemistry Letters*, *7* (17), 3341–3346, **2016**.

[138] Serevičius, T.; Skaisgiris, R.; Dodonova, J.; Fiodorova, I.; Genevičius, K.; Tumkevičius, S.; Kazlauskas, K.; Juršėnas, S. Temporal Dynamics of Solid-State Thermally Activated Delayed Fluorescence: Disorder or Ultraslow Solvation?, *The Journal of Physical Chemistry Letters*, *13* (7), 1839–1844, **2022-02**.

[139] Phan Huu, D. K. A.; Saseendran, S.; Dhali, R.; Franca, L. G.; Stavrou, K.; Monkman, A.; Painelli, A. Thermally Activated Delayed Fluorescence: Polarity, Rigidity, and Disorder in Condensed Phases, *Journal of the American Chemical Society*, *144* (33), 15211–15222, **2022-08**.

[140] Castner, E. W.; Maroncelli, M.; Fleming, G. R. Subpicosecond resolution studies of solvation dynamics in polar aprotic and alcohol solvents, *The Journal of Chemical Physics*, *86* (3), 1090–1097, **1987-02**.

[141] Sissa, C.; Painelli, A.; Blanchard-Desce, M.; Terenziani, F. Fluorescence Anisotropy Spectra Disclose the Role of Disorder in Optical Spectra of Branched Intramolecular-Charge-Transfer Molecules, *J. Phys. Chem. B*, *115* (21), 7009–7020, **2011**.

[142] Ahmad, Z. In *Dielectric Material*; InTech: 2012-10.

[143] Northey, T.; Stacey, J.; Penfold, T. J. The role of solid state solvation on the charge transfer state of a thermally activated delayed fluorescence emitter, *Journal of Materials Chemistry C*, *5* (42), 11001–11009, **2017**.

[144] Deng, C.; Zhang, L.; Wang, D.; Tsuboi, T.; Zhang, Q. Exciton- and Polaron-Induced Reversible Dipole Reorientation in Amorphous Organic Semiconductor Films, *Advanced Optical Materials*, *7* (8), 1801644, **2019-02**.

[145] Madigan, C. F.; Bulović, V. Solid State Solvation in Amorphous Organic Thin Films, *Physical Review Letters*, *91* (24), 247403, **2003-12**.

[146] Cotts, B. L.; McCarthy, D. G.; Noriega, R.; Penwell, S. B.; Delor, M.; Devore, D. D.; Mukhopadhyay, S.; Vries, T. S. D.; Ginsberg, N. S. Tuning Thermally Activated Delayed Fluorescence Emitter Photophysics through Solvation in the Solid State, *ACS Energy Letters*, *2* (7), 1526–1533, **2017-06**.

[147] De Vries, X.; Coehoorn, R. Vibrational mode contribution to the dielectric permittivity of disordered small-molecule organic semiconductors, *Physical Review Materials*, *4* (8), 085602, **2020-08**.

[148] Olivier, Y.; Yurash, B.; Muccioli, L.; D'Avino, G.; Mikhnenko, O.; Sancho-García, J. C.; Adachi, C.; Nguyen, T.-Q.; Beljonne, D. Nature of the singlet and triplet excitations mediating thermally activated delayed fluorescence, *Physical Review Materials*, *1* (7), 075602, **2017**.

[149] Terenziani, F. and Painelli, A. Two-dimensional electronic-vibrational spectra: modeling correlated electronic and nuclear motion, *Phys. Chem. Chem. Phys.*, *17*, 13074–13081, **2015**.

[150] Weaver, J. B.; Kozuch, J.; Kirsh, J. M.; Boxer, S. G. Nitrile Infrared Intensities Characterize Electric Fields and Hydrogen Bonding in Protic, Aprotic, and Protein Environments, *Journal of the American Chemical Society*, *144* (17), 7562–7567, **2022-04**.

[151] Terenziani, F. and Painelli, A. and Comoretto, D. Solvation Effects and Inhomogeneous Broadening in Optical Spectra of Phenol Blue, *The Journal of Physical Chemistry A*, *104* (47), 11049–11054, **2000**.

[152] Painelli, A. and Terenziani, F. Optical Spectra of Push-Pull Chromophores in Solution: A Simple Model, *The Journal of Physical Chemistry A*, *104* (47), 11041–11048, **2000**.

[153] Painelli, A.; Terenziani, F. Push–pull chromophores: NLO responses, solvatochromism and vibrational spectra in a simple non-perturbative model, *Synthetic Metals*, *116* (1-3), 135–138, **2001**.

[154] Di Maiolo, F.; Painelli, A. Dynamical disorder and resonance energy transfer: a novel quantum-classical approach, *Physical Chemistry Chemical Physics*, *22* (3), 1061–1068, **2020**.

[155] Terenziani, F.; Painelli, A. Time-resolved spectra of polar-polarizable chromophores in solution, *Chem. Phys.*, *295* (1), 35–46, **2003**.

[156] Diósi, L. Hybrid quantum-classical master equations, *Physica Scripta*, *2014* (T163), 014004, **2014**.

[157] Diósi, L.; Gisin, N.; Strunz, W. T. Quantum approach to coupling classical and quantum dynamics, *Phys. Rev. A*, *61*, 022108, **2000**.

[158] Xu, R.-X.; Tian, B.-L.; Xu, J.; Shi, Q.; Yan, Y. Hierarchical quantum master equation with semiclassical Drude dissipation, *The Journal of Chemical Physics*, *131* (21), 214111, **2009**.

[159] Kelly, A.; van Zon, R.; Schofield, J.; Kapral, R. Mapping quantum-classical Liouville equation: Projectors and trajectories, *The Journal of Chemical Physics*, *136* (8), 084101, **2012**.

[160] Painelli, A.; Terenziani, F. A non-perturbative approach to solvatochromic shifts of push–pull chromophores, *Chemical Physics Letters*, *312* (2), 211–220, **1999**.

[161] Jelley, E. E. Spectral Absorption and Fluorescence of Dyes in the Molecular State, *138* (3502), 1009–1010, **1936**.

[162] Scheibe, G. v. Reversible Polymerisation als Ursache neuartiger Absorptionsbanden von Farbstoffen, *Kolloid-Zeitschrift*, *82*, 1–14, **1938**.

[163] Frenkel, J. On the Transformation of light into Heat in Solids. I, *Phys. Rev.*, *37*, 17–44, **1931**.

[164] Davidov, A. S., *Theory of Molecular Excitons*; Plenum Press: 1971.

[165] Agranovich, V., *Excitations in Organic Solids*; Oxford University Press: 2008.

[166] Kasha, M.; Rawls, H. R.; El-Bayoumi, M. A., *Pure and Applied Chemistry*, *11* (3-4), 371–392, **1965**.

[167] McRae, E. G.; Kasha, M. Enhancement of Phosphorescence Ability upon Aggregation of Dye Molecules, *The Journal of Chemical Physics*, *28* (4), 721–722, **2004**.

[168] Hochstrasser, R. M.; Kasha, M. Applocation of the exciton model to mono-molecular lamellar systems, *Photochemistry and Photobiology*, *3* (4), 317–331, **1964**.

[169] Hestand, N. J. and Spano, F. C. Expanded Theory of H- and J-Molecular Aggregates: The Effects of Vibronic Coupling and Intermolecular Charge Transfer, *Chem. Rev.*, *118*, 7069–7163, **2018**.

[170] Terenziani, F.; Painelli, A.; Katan, C.; Charlot, M.; Blanchard-Desce, M. Charge instability in quadrupolar chromophores: Symmetry breaking and solvatochromism, *J. Am. Chem. Soc.*, *128* (49), 15742–15755, **2006**.

[171] Bardi, B.; Krzeszewski, M.; Gryko, D. T.; Painelli, A.; Terenziani, F. Excited-State Symmetry Breaking in an Aza-Nanographene Dye, *Chemistry–A European Journal*, *25* (61), 13930–13938, **2019**.

[172] Law, K. Y. Organic photoconductive materials: recent trends and developments, *Chemical Reviews*, *93* (1), 449–486, **1993**.

[173] Schwarzl, R.; Heim, P.; Schiek, M.; Grimaldi, D.; Hohenau, A.; Krenn, J. R.; Koch, M. Transient absorption microscopy setup with multi-ten-kilohertz shot-to-shot subtraction and discrete Fourier analysis, *Opt. Express*, *30* (19), 34385–34395, **2022**.

[174] Anzola, M.; Maiolo, F. D.; Painelli, A. Optical spectra of molecular aggregates and crystals: testing approximation schemes, *Phys. Chem. Chem. Phys.*, *21* (36), 19816–19824, **2019**.

[175] Duan, H.-G.; Nalbach, P.; Prokhorenko, V. I.; Mukamel, S.; Thorwart, M. On the origin of oscillations in two-dimensional spectra of excitonically-coupled molecular systems, *New Journal of Physics*, *17* (7), 072002, **2015**.

[176] Halpin, A.; Johnson, P. J. M.; Tempelaar, R.; Murphy, R. S.; Knoester, J.; Jansen, T. L. C.; Miller, R. J. D. Two-Dimensional Spectroscopy of a Molecular Dimer Unveils the Effects of Vibronic Coupling on Exciton Coherences, *Nature chemistry*, *6* (3), 196–201, **2014**.

[177] Zsila, F.; Bikádi, Z.; Keresztes, Z.; Deli, J.; Simonyi, M. Investigation of the Self-Organization of Lutein and Lutein Diacetate by Electronic Absorption, Circular Dichroism Spectroscopy, and Atomic Force Microscopy, *The Journal of Physical Chemistry B*, *105* (39), 9413–9421, **2001**.

[178] Egelhaaf, H.-J.; Gierschner, J.; Oelkrug, D. Characterization of oriented oligo(phenylenevinylene) films and nano-aggregates by UV/Vis-absorption and fluorescence spectroscopy, *Synthetic Metals*, *83* (3), 221–226, **1996**.

[179] Gierschner, J.; Egelhaaf, H.-J.; Oelkrug, D. Absorption, fluorescence and light scattering of oligothiophene and oligophenylenevinylene nanoaggregates, *Synthetic Metals*, *84* (1), 529–530, **1997**.

[180] Varghese, S.; Park, S. K.; Casado, S.; Fischer, R. C.; Resel, R.; Milián-Medina, B.; Wannemacher, R.; Park, S. Y.; Gierschner, J. Stimulated Emission Properties of Sterically Modified Distyrylbenzene-Based H-Aggregate Single Crystals, *The Journal of Physical Chemistry Letters*, *4* (10), 1597–1602, **2013**.

[181] Gierschner, J.; Lüer, L.; Milián-Medina, B.; Oelkrug, D.; Egelhaaf, H.-J. Highly Emissive H-Aggregates or Aggregation-Induced Emission Quenching? The Photophysics of All-Trans para-Distyrylbenzene, *The Journal of Physical Chemistry Letters*, *4* (16), 2686–2697, **2013**.

[182] Ahrens, M. J.; Sinks, L. E.; Rybtchinski, B.; Liu, W.; Jones, B. A.; Giaimo, J. M.; Gusev, A. V.; Goshe, A. J.; Tiede, D. M.; Wasielewski, M. R. Self-Assembly of Supramolecular Light-Harvesting Arrays from Covalent Multi-Chromophore Perylene-3,4:9,10-bis(dicarboximide) Building Blocks, *Journal of the American Chemical Society*, *126* (26), 8284–8294, **2004**.

[183] Lim, J. M.; Kim, P.; Yoon, M.-C.; Sung, J.; Dehm, V.; Chen, Z.; Würthner, F.; Kim, D. Exciton delocalization and dynamics in helical π-stacks of self-assembled perylene bisimides, *Chem. Sci.*, *4*, 388–397, **2013**.

[184] Kasha, M. Characterization of electronic transitions in complex molecules, *Discuss. Faraday Soc.*, *9*, 14–19, **1950**.

[185] Möbius, D. Scheibe Aggregates, *Advanced Materials*, *7* (5), 437–444, **1995**.

[186] Liu, H.; Shen, L.; Cao, Z.; Li, X. Covalently linked perylenetetracarboxylic diimide dimers and trimers with rigid "J-type" aggregation structure, *Phys. Chem. Chem. Phys.*, *16*, 16399–16406, **2014**.

[187] De Boer, S.; Wiersma, D. A. Dephasing-induced damping of superradiant emission in J-aggregates, *Chemical Physics Letters*, *165* (1), 45–53, **1990**.

[188] Ohno, O.; Kaizu, Y.; Kobayashi, H. J-aggregate formation of a water-soluble porphyrin in acidic aqueous media, *The Journal of Chemical Physics*, *99* (5), 4128–4139, **1993**.

[189] Shen, C.-A.; Würthner, F. NIR-emitting squaraine J-aggregate nanosheets, *Chem. Commun.*, *56*, 9878–9881, **2020**.

[190] Spano, F. C. The Spectral Signatures of Frenkel Polarons in H- and J-Aggregates, *Acc. Chem. Res.*, *43* (3), 429–439, **2010**.

[191] Fulton, R. L.; Gouterman, M. Vibronic Coupling. II. Spectra of Dimers, *The Journal of Chemical Physics*, *41* (8), 2280–2286, **2004**.

[192] McRae, E. Molecular Vibrations in the Exciton Theory for Molecular Aggregates. I. General Theory, *Australian Journal of Chemistry*, *14*, 329–343, **1961**.

[193] Philpott, M. R. Theory of the Coupling of Electronic and Vibrational Excitations in Molecular Crystals and Helical Polymers, *The Journal of Chemical Physics*, *55* (5), 2039–2054, **2003**.

[194] Spano, F. C. Absorption in regio-regular poly(3-hexyl)thiophene thin films: Fermi resonances, interband coupling and disorder, *Chemical Physics*, *325* (1), 22–35, **2006**.

[195] Kistler, K. A.; Pochas, C. M.; Yamagata, H.; Matsika, S.; Spano, F. C. Absorption, Circular Dichroism, and Photoluminescence in Perylene Diimide Bichromophores: Polarization-Dependent H- and J-Aggregate Behavior, *The Journal of Physical Chemistry B*, *116* (1), 77–86, **2012**.

[196] Austin, A.; Hestand, N. J.; McKendry, I. G.; Zhong, C.; Zhu, X.; Zdilla, M. J.; Spano, F. C.; Szarko, J. M. Enhanced Davydov Splitting in Crystals of a Perylene Diimide Derivative, *The Journal of Physical Chemistry Letters*, *8* (6), 1118–1123, **2017**.

[197] Zhong, C.; Bialas, D.; Collison, C. J.; Spano, F. C. Davydov Splitting in Squaraine Dimers, *The Journal of Physical Chemistry C*, *123* (30), 18734–18745, **2019**.

[198] Higgins, D. A.; Reid, P. J.; Barbara, P. F. Structure and Exciton Dynamics in J-Aggregates Studied by Polarization-Dependent Near-Field Scanning Optical Microscopy, *The Journal of Physical Chemistry*, *100* (4), 1174–1180, **1996**.

[199] Scheblykin, I.; Varnavsky, O.; Verbouwe, W.; De Backer, S.; Van der Auweraer, M.; Vitukhnovsky, A. Relaxation dynamics of excitons in J-aggregates revealing a two-component Davydov splitting, *Chemical Physics Letters*, *282* (3), 250–256, **1998**.

[200] Von Berlepsch, H.; Möller, S.; Dähne, L. Optical Properties of Crystalline Pseudoisocyanine (PIC), *The Journal of Physical Chemistry B*, *105* (24), 5689–5699, **2001**.

[201] Gierschner, J.; Huang, Y.-S.; Van Averbeke, B.; Cornil, J.; Friend, R. H.; Beljonne, D. Excitonic versus electronic couplings in molecular assemblies: The importance of non-nearest neighbor interactions, *The Journal of Chemical Physics*, *130* (4), 044105, **2009**.

[202] Aldo Brillante, C. T.; Zauli, C. The first $\pi^*\leftarrow\pi$ transition of the benzene single crystal in polarized light, *Molecular Physics*, *23* (6), 1179–1188, **1972**.

[203] Brillante, A.; Philpott, M. R.; Schlosser, D. W. Exciton transitions in quasi-one-dimensional crystals. 9-Cyanoanthracene, *The Journal of Chemical Physics*, *71* (3), 1050–1057, **2008**.

[204] Rivalta, A.; Salzillo, T.; Venuti, E.; Della Valle, R. G.; Sokolovič, B.; Werzer, O.; Brillante, A. Bulk and Surface-Stabilized Structures of Paracetamol Revisited by Raman Confocal Microscopy, *ACS Omega*, *3* (8), 9564–9571, **2018**.

[205] Sanyal, S.; Painelli, A.; Pati, S. K.; Terenziani, F.; Sissa, C. Aggregates of quadrupolar dyes for two-photon absorption: the role of intermolecular interactions, *Phys. Chem. Chem. Phys.*, *18* (40), 28198–28208, **2016**.

[206] Zheng, C.; Zhong, C.; Collison, C. J.; Spano, F. C. Non-Kasha behavior in quadrupolar dye aggregates: The red-shifted H-aggregate, *J. Phys. Chem. C*, *123* (5), 3203–3215, **2019**.

[207] Terenziani, F.; Painelli, A. Supramolecular interactions in clusters of polar and polarizable molecules, *Phys. Rev. B*, *68* (16), 165405, **2003**.

[208] Chang, X.; Balooch Qarai, M.; Spano, F. C. Intermolecular Charge Transfer in H- and J-Aggregates of Donor–Acceptor–Donor Chromophores: The Curious Case of Bithiophene-DPP, *The Journal of Physical Chemistry C*, *126* (44), 18784–18795, **2022**.

[209] Scholes, G. D. Long-Range Resonance Energy Transfer in Molecular Systems, *Annual Review of Physical Chemistry*, *54* (1), 57–87, **2003**.

[210] Anzola, M.; Sissa, C.; Painelli, A.; Hassanali, A. A.; Grisanti, L. Understanding Förster Energy Transfer through the Lens of Molecular Dynamics, *Journal of Chemical Theory and Computation*, *16* (12), 7281–7288, **2020**.

[211] Craig, D. P.; Walmsley, S. H., *Excitons in Molecular Crystals*; Benjamin: 1968.

[212] Kasha, M. Energy Transfer Mechanism and the Molecular Exciton Model for Molecular Aggregates, *Radiat. Res.*, *3*, 317–331, **1964**.

[213] Knoester, J. Modeling the optical properties of excitons in linear and tubular J-aggregates, *International Journal of Photoenergy*, *2006*, 1–10, **2006**.

[214] Maurer, R. J.; Askerka, M.; Batista, V. S.; Tully, J. C. Ab initio tensorial electronic friction for molecules on metal surfaces: Nonadiabatic vibrational relaxation, *Phys. Rev. B*, *94*, 115432, **2016**.

[215] Th. Förster 10th Spiers Memorial Lecture. Transfer mechanisms of electronic excitation, *Discuss. Faraday Soc.*, *27*, 7–17, **1959**.

[216] Th. Förster In *Modern Quantum Chemistry*, Sinanoglu, O., Ed.; Academic Press: 1965, p 93.

[217] Swathi, K.; Sissa, C.; Painelli, A.; Thomas, K. G. Supramolecular chirality: a caveat in assigning the handedness of chiral aggregates, *Chem. Commun.*, *56* (59), 8281–8284, **2020**.

[218] Bardi, B.; Dall'Agnese, C.; Tassé, M.; Ladeira, S.; Painelli, A.; Moineau-Chane Ching, K. I.; Terenziani, F. Multistimuli Responsive Materials from Benzothiadiazole Based Charge Transfer Chromophores: Interdependence of Optical Properties and Aggregation, *ChemPhotoChem*, *2*, 1027–1037, **2018**.

[219] Sissa, C.; Manna, A. K.; Terenziani, F.; Painelli, A.; Pati, S. K. Beyond the Förster formulation for resonance energy transfer: the role of dark states, *Phys. Chem. Chem. Phys.*, *13*, 12734–12744, **2011**.

[220] Krueger, B. P.; Scholes, G. D.; Fleming, G. R. Calculation of Couplings and Energy-Transfer Pathways between the Pigments of LH2 by the ab Initio Transition Density Cube Method, *The Journal of Physical Chemistry B*, *102* (27), 5378–5386, **1998**.

[221] Madjet, M. E.; Abdurahman, A.; Renger, T. Intermolecular Coulomb Couplings from Ab Initio Electrostatic Potentials: Application to Optical Transitions of Strongly Coupled Pigments in Photosynthetic Antennae and Reaction Centers, *The Journal of Physical Chemistry B*, *110* (34), 17268–17281, **2006**.

[222] Olaya-Castro, A.; Scholes, G. D. Energy transfer from Förster–Dexter theory to quantum coherent light-harvesting, *International Reviews in Physical Chemistry*, *30* (1), 49–77, **2011**.

[223] Wong, K. F.; Bagchi, B.; Rossky, P. J. Distance and Orientation Dependence of Excitation Transfer Rates in Conjugated Systems: Beyond the Förster Theory, *The Journal of Physical Chemistry A*, *108* (27), 5752–5763, **2004**.

[224] Scholes, G. D.; Curutchet, C.; Mennucci, B.; Cammi, R.; Tomasi, J. How Solvent Controls Electronic Energy Transfer and Light Harvesting, *The Journal of Physical Chemistry B*, *111* (25), 6978–6982, **2007**.

[225] Schröter, M.; Ivanov, S.; Schulze, J.; Polyutov, S.; Yan, Y.; Pullerits, T.; Kühn, O. Exciton–vibrational coupling in the dynamics and spectroscopy of Frenkel excitons in molecular aggregates, *Physics Reports*, *567*, 1–78, **2015**.

[226] Valeur, B.; Berberan-Santos, M. N., *Molecular Fluorescence: Principles and Applications*; Wiley-VCH Verlag GmbH & Co. KGaA: 2012.

[227] Malý, P.; Somsen, O. J. G.; Novoderezhkin, V. I.; Mančal, T.; van Grondelle, R. The Role of Resonant Vibrations in Electronic Energy Transfer, *ChemPhysChem*, *17* (9), 1356–1368, **2016**.

[228] Bhattacharyya, P.; Fleming, G. R. The role of resonant nuclear modes in vibrationally assisted energy transport: The LHCII complex, *The Journal of Chemical Physics*, *153* (4), 044119, **2020**.

[229] Tiwari, V.; Peters, W. K.; Jonas, D. M. Electronic energy transfer through non-adiabatic vibrational-electronic resonance. I. Theory for a dimer, *The Journal of Chemical Physics*, *147* (15), 154308, **2017**.

[230] Li, Z.-Z.; Ko, L.; Yang, Z.; Sarovar, M.; Whaley, K. B. Unraveling excitation energy transfer assisted by collective behaviors of vibrations, *New Journal of Physics*, *23* (7), 073012, **2021**.

[231] Kim, C. W.; Lee, W.-G.; Kim, I.; Rhee, Y. M. Effect of Underdamped Vibration on Excitation Energy Transfer: Direct Comparison between Two Different Partitioning Schemes, *The Journal of Physical Chemistry A*, *123* (6), 1186–1197, **2019**.

[232] Arsenault, E. A.; Schile, A. J.; Limmer, D. T.; Fleming, G. R. Vibronic coupling in energy transfer dynamics and two-dimensional electronic–vibrational spectra, *The Journal of Chemical Physics*, *155* (5), 054201, **2021**.

[233] Patra, S.; Tiwari, V. Vibronic resonance along effective modes mediates selective energy transfer in excitonically coupled aggregates, *The Journal of Chemical Physics*, *156* (18), 184115, **2022**.

[234] Yan, Y.; Liu, Y.; Xing, T.; Shi, Q. Theoretical study of excitation energy transfer and nonlinear spectroscopy of photosynthetic light-harvesting complexes using the nonperturbative reduced dynamics method, *WIREs Computational Molecular Science*, *11* (3), e1498, **2021**.

[235] Roden, J.; Schulz, G.; Eisfeld, A.; Briggs, J. Electronic energy transfer on a vibronically coupled quantum aggregate, *The Journal of Chemical Physics*, *131* (4), 044909, **2009**.

[236] Mulliken, R. S. Molecular compounds and their spectra. II, *Journal of the American Chemical Society*, *74* (3), 811–824, **1952**.

[237] Lippert, E. Spektroskopische Bestimmung des Dipolmomentes aromatischer Verbindungen im ersten angeregten Singulettzustand, *Zeitschrift für Elektrochemie, Berichte der Bunsengesellschaft für physikalische Chemie*, *61* (8), 962–975, **1957**.

[238] Kawski, A.; Bojarski, P.; Kukliński, B. Estimation of ground- and excited-state dipole moments of Nile Red dye from solvatochromic effect on absorption and fluorescence spectra, *Chemical Physics Letters*, *463* (4), 410–412, **2008**.

[239] Feinberg, D.; Ciuchi, S.; de Pasquale, F. Squeezing phenomena in interacting electron-phonon systems, *International Journal of Modern Physics B*, *04* (07n08), 1317–1367, **1990**.

[240] Giavazzi, D.; Di Maiolo, F.; Painelli, A. The fate of molecular excited states: modeling donor–acceptor dyes, *Phys. Chem. Chem. Phys.*, *24*, 5555–5563, **2022**.

[241] Mondelo-Martell, M.; Brey, D.; Burghardt, I. Quantum dynamical study of inter-chain exciton transport in a regioregular P3HT model system at finite temperature: HJ vs H-aggregate models, *The Journal of Chemical Physics*, *157* (9), 094108, **2022**.

[242] Chen, L.; Zheng, R.; Shi, Q.; Yan, Y. Optical line shapes of molecular aggregates: Hierarchical equations of motion method, *The Journal of Chemical Physics*, *131* (9), 094502, **2009**.

[243] Di Liberto, G.; Conte, R.; Ceotto, M. "Divide and conquer" semiclassical molecular dynamics: A practical method for spectroscopic calculations of high dimensional molecular systems, *The Journal of Chemical Physics*, *148* (1), 014307, **2018**.

[244] Fresch, E.; Meneghin, E.; Agostini, A.; Paulsen, H.; Carbonera, D.; Collini, E. How the Protein Environment Can Tune the Energy, the Coupling, and the Ultrafast Dynamics of Interacting Chlorophylls: The Example of the Water-Soluble Chlorophyll Protein, *The Journal of Physical Chemistry Letters*, *11* (3), 1059–1067, **2020**.

[245] Fresch, E.; Peruffo, N.; Trapani, M.; Cordaro, M.; Bella, G.; Castriciano, M. A.; Collini, E. The effect of hydrogen bonds on the ultrafast relaxation dynamics of a BODIPY dimer, *The Journal of Chemical Physics*, *154* (8), 084201, **2021**.

[246] Hong, Y.; Schlosser, F.; Kim, W.; Würthner, F.; Kim, D. Ultrafast Symmetry-Breaking Charge Separation in a Perylene Bisimide Dimer Enabled by Vibronic Coupling and Breakdown of Adiabaticity, *Journal of the American Chemical Society*, *144* (34), 15539–15548, **2022**.

[247] Das, S.; Thomas, K. G.; Ramanathan, R.; George, M. V.; Kamat, P. V. Photochemistry of squaraine dyes. 6. Solvent hydrogen bonding effects on the photophysical properties of bis(benzothiazolylidene)squaraines, *J. Phys Chem.*, *97* (51), 13625–13628, **1993**.

[248] Chung, S.-J. et al. Extended Squaraine Dyes with Large Two-Photon Absorption Cross-Sections, *J. Am. Chem. Soc.*, *128* (45), 14444–14445, **2006**.

[249] Jisha, V. S.; Arun, K. T.; Hariharan, M.; Ramaiah, D. Site-Selective Binding and Dual Mode Recognition of Serum Albumin by a Squaraine Dye, *J. Am. Chem. Soc.*, *128* (18), 6024–6025, **2006**.

[250] Sreejith, S.; Carol, P.; Chithra, P.; Ajayaghosh, A. Squaraine dyes: a mine of molecular materials, *J. Mater. Chem.*, *18* (3), 264–274, **2008**.

[251] Beverina, L.; Salice, P. Squaraine Compounds: Tailored Design and Synthesis towards a Variety of Material Science Applications, *Eur. J. Org.c Chem.*, *2010* (7), 1207–1225, **2010**.

[252] Sissa, C.; Terenziani, F.; Painelli, A.; Siram, R. B. K.; Patil, S. Spectroscopic Characterization and Modeling of Quadrupolar Charge-Transfer Dyes with Bulky Substituents, *J. Phys. Chem. B*, *116* (16), 4959–4966, **2012**.

[253] Liu, T.; Liu, X.; Wang, W.; Luo, Z.; Liu, M.; Zou, S.; Sissa, C.; Painelli, A.; Zhang, Y.; Vengris, M.; Bondar, M. V.; Hagan, D. J.; Van Stryland, E. W.; Fang, Y.; Belfield, K. D. Systematic Molecular Engineering of a Series of Aniline-Based Squaraine Dyes and Their Structure-Related Properties, *J. Phys. Chem. C*, *122* (7), 3994–4008, **2018**.

[254] Avila Ferrer, F. J.; Angeli, C.; Cerezo, J.; Coriani, S.; Ferretti, A.; Santoro, F. The Intriguing Case of the One-Photon and Two-Photon Absorption of a Prototypical Symmetric Squaraine: Comparison of TDDFT and Wave-Function Methods, *ChemPhotoChem*, *3* (9), 778–793, **2019**.

[255] He, J.; Jo, Y. J.; Sun, X.; Qiao, W.; Ok, J.; Kim, T.-i.; Li, Z. Squaraine Dyes for Photovoltaic and Biomedical Applications, *Adv. Funct. Mater.*, *31* (12), 2008201, **2020**.

[256] Avila Ferrer, F. J.; Angeli, C.; Cerezo, J.; Coriani, S.; Ferretti, A.; Santoro, F. The Intriguing Case of the One-Photon and Two-Photon Absorption of a Prototypical Symmetric Squaraine: Comparison of TDDFT and Wave-Function Methods, *ChemPhotoChem*, *3* (9), 778–793, **2019**.

[257] Basheer, M.; Santhosh, U.; Alex, S.; Thomas, K. G.; Suresh, C. H.; Das, S. Design and synthesis of squaraine based near infrared fluorescent probes, *Tetrahedron*, *63* (7), 1617–1623, **2007**.

[258] Ahn, H.-Y.; Yao, S.; Wang, X.; Belfield, K. D. Near-Infrared-Emitting Squaraine Dyes with High 2PA Cross-Sections for Multiphoton Fluorescence Imaging, *ACS Appl. Mater. Interfaces*, *4* (6), 2847–2854, **2012**.

[259] Magistris, C.; Martiniani, S.; Barbero, N.; Park, J.; Benzi, C.; Anderson, A.; Law, C.; Barolo, C.; O'Regan, B. Near-infrared absorbing squaraine dye with extended π conjugation for dye-sensitized solar cells, *Renewable Energy*, *60*, 672–678, **2013**.

[260] Strassel, K.; Hu, W.-H.; Osbild, S.; Padula, D.; Rentsch, D.; Yakunin, S.; Shynkarenko, Y.; Kovalenko, M.; Nüesch, F.; Hany, R.; Bauer, M. Shortwave infrared-absorbing squaraine dyes for all-organic optical upconversion devices, *Science and Technology of Advanced Materials*, *22* (1), 194–204, **2021**.

[261] Sreejith, S.; Joseph, J.; Lin, M.; Menon, N. V.; Borah, P.; Ng, H. J.; Loong, Y. X.; Kang, Y.; Yu, S. W.-K.; Zhao, Y. Near-Infrared Squaraine Dye Encapsulated Micelles for *in Vivo* Fluorescence and Photoacoustic Bimodal Imaging, *ACS Nano*, *9* (6), 5695–5704, **2015**.

[262] Abdullaeva, O. S.; Balzer, F.; Schulz, M.; Parisi, J.; Lützen, A.; Dedek, K.; Schiek, M. Organic Photovoltaic Sensors for Photocapacitive Stimulation of Voltage-Gated Ion Channels in Neuroblastoma Cells, *Adv. Funct. Mater.*, *29* (21), 1805177, **2019**.

[263] Avirah, R. R.; Jayaram, D. T.; Adarsh, N.; Ramaiah, D. Squaraine dyes in PDT: from basic design to in vivo demonstration, *Org. Biomol. Chem.*, *10* (5), 911–920, **2012**.

[264] Babu, P. S. S.; Manu, P. M.; Dhanya, T. J.; Tapas, P.; Meera, R. N.; Surendran, A.; Aneesh, K. A.; Vadakkancheril, S. J.; Ramaiah, D.; Nair, S. A.; Pillai, M. R. Bis(3,5-diiodo-2,4,6-trihydroxyphenyl)squaraine photodynamic therapy disrupts redox homeostasis and induce mitochondria-mediated apoptosis in human breast cancer cells, *Sci. Rep.*, *7* (1), 42126, **2017**.

[265] Chen, G.; Sasabe, H.; Lu, W.; Wang, X.-F.; Kido, J.; Hong, Z.; Yang, Y. J-aggregation of a squaraine dye and its application in organic photovoltaic cells, *J. Mater. Chem. C*, *1* (40), 6547, **2013**.

[266] Maeda, T.; Nguyen, T. V.; Kuwano, Y.; Chen, X.; Miyanaga, K.; Nakazumi, H.; Yagi, S.; Soman, S.; Ajayaghosh, A. Intramolecular Exciton-Coupled Squaraine Dyes for Dye-Sensitized Solar Cells, *J. Phys. Chem. C*, *122* (38), 21745–21754, **2018**.

[267] Chen, Y.; Zhu, W.; Wu, J.; Huang, Y.; Facchetti, A.; Marks, T. J. Recent Advances in Squaraine Dyes for Bulk-Heterojunction Organic Solar Cells, *Organic Photonics and Photovoltaics*, *6* (1), 1–16, **2019**.

[268] Das, S.; Thomas, K. G.; Thomas, K. J.; Madhavan, V.; Liu, D.; Kamat, P. V.; George, M. V. Aggregation Behavior of Water Soluble Bis(benzothiazolylidene)squaraine Derivatives in Aqueous Mediasup†/sup, *J. Phys. Chem.*, *100* (43), 17310–17315, **1996**.

[269] Alex, S.; Basheer, M. C.; Arun, K. T.; Ramaiah, D.; Das, S. Aggregation Properties of Heavy Atom Substituted Squaraine Dyes: Evidence for the Formation of J-Type Dimer Aggregates in Aprotic Solvents, *J. Phys. Chem. A*, *111* (17), 3226–3230, **2007**.

[270] Spencer, S. D.; Bougher, C.; Heaphy, P. J.; Murcia, V. M.; Gallivan, C. P.; Monfette, A.; Andersen, J. D.; Cody, J. A.; Conrad, B. R.; Collison, C. J. The effect of controllable thin film crystal growth on the aggregation of a novel high panchromaticity squaraine viable for organic solar cells, *Solar Energy Materials and Solar Cells*, *112*, 202–208, **2013**.

[271] Brück, S.; Krause, C.; Turrisi, R.; Beverina, L.; Wilken, S.; Saak, W.; Lützen, A.; Borchert, H.; Schiek, M.; Parisi, J. Structure–property relationship of anilino-squaraines in organic solar cells, *Phys. Chem. Chem. Phys.*, *16* (3), 1067–1077, **2014**.

[272] Zheng, C.; Jalan, I.; Cost, P.; Oliver, K.; Gupta, A.; Misture, S.; Cody, J. A.; Collison, C. J. Impact of Alkyl Chain Length on Small Molecule Crystallization and Nanomorphology in Squaraine-Based Solution Processed Solar Cells, *J. Phys. Chem. C*, *121* (14), 7750–7760, **2017**.

[273] Paternò, G. M.; Moretti, L.; Barker, A. J.; D'Andrea, C.; Luzio, A.; Barbero, N.; Galliano, S.; Barolo, C.; Lanzani, G.; Scotognella, F. Near-infrared emitting single squaraine dye aggregates with large Stokes shifts, *J. Mater. Chem. C*, *5* (31), 7732–7738, **2017**.

[274] Zheng, C.; Mark, M. F.; Wiegand, T.; Diaz, S. A.; Cody, J.; Spano, F. C.; McCamant, D. W.; Collison, C. J. Measurement and Theoretical Interpretation of Exciton Diffusion as a Function of Intermolecular Separation for Squaraines Targeted for Bulk Heterojunction Solar Cells, *J. Phys. Chem. C*, *124* (7), 4032–4043, **2020**.

[275] Wiegand, T.; Godoy, J.; Gupta, S.; Cody, J.; Coffey, T.; Collison, C.-J. Optimal morphology, H-aggregation, and ternary blend excited state disruption in equilibrated squaraine-based all small molecule solar-cells, *Thin Solid Films*, 139623, **2022**.

[276] D'Avino, G.; Terenziani, F.; Painelli, A. Aggregates of quadrupolar dyes: Giant two-photon absorption from biexciton states, *J. Phys. Chem. B*, *110* (51), 25590–25592, **2006**.

[277] Jyothish, K.; Hariharan, M.; Ramaiah, D. Chiral Supramolecular Assemblies of a Squaraine Dye in Solution and Thin Films: Concentration-, Temperature-, and Solvent-Induced Chirality Inversion, *Chemistry – A European Journal*, *13* (20), 5944–5951, **2007**.

[278] Schulz, M.; Zablocki, J.; Abdullaeva, O. S.; Brück, S.; Blazer, F.; Lützen, A.; Arteaga, O.; Schiek, M. Giant intrinsic circular dichroism of prolinol-derived squaraine thin films, *Nat. Commun.*, *9* (2413), 2413, **2018**.

[279] Hestand, N. J.; Zheng, C.; Penmetcha, A. R.; Cona, B.; Cody, J. A.; Spano, F. C.; Collison, C. J. Confirmation of the origins of panchromatic spectra in squaraine thin films targeted for organic photovoltaic devices, *J. of Phys. Chem. C*, *119* (33), 18964–18974, **2015**.

[280] Balzer, F.; Hestand, N. J.; Zablocki, J.; Schnakenburg, G.; Lützen, A.; Schiek, M. Spotlight on Charge-Transfer Excitons in Crystalline Textured *n*-Alkyl Anilino Squaraine Thin Films, *J. Phys. Chem. C*, *126* (32), 13802–13813, **2022**.

[281] Bernhardt, R.; Manrho, M.; Zablocki, J.; Rieland, L.; Lützen, A.; Schiek, M.; Meerholz, K.; Zhu, J.; Jansen, T. L. C.; Knoester, J.; van Loosdrecht, P. H. M. Structural Disorder as the Origin of Optical Properties and Spectral Dynamics in Squaraine Nano-Aggregates, *J. Am. Chem. Soc.*, *144* (42), 19372–19381, **2022**.

[282] Timmer, D.; Zheng, F.; Gittinger, M.; Quenzel, T.; Lünemann, D. C.; Winte, K.; Zhang, Y.; Madjet, M. E.; Zablocki, J.; Lützen, A.; Zhong, J.-H.; Sio, A. D.; Frauenheim, T.; Tretiak, S.; Lienau, C. Charge Delocalization and Vibronic Couplings in Quadrupolar Squaraine Dyes, *J. Am. Chem. Soc.*, *144* (41), 19150–19162, **2022**.

[283] Anzola, M. Modeling electrostatic interactions in complex systems, Ph.D. Thesis, University of Parma, 2021.

[284] Huu, D. K. A. P.; Sissa, C.; Terenziani, F.; Painelli, A. Optical spectra of organic dyes in condensed phases: the role of the medium polarizability, *Phys. Chem. Chem. Phys.*, *22* (44), 25483–25491, **2020**.

[285] Bardi, B.; Dall'Agnese, C.; Tassé, M.; Ladeira, S.; Painelli, A.; Moineau-Chane Ching, K. I.; Terenziani, F. Multistimuli-Responsive Materials from Benzothiadiazole-Based Charge-Transfer Chromophores: Interdependence of Optical Properties and Aggregation, *Chem. Photo. Chem.*, *2* (12), 1027–1037, **2018**.

[286] Kar, S.; Swathi, K.; Sissa, C.; Painelli, A.; Thomas, K. G. Emergence of Chiroptical Properties in Molecular Assemblies of Phenyleneethynylenes: The Role of Quasi-degenerate Excitations, *J. Phys. Chem. Lett.*, *9* (16), 4584–4590, **2018**.

[287] Giavazzi, D.; Saseendran, S.; Di Maiolo, F.; Painelli, A. A Comprehensive Approach to Exciton Delocalization and Energy Transfer, *Journal of Chemical Theory and Computation*, *19* (2), 436–447, **2023**.

[288] Condon, E. U. Theories of Optical Rotatory Power, *Reviews of Modern Physics*, *9* (4), 432–457, **1937**.

[289] Craig, D. P.; Thirunamachandran, T., *Molecular Quantum Electrodynamics*; Academic Press: 1984.

[290] Giavazzi, D.; Schumacher, M. F.; Grisanti, L.; Anzola, M.; Di Maiolo, F.; Zablocki, J.; Lützen, A.; Schiek, M.; Painelli, A. A marvel of chiral squaraine aggregates: chiroptical spectra beyond the exciton model, *J. Mater. Chem. C*, *11*, 8307–8321, **2023**.

[291] Bertocchi, F.; Sissa, C.; Painelli, A. Circular dichroism of molecular aggregates: A tutorial, *Chirality*, *35* (10), 681–691, **2023**.

[292] Bardi, B.; Dall'Agnese, C.; Moineau-Chane Ching, K. I.; Painelli, A.; Terenziani, F. Spectroscopic Investigation and Theoretical Modeling of Benzothiadiazole-Based Charge-Transfer Chromophores: From Solution to Nanoaggregates, *The Journal of Physical Chemistry C*, *121* (32), 17466–17478, **2017**.

[293] Padula, D.; Santoro, F.; Pescitelli, G. A simple dimeric model accounts for the vibronic ECD spectra of chiral polythiophenes in their aggregated states, *RSC Adv.*, *6*, 37938–37943, **2016**.

[294] Dhali, R.; Phan Huu, D. K. A.; Bertocchi, F.; Sissa, C.; Terenziani, F.; Painelli, A. Understanding TADF: a joint experimental and theoretical study of DMAC-TRZ, *Physical Chemistry Chemical Physics*, *23* (1), 378–387, **2021**.

[295] Hestand, N. J.; Spano, F. C. Interference between Coulombic and CT-mediated couplings in molecular aggregates: H- to J-aggregate transformation in perylene-based -stacks, *The Journal of Chemical Physics*, *143* (24), 244707, **2015**.